

# A Study of the Raindrop Size Distribution and its effect on Microwave Attenuation

Townsend, Adrian

*Award date:*
2011

*Awarding institution:*
University of Bath

# A STUDY OF THE RAINDROP SIZE DISTRIBUTION AND ITS EFFECT ON MICROWAVE ATTENUATION

**Adrian Justin Townsend**

**A thesis submitted for the degree of Doctor of Philosophy**
**University of Bath**
**Department of Electronic and Electrical Engineering**

**June 2011**

## COPYRIGHT



**Adrian Justin Townsend**

**Abstract**

Current frequency allocations below Ku- band are becoming increasingly congested. The problem continues to grow as the use of telecommunications becomes more popular. In order to compensate for increased in demand, telecommunication operating frequencies have to be raised, yielding larger channel capacity. However, raising the operating frequency has the adverse result of intensifying the attenuation effects of the troposphere. At high frequencies, such as V-band, rain is known to cause the most severe attenuation.

It has been shown that model data for numerical weather prediction, combined with propagation prediction models, can be used to forecast telecommunication link attenuation. The forecast of attenuation can be used to improve the effectiveness of fade mitigation techniques. A key problem in determining rain attenuation from rainfall rate is the considerable variability of the raindrop size distribution (DSD). Based on the analysis of disdrometer and numerical weather prediction model data, the aim of this work is to constrain the parameters of the DSD and ultimately generate probabilistic forecasts of attenuation.

Using disdrometer analysis, a relationship between mean raindrop size and rainfall rate is established, and a link between drop concentration and rainfall rate is also demonstrated. The DSD is shown to vary with season and shows some small relationships with meteorological parameters. It is concluded that, despite some relation of the DSD with rainfall rate and meteorological parameters, there are too many variables to conclusively recreate the DSD.

Analysis of the attenuation-rainfall rate relationship illustrates that variability due to the DSD increases with frequency above 40 GHz. At 30-40 GHz the DSD is shown to have little impact on the attenuation-rainfall rate relationship. Finally, this thesis examines the horizontal structure of rain cells in the UK, demonstrating the suitability of the EXCELL model and illustrating that rain cells are more elliptical in the UK.

# Acknowledgements

My thanks go to my supervisor Robert Watson for his advice and support during this project. I would also like to thank Ivan Astin, my personal mentor, and Peter Watson as well as the rest of the TSaR/CSAOS group at the University of Bath.

I am grateful for the financial support from the EPSRC. I would like to thank the BADC, RAL and the UK Met Office for supplying data for this project.

# Contents

# List of Figures

# List of Tables

# Acronyms

| | |
|---|---|
| AEHF | Advanced Extremely High Frequency |
| AH | Absolute Humidity |
| BADC | British Atmospheric Data Centre |
| BER | Bit Error Rate |
| CAPE | Convective Available Potential Energy |
| CDF | Cumulative Density Function |
| CLAI | Cloud Analysis Image |
| COMSAT | Communication Satellite Corporation |
| DP | Dew Point |
| DSD | Raindrop Size Distribution |
| DVB | Digital Video Broadcasting |
| EHF | Extra High Frequency |
| EIRP | Effective Isotropic Radiated Power |
| El | Equilibrium Level |
| ESA | European Space Agency |
| FMT | Fade Mitigation Technique |
| ITU | International Telecommunications Union |
| LFC | level of Free Convection |
| LI | Lifted Index |
| LWC | Liquid Water Content |
| MSG | Meteosat Second Generation |
| MRO | Mars Reconnaissance Orbiter |
| NASA | National Aeronautics and Space Administration |
| P | Pressure |
| PCA | Principal Component Analysis |
| PVAF | Percentage Variance Accounted For |
| RH | Relative Humidity |
| RMS | Root Mean Square |
| SHF | Super High Frequency |
| SMOS | Soil Moisture and Ocean Salinity |
| TTC | Tracking Telemetry and Command stations |
| UHF | Ultra High Frequency |
| UM | Unified Model |
| WD | Wind Direction |
| WS | Wind Speed |

# List of Symbols

| | |
|---|---|
| $\alpha$ | Linear fit coefficient of $A$-$R$ |
| $\Delta D$ | Bin width of drop size class |
| $\delta K$ | Percentage difference in specific attenuation |
| $\Delta y$ | Difference in measured data and true model |
| $\eta$ | Antenna efficiency |
| $\Gamma$ | Gamma function |
| $\kappa$ | Number of elements in data set |
| $\Lambda$ | Parameter of the Gamma raindrop size distribution, |
| $\Lambda_e$ | Parameter of the Marshall and Palmer raindrop size distribution, |
| $\mu$ | Distribution shape parameter |
| $\psi$ | Digamma function |
| $\rho_{max}$ | Max gyration radii of rain cell |
| $\rho_{min}$ | Min gyration radii of rain cell |
| $\rho_v$ | Water vapour density |
| $\rho_x$ | Cell radii along x axis |
| $\rho_y$ | Cell radii along y axis |
| $\sigma$ | Standard deviation |
| $\sigma_A$ | Attenuation standard deviation |
| $\sigma_g$ | Standard geometric deviation |
| $\theta$ | Angle of rotation |
| $a$ | Power law coefficient of $A$-$R$ relationship |
| $A$ | Specific attenuation |
| $\overline{A}$ | Mean attenuation |
| $A_d$ | Measurement area of disdrometer |
| $a_E$ | Exponential component x axis axial radii |
| $a_G$ | Gaussian component x axis axial radii |
| AH | Absolute Humidity |
| $A_l$ | Specific attenuation determined by linear fit to $A$-$R$ |
| $A_p$ | Specific attenuation determined by power law fit to $A$-$R$ |
| $A_r$ | Area of rain cell |
| $B$ | Bandwidth |
| $b$ | Power law coefficient of $A$-$R$ relationship |
| $b_E$ | Exponential component y axis axial radii |
| $b_G$ | Gaussian component y axis axial radii |
| $c$ | Power law coefficient of standard deviation $A$-$R$ relationship |
| $C$ | Ratio of received carrier power |
| $c$ | Total number of drops |
| $c_i$ | Disdrometer channel number |

| | |
|---|---|
| $c_l$ | Speed of light |
| $D$ | Drop diameter |
| $\overline{D}$ | Drop size arithmetic mean |
| $d$ | Power law coefficient of standard deviation $A$-$R$ relationship |
| $D_{ci}$ | Lower boundary of the disdrometer channel |
| $D_a$ | Antenna diameter |
| $D_g$ | Drop size geometric mean diameter |
| $D_{ir}$ | Directivity |
| $D_m$ | Mass weighted mean drop diameter |
| $d_{kr}^2$ | Spearman's rank difference in rank |
| $E$ | Elliptic integral of the second kind |
| $e$ | Partial pressure of water vapour |
| $E_{\mathrm{PVAF}}$ | Difference in PVAF |
| $E_a$ | Percentage difference in attenuation |
| $e_r$ | Elliptical ratio |
| $E_R$ | Percentage error of model and radar rain cell parameters |
| $E_v$ | Eigenvector |
| erf | Error function |
| $e_s$ | Saturation vapour pressure |
| $E^s$ | Electric field of the scattered wave in the far field region |
| $f$ | Frequency |
| $F_V$ | Feature vector |
| $G$ | Antenna gain |
| $\overline{G}$ | Mean horizontal gradient |
| $G_{rms}$ | RMS horizontal gradient |
| $h_c$ | Height from cloud base |
| $I_{xy}$ | Moment of inertia in the cell barycentre reference |
| $I_x$ | Central moments of inertia along x axis |
| $I_y$ | Central moments of inertia along y axis |
| $k$ | Free space propagation constant |
| $\overline{K}$ | Average specific attenuation |
| $k_r$ | Radiation efficiency |
| $l$ | Length of rain cell |
| $L$ | Likelihood |
| $L_{\mathrm{PVAF}}$ | PVAF of linear fit |
| $L_t$ | Link length |
| $\lambda$ | Wavelength |
| $m_d$ | Mass of dry air |
| $m_n$ | Moment of $n^{\mathrm{th}}$ order |
| $m_v$ | Mass of water vapour |
| $N$ | Number of data points |
| $n$ | Order of moment |
| $\overline{N(D)}$ | Mean raindrop size distribution |
| $N(D)$ | Raindrop size distribution |
| $N(D)_{\mathrm{Total}}$ | Sum total of DSD |
| $N_0$ | Noise power spectral density |
| $n_c$ | Number of disdrometer channels |
| $n_s$ | Number of data points |
| $N_T$ | Mean drop concentration |

| | |
|---|---|
| $N_t$ | Total number of drops in a given volume |
| $N_w$ | Normalise Gamma intercept parameter |
| $\overline{O}$ | Original PCA data mean |
| $P_{\mathrm{PVAF}}$ | PVAF of power law fit |
| $P_D$ | PCA derived data |
| $P_m$ | Mean centred PCA data |
| $P_o$ | PCA data set |
| PVAF | Percentage variance accounted for |
| $p_w(t)$ | Liquid water fraction |
| $Q_c$ | Cumulative rainfall rate |
| $Q$ | Specific humidity |
| $Q_a$ | Absorption cross section |
| $Q_s$ | Scattering cross section |
| $Q_t$ | Total cross section |
| $r$ | Distance from origin to observation point |
| $R$ | Rainfall rate |
| $R^2$ | Variance accounted for |
| $\overline{R}$ | Mean rainfall rate |
| $R_1$ | HYCELL threshold between exponential and Gaussian |
| $R_2$ | Rainfall rate threshold of rain cell |
| $R_G$ | Peak rainfall rate of HYCELL model |
| RH | Relative Humidity |
| $R_M$ | Peak rainfall rate of EXCELL model |
| $R_p$ | Peak rainfall rate of radar derived rain cell |
| $R_{pl}$ | Rainfall rate determined from power law fit of $A$-$R$ |
| $R_v$ | Specific gas constant for water |
| $S_{pr}$ | Spearman's rank coefficient |
| $T$ | Temperature |
| $T_i$ | Time interval |
| $t$ | Time |
| $T_d$ | Dew point |
| $U$ | Zonal wind component |
| $u_c$ | Critical humidity |
| $V$ | Meridional wind component |
| $v(D)$ | Raindrop fall velocity of drop diameter $D$ |
| $w$ | Liquid water content |
| $W$ | Vertical wind component |
| $w_r$ | Mixing ratio |
| $z$ | Height |

# Chapter 1

# Introduction

Telecommunications and broadcasting services are in a rapid phase of expansion. Users are demanding ever more multimedia services such as high-speed internet, on demand digital TV services, video conferencing and tele-education to name a few. Such services require high-speed data rates to cope with demand whilst guaranteeing customers a high quality of service.

The current microwave frequency spectrum allocated for telecommunication and broadcast services has become congested and proposed broadband systems will require higher bandwidths. SHF and EHF services are relatively free of congestion and can cope with higher data rates than current microwave systems. However, above Ka- band, attenuation due to atmospheric gases, clouds and rain increases significantly. Whilst attenuation is caused more frequently by clouds and gases, it is rain that causes the largest attenuation.

The use of numerical weather data combined with propagation models can be used to forecast telecommunication link attenuation, Hodges [2006]. The forecast of link attenuation can be used to improve the effectiveness of fade mitigation techniques. For a given rainfall rate, the raindrop size distribution (DSD) can vary considerably, resulting in significant variation in attenuation. This thesis investigates attenuation caused by rain and the effect of the DSD in order to better understand the impact of using SHF/EHF, and ultimately help improve the effectiveness of propagation models.

## 1.1 Satellite systems history

During World War II, the rapid advancement of missile and microwave technology led to the development of satellite communications. The initial satellite concept originated with RAF officer Arthur C Clarke, writing an article in *'Wireless World'*, describing manned satellites orbiting the Earth every 24 hours and distributing television broadcasts. Though famous today for both science fiction stories and his inventions, Clarke's satellite concept had little impact, even after being repeated in 1951. It was not until 1954 that the potential of satellite communications became evident, after John R Pierce, of AT&T's Bell Telephone Laboratories, conducted a detailed evaluation of the technical and financial potential of satellites. Pierce decided to compare the first transatlantic telephone cable, carrying only 35 simultaneous calls at an installation cost of 30-50 million dollars in 1954, to a satellite that could implement 1000 simultaneous calls, worth one billion dollars.

The satellite era truly began in 1957 when the first satellite, Sputnik I, was launched by Russia prompting America to respond by developing and producing its own satellites. Therefore, NASA decided to develop passive communication satellites, such as the passive repeater ECHO 1, while the Department of Defence concentrated on active satellites. In 1961, the formal start of medium-earth-orbit satellites such as TELSTAR, by AT&T, and RELAY, by the company RCA, began. A further contract was awarded to Hughes Aircraft Company to design a 24 hour orbiting satellite, known as SYNCOM. The TELSTAR and RELAY satellites were first launched in 1962 and successfully broadcasted parts of the 1964 Olympics from Tokyo. At this time, COMSAT, (Communication Satellite Corporation) began developing its first satellite, which lead to the launch of the EARLY BIRD, in 1965, initiating global communications. Early Bird or INTELSAT 1 was the first geostationary satellite. 1965 also saw the start of the first Soviet communication satellites launched with the MOLNYA series.

In 1964 an agreement was signed by thirteen countries with existing satellite technology (such as the United States, United Kingdom, France, Germany, Italy, Brazil, and Japan) to create the International Telecommunications Satellite Organisation, INTELSAT. The organisation had the ultimate aim to assume ownership of all satellites and take responsibility for the management of global systems. INTELSAT has grown to have more members than the United Nations and is able to provide hundreds of thousands of telephone circuits. The use of satellite communications has rapidly increased, facilitated by the development of new technology and reduced production costs that make the various services both affordable and useful to the consumer.

Increasing expertise, advancing technology and the reduction of costs in the satellite

industry have led to reliable launchers and more complex satellites with increasingly advanced technology for multiple uses. Satellite objectives range from measuring the Earth's water cycle, for example the SMOS (Soil Moisture and Ocean Salinity) satellite programme launched by ESA in 2009, to global navigation satellite systems such as the European Union project Galileo. New advancements include contoured multibeam antennas (where beams adapt to the shape of the continents) and frequency reuse from one beam to another. These advances have led to increased efficiency and capacity, which has in turn reduced costs further.

## 1.2 Satellite systems

The design of a satellite system is based on the service required (e.g. video, voice or data transmission) and is constrained by variables such as cost and available technology. It may also be required to form part of a larger network operating within the complete system, often requiring complex design to achieve an optimum configuration.

A typical satellite system consists of space, control and ground components. The space segment is comprised of several active and spare satellites. The control aspects, TTC (tracking telemetry and command stations), include facilities for monitoring and controlling satellite traffic and resources. Finally, the ground segment incorporates earth traffic stations, such as mobile stations or handsets.

Satellites orbit the Earth in a variety of different ways, including low earth orbits ($\approx$780 km), for real-time communication, medium earth orbits ($\approx$10 000 km with an orbit around 6 hours) and geostationary orbits (35 786 km) with period equal to the rotation of the earth.

Satellite communication links consist of uplinks, downlinks or inter-satellite links. Uplinks and downlinks are radio-frequency modulated carriers where as inter-satellite links can be radio or optical signals. When designing a satellite system it is important to consider the transmit performance, measured by the effective isotropic radiated power (EIRP). The transmitted power must be great enough to overcome propagation losses in order to ensure a signal is successfully received. Link performance can be measured by the ratio of received carrier power, C, and the noise power spectral density, $N_0$. This can be used to determine quality of service, in terms of signal to noise ratio or bit error rate (BER).

Other considerations include the amount and type of data being transmitted. A larger amount of data or users may require higher frequencies or larger bandwidths ($B$).

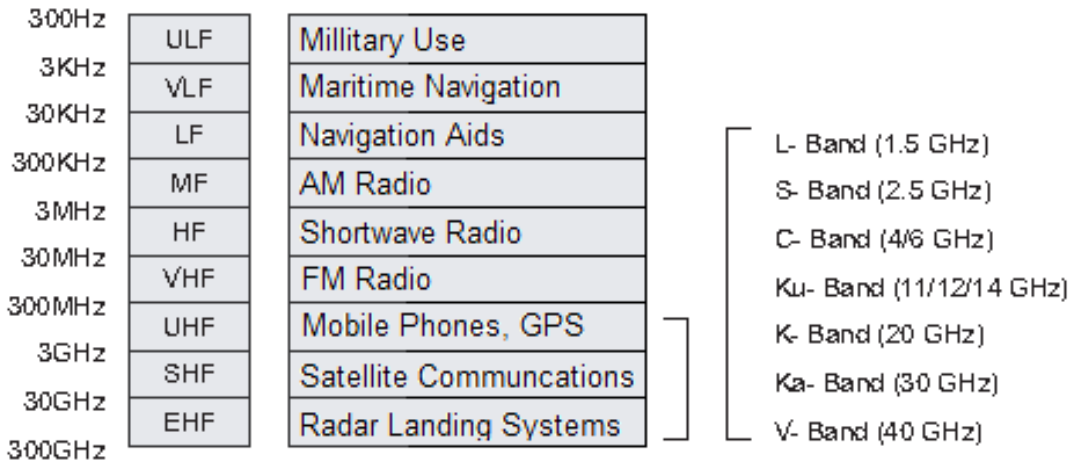


Figure 1.1: Radio frequency band allocations as defined in ITU-R V.431-7.

Bandwidth depends on base band signal and type of modulation. There is a trade off between the required carrier power and occupied bandwidth particularly users of satellites are charged for power or bandwidth resources used. Frequency not only affects the amount of data that can be transmitted but affects signal fade along the propagation path. To maintain efficient and economical use of the radio frequency spectrum, regulations are necessary. The International Telecommunication Union (ITU), a United Nations organisation, creates radio regulations.

## 1.3 EHF and SHF satellite systems

Typical satellite systems operate in the UHF, EHF and SHF frequency bands. Figure 1.1 shows the frequency allocation of the radio spectrum. EUTELSAT HOT BIRD 10 is an example of a Ku-band satellite broadcasting almost 1 100 channels to 120 million homes in Europe, North Africa and the Middle East. KA-SAT is an example of a Ka-band satellite launched December 2010. The satellite is an advanced, multi-spot satellite that utilises over 80 spot beams, which will be the beginning of a new satellite infrastructure that will expand the capacity of broadband services across Europe and the Mediterranean Basin. KA-SAT will join the HOT BIRD broadcasting satellites with the aim of providing new media services through Ka-band frequencies.

The growing demand on satellite communication systems has resulted in the current frequency bands becoming increasingly congested, Panagopoulos et al. [2004]. In order to compensate for the increase in demand, satellite operating frequencies have to be raised to deliver larger channel capacity, for example EUTELSAT HOT BIRD 6 and the

United States Air Force's Advanced Extremely High Frequency (AEHF) satellites are operating at Ku- and Ka-band frequencies. However, raising the operating frequency has both advantages and disadvantages on the design and implementation of satellite communications.

## 1.4 Advantages of EHF and SHF

There are several significant advantages to increasing satellite operating frequencies. These include reduction in satellite congestion, increased bandwidth for faster services and increased antenna gain.

### 1.4.1 Frequency allocations for Earth-space links

The current frequency allocations at L-, S-,C- and Ku- bands are becoming increasingly congested. This problem continues to escalate as the use of satellite communications becomes more popular and larger throughputs are required. Further allocation of frequency space requires increasingly complex methods for frequency re-use and allocation. It is for this reason that higher frequencies, such as V-band, are of great interest, since they are currently congestion free and theoretically have a larger capacity.

The number of geostationary satellites in orbit is another significant issue. Physical space in geostationary orbits above heavily populated areas, where communication is in great demand, is becoming limited. Increasing operating frequencies would reduce the number of satellites required, since the increased capacity of higher frequency systems would reduce the number of payloads for a given service. High frequency systems (Ka-bands and above) would also improve directivity of satellite beams, which could be exploited to increase satellite density.

### 1.4.2 Operating bandwidth

Increasing the operating frequency of satellites provides the option for larger bandwidths. This has the potential to provide services with bit-rates in the order of $\text{Gbs}^{-1}$, which is required for future high-definition services. Large bandwidths could also lead to the use of return-channel links and broadband connections via satellite. Internet protocol (IP) over satellite could be used to provide broadband services to remote areas of the world, disaster areas or locations without sufficient infrastructure to provide

broadband over terrestrial networks.

### 1.4.3 Antenna gain

A further advantage of increasing the satellite operating frequency is the increase in antenna gain, since gain of a parabolic antenna is linked with frequency through equation (1.1).

$$G = \eta \left( \frac{\pi D_a f}{c_l} \right)^2, \tag{1.1}$$

where $G$ is the antenna gain as a ratio to an isotropic antenna, $\eta$ is the antenna efficiency, $D_a$ is the antenna diameter (m), $f$ is the frequency (Hz) and $c_l$ is the speed of light ($\mathrm{ms}^{-1}$).

By increasing the frequency, the larger gain of the antenna can be used to either increase the effective isotropic radiated power or reduce the antenna size for the same radiated power. Reducing the size of antennas yields a substantial advantage for satellites since there are significant restrictions on both volume and weight when designing a satellite payload. Reduced antenna size also has the advantage of creating more attractive devices for commercial use and man-portable, high-gain antennas for network infrastructures in military applications.

The directivity of the antenna, Pennock and Shepherd [1998], will also increase with frequency, as shown by equation (1.2).

$$G = k_r D_{ir}, \tag{1.2}$$

where $k_r$ is the radiation efficiency and $D_{ir}$ is the directivity. Increased directivity can either be used to improve control over downlink spot beams or reduce separation between satellites, which can encourage frequency reuse and increased spectral efficiency.

## 1.5 Disadvantages of EHF

There are several disadvantages to using frequencies at KA-band and above. The use of extra high frequencies for satellite systems will lead to intensified attenuation as a signal propagates through the troposphere, as described by Arbesser-Rastburg and Paraboni [1997]. Further, high frequency electronic systems such as transistors become harder and more expensive to manufacture.

### 1.5.1 Technological limitations

The development of electronic systems to cope with high frequency operations is costly and problematic. Practicalities in developing and building transponders for EHF payloads have hampered the implementation of such technology for a long time. Travelling wave tube amplifiers (TWTAs) and other high power amplifiers were not readily available. It is also more difficult to develop and manufacture transistors to cope with high frequency switching.

However, as technology progresses and manufacturing processes improve, the implementation of high frequency payloads becomes easier and the cost of high frequency electronics reduces. High frequency, such 40 GHz, TWTAs are now available from Boeing.

### 1.5.2 Increased tropospheric attenuation

Increasing radio wave frequencies above Ka-band increases signal attenuation caused by factors in the troposphere. Radio waves propagating through rain, snow, hail or ice droplets will suffer from power loss due to hydrometeor scattering and absorption, Oguchi [1983]. At frequencies above 10 GHz scattering and absorption is increased. A typical rain fade incident can see peak values of approximately 15dB at the Ka-frequency band, Panagopoulos et al. [2004]. Cloud attenuation, tropospheric scintillation, oxygen and water vapour can also contribute to radio wave attenuation. However, whilst these factors occur more frequently, rain causes the largest magnitude of attenuation. Such effects are problematic since attenuation reduces the received power, which can lead to signal loss and a reduction in satellite system availability.

At frequencies Ka-band and above, rain is the largest cause of attenuation. Further, for a given rainfall rate the attenuation may vary considerably due to the DSD, Townsend et al. [2009]. The DSD, as described in Chapter2, is the number concentration of raindrops with diameter in a given volume of space. As the frequency of a radio wave is increased, the variability in attenuation caused by DSD increases, Townsend and Watson [2011], which makes it more difficult to counteract such attenuation.

Despite the disadvantages of increased radio wave attenuation, fade mitigation techniques (FMTs), Castanet [2001], can be implemented to compensate for attenuation effects and maintain a high system availability. The prediction of attenuation events can greatly improve the implementation and effectiveness of fade mitigation techniques, Panagopoulos et al. [2004]. There is a substantial advantage in predicting the rain fade

for satellites operating at such high frequencies, especially for systems broadcasting over great distances or long time-of-flight systems. For example, the Mars Reconnaissance Orbiter (MRO) could avoid loss of information due to rain attenuation.

## 1.6 Propagation channel modelling

The effectiveness of fade mitigation techniques can be improved with the use of propagation channel modelling. There are a variety of techniques used to model channel propagation in order to determine the total attenuation on a link. ITU-R P.618-8: Propagation data and prediction methods required for the design of Earth-space telecommunication systems, N-state Markov chain models, Synthetic storm technique, two sample model and the University of Bath propagation forecast engine are a few examples among many. Propagation modelling can be used to evaluate the behaviour and quality of service of communication systems, and helps the implementation of fade mitigation techniques, Panagopoulos et al. [2004].

### 1.6.1 ITU-R P.618-8

ITU-R recommendation P.618-8 estimates statistics of various propagation effects that should be considered in the design of earth-space links. Propagation effects such as absorption, scattering and depolarization by hydrometeors, absorption due to atmospheric gases, multipath effects and ionospheric effects (typically only notable below 1 GHz) can cause signal fade and need to be considered when implementing a satellite system to maintain a quality of service. Statistics for propagation effects provide an attenuation cumulative distribution function (CDF), which can be combined with further ITU-R recommendations to create an overall average annual attenuation CDF. Other ITU-R recommendations include rainfall rate, P.837-5, rain attenuation, P.838-3, cloud attenuation, P.840, and gas attenuation, P.676.

### 1.6.2 N-State Markov chain models

The N-state Markov model, Castanet et al. [2003], is based on two main components: a macroscopic model that has two states, rain or no rain: and the microscopic level, which fills rain events with attenuation time series. The macroscopic model is used to identify each rain event, based on two components, the probability of rain (typically based on ITU-R statistics) and the probability of change from rain to clear sky (typically defined

by Paraboni and Riva [1994]). The microscopic model follows an N-state Markov model, where N states are used to define attenuation levels. A fade slope model is used to define the probability of a particular fade slope given an attenuation level.

This approach uses ITU-R models (such as ITU-R P837 - Characteristics of precipitation for prorogation modelling) to provide annual statistics of rain occurrences, therefore, shorter periods could demonstrate considerable variation. The microscopic and macroscopic models are independent, which does not allow the microscopic model information about the length of an event.

### 1.6.3 Synthetic storm technique

The synthetic storm technique, developed by Matricciani [1996], takes a single site rainfall rate time series, typically from a rain gauge or disdrometer, and converts the values into an attenuation time series, based on a simple model of the vertical structure of precipitation. The model consists of two layers A and B. Layer A is a uniform rainfall rate, as measured at the ground, and layer B represents the melting layer, where ice hydrometeors begin at the top and transform into raindrops at the top of layer A, to calculate an attenuation time series. The synthetic storm technique is based on work by Drufuca [1974] proposing a similar method applied to terrestrial links in 1974, which was re-engineered for Earth space links.

### 1.6.4 Two sample model

The two sample model, developed by van de Kamp [2002b], can be used to generate attenuation time series for simulation or provide very short term ($\approx$ 10 seconds) propagation channel forecasts. The model predicts the probability distribution of attenuation given the previous two samples and the relative change in time. The technique is an extension of the hypothesis of near-future attenuation level as a function of the previous samples, Dossi [1990].

### 1.6.5 Hodges [2006] University of Bath propagation forecast engine

The Hodges [2006] University of Bath propagation forecast engine attempts to recreate the meteorological environment and hence a propagation channel, Hodges et al. [2006]. The method uses numerical weather predictions, which allows global coverage and has an abundance of data, including subtle meteorological phenomena. The technique is

not constrained to a single fixed link and may be used to model large variation in link characteristics. The system can provide information for time-coincident, multiple-site time series and use forecast data to create predictions of radio wave propagation. Rain attenuation is calculated based on the Leitao and Watson [1986] model, which uses two different raindrop size distributions (DSD) for convective and stratiform rain, in an attempt to reduce the effects caused by variability in raindrop size distribution.

## 1.7 Research objectives

The use of propagation channel modelling can help determine the attenuation on a radio link and improve the effectiveness of fade mitigation techniques. However, there is still uncertainty in the estimation of attenuation from propagation models, which could result in under estimation or overestimation of attenuation. Over estimation could see wasted power resources and underestimation could result in loss of signal and reduction in quality of service. In certain circumstances, such as finical transactions or safety critical systems, a loss of signal could lead to disastrous consequence.

Traditionally, a fixed fade margin is used to compensate for attenuation by assuming the worst case scenario. For example, a fade margin of 40 dB for a 48 GHz link is predicted to maintain a system availability of 99.99%, Hodges [2006]. Propagation models are used to determine a dynamic fade margin to increase the power efficiency of a system. Current propagation models do not accurately predict the effect of the DSD. Variation in the DSD could see attenuation vary in the order of 1-2 $\mathrm{dB\,Km^{-1}}$ at 20 GHz, as shown in Figure 3.11, which will require a large fade margin to prevent any loss of service. Accounting for variation caused by the DSD could significantly improve the prediction of attenuation, therefore reduce the necessary fade margin required to maintain the availability of a system.

The aim of this thesis is to quantify the uncertainty in the calculation of rain attenuation for a given rainfall rate. The attenuation calculation can be improved through a better understanding of the variability of the raindrop size distribution and its effects, since rain attenuation is a function of raindrop size distribution. The raindrop size distribution is also a function of rainfall rate and for every rainfall rate there are many raindrop size distributions. The ITU-R uses a single, on-average fit to represent all raindrop size distributions, while other models such as Leitao and Watson [1986] use two rain types representing widespread and convective rain. The goal is to improve the raindrop size distribution to attenuation prediction by either better estimating the raindrop size distribution from rainfall rate or using variables to express the raindrop size distribution as a function of rainfall rate. The eventual goal is to create a probability

of attenuation for a given rainfall rate, due to raindrop size distribution variance.

Chapter 2 discusses elements of the troposphere to understand possible parameters that could effect the DSD and attenuation on satellite links. The main focus is the formation and effects of rain, which includes the discussion of raindrop size distributions and electromagnetic scattering. Chapter 3 explores experimental data investigating effects of the raindrop size distribution and its relationship with rainfall rate. The investigation was pursued further by exploring possible links between raindrop size distribution and other meteorological factors in Chapter 4. In Chapter 5, a frequency region where the raindrop size distribution has no effect on attenuation, and hence the attenuation and rainfall relationship is linear, is explored. Chapter 6 looks at the statistical significance of rain cells over the UK and investigates possible relationships between rain cells and the DSD. The thesis concludes in Chapter 7 with a summary of conclusions and possible future work including a look at fade mitigation techniques to counteract the effects of rain.

# Chapter 2

# The Troposphere

This chapter introduces the troposphere and outlines factors which cause attenuation of propagating radio waves at frequencies above 20 GHz. The chapter focus's on rain since rain can cause the largest values of radio wave attenuation at Ka-band frequencies, as explained by Arbesser-Rastburg and Paraboni [1997]. Rain formation, shape, velocity, measurement and the micro-physics of precipitation are discussed.

The troposphere is the lowest region of the Earth's atmosphere, and accounts for approximately 75% of the atmosphere's mass. The height of the troposhpere (relative to sea level) ranges from 7 km near the poles to 20 km in tropical regions, with an approximate average of 17 km. The troposphere contains almost 99% of the atmosphere's water vapour and aerosols. It is the most dense atmospheric layer, and contains 78% nitrogen, 21% oxygen and small concentrations of other trace gases. The temperature of the troposphere decreases with altitude until it reaches the tropopause, a layer between the troposphere and stratosphere known as the region of temperature inversion.

## 2.1 Rain

Rain is the liquid precipitation of atmospheric water vapour. The formation of rain occurs in several different ways. The formation process is dependent on the type of cloud, i.e. warm or cold. In the case of warm clouds, there are two main processes through which rain drops are created. The first is condensation and the second is collision and coalescence. Condensation begins with the generation of small raindrops up to radii approximately 10 $\mu$m. Collision and coalescence generate larger rain drops.

### 2.1.1 Formation in warm clouds

#### Condensation

The process of condensation begins with the ascent of warm air parcels. This results in air expanding and adiabatically cooling until eventually reaching saturation. If the air continues to rise, the parcel will become supersaturated. A cloud of small water droplets forms as water vapour condenses onto some of the aerosol or cloud condensation nuclei in the air. The droplets could also form due to spontaneous nucleation where the aid of aerosol is not required. Spontaneous nucleation is described as a process of chance collisions of water droplets in vapour phase coming together to form small embryonic water droplets, Wallace and Hobbs [2006].

#### Collision and coalescence

Condensation forms small droplets, where as the collision and coalescence process creates larger droplets, Wallace and Hobbs [2006]. The fall velocity of larger droplets is greater than smaller drops. Faster droplets are likely to collide with slower droplets in their path. However, not all droplets necessarily collide, since many of the smaller drops may follow the stream lines around the larger ones. It is not guaranteed that colliding droplets will coalesce with one another as the droplets may bounce off a layer of air trapped between the two. Alternatively the resulting drop could become unstable and breakup. If the cushion of air is squeezed out from between the drops before rebound can occur, the two surfaces make physical contact and coalescence will occur.

### 2.1.2 Formation in cold clouds

A cloud that exists above the zero-degree isotherm level is typically called a 'cold cloud'. It may contain both ice crystals and supercooled water droplets. Supercooled droplets are water droplets that exist in clouds even though the temperature may be below $0\,^{o}$C. A mixed cloud contains both ice crystals and supercooled water droplets, a glaciated cloud contains only ice crystals. Rain can form in cold clouds by vapour, riming or aggregation. Growth by vapour can not produce significantly large ice crystals. Ice crystal growth can occur by riming, where supercooled droplets that collide with ice crystals increasing the mass of the ice crystal. An ice crystal can also grow by aggregation where ice crystals collide and adhere to one another. Growth by riming and aggregation can produce a wide range of particle sizes, which melt to create larger

raindrops.

## 2.2 Stratiform and convective rain

There are two main types of rain, stratiform and convective. Convective rain usually falls from cumulus and cumulonimbus clouds while stratiform rain precipitates from nimbostratus clouds, Houze [1993].

### 2.2.1 Stratiform rainfall

Stratiform rain is caused by frontal weather systems converging into areas of low pressure, the situation when warm air meets cool air. A warm front arises from warm air overriding cool air, as the warm air rises it cools leading to precipitation. Cold fronts dislodge masses of warm air, which leads to more intense but shorter rainfall. Generally, stratiform is more widespread rainfall that usually occurs for rainfall rates below $5\,\mathrm{mm\,hr^{-1}}$. Stratiform rain occurs in clouds with extensive horizontal development, such as nimbostratus clouds, rather than vertical development.

### 2.2.2 Convective rainfall

Convection occurs when a moist atmosphere is heated above the temperature of its surroundings leading to significant upward movement, which eventually leads to convective clouds. Convective rainfall may also occur from cold fronts. A cold front undercutting warm air dislodges masses of air at a rate much higher than the steady rise of air at a warm front. The air is usually more unstable leading to the formation of cumulonimbus clouds. Orographic uplift, when air is forced from a low elevation to a high elevation over rising terrain such as mountains, can lead to significant upward movement and convective rain. Convective rainfall usually consists of larger, heavier raindrops, which usually occurs at rainfall rates above $10\,\mathrm{mm\,hr^{-1}}$ over a relatively short time period, and when the atmosphere is more unstable.

## 2.3 Rain cells

In this work a rain cell is defined as the region of space composed of connected points where the rainfall rate exceeds a chosen threshold. There have been many studies into the size and shape of rain cells using radars, such as those by Konrad [1978], Crane [1990] and Goldhirsh [2000]. There have also been studies using long-term time series measurements made from rain gauges (with a time resolution such as 1 minute), which are used to estimate rain cell sizes using the synthetic storm technique, Yau and Rogers [1984].

The shape of a rain cell is generally irregular at the ground, however investigators have compared the perimeter of a rain cell to an ellipse. Féral et al. [2000] showed the statistics of rain cell geometry were independent of their location and threshold with an average ellipticity factor of 0.5. The ellipticity infers that, on average, rain cells were twice as long as they were wide.

A model could be used to represent a measured rain cell. There are several models that have been derived to estimate rain cells. Some profile models are based on a cylindrical or Gaussian shape, Mass [1987], Bryant et al. [2001]. Two well-known rain cell models include the EXCELL model, Capsoni et al. [1987], and the HYCELL model, Féral et al. [2003a]. The EXCELL model describes the variation in rainfall rate within a cell as exponential, with circular or elliptical profile. The HYCELL model is a hybrid cell that combines exponential and Gaussian shapes. The Gaussian component models the high-intensity, convective rainfall rate and the exponential component represents the surrounding widespread rainfall. Both these models may be defined only by a few parameters, which have significant advantages including reduced storage space and computational time when processing the cells in comparison to complete rainfall data.

Rain cells could be used to improve the effectiveness of propagation models, especially for systems with multiple paths, when predicting attenuation due to rain. The prediction of signal fade can greatly improve the effectiveness of fade mitigation techniques, Panagopoulos et al. [2004] and help maintain high-quality communication services. Chapter 6 investigates statistical information of rain cell size distributions such as average and maximum rainfall rate, ellipticity and area. The statistics could provide characteristic descriptions of intense parts of the rain field that could be linked to raindrop size distributions.

## 2.4 Fall velocity and shape of raindrops

### 2.4.1 Velocity

The velocity and shape of raindrops are vital factors for calculating the rainfall rate and resulting radio wave attenuation. Gunn and Kinzer [1949] determined a method to measure the terminal velocity of raindrops. The experiment involved a dropper capable of producing water drops of any size from 0.1 to 100,000 $\mu$g. Below was an insulated ring-shaped electrode. When droplets detached from nozzle, they would fall through it and a free charge would be placed on the droplet. To calculate the fall velocity, a drop was passed through two inducing rings approximately one metre apart. A free electrical charge, deposited on each droplet, generated a pulse on each inductive ring as it descended. The time difference and spacing of the rings were used to measure the average velocity. The drop masses were determined using a highly-sensitive chemical balance.

Using these results Gunn and Kinzer [1949], and similar work by other authors, (for example, D Atlas and Sekhon [1973]) an expression for the terminal velocity was calculated and is shown in equation (2.1). The results followed the pattern that the larger the raindrop the faster it would fall. However, as the diameter of the drop increases above 2 mm the increase in velocity begins to decrease. Once the diameter is close to 4 mm, the drops terminal velocity reaches a maximum.

$$v(D) = 9.65 - 10.3\exp(-0.6D), \tag{2.1}$$

$D$ is the drop diameter given in mm and $v(D)$ is the raindrop velocity of drop diameter $D$ in $\mathrm{m\,s^{-1}}$.

### 2.4.2 Raindrop shape

Raindrops vary in both shape and size, Spilhaus [1947]. A water drop with no noticeable motion relative to the surrounding air will assume a spherical shape due to the surface tension of water. The surface tension results in the inside spherical pressure of the drop being greater than atmospheric. When the drop falls, unequal pressure forms over the surface. Pressure increases at the bottom of the drop, and decreases at the top and sides. The pressure change deforms the water drop by flattening the bottom surface and spreading the shape sideways.

The size of the raindrop effects the way in which the raindrop is deformed. Exper-

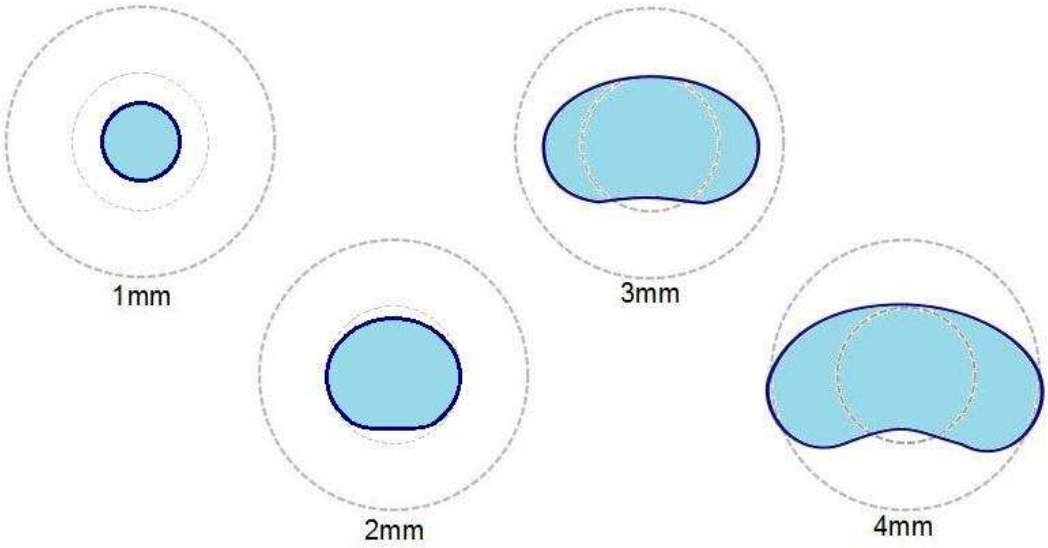


Figure 2.1: Equilibrium raindrop shapes at radius: 1 mm, 2 mm, 3 mm and 4 mm.

imental results which investigate photographs of raindrops falling were obtained by Pruppacher and Beard [1970]. Measurements showed that raindrops above 2.0 mm in diameter were affected by the change in pressure on the outside of the drop and became oblate spheroidal in shape. Figure 2.1 shows the different types of raindrop shapes for given sizes. Generally, raindrops larger than 8 mm in diameter are hydrodynamically unstable and tend to break up, as observed by Pruppacher and Pitter [1971].

### 2.4.3 Breakup of raindrops

Raindrops above 2 mm in diameter become flattened on their underside in free fall and gradually change from a spherical to an almost parachute shape. If the diameter of the drop is greater than 5 mm the parachute becomes a large inverted bag, with a toroidal ring of water around its rim. Studies have shown that the drop bag bursts to produce a fine spray of droplets, the toroidal ring breaks up into a number of large drops, which forms an exponential raindrop size distribution, Bossa and Villermaux [2009]. A representation of this process is shown in Figure 2.2. There is some controversy over whether collisions between drops are the largest cause of breakup. It has been suggested that the number of collisions is not large enough for a stable distribution to emerge, and coalescence is thought to be the main ingredient, Wallace and Hobbs [2006]. The bursting time is also much smaller than the falling time.

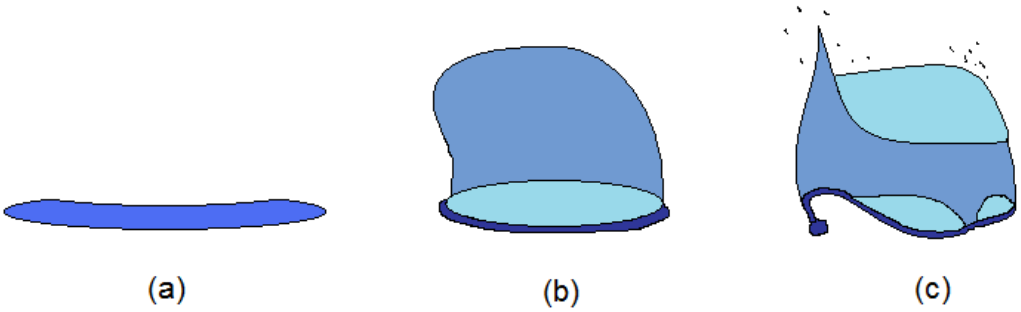


Figure 2.2: Raindrop with diameter greater than 5 mm forming a parachute (a), a large inverted bag (b) and breaking up (c).

### 2.4.4 Raindrop canting angle

Raindrops can fall with different canting angles, which will change the resultant fading levels for linear polarisation on non-spherical raindrops and reduce polarisation discrimination.

Horizontal wind speed varies with height, therefore relative airflow to a drop is not even along the length of the drop as it is accelerated or retarded in the horizontal direction, canting the drop. Vertical wind gradients also result in a horizontal force on raindrops, Brussaard [1974]. If the wind speed is constant and independent of height, the drops will assume the same horizontal speed as the surrounding air, therefore the relative airflow to the drop will be vertical. The canting angle is a function of the differential of the vertical wind profile, not the absolute value of the wind speed.

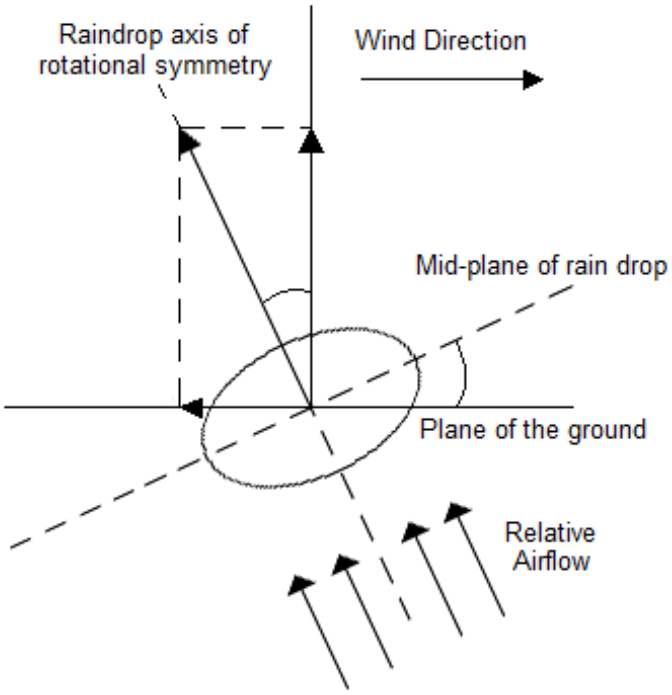


Figure 2.3: Illustration of the canting angle of a raindrop and the forces involved.

## 2.5 Raindrop size distribution

The raindrop size distribution (DSD), denoted by $N(D)$, is the number concentration of raindrops with equivolume diameter D in a given volume of space (number of drops $\mathrm{m}^{-3}\,\mathrm{mm}^{-1}$). DSDs can be used to calculate rainfall rate and radio wave attenuation. The DSDs can vary significantly and yet give the same rainfall rate. For instance, a large number of small drops can give the same rainfall rate as a small number of large drops, even though they are two very different raindrop size distributions. Two different DSDs resulting in the same rainfall rate may result in two different values of signal attenuation.

### 2.5.1 Disdrometers

Disdrometers are one of the most common tools used to measure rainfall rate and raindrop size distributions. There are several types of disdrometers available including optical, impact and video disdrometers. Video disdrometers have been shown to have better agreement with rain gauge measurements of rainfall rates in comparison to impact disdrometers, Tokay et al. [2001]. Both disdrometers partially underestimate rainfall rate by underestimating the number of smaller size raindrops. However, the

Figure 2.4: Images of video (left), optical (center) and impact (right) disdrometers.

video disdrometer had a better estimate of the number of small size drops.

A Joss-Waldvogel (impact) disdrometer measures the size and number of raindrops by the vibrations caused by each impact on the surface of the disdrometer. It is typically constructed of a conical Styrofoam body used to transmit the mechanical impulse, caused by vibrations, to two moving coils. A drop lands on the surface of the disdrometer and the resulting mechanical movement induces a voltage across the sensing coil. This voltage is processed to convert the vertical momentum of a raindrop into an electronic pulse that is proportional to the drop diameter, Baltas and Mimikou [2002]. The voltage is also amplified and applied to the drive coil to counteract the movement. This limits the movement so the device is quickly ready for the next drop. A Joss-Waldvogel disdrometer typically measures the number and size of raindrops over 128 bins at ten second intervals. The disdrometer has a measurement range of 0.3 mm to 5.0 mm raindrops. Drops smaller than 0.3 mm hold little significance when considering radio wave attenuation and drops greater than 5.0 mm are very rare as they are hydrodynamically unstable.

There are several disadvantages when measurements are made by disdrometers in general, as discussed by Brawn and Upton [2008]. Each disdrometer has a minimum drop size it can measure, which can bias the results. Similarly, disdrometers can have a maximum measurement size, which would result in the largest drops being measured incorrectly. Each disdrometer has a relatively small collection area, which makes drop counting for each diameter class noisy, especially in the case of larger drops. Optical disdrometer measurements may be effected during heavy rain when one drop may be obscured by another. Joss-Waldvogel disdrometers can be subject to noise caused by strong winds, high acoustics (in the case of an impact disdrometer), splashing drops or debris landing on the device. Further, impact disdrometers may exhibit a 'dead-time' caused by the impact of a drop, during which small drops cannot be measured. Despite

the disadvantages of the Joss-Waldvogel disdrometer, the device is a very good measure of raindrop size, which is cheaper, more widely available and has an abundance of data when compared to a video disdrometer.

In this research two Joss-Waldvogel disdrometers were used to obtain DSD data, one at Rutherford Appleton Laboratory, Chilbolton, UK(51°14 N,-1°44 E) and the other at Sparsholt, UK (51°07 N, 1°38 W). The data from the Chilbolton and Sparsholt disdrometers were acquired from the British Atmospheric Data Centre (BADC). A Thies Clima Laser Precipitation Monitor (optical disdrometer) was used for measurements at the University of Bath. Sheppard and Joe [1994] compared a Joss type disdrometer, a PMS 2DG Spectrometer and a POSS Doppler Radar. The results showed all three devices were in a good agreement, demonstrating the accuracy and reliability of the Joss type disdrometer.

In order to investigate the DSD an analytical form is fitted to measured DSDs. The parameters of the analytical distribution may be used in comparison to meteorological data to determine a way of predicting the DSD. A number of analytical forms of raindrop size distributions have been suggested. These include the exponential distribution (Marshall and Palmer [1948]), lognormal distribution (Feingold and Levin [1986]), the gamma distribution (Ulbrich [1983]) and the normalised gamma distribution (Testud et al. [2001]).

### 2.5.2 Exponential distribution

The first significant work on raindrop size distributions started with Laws and Parsons [1943] and continued with Marshall and Palmer [1948]. Marshall and Palmer measured raindrops on dyed filter paper to analyse the distribution of drop sizes. With the results obtained, Marshall and Palmer derived the general relation:

$$N(D) = N_0 \exp(\Lambda_e D), \tag{2.2}$$

where $D$ is the raindrop diameter, $N_0$ and $\Lambda_e$ are parameters of the distribution, and $N(D)$ is the number density of drops of diameter $D$ in a unit volume of space. Parameter $N_0$ is the value of $N(D)$ at $D = 0$. Marshall and Palmer found the best representation of their experimental data occurred when $N_0 = 0.08\,\mathrm{cm}^{-4}$ and $\Lambda_e = 41R^{-0.21}\,\mathrm{cm}^{-1}$, where $R$ is the rainfall rate in $\mathrm{mm\,hr}^{-1}$. The Marshall and Palmer distribution of raindrops with size is shown in Figure 2.5 for 0.25, 1, 5, 25 and $150\,\mathrm{mm\,hr}^{-1}$.

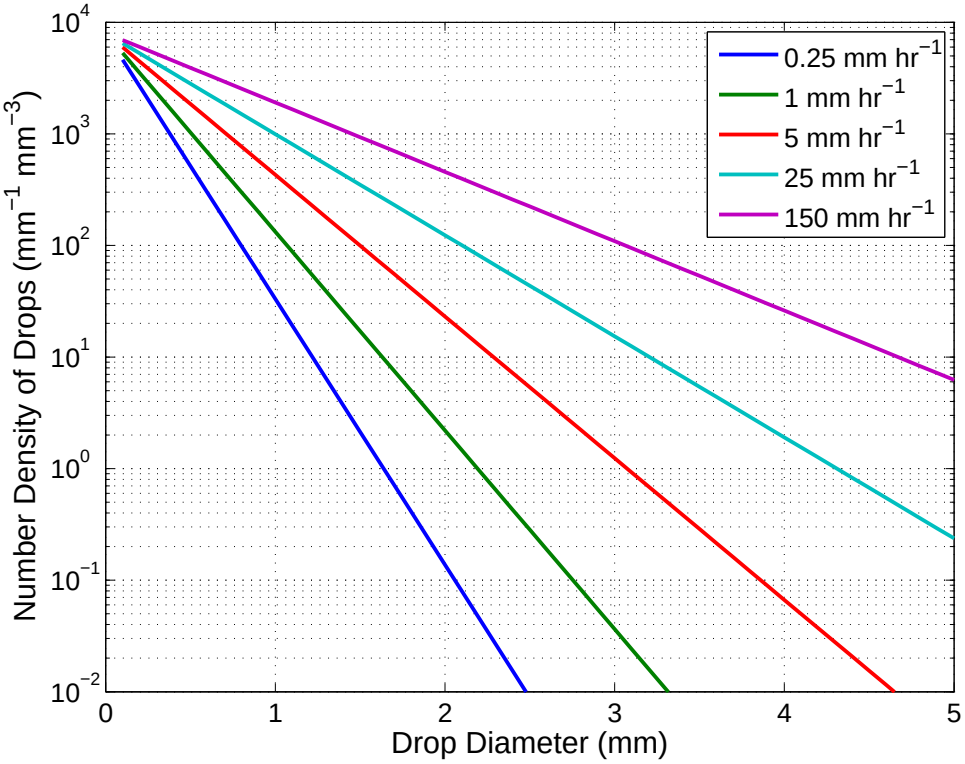


Figure 2.5: Marshall and Palmer raindrop size distribution.

The Marshall and Palmer DSD has been widely accepted by many, and is a good representation of the DSD over a long time period, Joss and Gori [1978]. The exponential distribution has been further developed by Best [1950] and Joss and Gori [1978] using new results. More recent studies, such as Joss and Gori [1978] and Ulbrich [1983], have assumed the DSD is an alternative analytical distribution.

### 2.5.3 Log-Normal distribution

An alternative representation of the DSD is the lognormal distribution, shown in Figure 2.6. The lognormal distribution can better estimate DSDs where there are fewer numbers of small drops sizes, i.e. for convective rain. Comparing Figures 2.5 and 2.6 shows the lognormal distribution has more versatility in representing different DSDs for a given rainfall rate. The lognormal distribution can represent instances of DSDs with few small drops, for example the distributions shown in Figure 2.6, to instances that with high numbers of small drops, which are more exponential in shape. Work, such as Feingold and Levin [1986] observed that the lognormal distribution is a better fit to observed DSD data in Israel compared to exponential and gamma distributions.

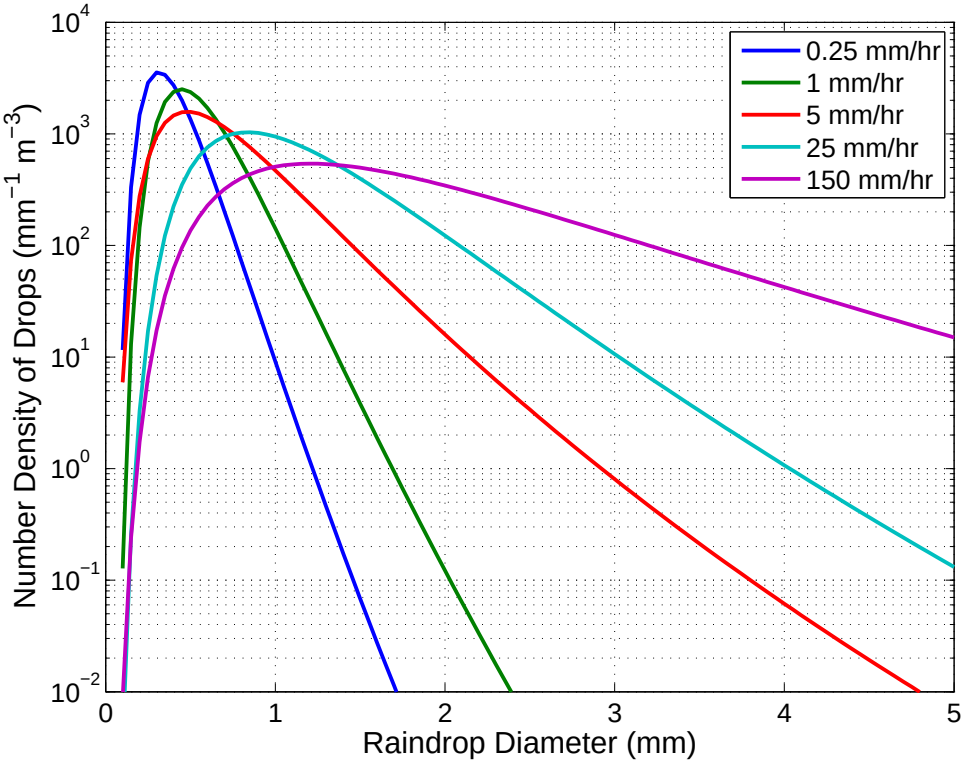


Figure 2.6: Lognormal raindrop size distribution.

The lognormal distribution is given by:

$$N(D) = \frac{N_t}{\sqrt{2\pi}\ln\sigma_g D}\exp\left[\frac{-\ln^2(D/D_g)}{2\ln^2\sigma_g}\right], \tag{2.3}$$

where $N_t$ is the total number of drops m$^{-3}$, $D_g$ is the geometric mean diameter and $\sigma_g$ is the standard geometric deviation, which can be defined by:

$$\ln(D_g) = \overline{\ln D}, \tag{2.4}$$

$$\ln^2(\sigma_g) = \overline{(\ln D - \ln D_g)^2}. \tag{2.5}$$

### 2.5.4 Gamma distribution

The gamma distribution improves the accuracy of estimates of the DSD, especially at high rainfall rates. Ulbrich [1983] suggested the use of the gamma distribution as follows;

$$N(D) = N_0 D^{\mu}\exp(-\Lambda D), \tag{2.6}$$

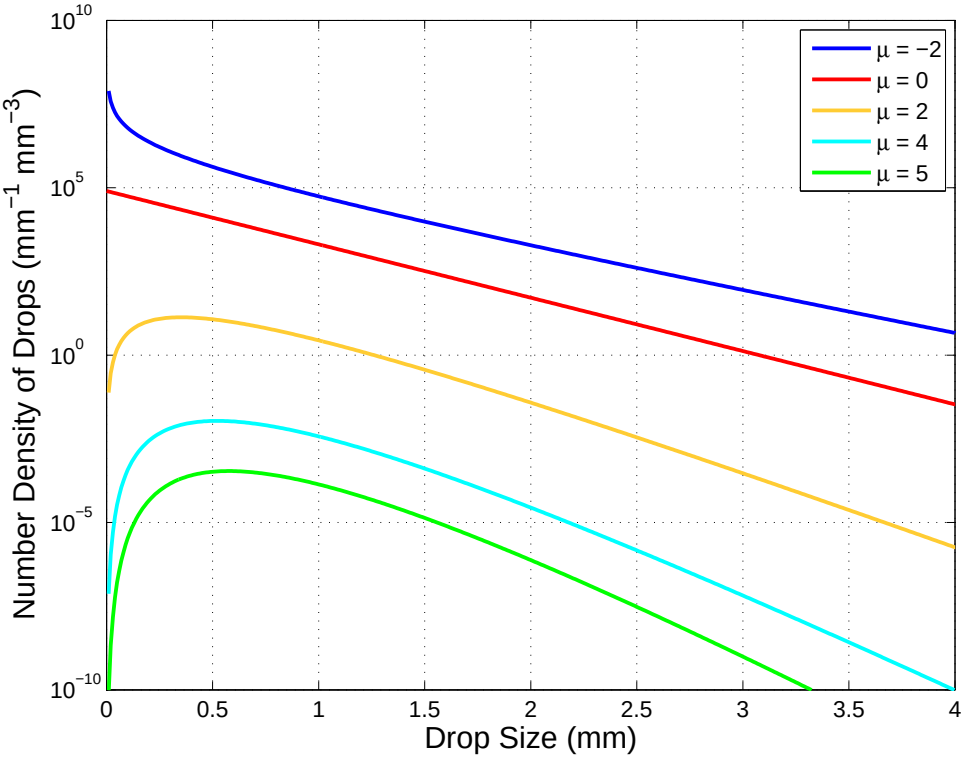


Figure 2.7: Example Gamma distributions for various values of $\mu$.

where $\mu$ is the shape parameter, $\Lambda$ is a parameter of the distribution, $N(D)$ is the drop distribution and $N_0$ is in $\mathrm{m}^{-3}$ $\mathrm{cm}^{-1-\mu}$. Ulbrich described how the shape parameter affects the raindrop size distribution, see the example shown in Figure 2.7. Ulbrich also states that, for non-zero values of $\mu$, the relationship between $\Lambda, D_0$ and $D_{max}$ is determined from:

$$2\int_0^{D_0} D^3 N(D) dD = \int_0^{D_{\max}} D^3 N(D) dD, \tag{2.7}$$

where the integral, on the right hand side of equation (2.7), is limited by the maximum raindrop size, $D_{\max} \approx 8\,\mathrm{cm}$.

This can be rearranged for an approximate expression for the slope parameter $\Lambda$, which is given in equation (2.8), where $D_0$ is the median drop diameter.

$$\Lambda = \frac{3.67 + \mu}{D_0}. \tag{2.8}$$

The mass-weighted drop diameter, $D_m$, can be derived from the fourth and third moments of the drop distribution, as in equation (2.9). $D_m$ is a very good approximation of $D_0$ and is often chosen since it is often more convenient to compute.

$$D_m = \frac{M_4}{M_3} = \frac{\int_0^\infty D^4 N(D) dD}{\int_0^\infty D^3 N(D) dD} = \frac{4+\mu}{\Lambda} = \left(\frac{4+\mu}{3.67+\mu}\right) D_0. \tag{2.9}$$

Finally, $N_0$ can be determined by equation (2.10),

$$N_0 = 6 \times 10^4 \exp(3.2\mu). \tag{2.10}$$

From this equation it is inferred that $N_0$ and $\mu$ are not independent. However, Testud et al. [2001] showed that the relationship between $N_0$ and $\mu$ generated infeasibly large values of $N_0$ given large values of $\mu$ (i.e. $\mu$>10). Further developments in the area led to the idea of the normalised gamma distribution to overcome this paradox.

### 2.5.5 Normalised Gamma distribution

The normalised gamma distribution, considered by Willis [1984], is defined by three parameters $D_m$, $\mu$ and $N_w$. Parameter $N_w$ is independent of $\mu$ in order to prevent high values of $\mu$ generating unrealistic values of $N_w$. The normalised gamma equation, Montopoli et al. [2008], is given by:

$$N(D) = N_w \cdot \frac{6}{4^4} \cdot \left[\frac{(4+\mu)^{(4+\mu)}}{\Gamma(4+\mu)}\right] \cdot \left(\frac{D}{D_m}\right)^\mu \cdot \exp\left[-(4+\mu) \cdot \frac{D}{D_m}\right]. \tag{2.11}$$

The normalised gamma distribution (2.11) has been cited by a number of authors as being the best fit to a wide variety of DSDs, Testud et al. [2001], Willis [1984]. The shape of the distribution can account for a decrease in smaller drops as rainfall rate increases, unlike the exponential distribution. An example of the normalised gamma distribution is shown in Figure 2.8 demonstrating the effects of a variety of changes in the DSD parameters.

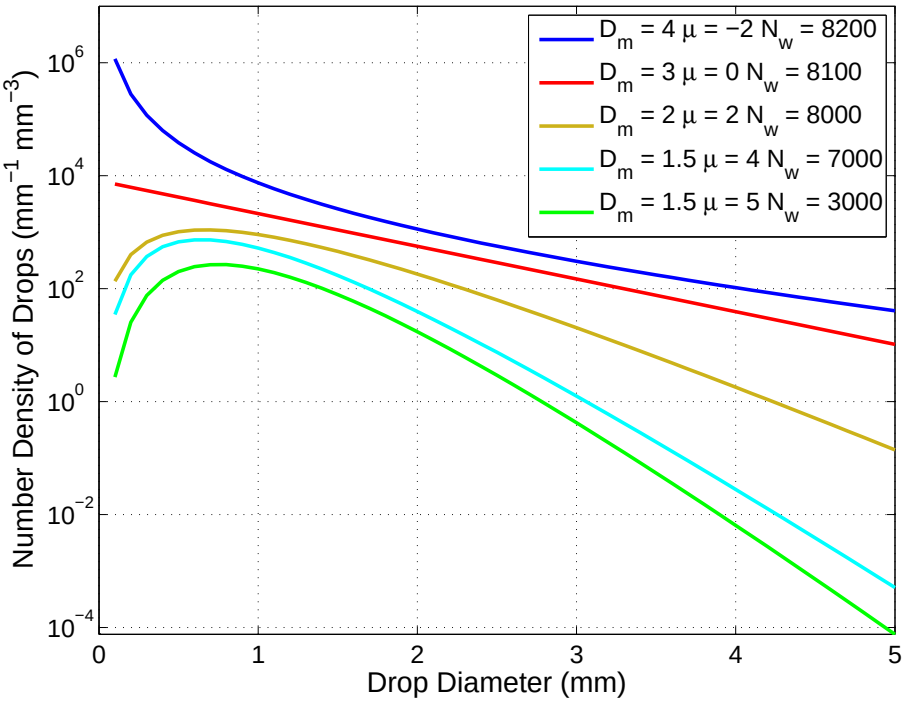


Figure 2.8: Example normalised Gamma distributions.

## 2.6 Rainfall rate

Rainfall rate is a measure of the amount of rain precipitation over a given time ($\mathrm{mm\,hr^{-1}}$) and is a function of the raindrop size distribution. Rainfall rate, as given by Baltas and Mimikou [2002], can be defined by the following:

$$R = \frac{3.6}{10^3} \cdot \frac{\pi}{6} \cdot \int_0^\infty v(D) D^3 N(D) dD, \tag{2.12}$$

where $R$ is the rainfall rate, $v(D)$ is the fall velocity of the drop at diameter $D$ and $N(D)$ is the raindrop size distribution.

Rainfall rate is proportional to the moment of $N(D,t)$, the measured DSD at the discrete instant $t$ (time in seconds), of order 3.67,Montopoli et al. [2008]. The fall velocity ($v(D)$) may be assumed to be $v(D) = 3.78 \cdot D^{0.67}$ as proposed in Atlas and Ulbrich [1977]. The general expression of the $\mathrm{n}^{th}$ order moment of the raindrop size distribution is given in equation (2.13):

$$m_n(t) = \int_0^\infty D^n \cdot N(D,t) \cdot dD = \sum_{i=1}^{n_c} D_i^n \cdot N_m(D_i,t) \cdot .\Delta D_i. \tag{2.13}$$

The following equation shows rainfall rate proportional to the moment of the raindrop size distribution of order 3.67:

$$R = 3.78 \cdot \frac{\pi}{6} \cdot m_{3.67}(t). \tag{2.14}$$

Rainfall rate can be measured over different time intervals. During a long time interval (an hour or more) a rain event may change considerably. Measuring rainfall rate over such a long time period effectively averages the rainfall rate. Small time intervals (such as 1 minute) will represent more changes in the rain event, which is discussed further in Chapter 3.

## 2.7 Rain attenuation

Radio waves at EHF and SHF are susceptible to the effects of the troposphere such as gaseous absorption, cloud attenuation, increased apparent noise temperature, scintillation and, most importantly, attenuation due to rain. Rain has the most significant effect on a satellite signal especially at extra high frequencies.

### 2.7.1 Electromagnetic scattering and absorption

Attenuation on communications links is caused by the scattering and absorption of electromagnetic waves. A plane wave incident on a raindrop ($E^i$) induces a transmitted field in the interior of the drop and a scattered field. $E^s$ denotes the electric field of the scattered wave in the far field region.

$$E^s = f(\hat{K_1}, \hat{K_2}) \frac{\exp(ikr)}{r} E_i, \tag{2.15}$$

where $k = 2\pi/\lambda$, is the free space propagation constant, $\lambda$ is the incident wavelength, $r$ is the distance from origin of the observation point, $E_i$ is the electric field of the incident wave, $f(\hat{K_1}, \hat{K_2})$ is a matrix function denoting scattering amplitude and the polarization state of the scattered wave, which is obtained from the solution of the boundary value. Therefore the scattering amplitude is a function of $\hat{K_1}$, $\hat{K_2}$, the frequency, size, shape and material of the raindrop, and the polarisation of the incident wave. The raindrop and fields are shown graphically in Figure 2.9.

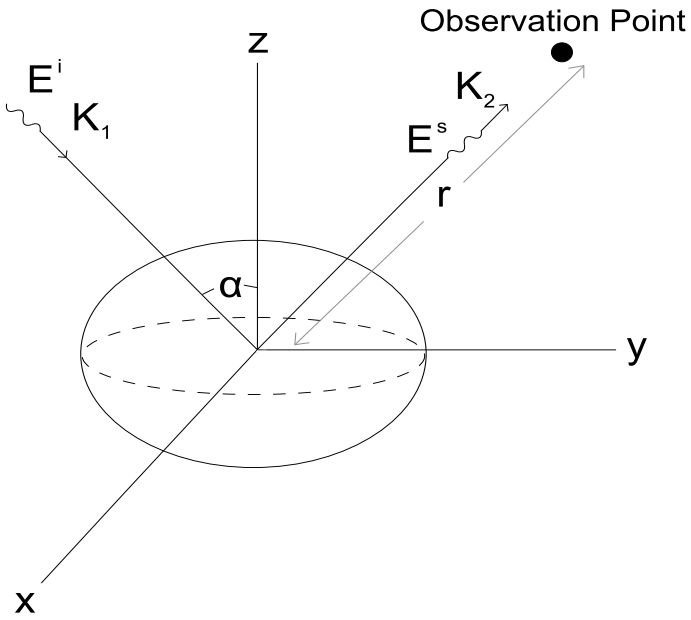


Figure 2.9: Electromagnetic scattering geometry.

A hydrometeor that has a physical cross section has an absorption, scattering and total attenuation cross section, Oguchi [1983], Aydin and Lure [1991], Barber and Hill [1990]. The absorption cross section, $Q_a$, is equivalent to the power absorbed by the hydrometeor, the scattering, $Q_s$, is equivalent to the power scattered in all directions and the total cross section, $Q_t$, gives the total power removed by the hydrometeor. $Q_t$ is directly related to attenuation of the transmitted signal, and is given by the relationship:

$$Q_t = -(4\pi/k)\mathrm{Im}[\hat{e} \cdot f(\hat{K_1}, \hat{K_1})], \tag{2.16}$$

where $\hat{e}$ is a unit vector of the polarization state. Note, in this case the investigation is only concerned with forward scattering, therefore $\hat{K_1} = \hat{K_2}$. The absorption and scattering can be modelled by several different methods depending on the frequency of the signal and the shape of the drop. Example methods include the use of Rayleigh theory, Mie theory and the T-matrix. The Rayleigh method applies to frequencies lower than those considered in this research. Mie theory assumes that the shape of the raindrop is spherical, which is not the case for raindrops above 2 mm in diameter. The T-matrix can model axisymmetric particles, which improves the representation of a raindrop and hence increases the accuracy of attenuation estimates.

**Mie theory**

Once an electromagnetic incident field is intercepted by a raindrop, the electric field induces an internal field and a scattered field. In this work, only the far fields are considered, since the near-field components are only significant up to a few wavelengths from the particle. Each particle is assumed to be a homogeneous sphere and the incident field is assumed to be a plane wave.

The calculation of the total extinction cross section, $Q_t$, begins with the knowledge of the incident field. There are three expressions for the incident, internal and scattered field, as given by Barber and Hill [1990]. These equations are shown in (2.17)-(2.19) respectively.

$$E^i(kr) = E_0 \sum_{n=1}^{\infty} i^n \frac{2n+1}{n(n+1)} (M^1_{o1n} - iN^1_{e1n}) \tag{2.17}$$

$$E^{int}(mkr) = E_0 \sum_{n=1}^{\infty} (c_{o1n} M^1_{o1n} + d_{e1n} N^1_{e1n}) \tag{2.18}$$

$$E^s(kr) = E_0 \sum_{n=1}^{\infty} \frac{2n+1}{2[n(n+1)]^2} (f_{o1n} M^3_{o1n} + g_{e1n} N^3_{e1n}), \tag{2.19}$$

where $c_{o1n}$, $d_{e1n}$, $f_{o1n}$, $g_{e1n}$ are unknown internal and scattered field expansion coefficients. $M^1_{o1n}$ and $N^1_{e1n}$ are vector spherical harmonics of the first kind and $M^3_{o1n}$ and $N^3_{e1n}$ are of the third kind. Using calculations based on Mie theory, and assuming the object is a sphere, the expansion coefficients can be calculated in closed form. The internal field and scattered field coefficients are calculated in terms of spherical triple indexes $\sigma$, $m$, $n$ and size parameter $x = ka$, where $a$ is sphere radius and $k$ is the wave number.

Using equations (2.16) and (2.19), Barber and Hill [1990] shows how the total cross section, $Q_t$, can be calculated. $Q_t$ can be expressed in the form of equation (2.20) as given by Oguchi [1983].

$$Q_t = -(2\pi/k^2)\mathrm{Re}\left[\sum_{n=1}^{\infty}(2n+1)(a^s_n + b^s_n)\right]. \tag{2.20}$$

The values of $a^s_n$ and $b^s_n$ are the expansion coefficients according to a spherical elementary solution.

**T-matrix**

The T-matrix is ideal for calculating scattering by axisymmetric dielectric particles, which is the typical shape of a raindrop. One method to calculate specific attenuation uses the normalised extinction cross section, which can be determined by the T-matrix, Oguchi [1983]. The normalised extinction cross section is given by (2.21).

$$Q_t = \frac{4\pi}{k_v^2}\mathrm{Im}(e_0 \cdot kF), \tag{2.21}$$

where $F$ is the vector far-field amplitude, $k_v$ is the wave propagation vector, $e_0$ is a unit polarization vector multiplied by a unit vector in the direction of propagation and $k = 2\pi/\lambda$.

This leads to:

$$E^s = F\frac{\exp(ik_v r)}{r}E_i. \tag{2.22}$$

Barber and Hill [1990] describes how the T-matrix method begins by the expansion of the incident, scattered and internal electric fields in terms of spherical harmonic functions.

The T-matrix provides a more accurate estimate of $Q_t$ for elliptical shape raindrops and hence an improved determination of specific attenuation compared to Mie theory. Waterman [1969], Barber and Hill [1990] and Ishimaru [1991] have further details on solving the expansion coefficients and using the T-matrix method.

### 2.7.2 Specific attenuation

The specific attenuation describes the attenuation of a radio wave per unit distance. The specific attenuation is a function of the total cross section of a raindrop, $Q_t$. In this work, $Q_t$ is calculated using the T-Matrix method with the drop shape model of Chuang and Beard [1990]. It is important to consider that the calculations are dependent on temperature, drop shape model, drop fall velocity model (Gunn and Kinzer [1949]) and the method of scattering function calculation. Assuming a plane wave propagating in a rainy medium, the governing equation of variation of wave intensity is given by;

$$\frac{dI}{dz} = -\left(\sum Q_t\right) I, \tag{2.23}$$

where $\sum Q_t$ is the sum of the total cross sections of all the raindrops in a unit volume in space. Equation (2.23) implies the rate of decrease of wave intensity in a thin slab of thickness $dz$ is proportional to the energy absorbed and scattered by the raindrops within the slab. Integrating,

$$I = I_0 \exp\left(-\left(\sum Q_t\right) z\right), \tag{2.24}$$

where $I_0$ is intensity at $z = 0$. The sum of the total cross sections in an area $da$ can be calculated as shown in equation (2.25).

$$\sum Q_t = \int Q_t(D) N(D) dD. \tag{2.25}$$

Considering $Q_t$ and intensity, specific attenuation is given by equation (2.26), Oguchi [1983].

$$A = 4.343 \times 10^3 \times \int Q_t(D) N(D) dD. \tag{2.26}$$

### 2.7.3 Multiple Scattering

Multiple scattering has not been considered when calculating specific attenuation. A radiowave scattered by a raindrop will leave in multiple directions, which could then be scattered through another drop and redirected towards a receiver. Oguchi [1991] and Ajewole and Oguchi [2001] show multiple scattering causing incoherent waves has little impact on satellite links and should only become an issue for frequencies greater than 300 GHz. Therefore multiple scattering has not been considered in this thesis.

### 2.7.4 Polarisation

Specific attenuation not only depends on frequency but also on polarisation, Katsambas and Kanellopoulos [2003]. Electromagnetic wave polarisation describes the orientation of the wave oscillations. There are several types of polarisation, including linear polarisation (vertical and horizontal), circular and elliptical polarisations. The polarisation of the electromagnetic signal alters the manner in which a raindrop scatters the signals and thus effects the specific attenuation. Figure 2.10 shows the effects of polarisation on specific attenuation at frequencies of 10-95 GHz for 5, 10, 20, 30 and 50 mm hr$^{-1}$. The specific attenuation was calculated based on the Marshall and Palmer exponential DSD model, Marshall and Palmer [1948], equation (2.2), and assuming a terrestrial link with horizontal elevation. These results show the difference between vertical and horizontal

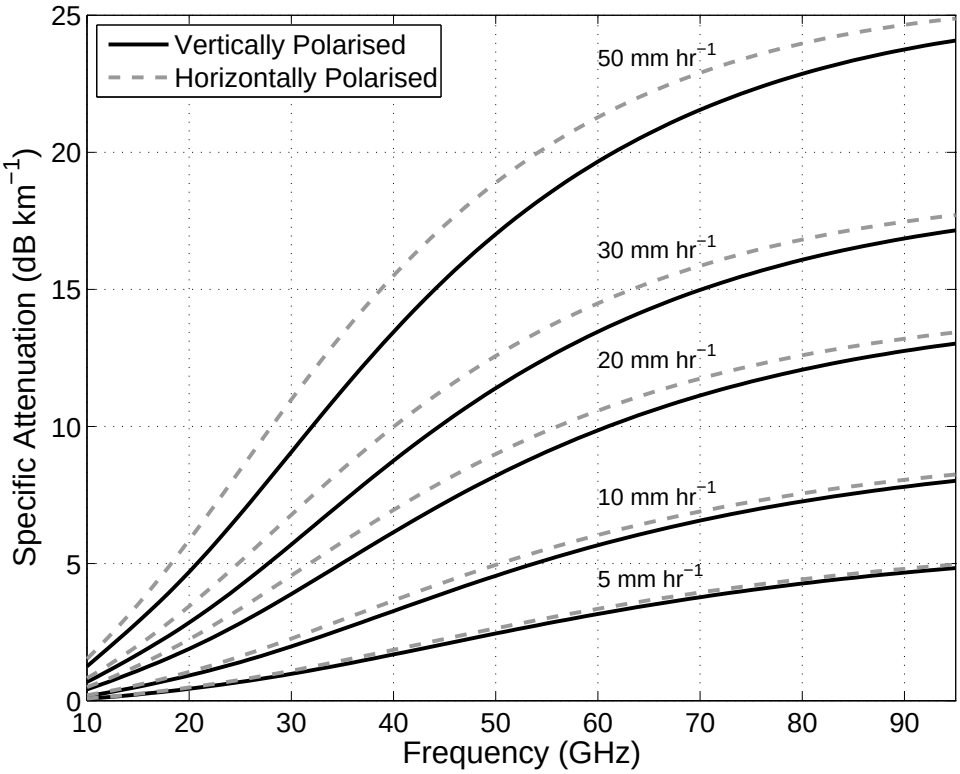


Figure 2.10: Specific attenuation for horizontal and vertical polarisation plotted against frequency for 5, 10, 20, 30 and 50 mm hr$^{-1}$ assuming a Marshall and Palmer distribution and horizontal elevation.

specific attenuation is relatively small, especially at low rainfall rates (e.g., 5 mm hr$^{-1}$). Typically, at low rainfall rates the mean drop size $D_m$ is relatively small (below 2 mm diameter), Townsend et al. [2009]. Raindrops below 2 mm diameter can be considered approximately spherical, hence the effect of polarisation is minimal, Beard and Chuang [1986]. Chapter 5 considers the effects of vertical and horizontal polarisation on attenuation of terrestrial links caused by rain. Chapter 3 investigates attenuation on satellite links and therefore assumes the electromagnetic waves are circularly polarised.

### 2.7.5 Raindrop oscillations

Raindrop oscillations are another consideration when determining scattering and attenuation caused by raindrops. Oscillations in raindrops, as studied by Beard [1984], Kubesh and Beard [1993], Tokay and Beard [1996] determine their average shape for scattering calculations, which is dependent on the mode of oscillation and how quickly the oscillation is damped. A heavy shower can affect microwave links by shifting the polarisation of the electromagnetic wave. The change in polarisation can lead to 'cross-talk' between two transmissions of similar frequency but opposite polarisations.

Large raindrop oscillations (2-6 mm in diameter) are believed to be caused by collisions between raindrops, which can occur frequently in heavy rainfall. For raindrops between 1-3 mm in diameter, collisions may not occur frequently enough and so the source of the oscillations may be intrinsic aerodynamic forces or eddy shedding.

### 2.7.6 The $aR^b$ relation

Attenuation due to rain can be calculated by two different methods.

1. A theoretical method using the raindrop size distribution of raindrops.
2. Using a relation empirically determined between the attenuation and rainfall rate. Typically this is a power law fit.

The relationship between attenuation and rainfall rate is often considered to be a power law relationship:

$$A = aR^b, \tag{2.27}$$

where $a$ and $b$ are functions of the frequency and rain temperature, as described by Olsen et al. [1978]. The $aR^b$ relationship is a straightforward method for calculating specific attenuation from rainfall rate. However, for the same rainfall rate, multiple raindrop size distributions exist therefore changing the value of $Q_t$ and specific attenuation. The $aR^b$ relationship therefore does not account for the effects of DSD. The nature of the power law relationship is investigated further in Chapter 5.

## 2.8 Tropospheric parameters

The troposphere is characterised by several parameters that can affect the formation and size distribution of raindrops. Each of these parameters could have the potential to influence the characteristics of the DSD, which is investigated in Chapter 4. The following tropospheric parameters have been considered in this thesis.

### 2.8.1 Temperature

Temperature is a measure of internal energy (the average kinetic energy) that a substance contains. It is a physical property that is related to the concept of hot and cold. Temperature is the most measured quantity in the atmosphere and is given in degrees Celsius (°C), Fahrenheit (°F) or Kelvin (K). The troposphere is marked by generally decreasing temperatures with increasing height, at an average lapse rate of $6.5°\mathrm{C\,km^{-1}}$.

Temperature is analysed to determine if the parameter has an effect on the size of a raindrop forming or the likelihood of coalescence (Section 2.1.1), altering the raindrop size distribution. Small differences in the lower troposphere temperature (i.e. 1°C) have also been shown to make a difference between no initiation and intense convection, Crook [1996]. Therefore, temperature could potentially show some correlation with the mean drop size, shape parameter and drop concentration of the DSD.

### 2.8.2 Pressure

Atmospheric pressure (P) is defined as the product of the gravitational acceleration and the mass of the unit area of air above a point. That is to say, it is the force per unit area exerted against a surface by the weight of the air above that surface. Typically pressure is measured in pascals (Pa) or millibars (mb), where $1\,\mathrm{mb} = 100\,\mathrm{Pa}$. In general, pressure exponentially decreases from the earth's surface to the mesosphere. The average atmospheric pressure at sea level is approximately 101 kPa.

Pressure is investigated to determine if the parameter affects the formation and concentration of drops or ($N_w$), which could influence the DSD. A sudden drop in pressure over a few hours often forecasts an approaching storm with heavy rain and strong winds. A sudden drop in pressure could correlate with larger mean drop sizes, fewer small drops and a reduced drop concentration.

### 2.8.3 Humidity

Atmospheric humidity is the amount of water vapour present in the air, for example Holton et al. [2003]. There are several different measures of humidity including relative humidity, absolute humidity, specific humidity and humidity ratio (or mixing ratio), Wallace and Hobbs [2006].

Absolute humidity, AH $= (m_v/V_a)$, is the quantity of water in a particular volume of air ($\mathrm{g\,m^{-3}}$), where $m_v$ is the mass of water vapour and $V_a$ is the volume.

Relative humidity, RH, is the ratio of partial pressure from water vapour to the saturated vapour pressure of water at a given temperature and is given by:

$$\mathrm{RH} = \frac{e}{e_s} \times 100, \tag{2.28}$$

where $e = \rho_v R_v T$ is the pressure due to water vapour, $\rho_v$ is the water vapour density (or absolute humidity), $R_v$ is the specific gas constant for water, $T$ is the atmospheric temperature and $e_s$ is the saturation vapour pressure at the temperature of the air. Dew point is the temperature at which the saturation vapour pressure becomes equal to the pressure due to water vapour.

The mixing ratio, $w_r$, can be defined as the ratio of mass of water vapour, $m_v$, to the mass of dry air, $m_d$, where $w_r$ is given by:

$$w_r = \frac{m_v}{m_d}. \tag{2.29}$$

Specific humidity, $Q$, is the mass of water vapour in a unit mass of air and can be expressed as:

$$Q = \frac{m_v}{m_v + m_d} = \frac{w_r}{1 + w_r}. \tag{2.30}$$

High levels of humidity will result in higher levels of water vapour in the air. Humidity is investigated to determine if the measured levels of humidity relate to the DSD. Higher levels of humidity and water vapour could lead to larger numbers of raindrops. The high number of drops could alter the DSD drop concentration. A larger number of drops in the air will result in an increased chance of collisions between drops, which could result in increased mean raindrop size. Humidity could show a correlation in an increased raindrop concentration and variability in raindrop concentration.

### 2.8.4 Dew point

Dew point (DP), denoted $T_d$, is the temperature to which air must be cooled, at a constant pressure, for water vapour to condense into water. Dew point is often associated with relative humidity. A high relative humidity indicates that the dew point is close to the surrounding temperature. Dew point may be determined from relative humidity, based on the commonly known Magnus formula, Lawrence [2005] (2.31),

$$T_d = \frac{B\left[\ln(\mathrm{RH}/100) + AT_b/(B+T_b)\right]}{A - \ln(\mathrm{RH}/100) - AT_b/(B+T_b)}, \tag{2.31}$$

where constants $A = 17.625$ and $B = 243.04$ (°C), RH is relative humidity and $T_b$ is dry bulb temperature (°C).

If the temperature drops well below the dew point temperature, more water vapour condenses into water. The increase in conversion of water vapour to water could lead to more convective rain and higher numbers of raindrops. Dew point is investigated to determine if measured dew point temperature correlates with the DSD parameters such as the raindrop concentration and mean drop size.

### 2.8.5 Liquid water content

Liquid water content (LWC), denoted $w$, is the measure of mass of water in a cloud in a specified amount of dry air, typically given in $\mathrm{gm}^{-3}$, Wallace and Hobbs [2006]. The liquid water content could potentially show correlation to the mean and variability of the drop concentration in the DSD. Higher volumes of liquid water content could show a relation to more convective rain and larger rain drops. The moisture in the boundary layer has been shown to make the difference between no initiation and intense convection, Crook [1996].To determine LWC a cloud must first be detected using a critical humidity function, Salonen and Uppala [1991]. The critical humidity, $u_c$, is given by the following:

$$u_c = 1 - \alpha_w \cdot \sigma_w(1-\sigma_w) \cdot [1 + \beta_w(\sigma_w - 0.5)], \tag{2.32}$$

where the parameters $\alpha_w = 1$ and $\beta_w = \sqrt{3}$, $\sigma_w$ is the ratio of the pressure on the considered level and at the surface. If the measured humidity is higher than the critical humidity at the measurement level, then the measurement level is assumed to be in cloud. Since cloud has been established, liquid water content is determined by:

$$w = w_0(1 + c \cdot t)\left(\frac{h_c}{h_r}\right)^a p_w(t), \tag{2.33}$$

where $h_c$ is height from cloud base, $a = 1.4$ is the parameter of height dependence, $c = 0.041\,^{\circ}\mathrm{C}$ is the factor of temperature dependence, $w_0 = 0.014\,\mathrm{gm}^{-3}$ is the liquid water content calculated when $h_c = h_r = 1500\,\mathrm{m}$ at 0°C. The liquid water fraction $p_w(t)$ is given by:

$$p_w(t) = \left\{ \begin{array}{ll} 1 & 0^{\circ}\mathrm{C} < t \\ 1 + \frac{t}{20} & -20^{\circ}\mathrm{C} < t < 0^{\circ}\mathrm{C} \\ 0 & t < -20^{\circ}\mathrm{C} \end{array} \right\}. \tag{2.34}$$

### 2.8.6 Lifted index

Lifted index (LI) is the temperature difference between an air parcel lifted adiabatically and the temperature of the environment at a given height, Wallace and Hobbs [2006]. Positive values of lifting index indicate a stable atmosphere, where as a negative index indicates an unstable atmosphere (or deep convection) and thunderstorms may be likely. A big negative index indicates the air parcel may have been risen quickly and result in more convective rain. Lifted index is investigated to determine if decreasing lifted index will have a correlation to an increase in mean raindrop size and a reduction in small raindrop sizes changing the shape parameter of a DSD.

### 2.8.7 Convective available potential energy

Convective available potential energy (CAPE), ($\mathrm{J\,kg}^{-1}$), is the maximum amount of energy available to an ascending parcel of air if lifted a certain distance vertically through the atmosphere, Doswell-III and Rasmussen [1994]. It is effectively the positive buoyancy on an air parcel and indicates atmospheric instability, which allows the prediction of severe weather. The air mass is moved vertically up, accelerated by the pressure differential between the displaced air and the ambient air at higher altitude to which it is displaced. Usually it creates vertically-developed clouds due to the rising motion from convection, which can eventually lead to thunderstorms. Values of CAPE greater than zero indicate an unstable atmosphere, where values above $2500\,\mathrm{J\,kg}^{-1}$ indicates a very unstable atmosphere. Large values of CAPE indicate more convective rain. CAPE is compared with the DSD to determine if high values of CAPE correlate with larger mean drop sizes and a decrease in small drops, changing the shape parameter of the distribution.

A measure of the amount of energy available for convection, CAPE is directly related

to the maximum potential vertical speed within an updraft. CAPE is given by

$$\text{CAPE} = g \int_{z_{\text{LFC}}}^{z_{\text{EL}}} \left( \frac{T_{v_p}(z) - T_{v_e}(z)}{T_{v_e}(z)} \right) dz, \tag{2.35}$$

where $T_{v_p}$ is the virtual temperature of the parcel and $T_{v_e}$ is the virtual temperature of the environment, $z_{\text{EL}}$ is the height of the equilibrium level, $z_{\text{LFC}}$ is the height of the level of free convection, $g$ is gravity and $z$ is height.

CAPE can also be determined from a Skew-T diagram. The convective available potential energy is taken as the positive area between the moist adiabatic lapse rate curve and the temperature of the air parcel rising through the atmosphere. The area taken is confined by the crossing of the level of free convection (LFC) and equilibrium level (EL), the dry adiabatic lapse rate curve on the skew-t diagram. The level of free convection is the altitude where the temperature of the environment decreases faster than the moist adiabatic lapse rate of a saturated air parcel at the same level. The level of equilibrium is the height at which the air parcel is the same temperature as the surrounding temperature. These two points define the area in which the convective available potential energy can be integrated over.

### 2.8.8 Wind speed

Wind speed (WS) is the rate of movement of air or other gases in the atmosphere. Wind can be separated into three components: the zonal component ($U$) in the west-east direction; the meridional component ($V$) in the north-south direction; and the vertical component ($W$). Change in wind speed alters the transportation of water vapour and water drops in the air, which could affect the formation of raindrops and the DSD seen at the ground. Vertical upward winds increases the time raindrops are in the air, which allows for more collisions and an increase in the mean raindrop size. Wind speed is investigated to determine if the DSD correlates to wind speed.

The boundary layer is a turbulent layer of air that occurs between the Earth's surface and 1-2 km in height, Wallace and Hobbs [2006]. The boundary layer is directly influenced by the Earth's surface where varying terrain and surface drag causes turbulent eddies in the wind. Turbulence and eddies in the wind could lead to raindrop size sorting. The wind speed in the boundary level will not be uniform and subject to a lot of spatial inhomogeneities, therefore correlation to the DSD may be difficult to determine.

## 2.9 Other tropospheric attenuation

Other factors of the troposphere can cause attenuation of propagating radio waves. Cloud attenuation, gaseous absorption and scintillation are three elements which cause significant attenuation. These elements should be considered when designing a communications link.

### 2.9.1 Cloud attenuation

Clouds are constituted of suspended water drops, which form in air that is supersaturated. The most common types of cloud include convective, layered and orographic clouds. Convective clouds are caused by the turbulent ascent of warm, buoyant air parcels. As the clouds develop the air parcels lose their buoyancy and ice particles are created which mix with the ambient air diffusing the cloud boundary, Wallace and Hobbs [2006]. Layer clouds are formed by forced lifting of stable air, often caused by the development of a warm weather front. Orographic clouds are caused by air being lifted above the condensation level as it passes over hills and mountains.

Cloud attenuation is dependent on the amount of liquid water content and is a function of the type of cloud. Attenuation can be determined from ITU-R P.840. Attenuation due to clouds increases with frequency and is becoming more of an issue with new high frequency (Ka-band and above) technology.

### 2.9.2 Gaseous absorption

Gaseous absorption is caused by two main contributors: oxygen and water vapour, Castanet [2001]. Increasing radio wave frequencies generally results in larger attenuation due to atmospheric gases. Attenuation due to atmospheric oxygen is caused by resonant absorption of radio waves by oxygen molecules. Water vapour acts as a permanent electric dipole which causes resonance and attenuation of radio waves. Nitrogen does not resonate at EHF and SHF frequencies and therefore does not cause significant attenuation. One of the most common methods to determine gaseous absorption is ITU-R P.676-8.

### 2.9.3 Tropospheric scintillation

Scintillation is a result of small-scale variations in refractive index caused by turbulent irregularities in temperature, pressure and humidity. It is often thought that increasing temperature and humidity lead to larger variance in tropospheric scintillation. It was shown by de Kamp [1999] that variance of tropospheric scintillation is better correlated with the presence of heavy clouds. Scintillation fade, which could cause burst errors, can be avoided with the use of either a signal fade margin large enough to encompass the scintillation fade or fade mitigation techniques that respond fast enough to scintillation, Gremont et al. [1999]. Scintillation is becoming more of an issue since scintillation fade increases with operating frequency.

These attenuating tropospheric elements are significant especially with increasing operating frequencies of communication links. However, rain exhibits the largest increase and effect on signal fade with rising operating frequencies. Therefore, the focus of this thesis is on rain attenuation and the raindrop size distribution.

# Chapter 3

# Raindrop size distributions

This chapter explores the relationship between the raindrop size distribution with rainfall rate and its effect on attenuation. Least squares, method of moments and maximum likelihood are investigated to determine a suitable method of fitting an analytical distribution to the DSD. A normalised gamma distribution is determined to be the most suitable representation of the DSD for disdrometer data in the UK. The disdrometer time interval, the cumulative distribution function for rainfall rate and the relationship between analytical DSD with rainfall rate are also discussed.

## 3.1 Fitting an analytical distribution

An analytical distribution was fitted to all the measured raindrop size distributions in order to define a distribution by several parameters. Various analytical forms have been suggested, such as Marshall & Palmer (exponential) and Ulbrich (Gamma shaped DSD), discussed in Chapter 2.5.

There are several possible approaches to fitting an analytical distribution to a measured raindrop size distribution. These include the method of moments (as discussed by Shenton [1958], Robertson and Fryer [1970]), least squares (shown by Press et al. [2007]) and maximum likelihood (as described by Myung [2003] and Kliche et al. [2006]).

The least squares estimation seeks the most accurate representation of the data in terms of how accurately the model fits the data, Press et al. [2007]. The square of the difference between the data and the analytical solution is calculated. The solution is found by iteratively minimising this difference.

### 3.1.1 Maximum likelihood

The maximum likelihood function identifies the solution that is the "most likely" fit to the data, i.e. maximises the likelihood function. The normalised gamma distribution (3.1), Kliche et al. [2006], has been used as an example for a maximum likelihood fit.

$$N(D) = N_T \frac{(\mu+4)^{\mu+1}}{\Gamma(\mu+1)} \frac{D^\mu}{D_m^{\mu+1}} \exp\left[-(\mu+4)D/D_m\right], \tag{3.1}$$

where D is the drop diameter, $D_m$ is the mass-weighted mean drop diameter, $N_T$ is the mean drop concentration, $\mu$ is the distribution shape parameter and $\Gamma$ represents the Gamma function.

The maximum likelihood method compares the probability density functions of the data and the fitting equation. Normalising by the value of $N_T$ yields the two-parameter gamma density function given in equation (3.2).

$$f(D) = \frac{(\mu+4)^{\mu+1}}{\Gamma(\mu+1)} \frac{D^\mu}{D_m^{\mu+1}} \exp\left[-(\mu+4)D/D_m\right]. \tag{3.2}$$

Measured data is transformed into a probability density distribution for comparison with the analytical probability density function. Since the integrand of a probability density function is unity, it can be said that:

$$f(D) = \left[\frac{N(D)}{N(D)_{\text{Total}}\Delta D}\right], \tag{3.3}$$

where $\Delta D$ is the bin width of drop size class and $N(D)_{\text{Total}}$ is the sum total of $N(D)$. The "likelihood" of the normalised gamma density equation, (3.2), is calculated giving the following:

$$L = \prod_{i=1}^{c} f(D_i, \mu, D_m), \tag{3.4}$$

where $c$ is the total number of drops and $D_i$ is the diameter of the $\text{i}^{\text{th}}$ drop. The log of the resulting likelihood function is shown in equation (3.5), Kliche et al. [2007].

$$\ln L(D; \lambda_m, \mu) = c(\mu+1)\ln\lambda_m - c\ln\Gamma(\mu+1) + \mu\ln\left(\prod_{i=1}^{c} D_i\right) - \lambda_m \sum_{i=1}^{c} D_i, \tag{3.5}$$

where $\lambda_m = (\mu+4)/D_m$.

Equations (3.6) & (3.7) are known as the likelihood equations, which maximise the

likelihood function when equal to zero.

$$\frac{\partial \ln L}{\partial \lambda_m} = \frac{c(\mu+1)}{\lambda_m} - \sum_{i=1}^{c} D_i = 0, \tag{3.6}$$

$$\frac{\partial \ln L}{\partial \mu} = \ln \frac{\mu+1}{\overline{D}} - \Psi(\mu+1)\Gamma(\mu+1) + \frac{1}{c} \ln \left( \prod_{i=1}^{c} D_i \right) = 0, \tag{3.7}$$

where $\overline{D}$ is the drop size arithmetic mean and $\Psi$ is the digamma function, Abramowitz and Stegun [1965]. Substituting (3.6) to (3.7) results in:

$$\lambda_m = \frac{c(\mu+1)}{\sum_{i=1}^{c} D_i} = \frac{\mu+1}{\overline{D}}. \tag{3.8}$$

Rearranging gives $D_m$ in terms of $\mu$:

$$D_m = \frac{(\mu+4)}{(\mu+1)} \overline{D}. \tag{3.9}$$

The following equation is derived from maximising the partial derivative of (3.7), with respect to $\mu$.

$$\ln(\mu+1) - \Psi(\mu+1) = \ln \left( \frac{\overline{D}}{(\prod_{i=1}^{c} D_i)^{1/c}} \right). \tag{3.10}$$

Equation (3.10) is complex and may not be analytically solved in terms of $\mu$. In this approach an iterative-numerical method using recursion, Bowman and Shenton [1988], is used. The method has been shown to produce excellent results that converge based on evidence of computational results. The following equation in terms of $\zeta$ (where $\zeta = \mu + 1$) is iterated until convergence;

$$\zeta_{l+1} = \zeta_l \frac{\ln(\zeta_l) - \Psi(\zeta_l)}{\ln \left( \frac{\overline{D}}{(\prod_{i=1}^{c} D_i)^{1/c}} \right)} \tag{3.11}$$

The starting value of $\zeta$ has been derived by Thom [1958], given by (3.12).

$$\zeta = \frac{1 + \sqrt{1 + 4z/3}}{4z}, \tag{3.12}$$

where $z$ is given by:

$$z = \frac{\overline{D}}{(\prod_{i=1}^{c} D_i)^{1/c}}. \tag{3.13}$$

Once the iteration procedure has converged, the value of $\zeta$ is used to determine $\mu$, where $\mu = \zeta - 1$. The parameter $D_m$ can then be solved by substituting $\mu$ into equation (3.9).

The calculated parameters define the probability distribution function. The final parameter $N_T$ is defined by the value used to transform the original data into the proba-

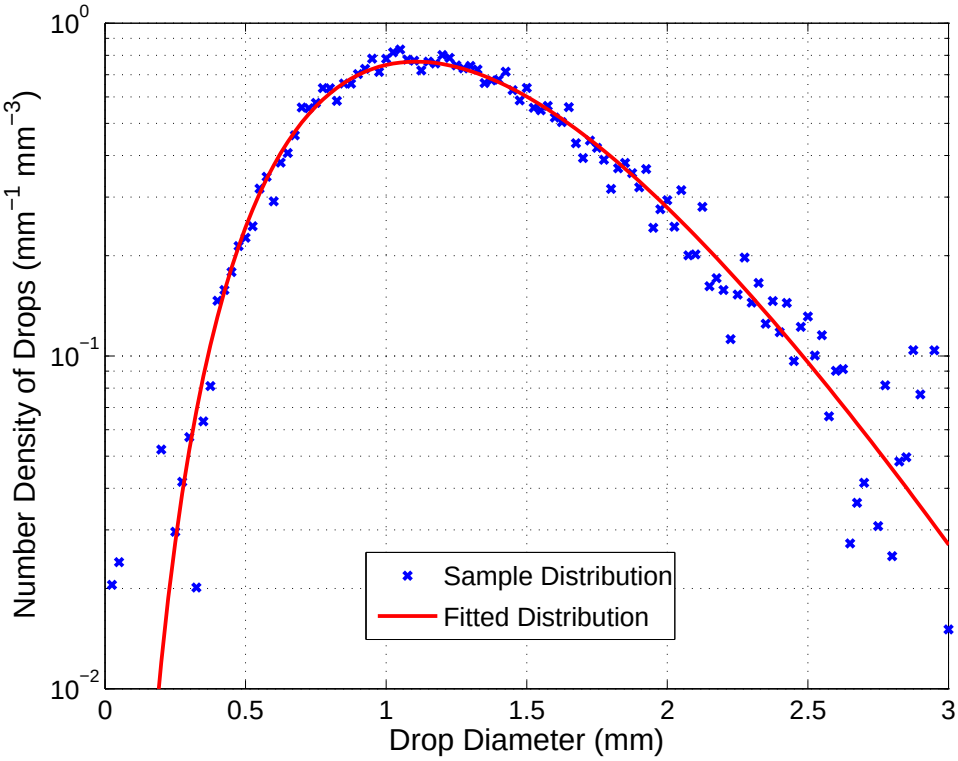


Figure 3.1: Example of a sample distribution fitted using maximum likelihood.

bility distribution. An example fit using the maximum likelihood method to a sample distribution is shown in Figure 3.1.

The Joss-Type disdrometers at Chilbolton and Sparsholt do not have uniformly distributed drop size bin widths, which biases the smaller drops when using this method of fitting. The large number of small drop size bins biases the results towards smaller drops sizes when the raindrop size distribution is converted to a probability density function. Secondly this method establishes a dependency for $\mu$ and $D_m$.

### 3.1.2 Method of moments

The method of moments is a well established and easy to implement technique for fitting distributions, Shenton [1958], Robertson and Fryer [1970]. However, the method is known to produce some bias on the derived parameters, Kliche et al. [2007]. In the case of a raindrop size distribution the moments are defined by:

$$m_n(t) = \int_0^\infty D^n N(D,t) dD = \sum_{i=1}^{n_c} D_i^n N(D_i,t) \Delta D_i, \tag{3.14}$$

where $n$ is the order of the moment and $n_c$ is the number of disdrometer channels. The mass weighted mean diameter, $D_m$, is calculated from the ratio of the third and fourth moments of the raindrop size distribution. Similarly, $N_w$ is solved using the third and fourth moments, (3.16).

$$D_m = \frac{m_4}{m_3}, \tag{3.15}$$

$$N_w = \frac{256}{6} \cdot \frac{(m_4)^5}{(m_3)^4}. \tag{3.16}$$

The parameter $\mu$ is calculated using the second, fourth and sixth moments based on (3.17), below, where $\eta = m_4^2/(m_2 \cdot m_6)$.

$$\mu = \frac{(7 - 11\eta) - \sqrt{(7 - 11\eta)^2 - 4(\eta - 1)(30\eta - 12)}}{2 \cdot (\eta - 1)}. \tag{3.17}$$

### 3.1.3 Maximum likelihood estimated using least squares

This method works on the principle of maximum likelihood but using least squares methodology. Press et al. [2007] describes the maximum likelihood estimate process. Each data point, $y_i$, is considered to be normally distributed around the true model, $y(x)$, with a measurement error that is independently random. By assuming that the standard deviations of these error distributions are the same for all values, the probability of the data is the product of the probabilities of each point.

$$P(\text{data}|\text{model}) \propto \prod_{i=0}^{N-1} \left\{ \exp\left[ -\frac{1}{2} \left( \frac{y_i - y(x_i)}{\sigma} \right)^2 \right] \Delta y \right\}, \tag{3.18}$$

where $N$ is the number of data points to be fitted, $\sigma$ is the standard deviation and $\Delta y$ is the difference in measured data and true model. Bayes' theorem can be given in the form of equation (3.19):

$$P(\text{model}|\text{data}) \propto P(\text{data}|\text{model}) P(\text{model}), \tag{3.19}$$

where $P(\text{model})$ is the prior probability distribution on all models. Following Bayes' theorem the most probable model is the model that maximises equation (3.18). Equivalently, the negative of its logarithm can be minimised, given in the form of equation (3.20):

$$\left[ \sum_{i=0}^{N-1} \frac{[y_i - y(x_i)]^2}{2\sigma^2} \right] - N \log \Delta y. \tag{3.20}$$

Since $N$, $\sigma$ and $\Delta y$ are constants, minimising equation (3.20) is equivalent to minimising the least squares equation shown in (3.21).

$$\sum_{i=0}^{N-1} [y_i - y(x_i|a_0...a_{M-1})]^2. \tag{3.21}$$

Applying this method to fitting the raindrop size distribution gives the following equation, as given by Montopoli et al. [2008].

$$\mu(t) = \min_{\mu} \left\{ \sum_{i=1}^{Nc} [N_m(D_i, t) - N(D_i, \mu(t))]^2 \right\}, \tag{3.22}$$

where $t$ is the discrete instant in seconds. Solving equation (3.22) for a raindrop size distribution will in theory produce the most likely value of $\mu$. The equation can be solved by a Nelder-Mead approach, such as that provided by MATLAB via the *fminsearch* function. This approach effectively minimises the difference between the measured data and the analytical distribution.

The maximum likelihood method estimated by least squares can also be implemented to solve all three parameters at once. Montopoli et al. [2008] investigated the difference between the fitting methods and established that even though the three parameter solution provided the best overall fit, it did not provide accurate estimates of the rainfall rate when compared to measured results. Parameters $D_m$ and $N_w$ were determined using the method of moments. Montopoli determined the moment method using relatively high-order moments was mainly controlled by the tail of the distribution, which gave better results since the disdrometer accuracy when predicting very small drops is considerably lower.

### 3.1.4 Disdrometer data analysis

Two Joss-Waldvogel disdrometers were used to measure DSDs at Chilbolton, UK (51°14 N, 1°44 W) and Sparsholt, UK (51°07 N, 1°38 W) over six years from 2003-2008, Figure 3.2. A third optical disdrometer (Thies Clima Laser Precipitation Monitor) was used at the University of Bath, UK (51°23 N, 2°22 W) to obtain a further two years of data from 2007-2008. The raindrop size distribution from each disdrometer can be written, Montopoli et al. [2008], as follows:

$$N(D_i) = \frac{N_A(D_i)}{A_d T_i v(D_i) \Delta D_i}, \tag{3.23}$$

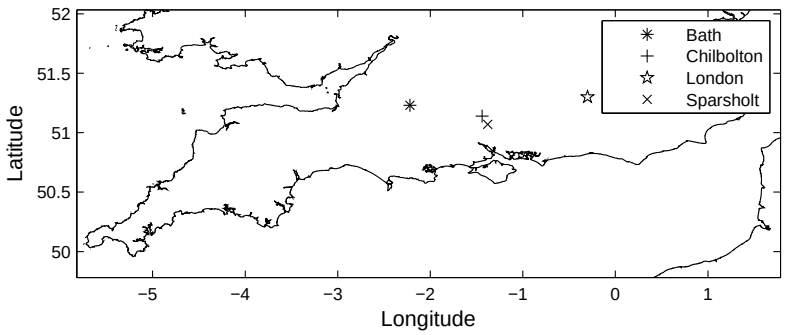


Figure 3.2: Map of the UK showing disdrometer locations (Bath to Chilbolton ≈80 km, Chilbolton to Sparsholt ≈7.5 km).

where $N_A(D_i)$ is the number of drops measured in the drop-size class, $D_i$ is average raindrop diameter of the drop-size class (mm), $A_d$ is the measurement area of the disdrometer ($m^2$), $T_i$ is the time interval for one measurement (s), $v(D_i)$ is the fall velocity of the drop ($ms^{-1}$) and $\Delta D_i$ is the bin-width of each of the drop-size classes. $\Delta D_i$ is defined as $D_{ci+1} - D_{ci}$, where $D_{ci}$ is the lower boundary of the disdrometer channel ($c_i$) and is given by

$$D_{ci} = \left[\frac{10^{[1-\alpha_d \cdot (n_c - i)]}}{\gamma_d}\right]^{\beta_d}, \tag{3.24}$$

where $n_c$ is the number of disdrometer channels, index $i$ assumes values from 1 to $n_c$, and instrument constants $\alpha_d = 0.014253$, $\beta_d = 0.6803$ and $\gamma_d$=0.94.

In this work the time interval is considered to be one minute. This is a compromise between observing the rain dynamics versus reducing the uncertainty in the DSD, which is discussed further shortly. A moving average filter with a span of three drop diameters for each disdrometer sample was used to remove intrinsic noise, similar to Montopoli et al. [2008]. In order to improve the fitting accuracy the noisiest and most unreliable disdrometer channels (1-23) were removed. These channels are more susceptible to external noise (exaggerating smaller drop numbers) and 'dead-time' (underestimating smaller drops), see Chapter 2.

### Raindrop size distribution fitting results

The normalised gamma distribution was fitted using a combination of the method of moments and maximum likelihood estimated by least squares. The normalised gamma distribution (2.11) parameters, $D_m$ and $N_w$, were determined using the method of moments, (3.15) and (3.16) respectively. The maximum likelihood estimated by the

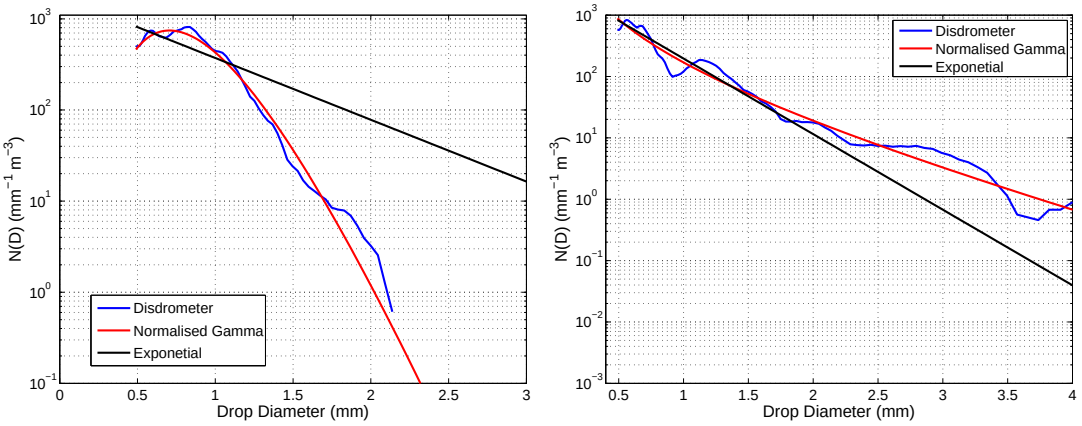


(a) 2.4 mm hr$^{-1}$ (b) 5.9 mm hr$^{-1}$

Figure 3.3: Example comparisons of the normalised Gamma, exponential and disdrometer-measured raindrop size distributions.

least squares method was used to determine $\mu$ (3.22). An exponential distribution was also fitted to the data using non-linear least squares fit.

A comparison was made between the exponential and normalised gamma distributions for all the Chilbolton disdrometer data from 2003-2008. Figure 3.3 shows disdrometer measured raindrop size distributions (blue), normalised gamma distribution fit (red) and an exponential distribution (black) for Figure 3.3(a) at 2.4 mm hr$^{-1}$ and Figure 3.3(a) at 5.9 mm hr$^{-1}$. The results show two typical examples of raindrop size distributions, which illustrate that the normalised gamma distribution captures the shape of the DSD.

A goodness of fit between the disdrometer and analytical data was determined in terms of percentage variance accounted for (PVAF) or R-squared ($R^2$), Pitt and Myung [2002], Bevington and Roninson [1992]. PVAF was determined for all the disdrometer data above 0.1 mm hr$^{-1}$ at Chilbolton. PVAF is given by:

$$\text{PVAF} = \left[1 - \frac{\sum(N(D_i) - N(D_{Fi})^2}{\sum(N(D_i) - \overline{N(D)})^2}\right] \times 100, \tag{3.25}$$

where $N(D_i)$ is the raindrop size distribution determined from the disdrometer, $N(D_{Fi})$ is the analytical distribution determined by the fitting process and $\overline{N(D)}$ is mean raindrop size distribution measured from the disdrometer.

The PVAF was, on average, higher and the standard deviation smaller for the normalised gamma distribution. Therefore, the analytical distribution is assumed the better fit for raindrop size distribution measured in the UK. Table 3.1 shows the results of the percentage variance accounted for.

Table 3.1: PVAF results for the normalised gamma and exponential distribution.

| | Normalised Gamma Distribution | Exponential Distribution |
|---|---|---|
| Mean PVAF | 82.90 | 76.55 |
| $\sigma$ PVAF | 15.41 | 33.78 |

**Disdrometer integration time interval**

The disdrometer measures the number and size of raindrops over ten second intervals. The data is accumulated to produce a time interval of one minute. This period balances uncertainty in the estimation of DSD parameters from measurements taken against the dynamics of the rain event. In Figure 3.4 DSDs determined from the Chilbolton disdrometer are illustrated for different time integration periods. Long integration periods (e.g., one hour) reduce the uncertainty in estimating the DSD parameters but may not represent well the dynamics of rain events. Conversely, short integration periods (e.g., 30 seconds) may not yield sufficient samples to reliably estimate the DSD parameters, especially at low rainfall rates. The number of instances of large raindrops is relatively low due to the formation process of raindrops. Therefore, only longer time periods may obtain enough samples to effect the DSD for larger raindrops. To capture the dynamics of intense convective rain events, which may last only a few minutes, a one-minute integration time was selected (unless otherwise stated) as a compromise between uncertainty in the DSD parameters and rain dynamics.

**Data analysis**

The data was processed following the steps outlined in Figure 3.5. The raindrop size distribution is calculated from the disdrometer data, which is used to determine specific attenuation (2.26) and rainfall rate (2.12). A normalised gamma distribution is fitted to each raindrop size distribution using a combination of the method of moments and the maximum likelihood estimated by least squares. A normalised gamma DSD was selected because it was shown to be the best fit to the data (normalised gamma DSD: $R^2 = 0.829$, exponential DSD: $R^2 = 0.766$). Furthermore, the normalised gamma distribution (2.11) has been cited by a number of authors as being the best fit in a variety of climates Testud et al. [2001], Willis [1984]. The fitting parameters are used to recreate the raindrop size distribution and calculate attenuation and rainfall rate.

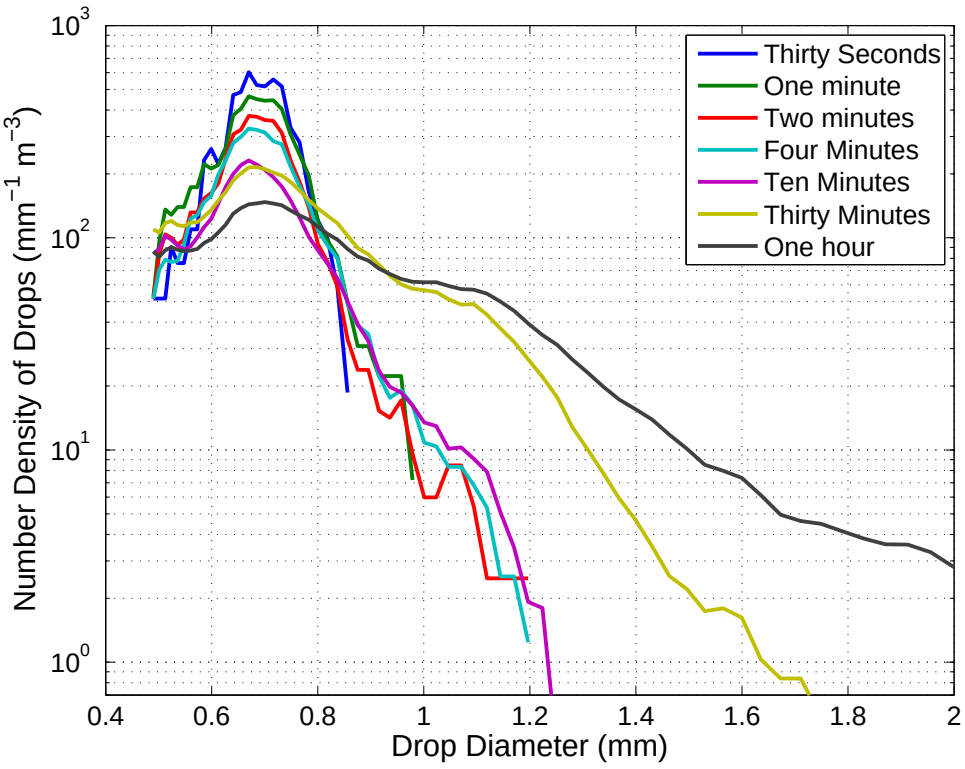


Figure 3.4: Raindrop size distribution measured by the Chilbolton disdrometer for different time intervals from 30 seconds to one hour.

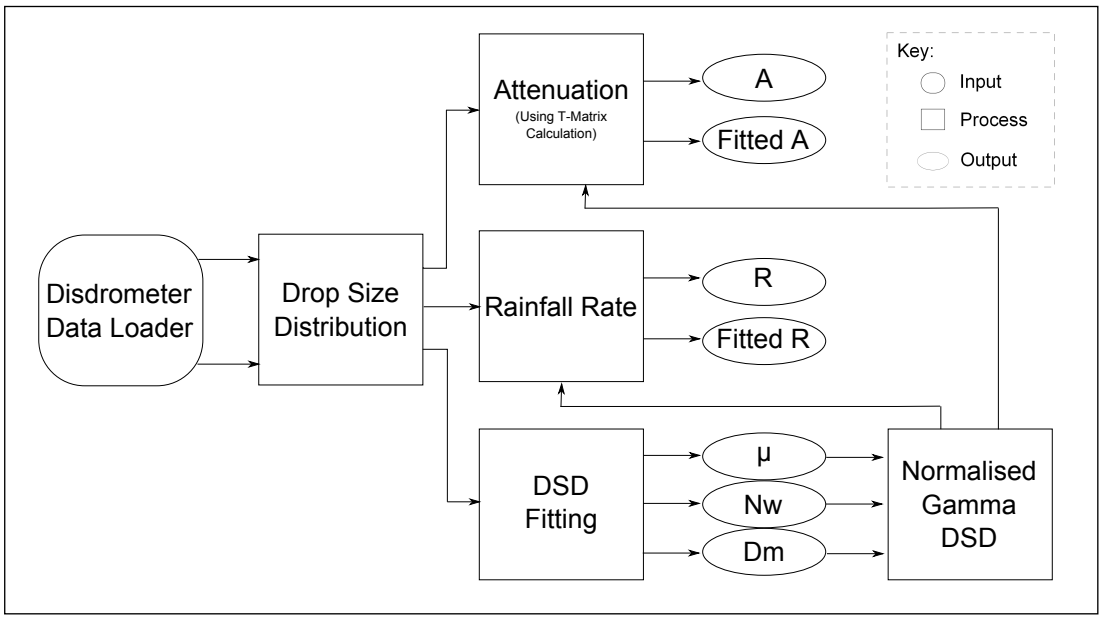


Figure 3.5: Raindrop size distribution fitting program block diagram.

## 3.2 Disdrometer results

### 3.2.1 Cumulative distribution of rainfall rate

Figure 3.6 shows the cumulative distribution function of rainfall intensity for Chilbolton disdrometer data, a second disdrometer at Sparsholt ($\approx$12 km away) and Rec. ITU-R P.837-5 [August, 2007]. The Chilbolton and Sparsholt disdrometer data is broadly consistent with P.837-5. The UK is subject to regional climates, where the western parts of England and Scotland are generally wetter and windier influenced by the Atlantic Ocean. Scotland and the north-east England are subject to continental polar mass air (cold and dry) and south-east England is exposed to continental tropical air masses, which is mostly warmer and drier air. The proximity of Sparsholt and Chilbolton is relatively small and can be considered in very similar climatic regions. Variations between disdrometer results are likely caused by differences in the surrounding environment such as trees and buildings, which can effect wind and cause differences in measured rainfall rate. For rainfall rates above 50 mm hr$^{-1}$ the Sparsholt results differ slightly, which may also be due to insufficient data at high rainfall rates. Although there are small differences below 20 mm hr$^{-1}$ the data from Chilbolton generally shows good agreement with P.837-5 for all rainfall rates and can be considered representative.

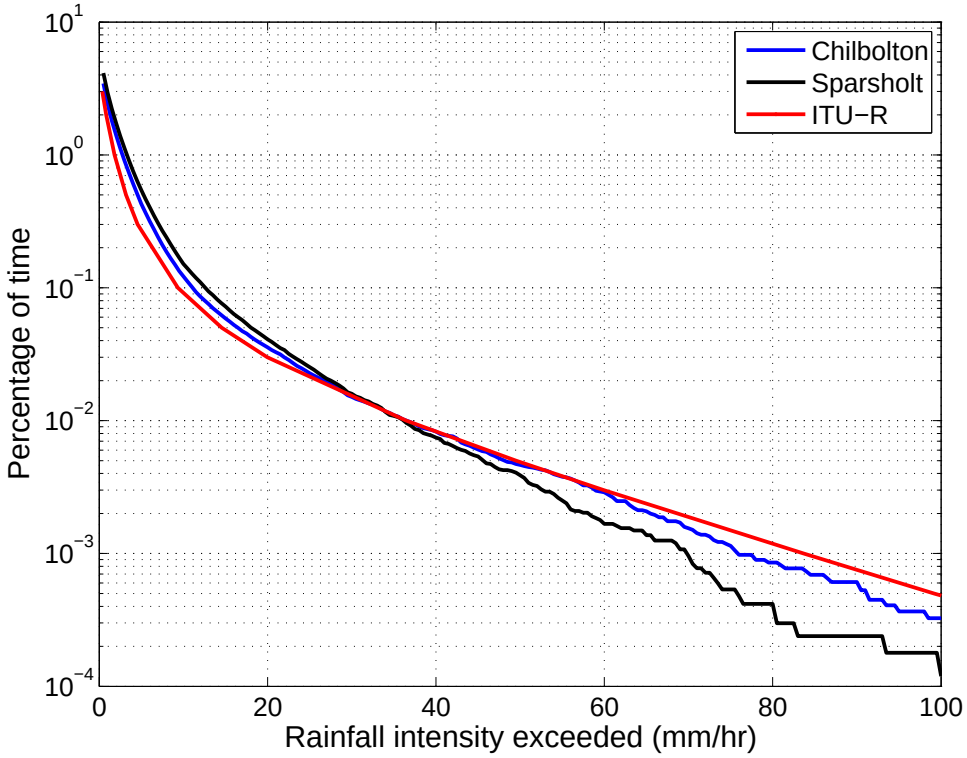


Figure 3.6: Cumulative distribution function of rainfall intensity derived from the ITU-R P.837-5 and the Chilbolton and Sparsholt Disdrometers.

### 3.2.2 Variability of the DSD as a function of rainfall rate and time

The variation in the raindrop size distribution was analysed by comparing the analytical distribution parameters with rainfall rate and time of year. Figure 3.7(a) shows the mean of $D_m$ calculated over $1\,\mathrm{mm\,hr^{-1}}$ rainfall rate and monthly intervals. The mean value of $D_m$ increases with rainfall rate with some variation over each month. The mean of $D_m$ is marginally higher for summer months when compared to the rest of the year. A larger mean drop size for high rainfall rates during the summer suggests more convective rain. The standard deviation of $D_m$ (shown in Figure 3.7(b)) is still relatively low in comparison to the mean. The variation in mean drop size over each rainfall rate interval is higher for summer and spring months.

Mean values of the shape parameter $\mu$ were evaluated over $1\ \mathrm{mm\,hr^{-1}}$ rainfall rate and monthly intervals, see Figure 3.7(c). No discernible pattern is shown in terms of $\mu$. Rainfall rates up to $1\,\mathrm{mm\,hr^{-1}}$ yield high values of $\mu$ ($>7$), with values that are higher still ($>15$) during summer and autumn. For rainfall rates above $1\,\mathrm{mm\,hr^{-1}}$ on average $\mu$ is less than 7. The standard deviation, Figure 3.7(d), is high in comparison to the mean of $\mu$. Below $1\ \mathrm{mm\,hr^{-1}}$ the variation is very high (greater than 17) for rainfall rates especially during summer and autumn.

The mean value of $N_w$, calculated over $1\,\mathrm{mm\,hr^{-1}}$ intervals, is approximated at 8000. There is little correlation between $N_w$ and rainfall rate, as shown in Figure 3.7(e). Between July to September, for rainfall rates up to 15 $\mathrm{mm\,hr^{-1}}$, there is an increase in the average value of $N_w$. The high mean values of $N_w$ are matched by an increased standard deviation, as shown in Figure 3.7(f). Parameter $N_w$ experiences a lot of variation demonstrated by the very high standard deviation.

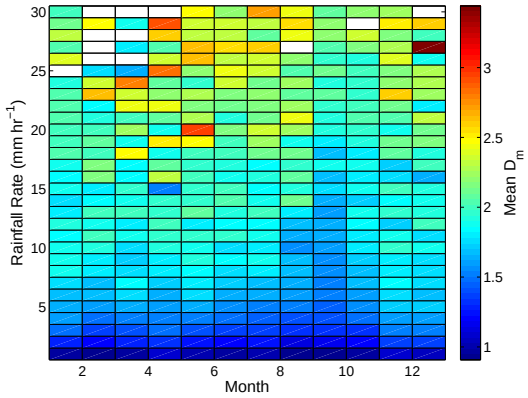


(a) Mean $D_m$.

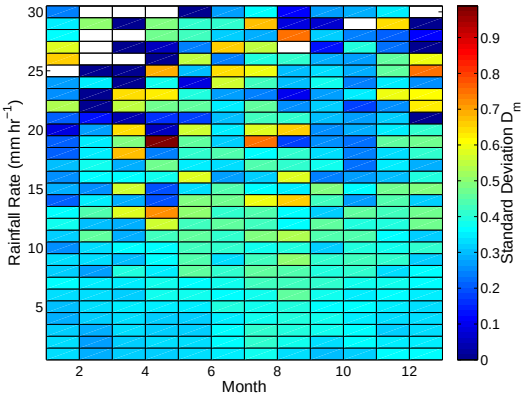


(b) Standard Deviation $D_m$.

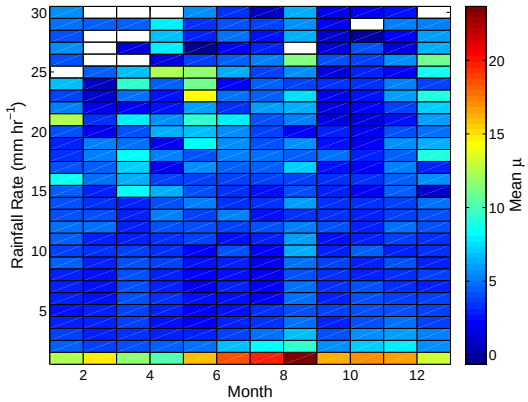


(c) Mean $\mu$.

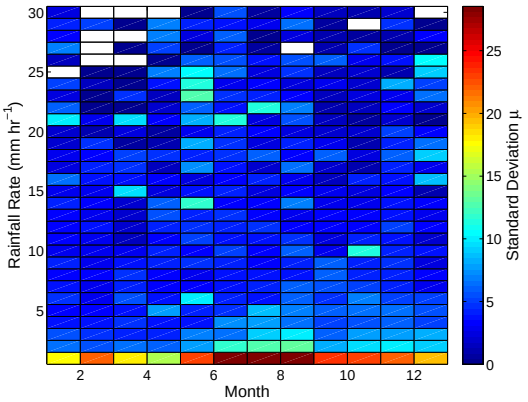


(d) Standard Deviation $\mu$.

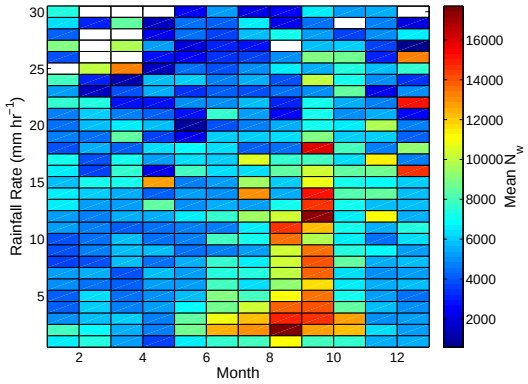


(e) Mean $N_w$.

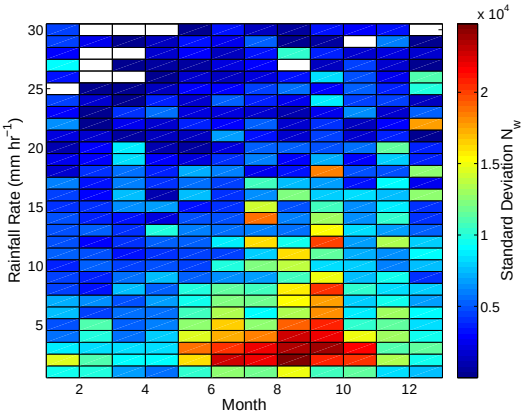


(f) Standard Deviation $N_w$.

Figure 3.7: $D_m$, $\mu$ and $N_w$ compared over 1 mm hr$^{-1}$ rainfall rate and monthly intervals.

### 3.2.3 Variability of the DSD as a function of rainfall rate and season

Histograms of $D_m$, $\mu$ and $N_w$ were determined for rainfall rates between 0 and 30 mm hr$^{-1}$ in intervals of 1 mm hr$^{-1}$. The data was partitioned into seasons; Spring (March, April, May), Summer (June, July, August), Autumn (September, October, November) and Winter (December, January, February).

Figures 3.8-3.10 show the histograms of the normalised Gamma DSD parameters as a function of rainfall rate. From Figure 3.8 it can be seen that $D_m$ generally increases with increasing rainfall rate. The variability of $D_m$ also increases with rainfall rate. Similar patterns are seen for $D_m$ in all seasons. However, both summer and spring show increased variation at high rainfall rates in comparison to Winter and Autumn.

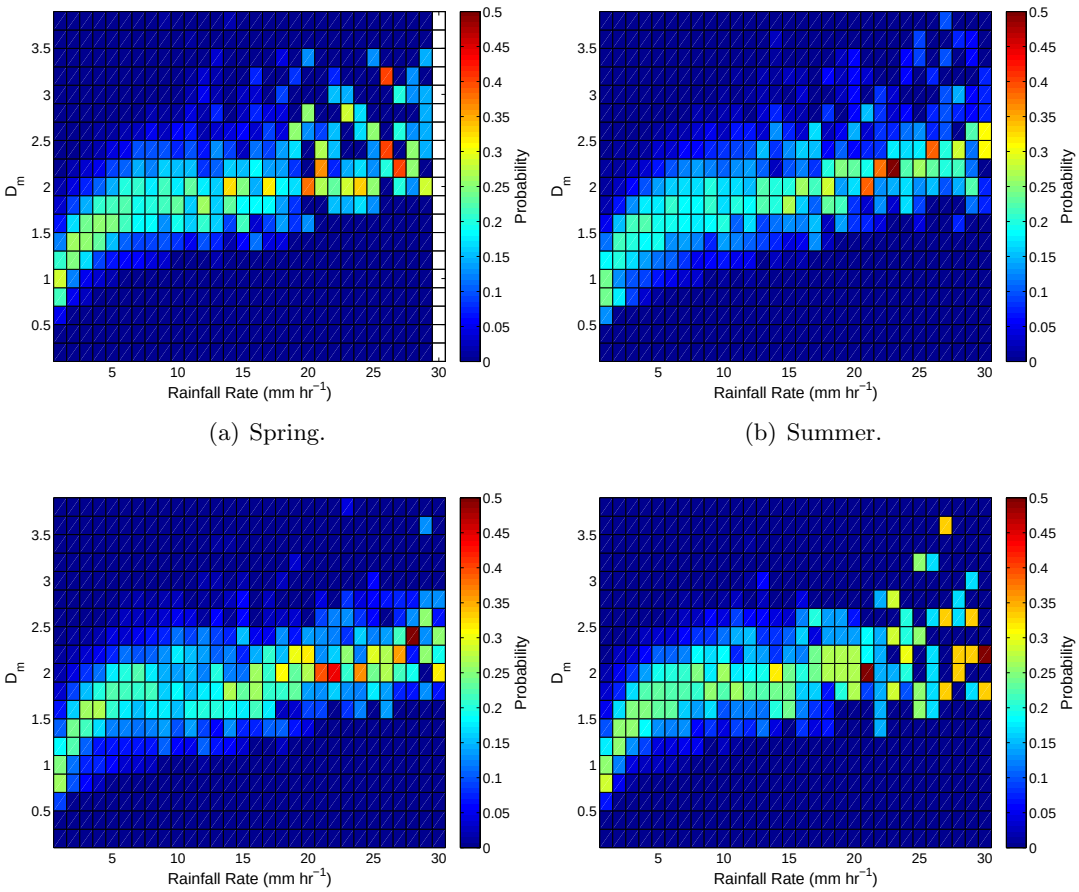


(a) Spring.

(b) Summer.

(c) Autumn.

(d) Winter.

Figure 3.8: Normalised Gamma parameter $D_m$ probability histograms versus rainfall rate separated in to seasons (Chilbolton).

From Figure 3.9, it can be seen that no clear pattern is observed for $\mu$. The $N_w$ parameter, see Figure 3.10, shows significant variation at lower rainfall rates but tends towards the value suggested by Marshall-Palmer at higher rainfall rates (larger than $10\,\mathrm{mm\,hr^{-1}}$). The distributions for $N_w$ and $\mu$ show more variability. Examination of Figures 3.8-3.10 shows that qualitatively there are two regions delineated at approximately $10\,\mathrm{mm\,hr^{-1}}$. The two regions likely represent the transition between stratiform and convective rain.

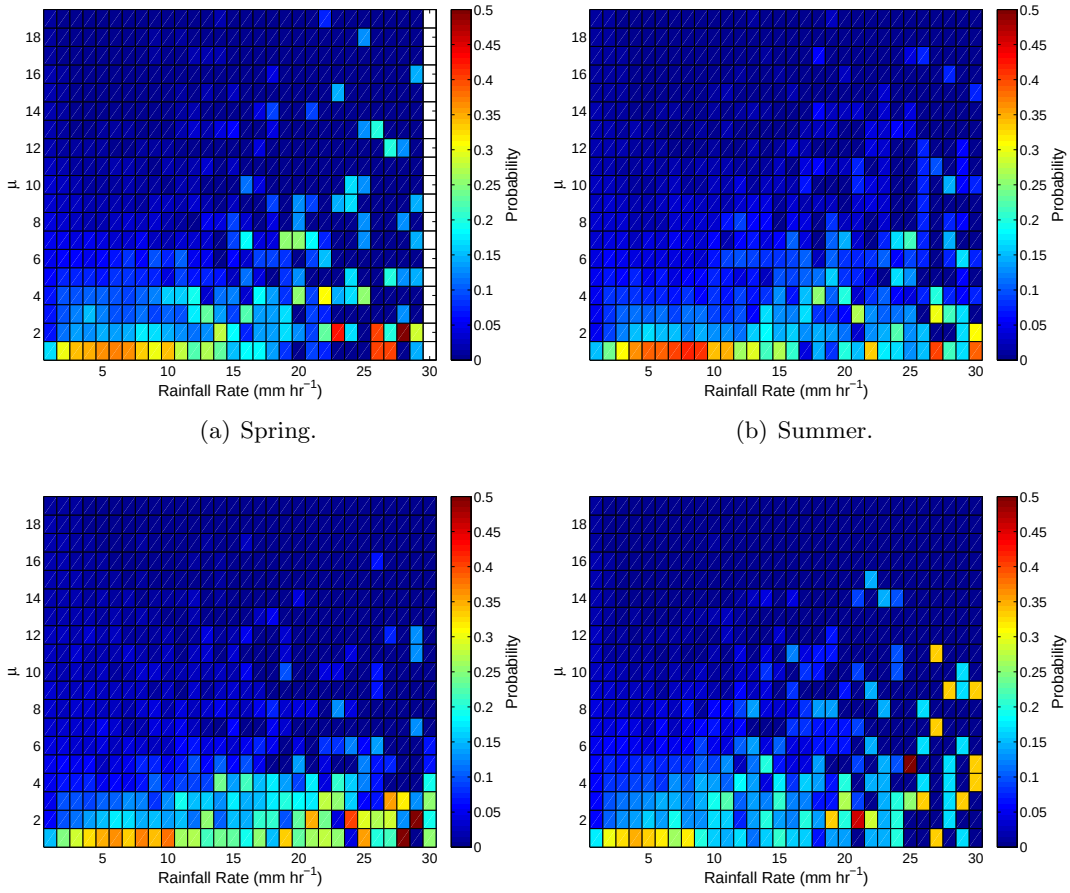


(a) Spring.

(b) Summer.

(c) Autumn.

(d) Winter.

Figure 3.9: Probability histograms of parameter $\mu$ versus rainfall rate separated in to seasons (Chilbolton).

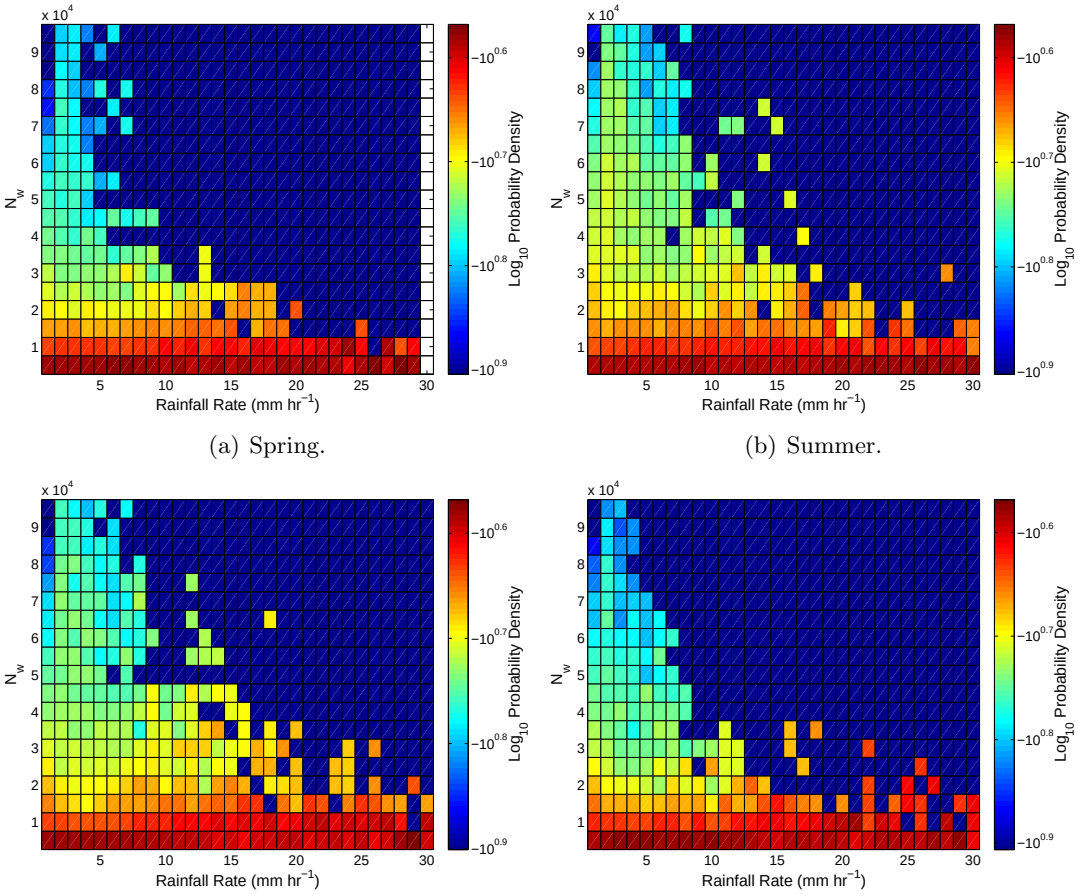


(a) Spring.

(b) Summer.

(c) Autumn.

(d) Winter.

Figure 3.10: Normalised gamma parameter $N_w$ probability histograms versus rainfall rate separated in to seasons (Chilbolton).

Atlas et al. [1999] defines a region of transition from convective to stratiform rain using rainfall measurements from a radar and disdrometer. A sharp rise to a peak rainfall rate in excess of $10\,\mathrm{mm\,hr^{-1}}$ while $D_0$ (median volume diameter) remains fairly constant is classified as initial convective rain. A transitional period occurs when $D_0$ decreases with rainfall rate. A stratiform period occurs during a steady rainfall rate period less than $10\,\mathrm{mm\,hr^{-1}}$ usually with an increasing value of $D_0$. The stratiform and convective regions are considered further in Chapter 6.

### 3.2.4 Variability in the attenuation and rainfall rate relationship

In this section of analysis, frequencies from 20 to 40 GHz are considered and the effects of frequency on the attenuation and rainfall rate relationship. The figures presented in this section relate to frequency of 20.7 GHz due to the availability of beacon data used to validate estimates of the attenuation rainfall rate relationship. Further consideration of the effect of frequency and polarisation are discussed in Chapter 5. Figure 3.11 shows the variability in the attenuation rainfall relationship for five years of data from Chilbolton, collected between 2003 and 2008.

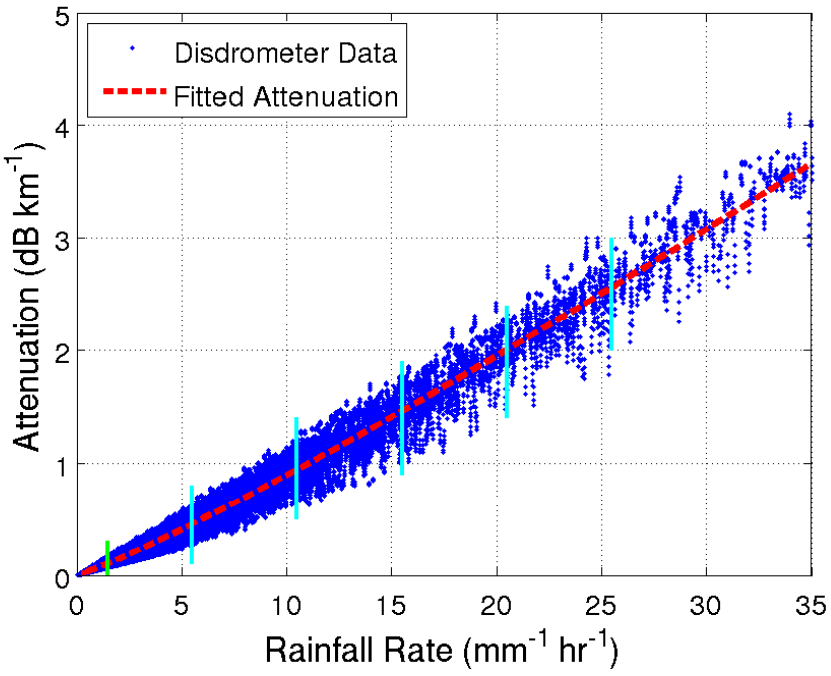


Figure 3.11: Attenuation vs rainfall rate for five years of disdrometer data at Chilbolton with fitted power law parameters $a = 0.066$ and $b = 1.13$ (frequency = 20.7 GHz).

To investigate the variability in the estimation of attenuation from rainfall rate, it is instructive to analyse histograms of attenuation conditioned on rainfall rate interval rather than just scatter plots. Several examples in Figure 3.12 show normalised histograms of specific attenuation at 20.7 GHz conditioned on rainfall rates between 1-2, 5-6, 10-11, 15-16, 20-21 and 25-26 mm $\mathrm{hr}^{-1}$ for the three sites based on attenuation bin-widths of 0.025 dB $\mathrm{km}^{-1}$. The cyan vertical lines in Figure 3.11 show the effective coverage of the histograms. It can be seen that there is general agreement between the mean values and the shapes of the distributions between sites. The histograms for other rainfall rates are of similar shape and can be approximated by a Gaussian distribution.

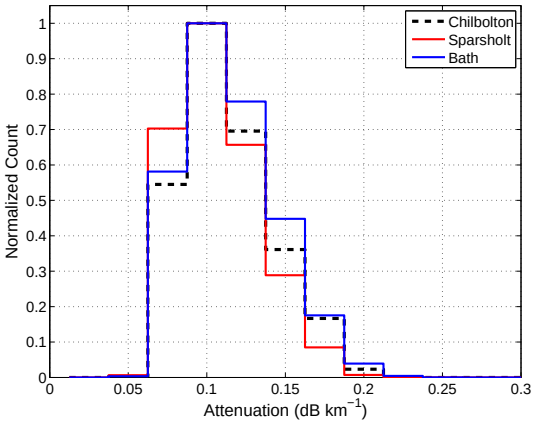


(a) 1-2 mm hr$^{-1}$.

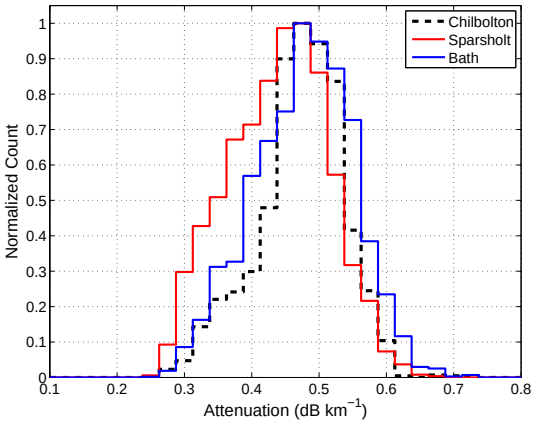


(b) 5-6 mm hr$^{-1}$.

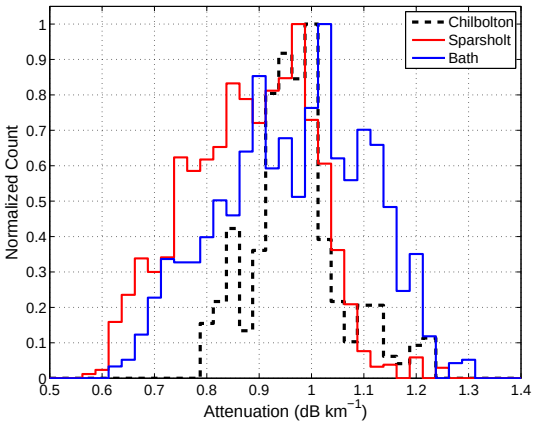


(c) 10-11 mm hr$^{-1}$.

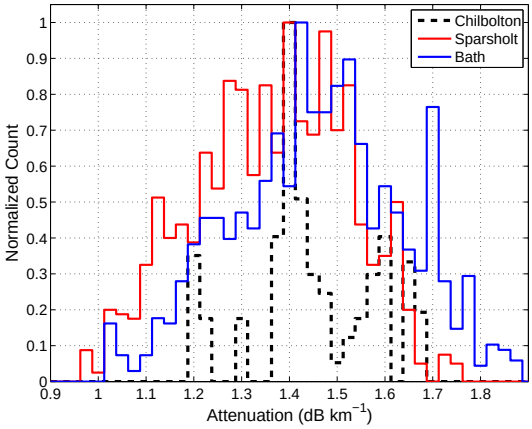


(d) 15-16 mm hr$^{-1}$.

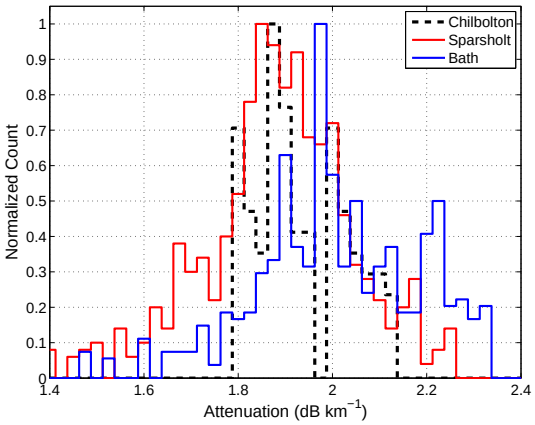


(e) 20-21 mm hr$^{-1}$.

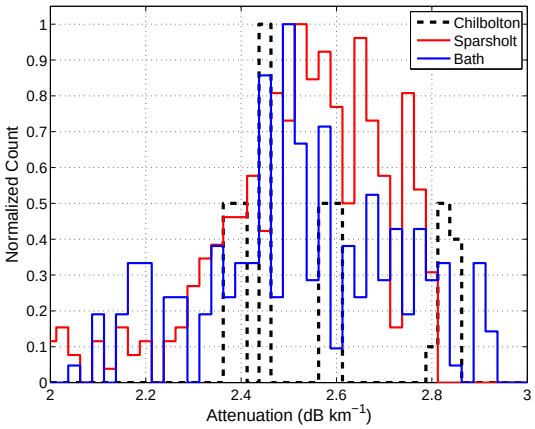


(f) 25-26 mm hr$^{-1}$.

Figure 3.12: Examples of normalised specific attenuation histograms over a 1 mm hr$^{-1}$ rainfall rate interval at 20.7 GHz for Bath, Chilbolton and Sparsholt.

For rainfall rates between 0 and 30 mm hr$^{-1}$ the mean and the variance of the attenuation histograms were determined. This rainfall rate range was selected as it is representative of 99.99 % of rainfall for most of the UK. Furthermore, this interval also ensures a statistically significant number of data points at the highest rainfall rates. A power law relationship was fitted to the mean ($\overline{A}$) and standard deviation ($\sigma_A$) of the data as follows;

$$\overline{A} = aR^b, \qquad \sigma_A = cR^d, \tag{3.26}$$

where $\overline{A}$ is the fitted attenuation, $a$ and $b$ are coefficients determined by the power law fit, $\sigma_A$ is the fitted standard deviation, $c$ and $d$ are coefficients determined by the power law fit to the standard deviation.

Figures 3.13 and 3.14 show the mean and standard deviation (respectively) of the histogram fits as a function of rainfall rate. It can be seen that there is good agreement between the means but the standard deviation shows significantly more scatter (as illustrated by the differences in the shape of the histograms in Figure 3.12). Although the difference in scatter can be partially explained by instrument differences at the sites, it does indicate the possibility of climatic differences affecting the variability of the DSD even for small separation distances (Chilbolton-Bath $\approx$ 80 km, Sparsholt-Chilbolton $\approx$ 7.5 km). As expected, the means agree well with ITU-R P.838-2. The fit to the mean effectively represents a least-squares fit to the data. Similar analysis was performed at 30 and 40 GHz, again with the mean showing good agreement with the ITU-R. Table 3.2 summarises the power law coefficients for the fits, which shows the effect of change in frequency on the curve fitting parameters. The effect of frequency on the attenuation and rainfall rate relationship is discussed further in Chapter 5.

Table 3.2: Curve fitted parameters for calculating mean specific attenuation ($\overline{A} = aR^b$ for R = 0-30 mm hr$^{-1}$) and standard deviation ($\sigma_A = cR^d$ for R = 0-30 mm hr$^{-1}$).

| Freq(GHz) | Mean | | | | | | Standard Deviation | | | | | |
|---|---|---|---|---|---|---|---|---|---|---|---|---|
| | Bath | | Chilbolton | | Sparsholt | | Bath | | Chilbolton | | Sparsholt | |
| | $a$ | $b$ | $a$ | $b$ | $a$ | $b$ | $c$ | $d$ | $c$ | $d$ | $c$ | $d$ |
| 20.7 | 0.075 | 1.08 | 0.066 | 1.13 | 0.057 | 1.16 | 0.029 | 0.58 | 0.030 | 0.64 | 0.015 | 0.72 |
| 30 | 0.162 | 1.02 | 0.170 | 1.04 | 0.149 | 1.07 | 0.057 | 0.12 | 0.060 | 0.41 | 0.077 | 0.19 |
| 40 | 0.284 | 0.96 | 0.350 | 0.94 | 0.322 | 0.97 | 0.038 | 0.66 | 0.019 | 1.14 | 0.019 | 1.03 |

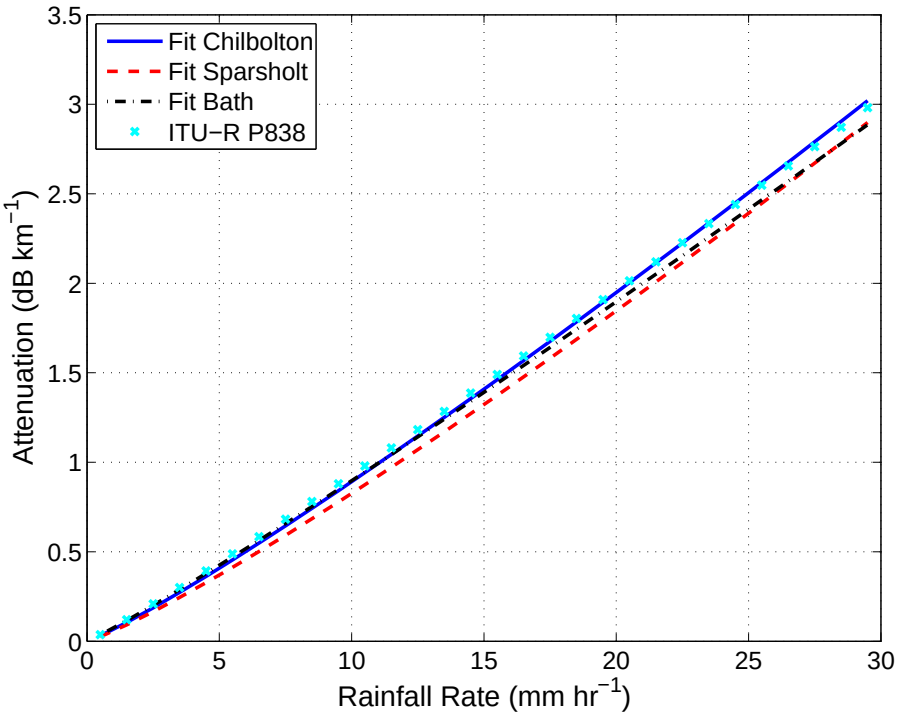


Figure 3.13: Mean specific attenuation at 20.7 GHz against rainfall rate for fitted estimates of attenuation, Chilbolton histogram attenuation and the ITU-R.

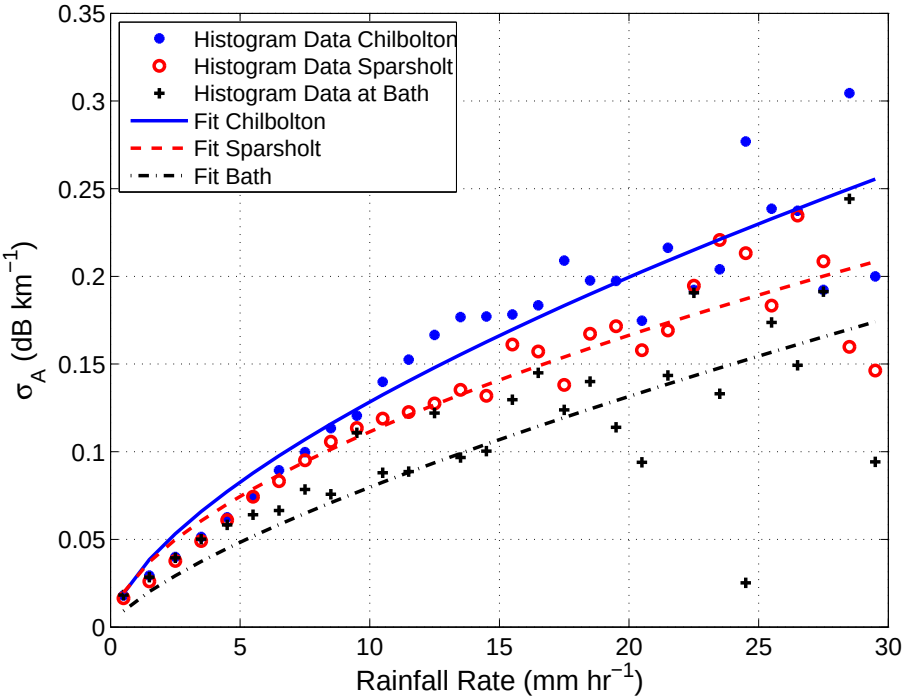


Figure 3.14: Fitted attenuation standard deviation vs rainfall rate at 20.7 GHz at Chilbolton, Sparsholt and Bath.

### 3.2.5 Global broadcast satellite comparison

Link attenuation from the Global Broadcast Satellite (GBS) beacon measurements at Chilbolton have been compared with attenuation estimated from disdrometer rainfall rate data to consider the effect of the DSD variability on earth space link attenuation. The GBS is a geostationary satellite with a beacon at 20.7 GHz. The rain height was estimated 0.36 km above the zero degree isotherm determined from surface temperature measurements close to the link and the disdrometer using a temperature lapse rate of $6.5\,\mathrm{K\,km^{-1}}$. The ITU-R P.618-8 effective path length model was used to scale the specific attenuation to yield the link attenuation.

Figure 3.15 shows typical link attenuation measured from the GBS beacon and the estimated link attenuation based on rainfall rate determined from the disdrometer on 22$^{\mathrm{nd}}$ June 2004. Note that the link attenuation was estimated from rainfall only, ignoring the raindrop size distribution data available from the disdrometer. The small negative excursions are remnants of the beacon post processing required since the GBS satellite is in an inclined geosynchronous orbit ($\approx 4°$), Hodges and Watson [2009]. The shaded region shown represents plus or minus one standard deviation above and below the mean of the estimated attenuation. This area shows the uncertainty in attenuation that could be expected due to variability in the raindrop size distribution alone. It can be seen that although there is some disagreement between the GBS beacon and mean attenuation the data is generally bounded within the shaded region. The occasions where this is not the case generally correspond to low attenuation and may be due to the different sampling volumes of the two measurements, variation in the rain height or incorrect attenuation baseline determination.

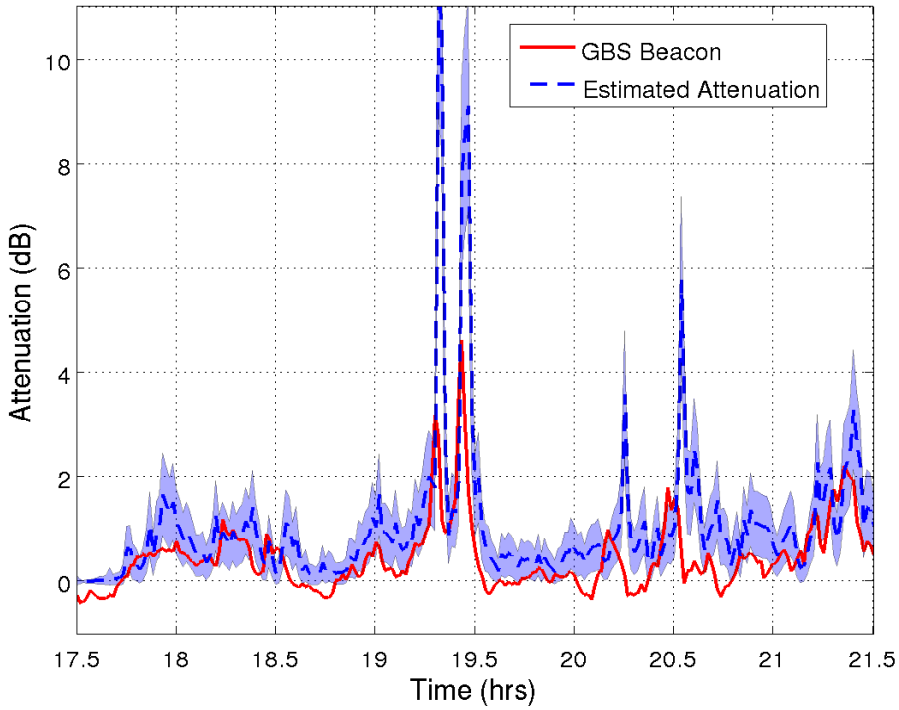


Figure 3.15: Chilbolton GBS beacon and estimated satellite signal attenuation at 20.7 GHz vs time on 22$^{\text{nd}}$ June 2004, where shaded region shows $\pm\sigma_A$.

## 3.3 Conclusion

Twelve years of drop size distribution data from three sites has been examined. The normalised gamma distribution was found to be a better fit than the exponential distribution to measured DSDs in the UK for time intervals of 60 seconds. Normalised gamma distribution parameters $N_w$ and $D_m$ show some patterns with rainfall rate and season. However, the shape parameter $\mu$ is not well correlated with rainfall rate.

The disdrometer results have shown the mean value of $N_w$ is broadly consistent with the value of $N_0$ determined by Marshall and Palmer [1948]. However, this investigation has shown $N_w$ is subject to seasonal variation, where the mean and standard deviation of $N_w$ is greater during the autumn. The drop concentration is higher during more stratiform rain and is subject to much more variation, which is more apparent during the autumn. The shape parameter $\mu$ is far more varied for rainfall rates below 1 mm hr$^{-1}$. The mean value of the shape parameter is smaller for rainfall rates between 1 and 10 mm hr$^{-1}$, which results in a more exponentially or stratiform shaped distribution. It has also been shown the mean drop diameter increases with rainfall rate, which is consistent with work such as Illingworth and Caylor [1989]. All three DSD parameters show two regions delineated at approximately 10 mm hr$^{-1}$, which is

likely as transition between stratiform and convective rain. The transition between stratiform and convective rain is supported by the work of Atlas et al. [1999]. Atlas et al. [1999] showed that the mean drop size is fairly consistent as rainfall rate increases above $10\,\mathrm{mm\,hr^{-1}}$, which is demonstrated by the results of $D_m$. Summer and spring months showed an increase in variation and standard deviation in the mean raindrop size.

The impact of the variability of the drop size distribution on attenuation is dependent on both season and rainfall intensity. Attenuation can see variation in the order of decibels per kilometre due the DSD alone at 20 GHz. The variation caused by the DSD increases with frequency, which is discussed further in Chapter 5. Although there are undoubtedly other effects, the differences between measured and estimated slant-path attenuations could be explained by variability of the raindrop size distribution.

Further work will consider how the parameters of the raindrop size distribution could be estimated or at least constrained by other meteorological information, such as temperature, pressure gradients and wind speed. Such data is available from, for example, numerical weather prediction models. This approach could be integrated into propagation prediction schemes and fade mitigation techniques. In its simplest form this could merely be a classifier between stratiform and convective rain. A more elaborate scheme might attempt to estimate numerical values of the DSD parameters.

# Chapter 4

# The effect of meteorology on raindrop size distribution

In this chapter, a relationship is sought between the raindrop size distribution parameters and other atmospheric elements in the troposphere such as pressure, temperature and wind speed. A pattern between one DSD parameter other than $D_m$ would allow the recreation of raindrop size distribution given meteorological data. The chapter uses meteorological data from surface measurements at Chilbolton and data provided by the Met Office Unified Model. The data is analysed with techniques such as correlation, Spearman's rank correlation and principal component analysis.

## 4.1 Introduction

In Chapter 3, correlation between the DSD parameters and rainfall rate was shown. It was also demonstrated that season has some impact on the relationships between rainfall rate and the DSD parameters. Seasons are caused by the change in position of the Earth relative to the sun, which result in different climatic environments. In this chapter, a more detailed analysis of the difference in climate is presented, in an attempt to establish a relation to the DSD. The meteorological parameters outlined in Chapter 2 are compared with the DSD parameters. The analysis attempts to find a correlation between one DSD parameter other than $D_m$. A relationship with one other DSD parameter and a meteorological variable would allow the DSD to be recreated given meteorological data. This chapter analyses both surface and aloft meteorological measurements in an attempt to define a relationship between meteorological and DSD parameters.

Variables such as CAPE, humidity, liquid water content and wind speed are compared with the DSD parameters. A variable such as CAPE, an indicator of the stability of the atmosphere and likelihood of storms or convective rain, is investigated to determine if there is correlation with the DSD parameters. CAPE is analysed to determine if an increase in CAPE, therefore more convective rain, has an inverse relationship with the drop concentration. This chapter also investigates variables such has humidity, an indication of the level water vapour in the air, in an attempt to determine if there is a relation with the DSD parameters $\mu$ and $N_w$. Vertical wind speed was analysed to determine if there is a correlation with drop concentration as drops are blown up in air allowing more time for collisions and the formation of bigger drops.

## 4.2 Meteorological measurements

Meteorological measurements were taken from surface measurements near the disdrometer, weather calculations made from the Met Office Unified Model and cloud type from Meteosat Second Generation satellites (MSG).

### 4.2.1 Surface measurements

Chilbolton observatory has several commercially available sensors that record surface meteorological data such as air temperature, dew point, atmospheric pressure, wind speed and wind direction. The meteorological instruments include a Rotronic temperature and relative humidity sensor, General Eastern Temperature and Chilled Mirror Dew Point Sensor, KDG 4000 series Pressure Transducer, Vector Instruments A100H Anemometer and a Vector Instruments W200 Windvane.

### 4.2.2 Unified Model

The Unified Model is based on a numerical weather modelling system, which has been in development by the Met Office since 1990, Met Office [2009]. The system is capable of modelling a wide range of time and space scales including kilometre-scale mesoscale nowcasts, limited-area weather forecasts, global weather forecasts, seasonal and climate predictions. The Unified Model produces outputs for pressure, temperature, wind speed components ($U$, $V$, $W$), liquid water content, specific humidity for a range of heights, large scale rainfall rates, convective rainfall rates and surface pressure.

### 4.2.3 Satellite cloud data

EUMETSAT is the European operational satellite agency for monitoring weather, climate and the environment. Meteosat Second Generation satellite data (located over Chilbolton, UK) was used to analyse the cloud type and determine if a relationship between cloud type and raindrop size distribution parameters existed. The cloud types were split into several categories: nimbostratus, stratus, altostratus, cumulus, and cirrus.

## 4.3 Review of Principle Component Analysis

Principal component analysis (PCA) identifies patterns within data with a high number of dimensions. The method transforms a number of possibly correlated variables into a smaller number of uncorrelated variables called principal components, Shlens [2009], Jolliffe [2002]. The first principal component accounts for as much variance in the data as possible.

To calculate principal component analysis the first step is to mean centre the data ($P_m$) by subtracting the mean from each data set dimension. Following this, the covariance matrix is calculated, which is used to determine the eigenvectors and eigenvalues. The eigenvectors provide information about the patterns within the data, whilst the eigenvalues determine the importance of the eigenvectors. An eigenvector is a special case of a multiplication between a matrix and a vector where the resultant vector is a multiple of the original vector. The eigenvalue is the multiple of the original vector. If the eigenvector is scaled before it is multiplied the result will still be the same. The covariance can be written as:

$$\mathrm{cov}(X,Y) = \frac{\sum_{i=1}^{\kappa}(X_i - \overline{X})(Y_i - \overline{Y})}{(\kappa - 1)}, \tag{4.1}$$

where $X$ and $Y$ are the two data sets of interest with means $\overline{X}$ and $\overline{Y}$, and $\kappa$ is the number of elements in the data. Once the eigenvectors and eigenvalues are calculated a feature vector, $F_V$, is created. The feature vector is a matrix which collects the eigenvectors with the highest eigenvalue first. Eigenvectors with the smallest eigenvalues may be removed to reduce the dimensions of the problem, as smaller eigenvalues account for little variance in the data and are of little significance. Shlens [2009], Jolliffe [2002] describe principal component analysis in further detail.

## 4.4 Review of Spearman's Rank Correlation

Spearman's rank correlation, James [1993], determines the statistical dependence between two variables using a non-parametric (or distribution-free) measure. The Spearman correlation is given between 1 and -1, where 1 is a perfect positive association, -1 is a perfect negative association and 0 indicates no association. Spearman's rank correlation is non-parametric, therefore data X and Y are not required to have linear relationship and the exact sampling distribution can be obtained without prior knowledge of the joint probability distribution of X and Y. The method is less sensitive to non-linear relationships and outliers in comparison to correlation.

The data must be given a rank (i.e. from smallest to largest) for the X and Y values separately. The difference in rank squared is represented by $d_{kr}^2$. If the number of tied ranks is small compared with the number of data points, where a tied rank occurs if two or more values of X (or Y) are the same, then Spearman's rank correlation ($S_{pr}$) is given by:

$$S_{pr} = 1 - \frac{6 \sum d_{kr}^2}{n_s(n_s^2 - 1)}, \tag{4.2}$$

where $n_s$ is the number of data points.

## 4.5 Surface meteorological sensor results

Normalised Gamma distribution parameters ($D_m$, $\mu$ and $N_w$) were compared with surface meteorological data to determine if the DSD parameters may be predicted using meteorological data. The meteorological sensors recorded data over 10 second intervals from 2003 to 2006. The measurements were averaged over six samples to determine results over one minute intervals for comparison with the DSD data.

### 4.5.1 Surface measurement analysis

#### Temperature

Each DSD parameter was compared with temperature using probability histograms calculated over temperature intervals of 0.5 K and parameter intervals $D_m$, $\mu$ and $N_w$ of 0.1, 1 and 1500 respectively. Each interval was chosen to comparable with uncertainty in the parameters. The mean and standard deviation for $D_m$, $\mu$ and $N_w$ were calculated

over 0.5 K intervals and are shown by the solid and dashed white lines respectively.

Figure 4.1(a) compares $D_m$ and temperature using probability histograms. The results show a slight increase in the mean and standard deviation of $D_m$ with temperature. However, there is little correlation to be seen. The majority of the results occur between 280 and 285 K with $D_m$ in the range of 0.6-2. As temperatures reaches freezing point (below ≈273 K) the mean drop size is smaller. Figure 4.1(b) shows the results of $\mu$ in relation to temperature. The highest concentration of $\mu$ occurs between 0 and 5 for 280 K to 285 K. The results show little correlation between $\mu$ and temperature, which is substantiated by a higher standard deviation than mean. Similarly, $N_w$ shows little relation with temperature, as shown in Figure 4.1(c).

**Pressure**

Probability histograms were generated for pressure over intervals of 125 Pa. On average $D_m$ decreases with pressure, as shown in Figure 4.1(d). Pressure compared with $\mu$, Figure 4.1(e), shows little correlation between the two where the standard deviation is higher than the mean. The highest variance in $\mu$ occurs around 100-101 kPa, approximately average pressure at sea level. In a similar manner, $N_w$ shows little relation with pressure and its highest variance occurs at average pressure at sea level.

**Wind speed**

Wind speed has been divided into probability histogram intervals of 0.5 $\mathrm{ms}^{-1}$, which is compared to $D_m$, $\mu$ and $N_w$ in Figures. 4.2(a) to 4.2(c). The mean of $D_m$ increases with horizontal wind speed, whilst $\mu$ and $N_w$ decreases. However, $\mu$ and $N_w$ have larger standard deviations than their respective means. The highest concentration of DSD parameters occur at approximate wind speeds of 4 $\mathrm{ms}^{-1}$.

**Dew point**

Probability histograms for dew point have been calculated over 0.5 K intervals. Figures 4.2(d) to 4.2(f) compare $D_m$, $\mu$ and $N_w$ with dew point. The majority of points lie within 278 to 285 K. The mean of $D_m$ shows little variation with dew point. The mean of $\mu$ and $N_w$ both increase with dew point but have a very high standard deviation. The DSD parameters show little correlation with dew point.

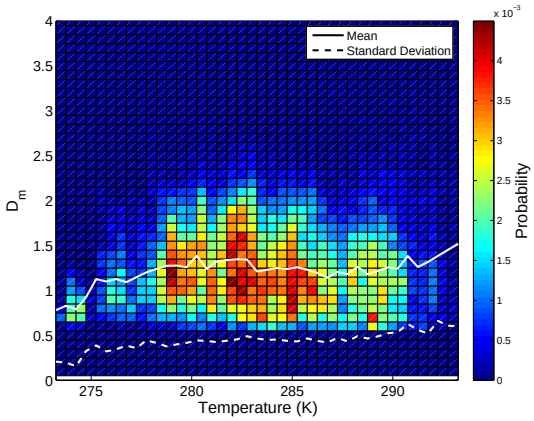


(a) Comparison of temperature and $D_m$.

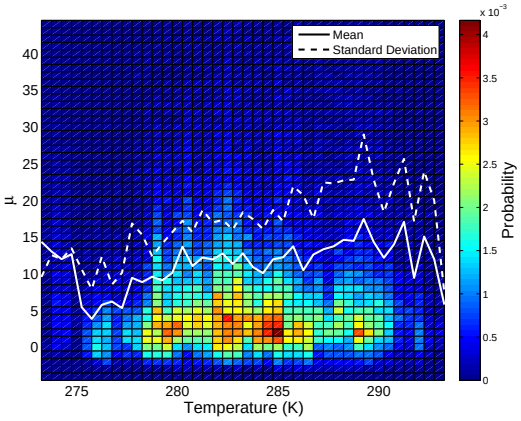


(b) Comparison of temperature and $\mu$.

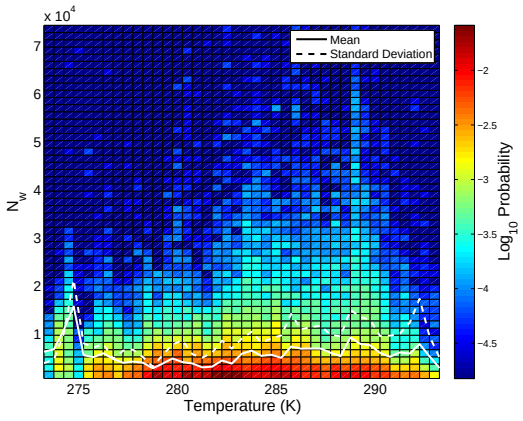


(c) Comparison of temperature and $N_w$.

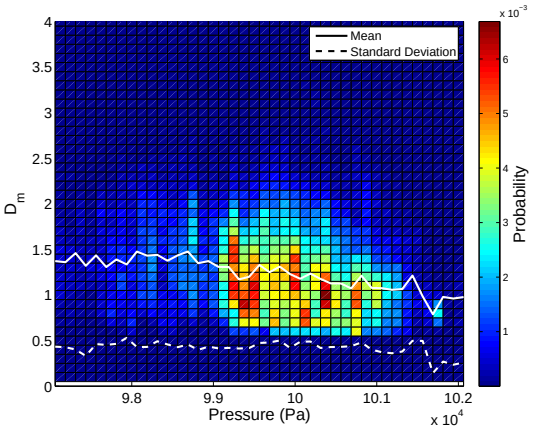


(d) Comparison of pressure and $D_m$.

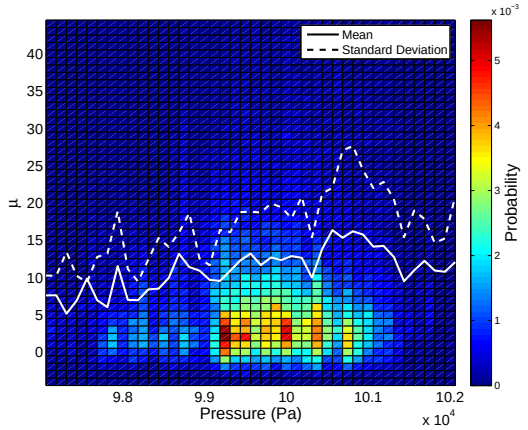


(e) Comparison of pressure and $\mu$.

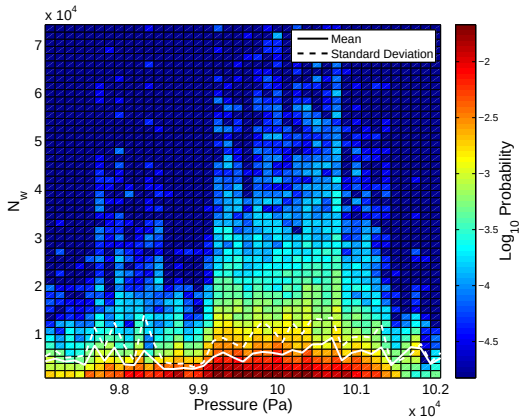


(f) Comparison of pressure and $N_w$.

Figure 4.1: Comparisons of surface measurements of temperature and pressure with normalised gamma distribution parameters $D_m$, $N_w$ and $\mu$.

### Surface lifting index

Figures 4.3(a) to 4.3(c) compare surface lifting index with $D_m$, $\mu$ and $N_w$ in the form of probability histograms over intervals of 0.1 (chosen since the interval is comparable to the variability in lifting index). The majority of lifting index values lie approximately at -1 where the highest variation in $\mu$ and $N_w$ occur. As the lifting index decreases, therefore the atmosphere becomes more unstable, the variation in $\mu$ and $N_w$ reduces. However, standard deviation of $\mu$ and $N_w$ is high in comparison to the mean values, demonstrating very little correlation with surface index. The mean and standard deviation of $D_m$ shows little change with lifting index demonstrating little relation between the two.

### Wind direction

Wind direction was compared to $D_m$, $\mu$ and $N_w$ using probability histograms over intervals of $10\,^\circ$, as shown in Figures 4.3(d) to 4.3(f). The results show $D_m$, $\mu$ and $N_w$ have little relation with wind direction. Both $\mu$ and $N_w$ had large standard deviation regardless of the wind direction.

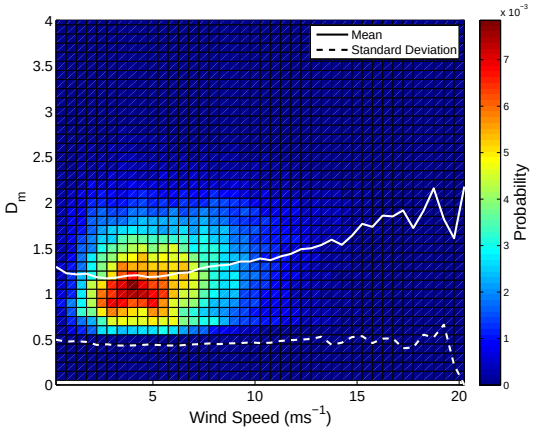


(a) Horizontal wind speed plotted against $D_m$.

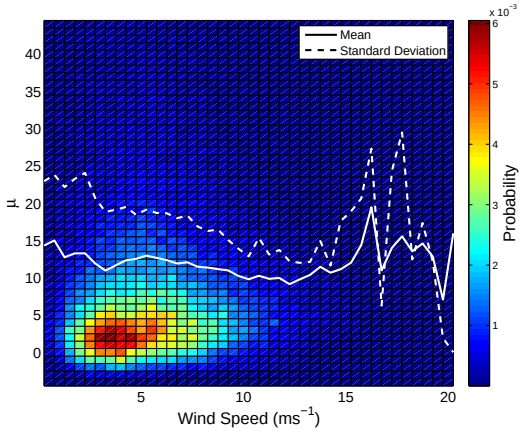


(b) Horizontal wind speed plotted against $\mu$.

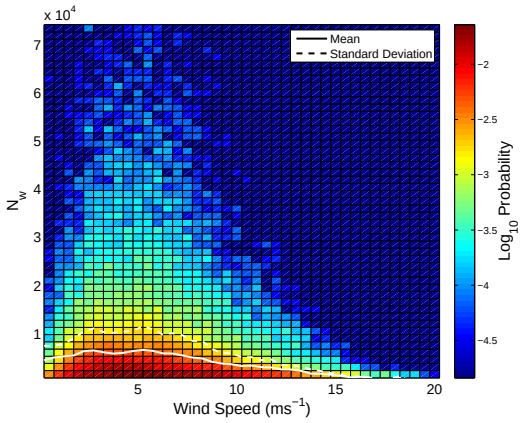


(c) Horizontal wind speed plotted against $N_w$.

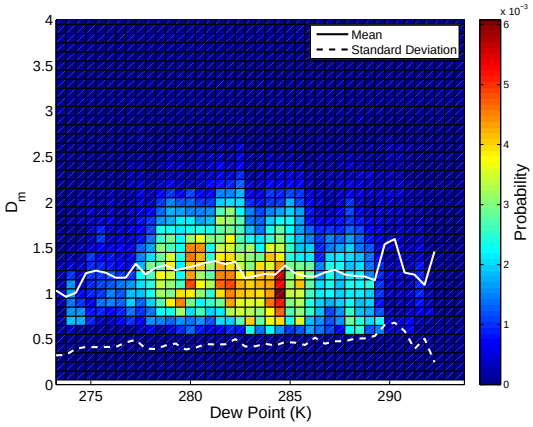


(d) Dew point plotted against $D_m$.

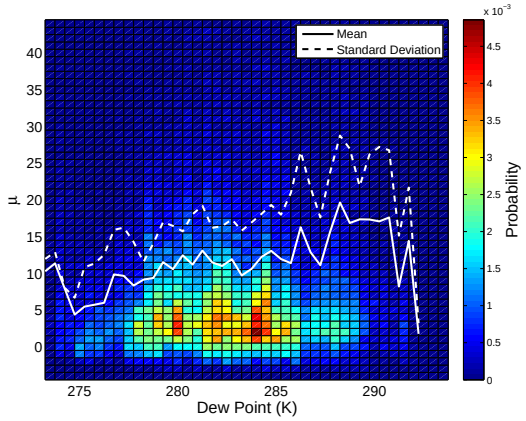


(e) Dew point plotted against $\mu$.

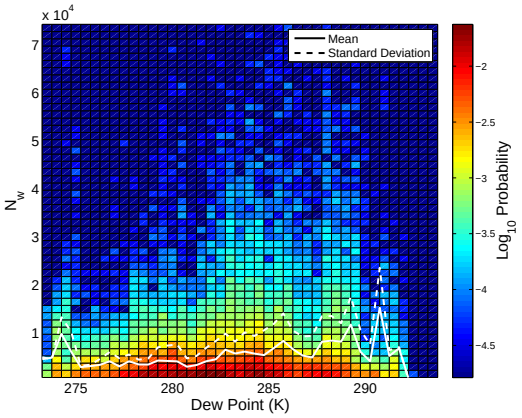


(f) Dew point plotted against $N_w$.

Figure 4.2: Comparisons of surface measurement of horizontal wind speed and dew point with normalised gamma distribution parameters $D_m$, $N_w$ and $\mu$.

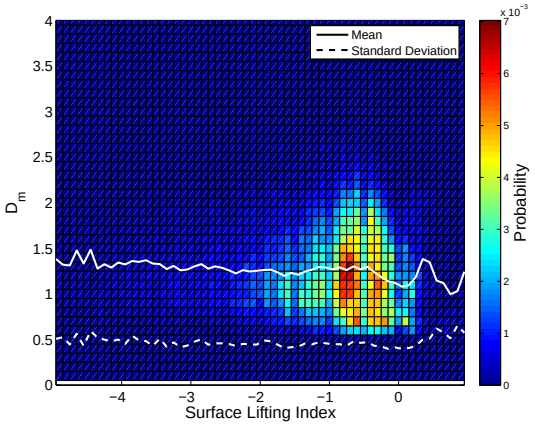


(a) Surface index plotted against $D_m$.

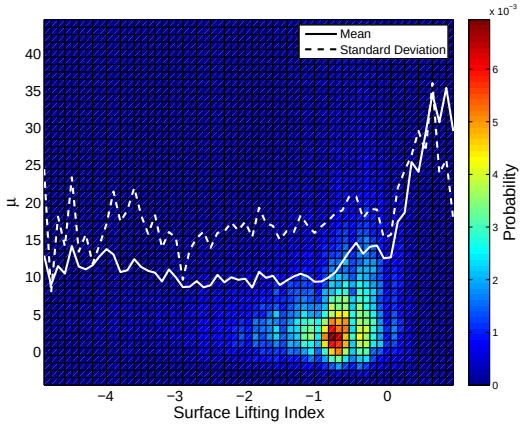


(b) Surface index plotted against $\mu$.

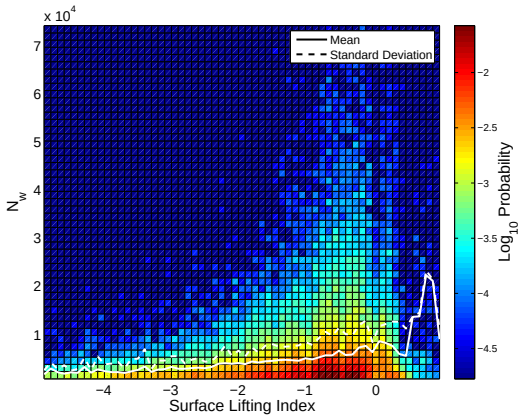


(c) Surface index plotted against $N_w$.

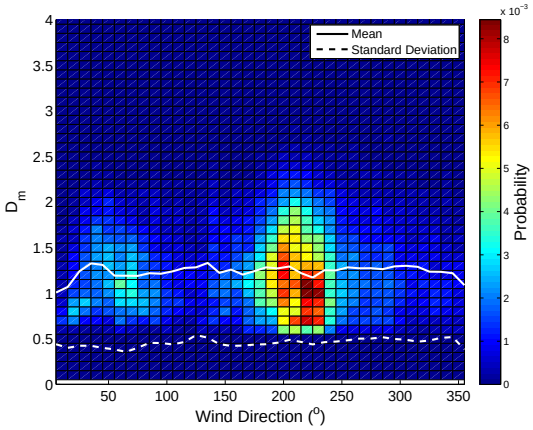


(d) Wind direction plotted against $D_m$.

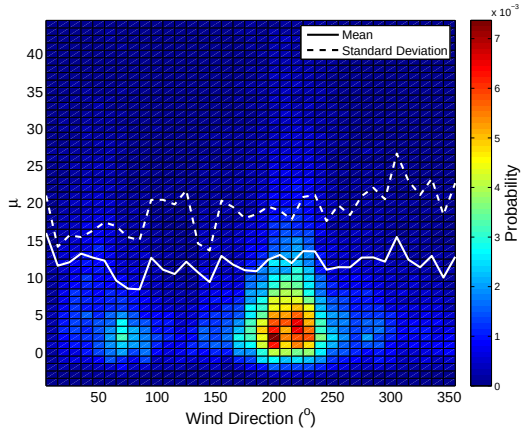


(e) Wind direction plotted against $\mu$.

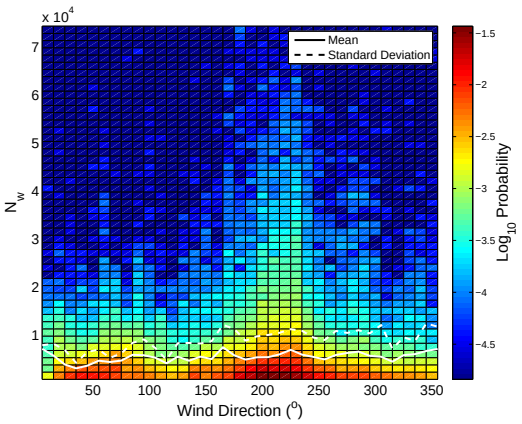


(f) Wind direction plotted against $N_w$.

Figure 4.3: Comparisons of surface measurements of lifting index and wind direction with normalised gamma distribution parameters $D_m$, $N_w$ and $\mu$.

### 4.5.2 Joint statistical analysis of surface measurements

The raindrop size distribution has shown little correlation with individual meteorological variables. However, the DSD parameters may be dependent on two meteorological components, which are examined using the following results. To limit the scope of this investigation the DSD parameters have only been compared to rainfall rate and one other surface measurement, as results in Chapter 3 have shown each DSD parameter has some relation to rainfall rate.

#### Dew point and rainfall rate

Figure 4.4 compares $D_m$, $\mu$ and $N_w$ with rainfall rate and dew point. The mean and standard deviation has been calculated over $1\,\mathrm{mm\,hr^{-1}}$ and 1 K intervals. Figure 4.4(a) shows mean $D_m$ increasing with rainfall. The mean increases at a higher rate with rainfall rate as dew point increases or decreases from 283 K. The standard deviation, Figure 4.4(b), is higher for the upper and lower ranges of dew point, i.e., above ≈287 K and below ≈278 K.

Parameter $\mu$ has high variance and high mean values at rainfall rates below $1\,\mathrm{mm\,hr^{-1}}$. Below this rainfall rate, the mean and standard deviation increases with dew point. Above $1\,\mathrm{mm\,hr^{-1}}$ the mean and standard deviation of $\mu$ shows little correlation with dew point.

Chapter 3 shows $N_w$ to have a considerably high mean and variance at rainfall rates below $10\,\mathrm{mm\,hr^{-1}}$. Figure 4.4(e) shows that for dew points above 283 K and rainfall rates less than $10\,\mathrm{mm\,hr^{-1}}$, $N_w$ has high mean and standard deviation. For rainfall rates below $10\,\mathrm{mm\,hr^{-1}}$ and dew points less than 283 K, $N_w$ has a considerably smaller mean and standard deviation (i.e. approximately $0.4 \times 10^4$). The smaller mean and standard deviation could potentially be used to determine a better approximation of $N_w$ conditioned on rainfall rate and dew point. Above $10\,\mathrm{mm\,hr^{-1}}$ $N_w$ is similar to results in Chapter 3 where $N_w$ is smaller and has a lower standard deviation, which showed little notable relation with dew point.

It has already been noted that a rain rate of $10\,\mathrm{mm\,hr^{-1}}$ could be a delimiter between stratiform and convective rain, in Chapter 3. However, convective rain could potentially occur below $10\,\mathrm{mm\,hr^{-1}}$. For a high dew point (above 283 K) air must be cooled to a higher temperature for water vapour to condense, where a high drop concentration ($N_w$) is present. Higher drop concentration could suggest more widespread rain, therefore dew point may also be an approximate delimiter for convective rain below $10\,\mathrm{mm\,hr^{-1}}$.

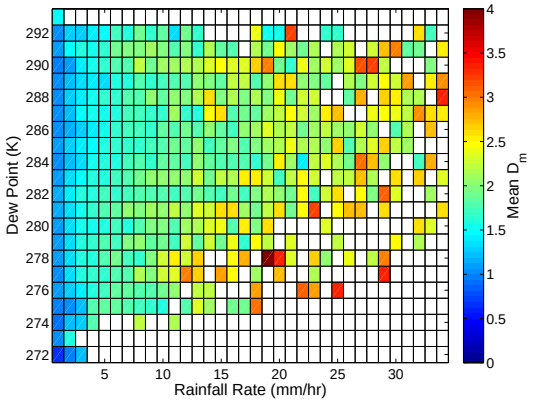


(a) Mean $D_m$ compared with dew point and rainfall rate.

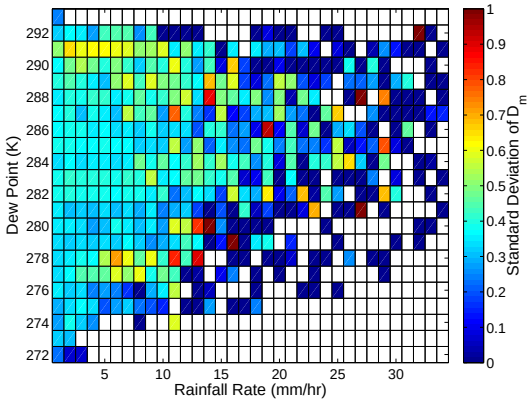


(b) Standard Deviation of $D_m$ compared with dew point and rainfall rate.

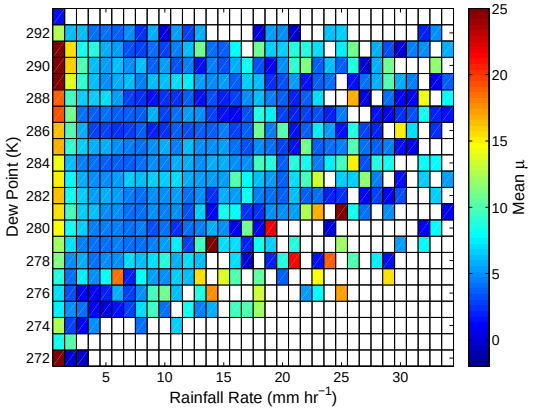


(c) Mean $\mu$ compared with dew point and rainfall rate.

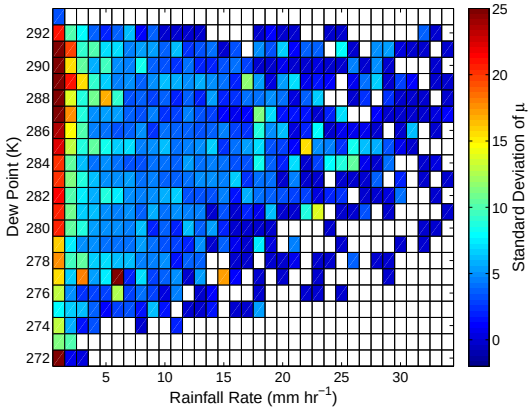


(d) Standard Deviation of $\mu$ compared with dew point and rainfall rate.

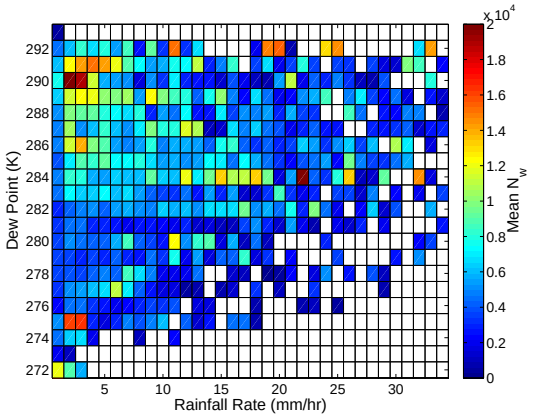


(e) Mean $N_w$ compared with dew point and rainfall rate.

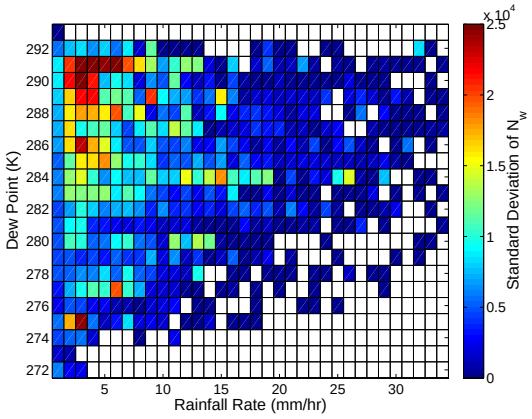


(f) Standard Deviation of $N_w$ compared with dew point and rainfall rate.

Figure 4.4: Mean and standard deviation of $D_m$, $\mu$ and $N_w$ over rainfall rate intervals of $1\,\mathrm{mm\,hr^{-1}}$ and dew point surface measurements at intervals of 1 K.

### Temperature and rainfall rate

Temperature and rainfall rate were compared with the DSD parameters. The mean and standard deviation were calculated over 1 K and 1 mm hr$^{-1}$ intervals, see Figures 4.5(a)-4.5(b). Since dew point and temperature are fairly correlated there is little difference in the comparison with DSD parameters. For temperatures above 285 k the mean of $D_m$ increases at a higher rate with increasing temperature. In a similar manner, temperatures below 285 K mean $D_m$ increases at a higher rate as the temperature falls. The standard deviation also mimics this relationship with temperature. Temperatures above or below average result in larger mean drop sizes with corresponding rainfall rates, which could be an indication of convective rain.

Figures 4.5(c) and 4.5(d) shows the mean and standard deviation of $\mu$ compared with rainfall rate and temperature. There is little additional correlation with $\mu$, temperature and rainfall rate. However, for rainfall rates below 5 mm hr$^{-1}$ the mean and standard deviation of $\mu$ increases.

The mean and standard deviation of $N_w$ shows a similar relationship with temperature and rainfall rate as dew point and rainfall rate. As temperature rises above 285 K for rainfall less than 10 mm hr$^{-1}$, the mean and standard deviation is higher than temperatures below 285 K and rainfall less than 10 mm hr$^{-1}$.

### Pressure and rainfall rate

The DSD parameters were compared with pressure and rainfall rate, where the mean and standard deviation were calculated over 250 Pa and 1 mm hr$^{-1}$ intervals. The mean of $D_m$, Figure 4.6(a), shows little overall correlation with pressure but is still dependent on rainfall rate. The standard deviation of $D_m$ confirms there is little correlation with pressure. Parameter $\mu$ shows the familiar pattern of high variance and mean at rainfall rates below 3 mm hr$^{-1}$ and shows little additional correlation with pressure and rainfall rate, Figure 4.6(d).

Figure 4.6(e) shows mean $N_w$ is higher for rainfall rates below 10 mm hr$^{-1}$ during pressures above 99 kPa than pressure below 99 kPa. The standard deviation, Figure 4.6(f), is also higher for the same described region. The rainfall rate and pressure boundaries could potentially improve estimates of $N_w$ and be a delimiter between stratiform and convective rain. The relationship is similar to the comparison of $N_w$ with rainfall rate and dew point.

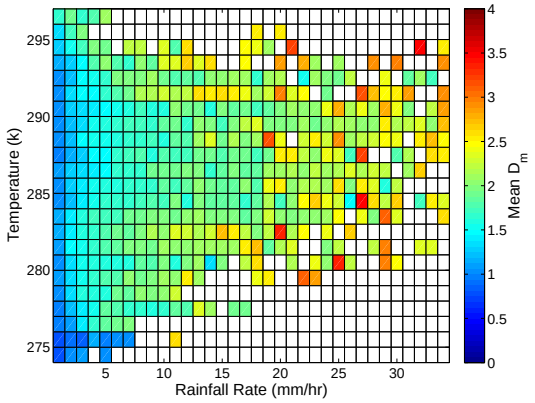


(a) Mean $D_m$ compared with temperature and rainfall rate.

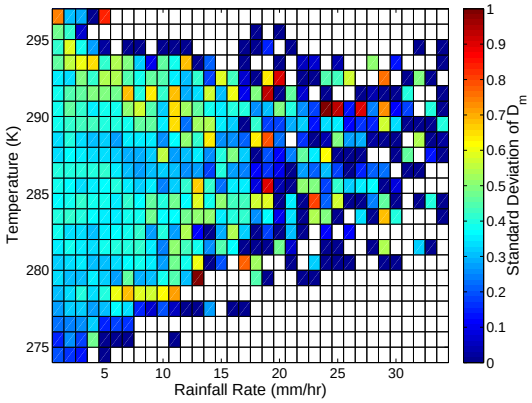


(b) Standard Deviation of $D_m$ compared with temperature and rainfall rate.

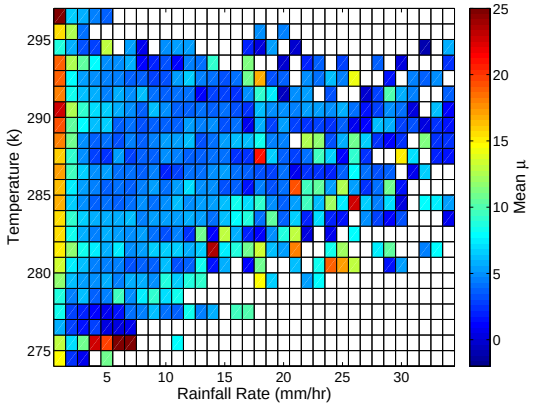


(c) Mean $\mu$ compared with temperature and rainfall rate.

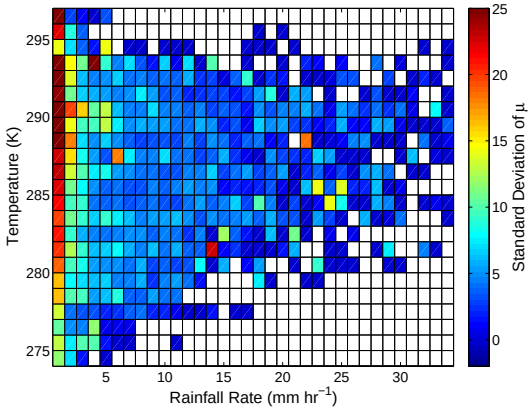


(d) Standard Deviation of $\mu$ compared with temperature and rainfall rate.

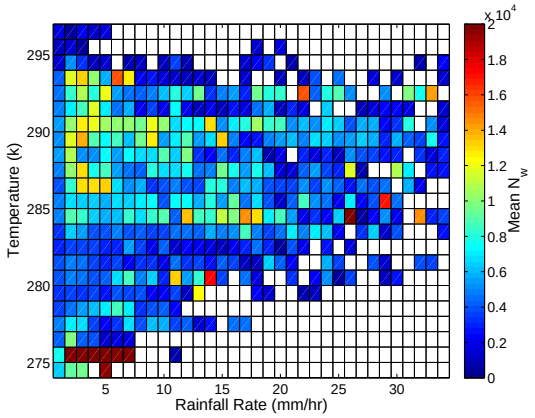


(e) Mean $N_w$ compared with temperature and rainfall rate.

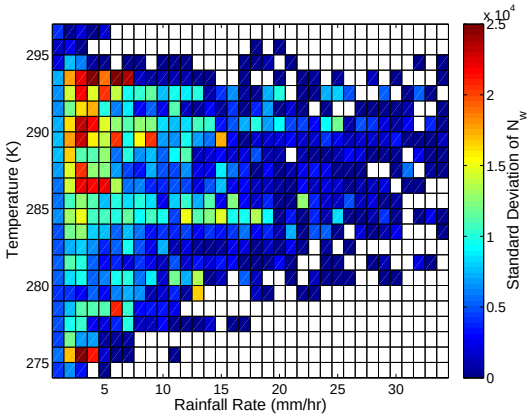


(f) Standard Deviation of $N_w$ compared with temperature and rainfall rate.

Figure 4.5: Mean and standard deviation of $D_m$, $\mu$ and $N_w$ over rainfall rate intervals of $1\,\mathrm{mm\,hr^{-1}}$ and surface temperature intervals of 1 K.

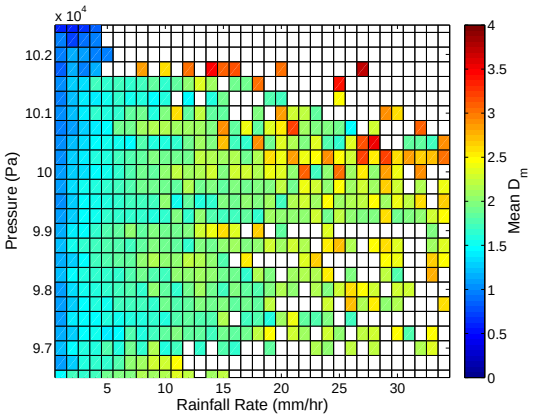


(a) Mean $D_m$ compared with pressure and rainfall rate.

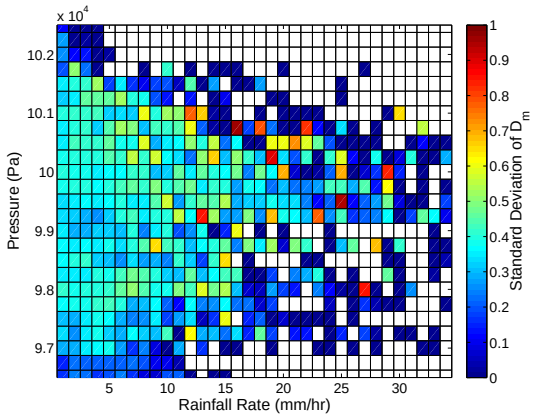


(b) Standard deviation of $D_m$ compared with pressure and rainfall rate.

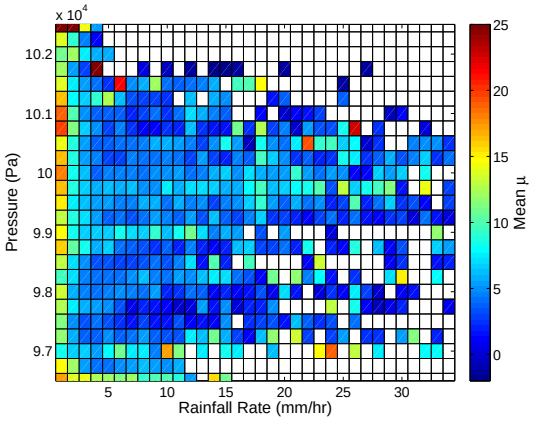


(c) Mean $\mu$ compared with pressure and rainfall rate.

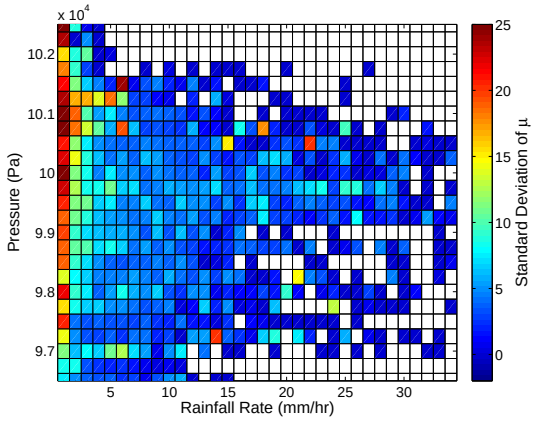


(d) Standard deviation of $\mu$ compared with pressure and rainfall rate.

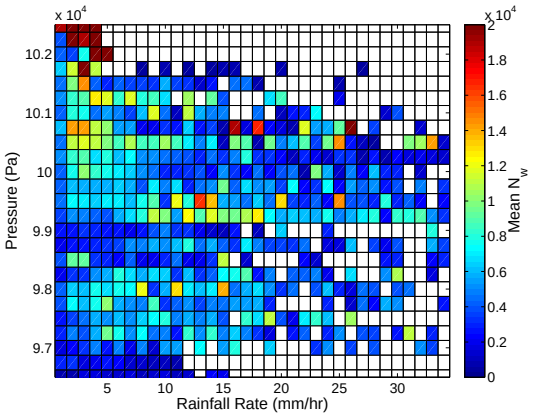


(e) Mean $N_w$ compared with pressure and rainfall rate.

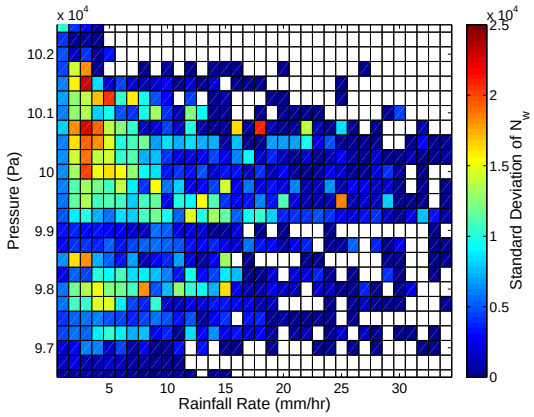


(f) Standard deviation of $N_w$ compared with pressure and rainfall rate.

Figure 4.6: Mean and standard deviation of $D_m$, $\mu$ and $N_w$ over rainfall rate intervals of $1\,\mathrm{mm\,hr^{-1}}$ and surface pressure intervals of 250 Pa.

### Surface lifting index and rainfall rate

Surface lifting index was compared with rainfall rate, Figure 4.7, for each DSD parameter mean and standard deviation calculated over intervals of a lifting index of 0.2 and rainfall rate of $1\,\mathrm{mm\,hr^{-1}}$. The mean of $D_m$ is larger with smaller values of lifting index, where thunderstorms are more likely. The highest mean of $\mu$ occurs for high values of surface lifting index but has a high standard deviation. The mean and standard deviation of $N_w$ is also highest for lifting indexes above -1. The low values of lifting index indicate a more unstable environment and thunderstorms, therefore convective rain is likely. The lifting index could provide information to determine a convective and stratiform boundary.

### Rainfall rate and wind speed

Figure 4.8 compares DSD parameters with wind speed and rainfall rate over intervals of $0.5\,\mathrm{ms^{-1}}$ (an interval chosen to be comparable to the variability in wind speed) and $1\,\mathrm{mm\,hr^{-1}}$. Figure 4.8(a) shows $D_m$ increases with rainfall rate, but at a higher rate for wind speeds above $10\,\mathrm{ms^{-1}}$ or below $5\,\mathrm{ms^{-1}}$. Within the boundary of 5 to $10\,\mathrm{ms^{-1}}$ the rate of increase in $D_m$ is less, which suggests that, on average, the mean raindrop size is smaller and could be an indicator of stratiform rainfall. As wind speed increases, the maximum rainfall reduces. At high wind speeds (above $10\,\mathrm{ms^{-1}}$) on average the mean drop diameter is larger, which could be an indicator of more convective rain. The higher rate of increase in $D_m$ for wind speeds below $5\,\mathrm{ms^{-1}}$ could also suggest convective rain. Precipitation accompanied by strong winds (often during winter) usually have larger raindrops. During the summer, convective rain is more frequent and can be accompanied by low wind speeds. The standard deviation of $D_m$, Figure 4.8(b), is slightly higher for low wind speeds (below $5\,\mathrm{ms^{-1}}$) and rainfall rates above $10\,\mathrm{mm\,hr^{-1}}$, however the standard deviation is relatively low.

Figures 4.8(c) and 4.8(d) show the comparison of the mean and standard deviation of $\mu$ between wind speed and rainfall rate. The value and variation in $\mu$ has little correlation with rainfall rate and wind speed. The parameter $N_w$ (shown in Figures 4.8(e) and 4.8(f)) has higher values of mean and standard deviation for rainfall rates below $15\,\mathrm{mm\,hr^{-1}}$ and wind speeds below $8\,\mathrm{ms^{-1}}$. Above a wind speed of $8\,\mathrm{ms^{-1}}$ the mean and standard deviation are smaller in comparison to wind speeds below $8\,\mathrm{ms^{-1}}$. In order for a DSD with a smaller drop concentration to match the rainfall rate with a DSD with high drop concentration, the average rain drop size must be larger. Therefore, the smaller drop concentration at wind speeds above $8\,\mathrm{ms^{-1}}$ suggests convective rain due to larger rain drops. The combination of wind speed, dew point, pressure and rainfall

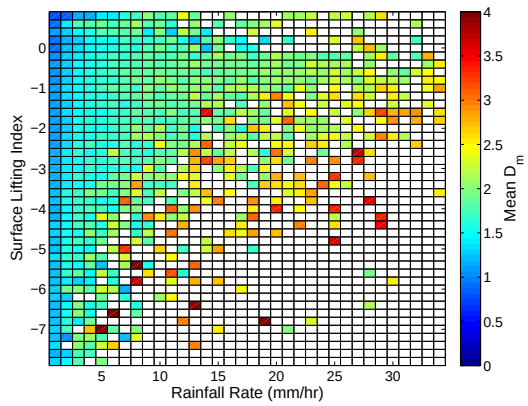


(a) Mean of $D_m$ over surface lifting index and rainfall rate.

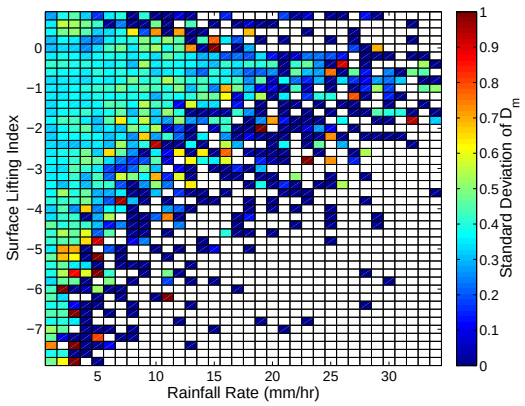


(b) Standard deviation of $D_m$ over surface lifting index and rainfall rate.

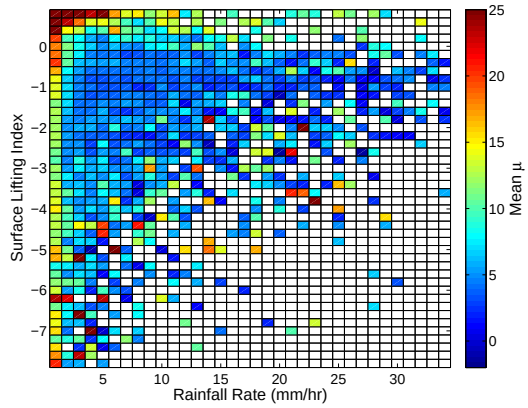


(c) Mean of $\mu$ over surface lifting index and rainfall rate.

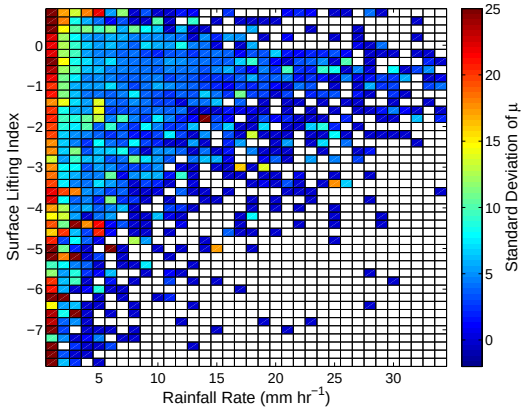


(d) Standard deviation of $\mu$ over surface lifting index and rainfall rate.

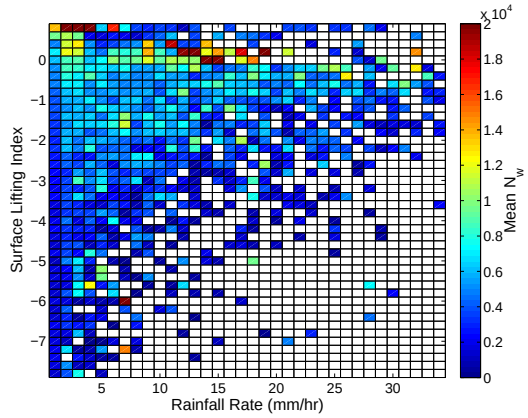


(e) Mean of $N_w$ over surface lifting index and rainfall rate.

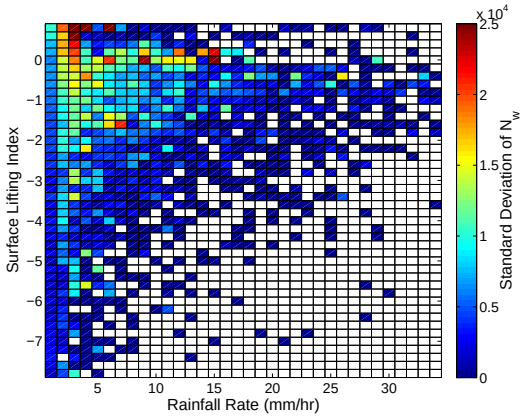


(f) Standard deviation of $N_w$ over surface lifting index and rainfall rate.

Figure 4.7: Mean and standard deviation of $D_m$, $\mu$ and $N_w$ over rainfall rate intervals of $1\,\mathrm{mm\,hr^{-1}}$ and surface lifting index intervals of $0.2\,\mathrm{ms^{-1}}$.

rate information could be used to help quantify the value of $N_w$ and better estimate the DSD.

### Change in wind speed

Change in wind speed was calculated and compared with rainfall rate and the mean values of the DSD over intervals of $0.1\text{ms}^{-2}$. The results are similar to the previous wind speed and DSD parameter comparison. Figure 4.9(a) shows $D_m$ is, on average, larger for rainfall rates below $10\,\text{mm}\,\text{hr}^{-1}$ and changes in wind speed exceeding $\approx 1.5\,\text{ms}^{-2}$. There is very little correlation with $\mu$, whilst $N_w$ has a high mean and standard deviation for gradients less than $1\,\text{ms}^{-2}$ and rainfall rates below $15\,\text{mm}\,\text{hr}^{-1}$.

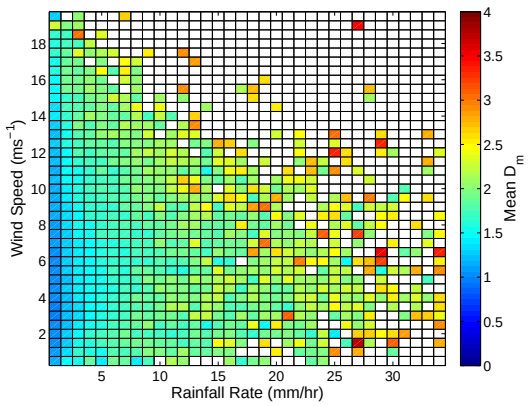


(a) Mean of $D_m$ over wind speed and rainfall rate.

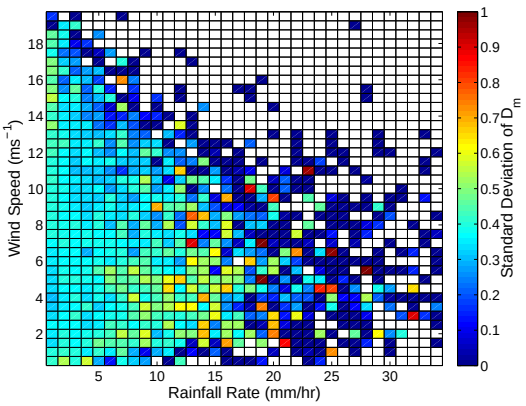


(b) Standard deviation of $D_m$ over wind speed and rainfall rate.

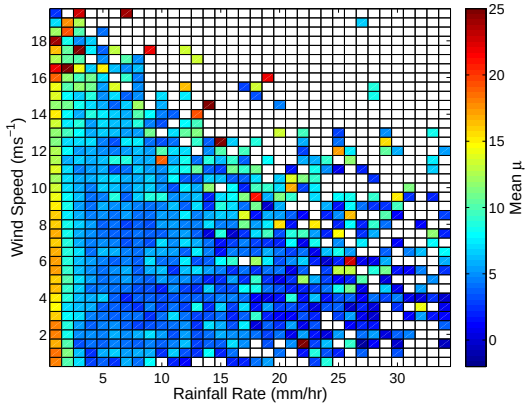


(c) Mean of $\mu$ over wind speed and rainfall rate.

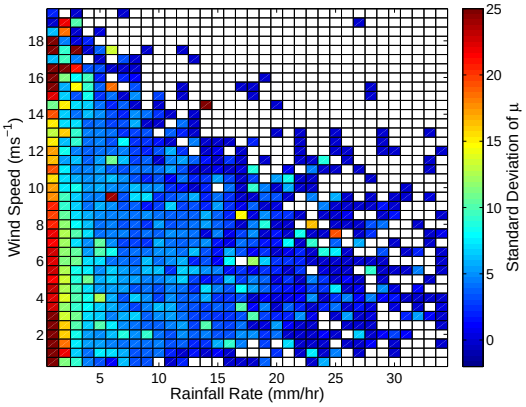


(d) Standard deviation of $\mu$ over wind speed and rainfall rate.

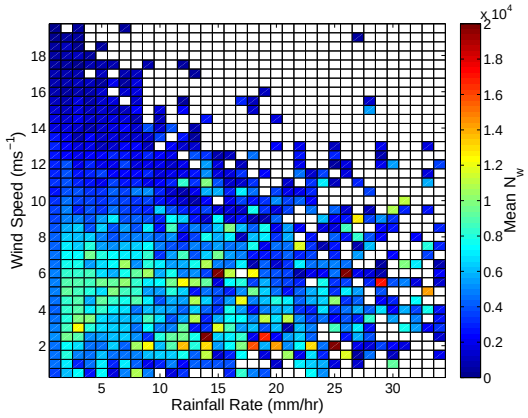


(e) Mean of $N_w$ over wind speed and rainfall rate.

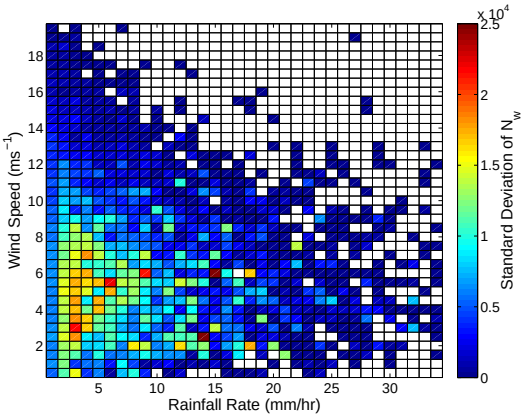


(f) Standard deviation of $N_w$ over wind speed and rainfall rate.

Figure 4.8: Mean and standard deviation of $D_m$, $\mu$ and $N_w$ over rainfall rate intervals of $1\,\mathrm{mm\,hr^{-1}}$ and surface wind speed intervals of $0.6\,\mathrm{ms^{-1}}$.

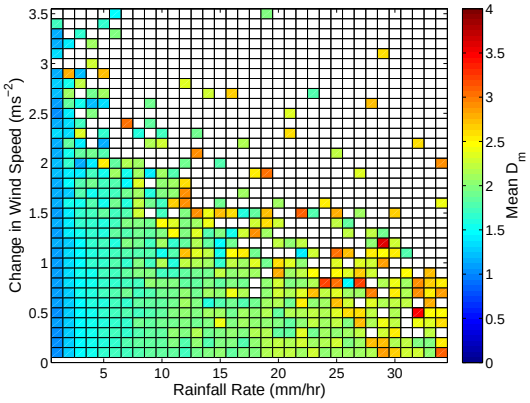


(a) Mean of $D_m$ over wind speed gradient and rainfall rate.

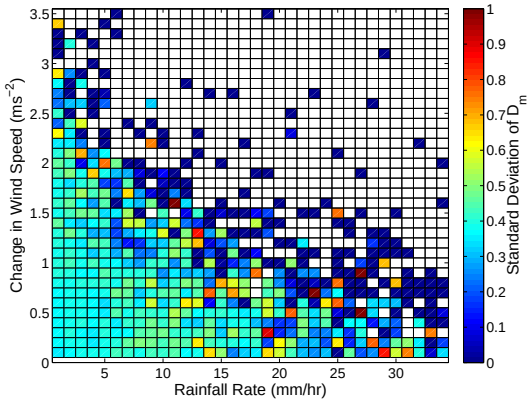


(b) Standard deviation of $D_m$ over wind speed gradient and rainfall rate.

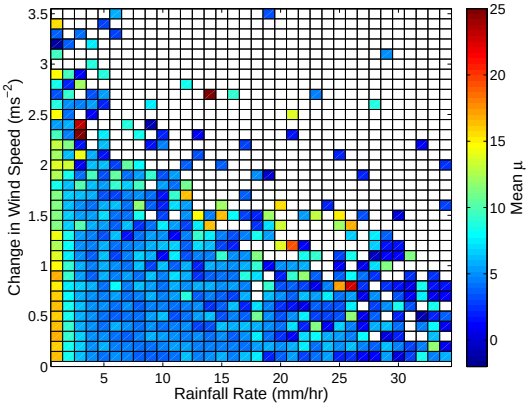


(c) Mean of $\mu$ over wind speed gradient and rainfall rate.

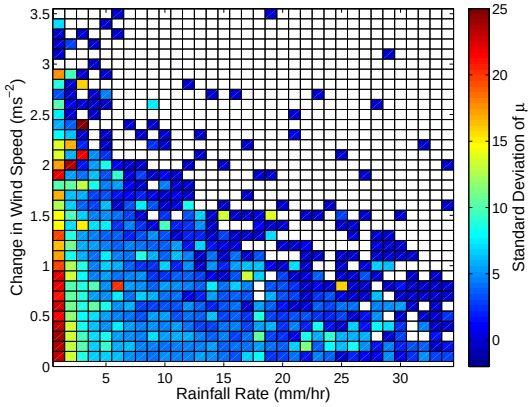


(d) Standard deviation of $\mu$ over wind speed gradient and rainfall rate.

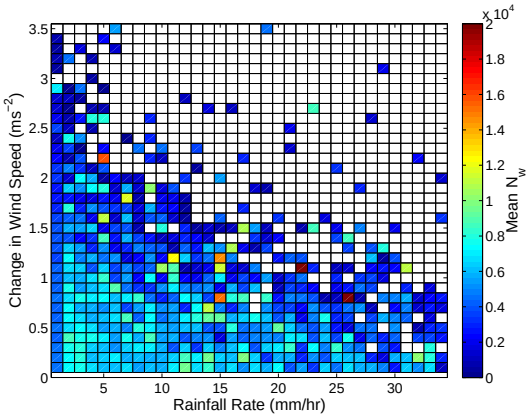


(e) Mean of $N_w$ over wind speed gradient and rainfall rate.

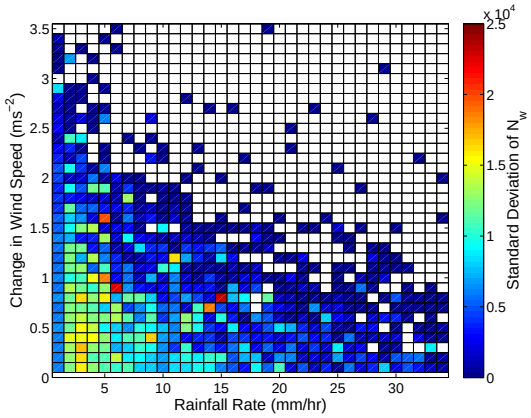


(f) Standard deviation of $N_w$ over wind speed gradient and rainfall rate.

Figure 4.9: Mean and standard deviation of $D_m$, $\mu$ and $N_w$ over rainfall rate intervals of $1\,\mathrm{mm\,hr^{-1}}$ and change in wind speed surface measurements over intervals of $0.11\,\mathrm{ms^{-1}}$.

### 4.5.3 Correlation of surface meteorological and DSD parameters

Correlation indicates, on a scale from -1 to 1, the dependency between two variables, where 1 is a perfect positive linear relationship and -1 indicates a perfect negative linear relationship. Table 4.1 shows the results of correlation between all surface meteorological variables and DSD parameters at Chilbolton. Additionally, Figure 4.10 includes all possible plot combinations comparing two variables at a time, with a layout matching the correlation matrix in Table 4.1. The figure summaries the relationships between each of the variables.

The correlation between the DSD parameters and meteorological parameters is low. Rainfall rate and $D_m$ have the highest correlation, which supports the $D_m$ and rainfall rate relationship established in Chapter 3.2.3. There is also a reasonable correlation between $N_w$ and $D_m$ and some correlation between $N_w$ and $\mu$. However, these correlations are small and show high variability. Dew point and temperature show the highest correlation, which is expected as they are related to humidity.

### 4.5.4 Spearman's Rank Correlation of surface meteorological and DSD parameters

Spearman's rank correlation looks for non-linear relationships (or association) between two variables. Table 4.2 shows the Spearman's rank correlation values for all surface meteorological and DSD parameters. The results show a numerical increase in the relationship between rainfall rate and $D_m$ as the relationship is non-linear. The Spearman's rank correlation value between $N_w$ and $D_m$ is also higher, indicating that

Table 4.1: Correlation matrix of surface meteorological data and DSD parameters.

| | T | WD | WS | R | P | DP | LI | $N_w$ | $D_m$ | $\mu$ |
|---|---|---|---|---|---|---|---|---|---|---|
| T | 1.00 | 0.17 | -0.06 | 0.09 | 0.06 | 0.95 | -0.23 | 0.09 | 0.03 | 0.09 |
| WD | 0.17 | 1.00 | 0.16 | 0.03 | 0.01 | 0.12 | -0.19 | 0.04 | 0.03 | 0.02 |
| WS | -0.06 | 0.16 | 1.00 | 0.02 | -0.22 | -0.07 | -0.01 | -0.09 | 0.16 | -0.03 |
| R | 0.09 | 0.03 | 0.02 | 1.00 | -0.13 | 0.10 | 0.02 | 0.03 | 0.46 | -0.13 |
| P | 0.06 | 0.01 | -0.22 | -0.13 | 1.00 | 0.02 | -0.11 | 0.11 | -0.24 | 0.10 |
| DP | 0.95 | 0.12 | -0.07 | 0.10 | 0.02 | 1.00 | 0.08 | 0.14 | 0.00 | 0.11 |
| LI | -0.23 | -0.19 | -0.01 | 0.02 | -0.11 | 0.08 | 1.00 | 0.15 | -0.08 | 0.06 |
| $N_w$ | 0.09 | 0.04 | -0.09 | 0.03 | 0.11 | 0.14 | 0.15 | 1.00 | -0.44 | 0.23 |
| $D_m$ | 0.03 | 0.03 | 0.16 | 0.46 | -0.24 | 0.00 | -0.08 | -0.44 | 1.00 | -0.18 |
| $\mu$ | 0.09 | 0.02 | -0.03 | -0.13 | 0.10 | 0.11 | 0.06 | 0.23 | -0.18 | 1.00 |

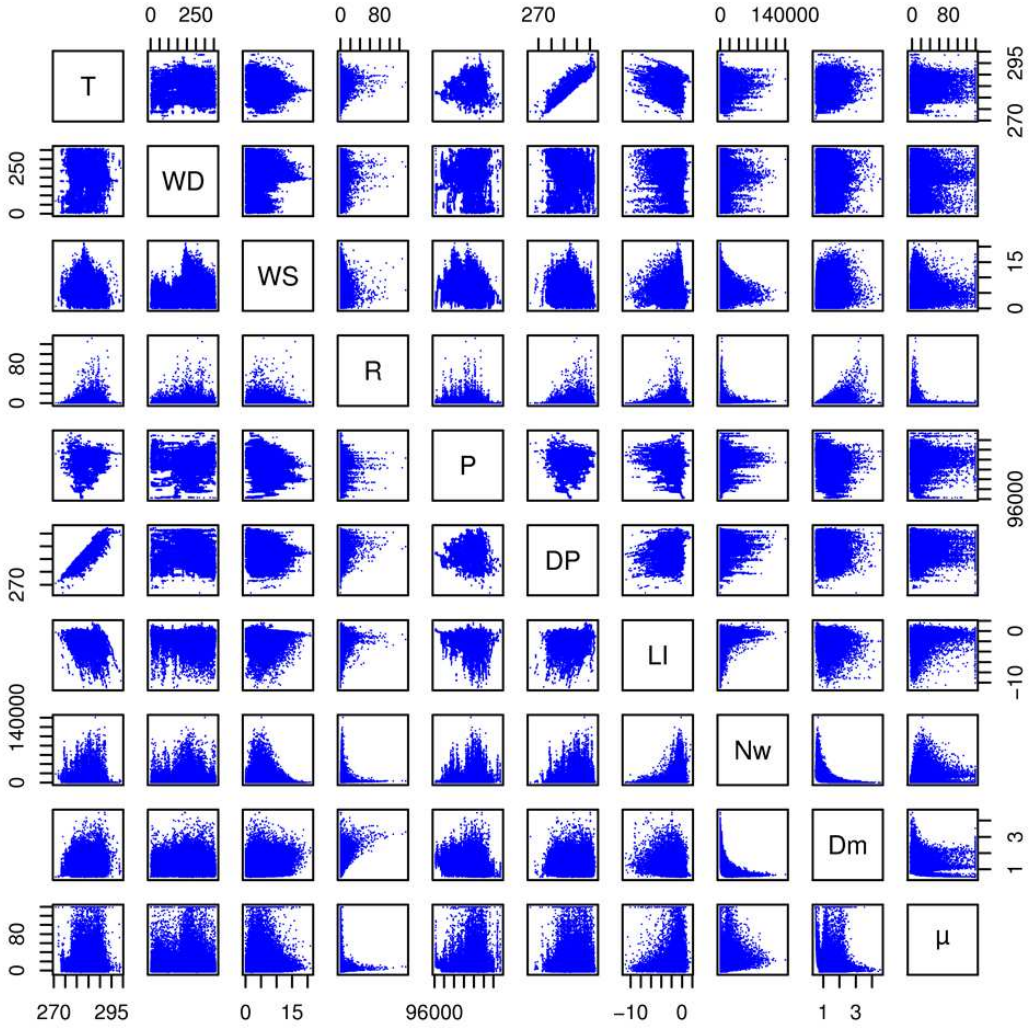


Figure 4.10: Collection of figures showing correlation between sets of surface meteorological variables and DSD parameters.

Table 4.2: Spearman's rank correlation matrix of surface meteorological data and DSD parameters.

| | T | WD | WS | R | P | DP | LI | $N_w$ | $D_m$ | $\mu$ |
|---|---|---|---|---|---|---|---|---|---|---|
| T | 1.00 | 0.11 | -0.05 | 0.02 | 0.08 | 0.96 | -0.23 | 0.05 | -0.02 | 0.05 |
| WD | 0.11 | 1.00 | 0.14 | -0.04 | 0.08 | 0.06 | -0.20 | -0.02 | 0.00 | -0.01 |
| WS | -0.05 | 0.14 | 1.00 | 0.04 | -0.20 | -0.06 | -0.05 | -0.13 | 0.15 | 0.05 |
| R | 0.02 | -0.04 | 0.04 | 1.00 | -0.22 | 0.06 | 0.12 | 0.21 | 0.51 | -0.29 |
| P | 0.08 | 0.08 | -0.20 | -0.22 | 1.00 | 0.05 | -0.07 | 0.12 | -0.26 | 0.05 |
| DP | 0.96 | 0.06 | -0.06 | 0.06 | 0.05 | 1.00 | 0.01 | 0.10 | -0.03 | 0.06 |
| LI | -0.23 | -0.20 | -0.05 | 0.12 | -0.07 | 0.01 | 1.00 | 0.19 | -0.08 | 0.13 |
| $N_w$ | 0.05 | -0.02 | -0.13 | 0.21 | 0.12 | 0.10 | 0.19 | 1.00 | -0.69 | 0.10 |
| $D_m$ | -0.02 | 0.00 | 0.15 | 0.51 | -0.26 | -0.03 | -0.08 | -0.69 | 1.00 | -0.27 |
| $\mu$ | 0.05 | -0.01 | 0.05 | -0.29 | 0.05 | 0.06 | 0.13 | 0.10 | -0.27 | 1.00 |

the relationship may be non-linear. The rank for the DSD parameters with all other meteorological parameters is relatively small, showing little relation.

### 4.5.5 Principal Component Analysis

Association between two variables has shown little relation that could potentially recreate a DSD parameter, excluding $D_m$ and rainfall rate. Further, joint statistical analysis has shown limited relationships with two meteorological and DSD parameters. Principal component analysis has been used to consider if more than two meteorological parameters could be used to recreate a DSD parameter.

Matrix (4.7) shows the results of the principal component matrix, whilst the vector (4.3) shows the eigenvector ($E_v$) of the principal components. The highest eigenvector value is given to the first principal component. The highest value is likely created by the relation between dew point and temperature. There are a high number of principal components with large eigenvalues, therefore the number of dimensions of the problem cannot be downscaled. The smallest eigenvalues are related to $D_m$, $\mu$ and $N_w$, which means they have the least significance. The higher eigenvalue components contain the majority of correlation between them. Consequently, Principal component analysis has shown that no substantial relationship between the surface meteorological and DSD parameters exists.

$$E_v = \begin{bmatrix} 8.7\times10^7 & 1.07\times10^6 & 6308.1 & 321.2 & 29.8 & 14.0 & 8.6 & 2.1 & 0.1 & 1.8\times10^{-11} \end{bmatrix} \tag{4.3}$$

$$
\text{PC} = \begin{pmatrix}
-0.00004 & -0.00018 & 0.00856 & 0.01597 & -0.70550 & -0.10812 & -0.04302 & -0.39372 & 0.00642 & 0.57735 \\
-0.00035 & -0.00046 & 0.99992 & -0.00260 & 0.00974 & -0.00023 & 0.00687 & 0.00350 & 0.00004 & 0.00000 \\
0.00003 & 0.00061 & 0.00627 & 0.00025 & 0.05984 & 0.00833 & -0.99805 & -0.00008 & 0.01422 & 0.00000 \\
-0.00001 & 0.00050 & 0.00160 & -0.02969 & -0.14621 & 0.98727 & 0.00025 & -0.00944 & 0.05420 & 0.00000 \\
-0.01232 & -0.99992 & -0.00046 & -0.00137 & 0.00008 & 0.00048 & -0.00061 & 0.00019 & -0.00005 & 0.00000 \\
-0.00006 & -0.00003 & 0.00556 & 0.01833 & -0.69030 & -0.09744 & -0.04225 & 0.42249 & -0.00363 & -0.57735 \\
-0.00002 & 0.00016 & -0.00300 & 0.00236 & 0.01521 & 0.01068 & 0.00077 & 0.81621 & -0.01005 & 0.57735 \\
-0.99992 & 0.01232 & -0.00034 & -0.00043 & 0.00006 & -0.00002 & -0.00002 & -0.00003 & -0.00002 & 0.00000 \\
0.00002 & 0.00008 & 0.00029 & -0.00173 & -0.00926 & 0.05326 & -0.01433 & -0.01280 & -0.99835 & 0.00000 \\
-0.00045 & -0.00135 & 0.00241 & 0.99925 & 0.01955 & 0.03291 & 0.00171 & -0.00368 & -0.00014 & 0.00000
\end{pmatrix} \tag{4.7}
$$

## 4.6 Unified Model results

### 4.6.1 Meteorological data

The unified model was used to compare meteorological data to DSD parameters from 2003 to 2005. The Unified Model data is sampled over a one hour time period, therefore the disdrometer data sample time has been increased to match the time interval. A one hour period averages the raindrop size distribution, reducing variability of individual events. The longer time period may help to establish a more general relation in the raindrop size distribution parameters.

Figure 4.11 shows a comparison of total liquid water content and convective available potential energy determined from the Unified Model, which are not dependent on height. Liquid water content and CAPE show little correlation with DSD parameters. Parameters $\mu$ and $N_w$ show very high deviation with change in liquid water content and CAPE.

### 4.6.2 Unified Model meteorological data at ≈1 km

The unified model provided additional meteorological properties and data over a range of heights from 0.019-46.27 km above sea level. The results considered in this section look at heights approximately 1 km. This height was chosen to measure meteorological parameters within rain, i.e. below the maximum rain height and at sufficient height above the disdrometer to avoid surrounding influences on the ground, such as trees.

#### Temperature

The results in Figures 4.12(a)-4.12(c) compare the DSD parameters with temperature determined by the unified model at a height of 1 km. The extended time sample of one hour has not yielded a generalised relation between the DSD parameters and temperature. The standard deviation is very high for both $\mu$ and $N_w$ showing little relation with temperature. The parameter $D_m$ has a lower standard deviation but shows little correlation with temperature.

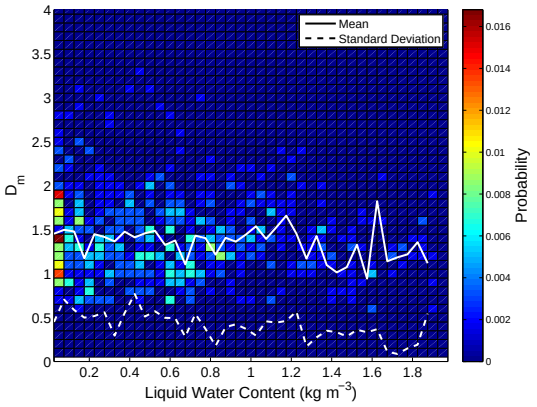


(a) Liquid water content compared against $D_m$.

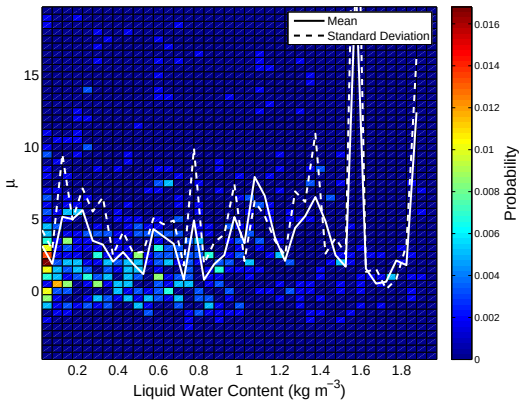


(b) Liquid water content compared against $\mu$.

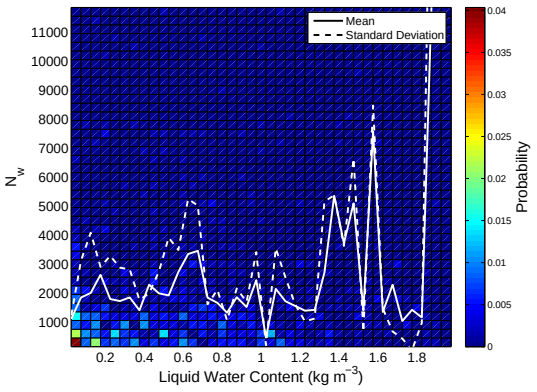


(c) Liquid water content compared against $N_w$.

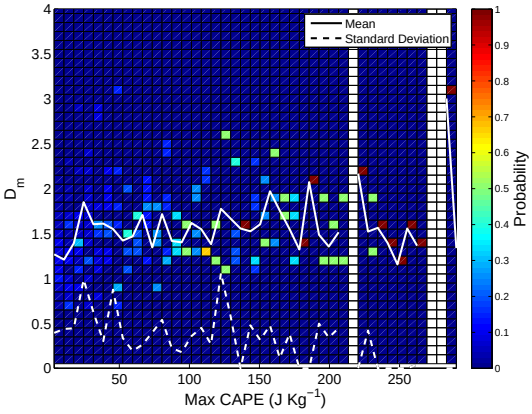


(d) CAPE compared against $D_m$.

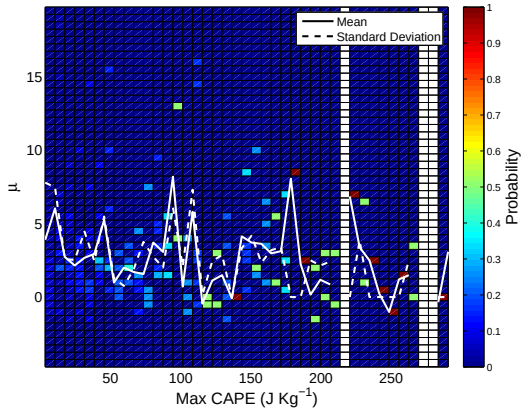


(e) CAPE compared against $\mu$.

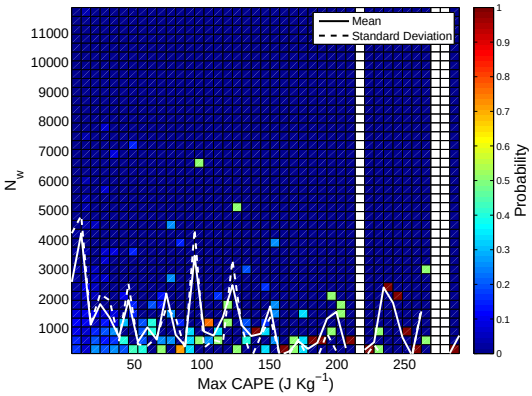


(f) CAPE compared against $N_w$.

Figure 4.11: Comparison of Unified Model data liquid water content and CAPE with normalised gamma distribution parameters $D_m$, $N_w$ and $\mu$.

### Pressure

Figures 4.12(d)-4.12(f) compare the pressure with the DSD parameters. There is little correlation with the pressure at 1 km and the DSD parameters measured on the surface. The variation in $\mu$ and $N_w$ is very high whilst $D_m$ shows little relation with pressure.

### Lifted index

The lifting index, shown in Figures 4.13(a)-4.13(c), has little correlation with $D_m$, $\mu$ and $N_w$. The variation in $\mu$ and $N_w$ is high regardless of lifting index.

### Relative humidity

Relative humidity shows little correlation with the DSD parameters $D_m$ and $\mu$, as shown in Figures. 4.13(d) and 4.13(e). Figure 4.13(f) shows the mean of $N_w$ generally increases with relative humidity. However, the standard deviation is very high.

### Wind speed

Wind speed has been separated into three different components: zonal component ($U$) in the west-east direction; meridional component ($V$) in the north-south direction; and the vertical component ($W$). Figures 4.14 and 4.15 show all the components $U$,$V$ and $W$ compared to parameters $D_m$, $\mu$ and $N_w$. The zonal and meridional components show little correlation between wind speed components and DSD parameters. Vertical wind speed shows some correlation with $\mu$ and $N_w$. As vertical wind speed changes from $0\,\mathrm{ms}^{-1}$ the mean and variability of $\mu$ and $N_w$ decreases. Increasing vertical wind speed potentially gives smaller drops more time to collide and converge into larger drops reducing the drop concentration, $N_w$. However, small values of $\mu$ indicate a more exponential shaped distribution, which means there are a larger number of small drops for increased vertical wind speed. Overall, stronger vertical winds speeds show some correlation with an increase in the proportion of smaller drops and a decrease in the total number of drops.

The wind speed results were determined at a height of 1 km, which is just above the turbulent layer. The DSD measured by the disdrometer at the ground will be affected by the turbulent layer. Any affect the wind speed has on the DSD will be convoluted by

the turbulent layer and other meteorological affects as raindrops fall from 1 km to the ground. Analysis of correlation between wind speed and the DSD could be investigated further by the inferring the DSD from radar measurements, Illingworth and Blackman [2002], Illingworth [2004]. The DSD could be inferred at a height of 1 km, above the effect of the turbulent layer.

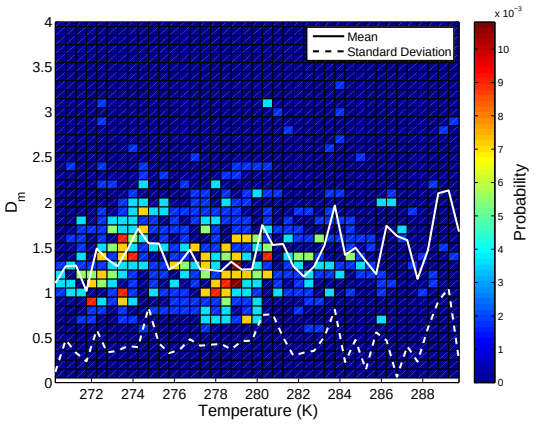


(a) Temperature compared against $D_m$.

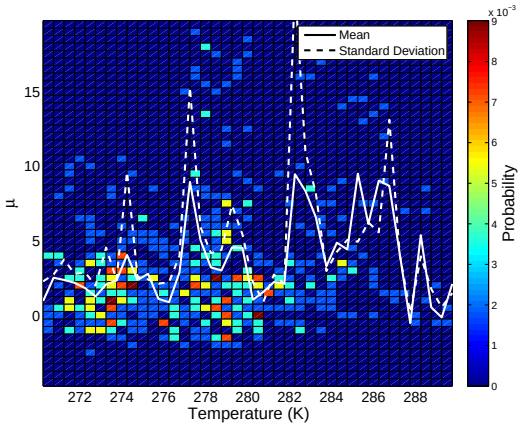


(b) Temperature compared against $\mu$.

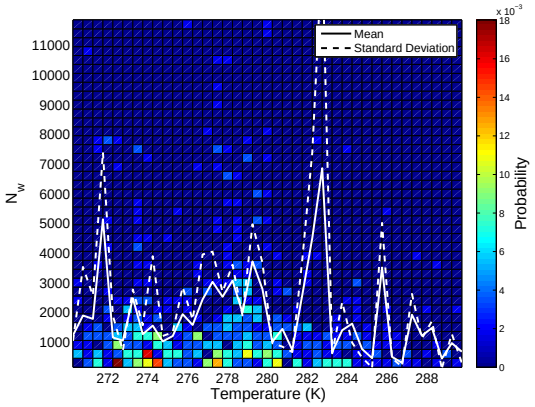


(c) Temperature compared against $N_w$.

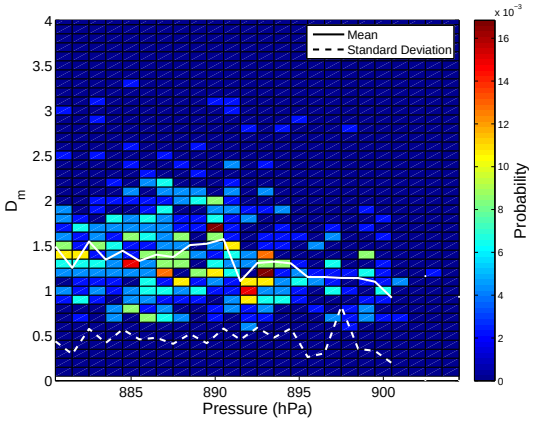


(d) Pressure compared against $D_m$.

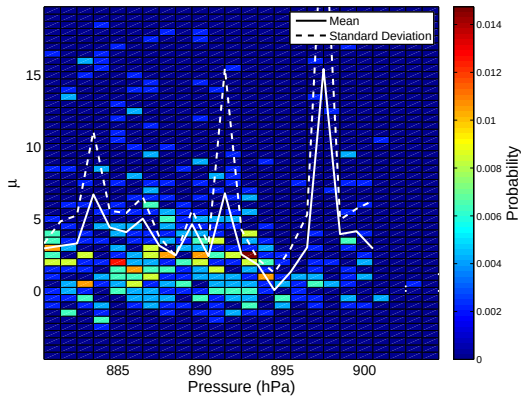


(e) Pressure compared against $\mu$.

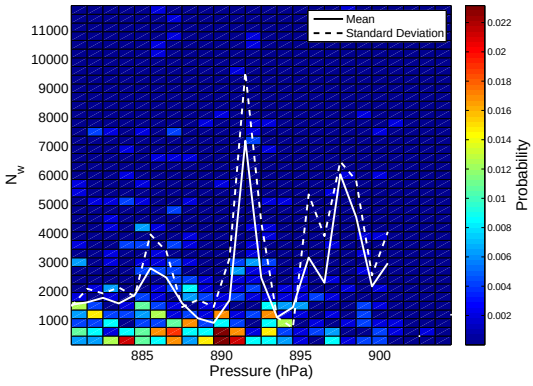


(f) Pressure compared against $N_w$.

Figure 4.12: Comparison of temperature and pressure at a height of ≈1 km with normalised gamma distribution parameters $D_m$, $N_w$ and $\mu$.

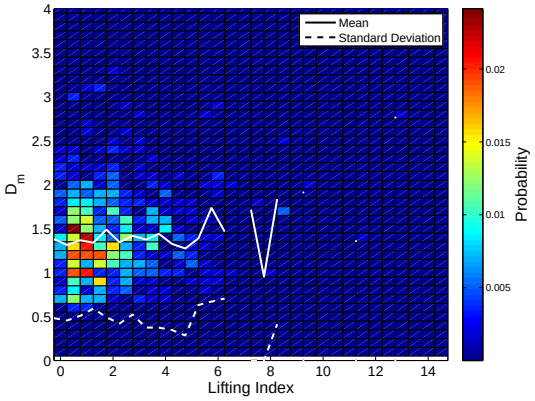


(a) Lifted index compared against $D_m$.

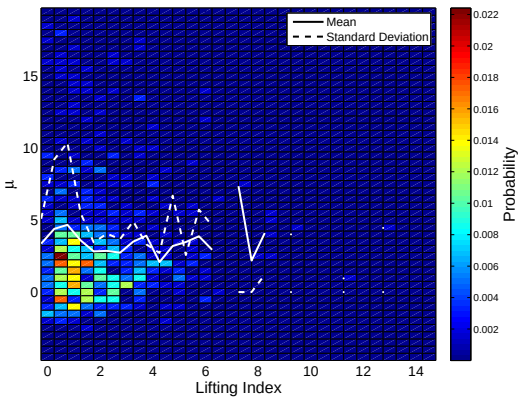


(b) Lifted Index compared against $\mu$.

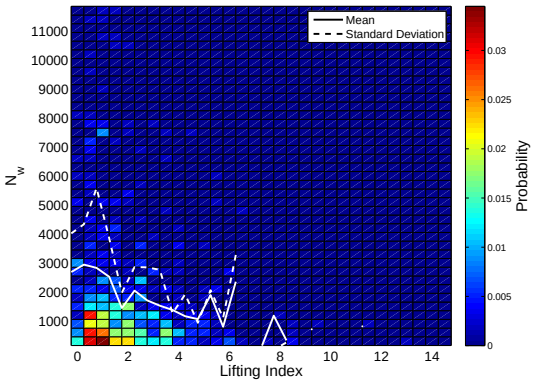


(c) Lifted index compared against $N_w$.

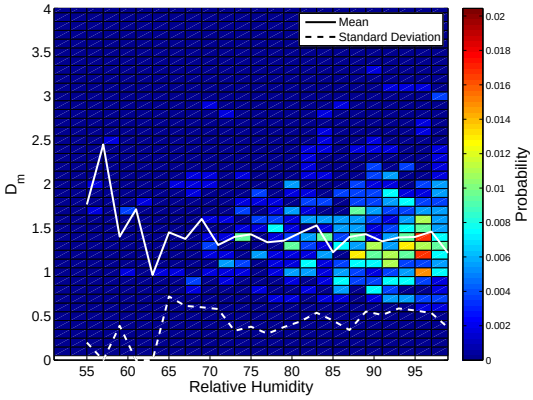


(d) Relative humidity compared against $D_m$.

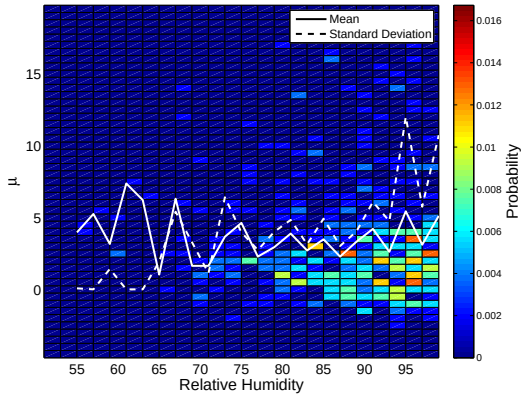


(e) Relative humidity compared against $\mu$.

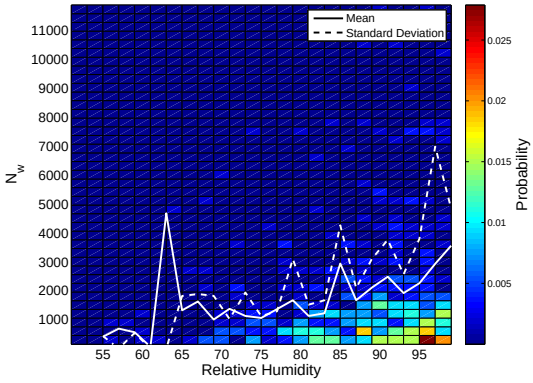


(f) Relative humidity compared against $N_w$.

Figure 4.13: Comparison of lifted index and relative humidity at a height of ≈1 km with normalised gamma distribution parameters $D_m$, $N_w$ and $\mu$.

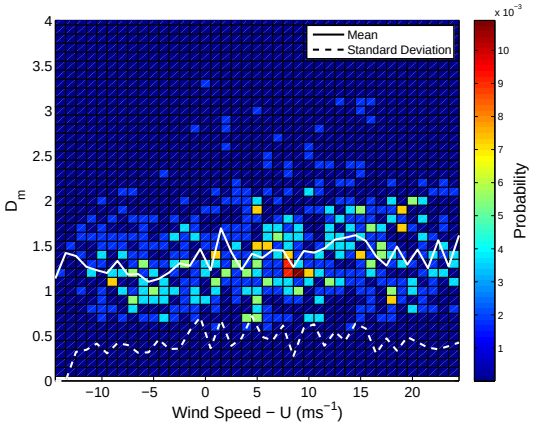


(a) Wind speed U compared against $D_m$.

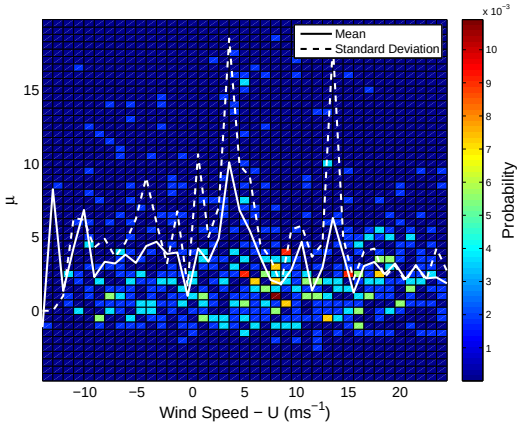


(b) Wind speed U compared against $\mu$.

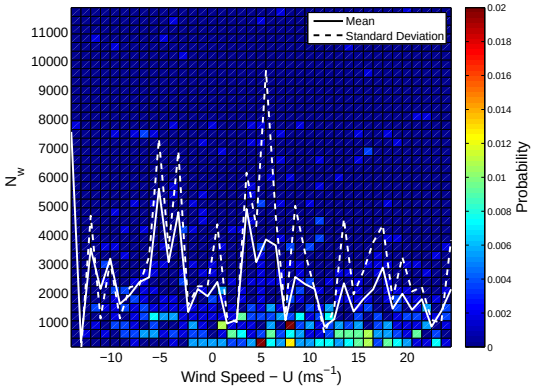


(c) Wind speed U compared against $N_w$.

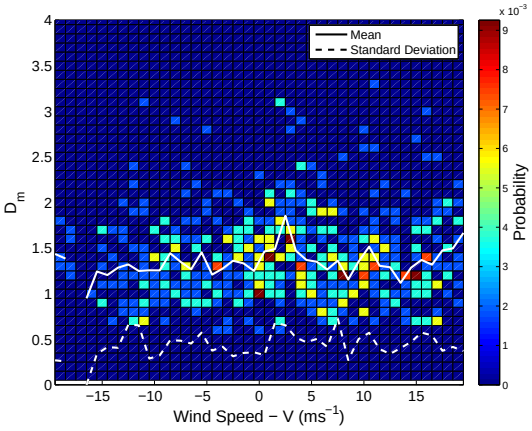


(d) Wind speed V compared against $D_m$.

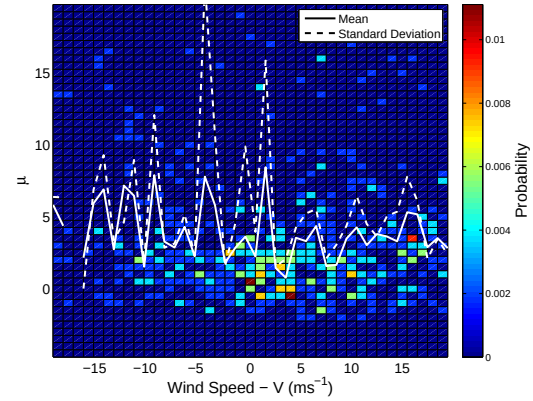


(e) Wind speed V compared against $\mu$.

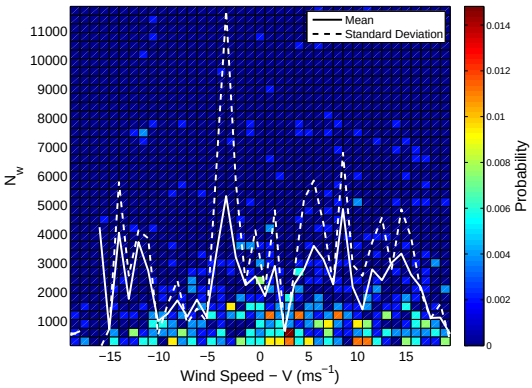


(f) Wind speed V compared against $N_w$.

Figure 4.14: Comparison of wind speed $U$ and $V$ at a height of ≈1 km with normalised gamma distribution parameters $D_m$, $N_w$ and $\mu$.

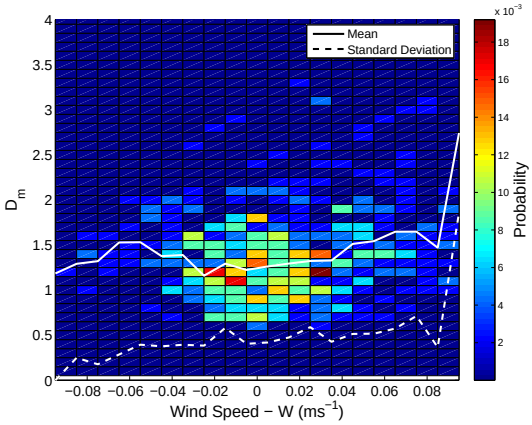


(a) Wind speed W compared against $D_m$.

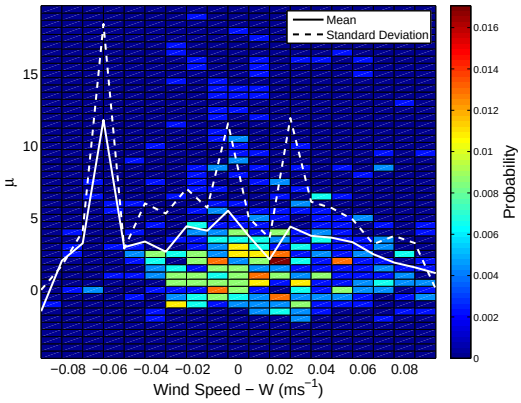


(b) W compared against $\mu$.

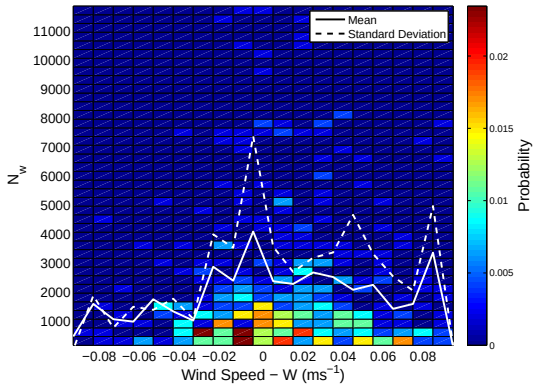


(c) Wind speed W compared against $N_w$.

Figure 4.15: Comparison of wind speed, $W$, at a height of $\approx$1 km with normalised gamma distribution parameters $D_m$, $N_w$ and $\mu$.

### 4.6.3 Correlation of meteorological data at a height of ≈1 km

Correlation was calculated between the Unified Model at 1 km and disdrometer data at Chilbolton. The numerical results are shown in Table 4.3. For an extensive comparison of each variable, Figure 4.16 presents comparison plots of all combinations of two variables. Figure 4.16 illustrates that there is little relationship between meteorological and DSD variables, with the exception of $D_m$ and rainfall rate.

Spearman's rank correlation, for which numerical results are shown in Table 4.4, is included for further analysis, to determine any association between two variables. There is little association between the majority of variables. The DSD parameters show very little correlation or association with the meteorological data. The increase in sample time to a period of 1 hour shows a slight increase in association between $N_w$ and $D_m$ when compared with results over 60-second time periods.

Table 4.3: Correlation matrix of meteorological data at a height of ≈1 km and DSD parameters.

| | U | V | W | WD | R | RHt | CAPE | LWC | DP | T | RH | P | LI | $N_w$ | $D_m$ | $\mu$ |
|---|---|---|---|---|---|---|---|---|---|---|---|---|---|---|---|---|
| U | 1.00 | 0.34 | 0.23 | 0.07 | 0.04 | 0.04 | 0.02 | 0.02 | 0.06 | -0.01 | 0.22 | -0.10 | -0.21 | -0.08 | 0.16 | -0.06 |
| V | 0.34 | 1.00 | 0.35 | 0.22 | 0.10 | 0.36 | 0.16 | 0.35 | 0.44 | 0.35 | 0.26 | -0.14 | -0.23 | 0.03 | 0.06 | -0.03 |
| W | 0.23 | 0.35 | 1.00 | 0.09 | 0.25 | 0.04 | 0.07 | 0.20 | 0.17 | 0.07 | 0.31 | -0.09 | -0.31 | 0.03 | 0.14 | -0.07 |
| WD | 0.07 | 0.22 | 0.09 | 1.00 | 0.14 | 0.11 | 0.05 | 0.04 | 0.13 | 0.11 | 0.09 | 0.00 | -0.07 | -0.06 | 0.14 | -0.05 |
| R | 0.04 | 0.10 | 0.25 | 0.14 | 1.00 | 0.10 | 0.20 | 0.03 | 0.14 | 0.14 | 0.02 | -0.20 | -0.02 | 0.02 | 0.45 | -0.14 |
| RHt | 0.04 | 0.36 | 0.04 | 0.11 | 0.10 | 1.00 | 0.32 | 0.51 | 0.94 | 0.97 | -0.05 | 0.18 | 0.10 | 0.00 | 0.13 | 0.14 |
| CAPE | 0.02 | 0.16 | 0.07 | 0.05 | 0.20 | 0.32 | 1.00 | -0.07 | 0.37 | 0.37 | 0.00 | -0.04 | 0.01 | -0.14 | 0.38 | -0.01 |
| LWC | 0.02 | 0.35 | 0.20 | 0.04 | 0.03 | 0.51 | -0.07 | 1.00 | 0.59 | 0.45 | 0.44 | 0.07 | -0.40 | 0.21 | -0.15 | 0.11 |
| DP | 0.06 | 0.44 | 0.17 | 0.13 | 0.14 | 0.94 | 0.37 | 0.59 | 1.00 | 0.94 | 0.20 | 0.15 | -0.15 | 0.03 | 0.15 | 0.11 |
| T | -0.01 | 0.35 | 0.07 | 0.11 | 0.14 | 0.97 | 0.37 | 0.45 | 0.94 | 1.00 | -0.14 | 0.18 | 0.20 | -0.03 | 0.18 | 0.09 |
| RHt | 0.22 | 0.26 | 0.31 | 0.09 | 0.02 | -0.05 | 0.00 | 0.44 | 0.20 | -0.14 | 1.00 | -0.10 | -0.99 | 0.17 | -0.08 | 0.07 |
| P | -0.10 | -0.14 | -0.09 | 0.00 | -0.20 | 0.18 | -0.04 | 0.07 | 0.15 | 0.18 | -0.10 | 1.00 | 0.10 | 0.12 | -0.19 | 0.07 |
| LI | -0.21 | -0.23 | -0.31 | -0.07 | -0.02 | 0.10 | 0.01 | -0.40 | -0.15 | 0.20 | -0.99 | 0.10 | 1.00 | -0.16 | 0.09 | -0.06 |
| $N_w$ | -0.08 | 0.03 | 0.03 | -0.06 | 0.02 | 0.00 | -0.14 | 0.21 | 0.03 | -0.03 | 0.17 | 0.12 | -0.16 | 1.00 | -0.46 | 0.43 |
| $D_m$ | 0.16 | 0.06 | 0.14 | 0.14 | 0.45 | 0.13 | 0.38 | -0.15 | 0.15 | 0.18 | -0.08 | -0.19 | 0.09 | -0.46 | 1.00 | -0.20 |
| $\mu$ | -0.06 | -0.03 | -0.07 | -0.05 | -0.14 | 0.14 | -0.01 | 0.11 | 0.11 | 0.09 | 0.07 | 0.07 | -0.06 | 0.43 | -0.20 | 1.00 |

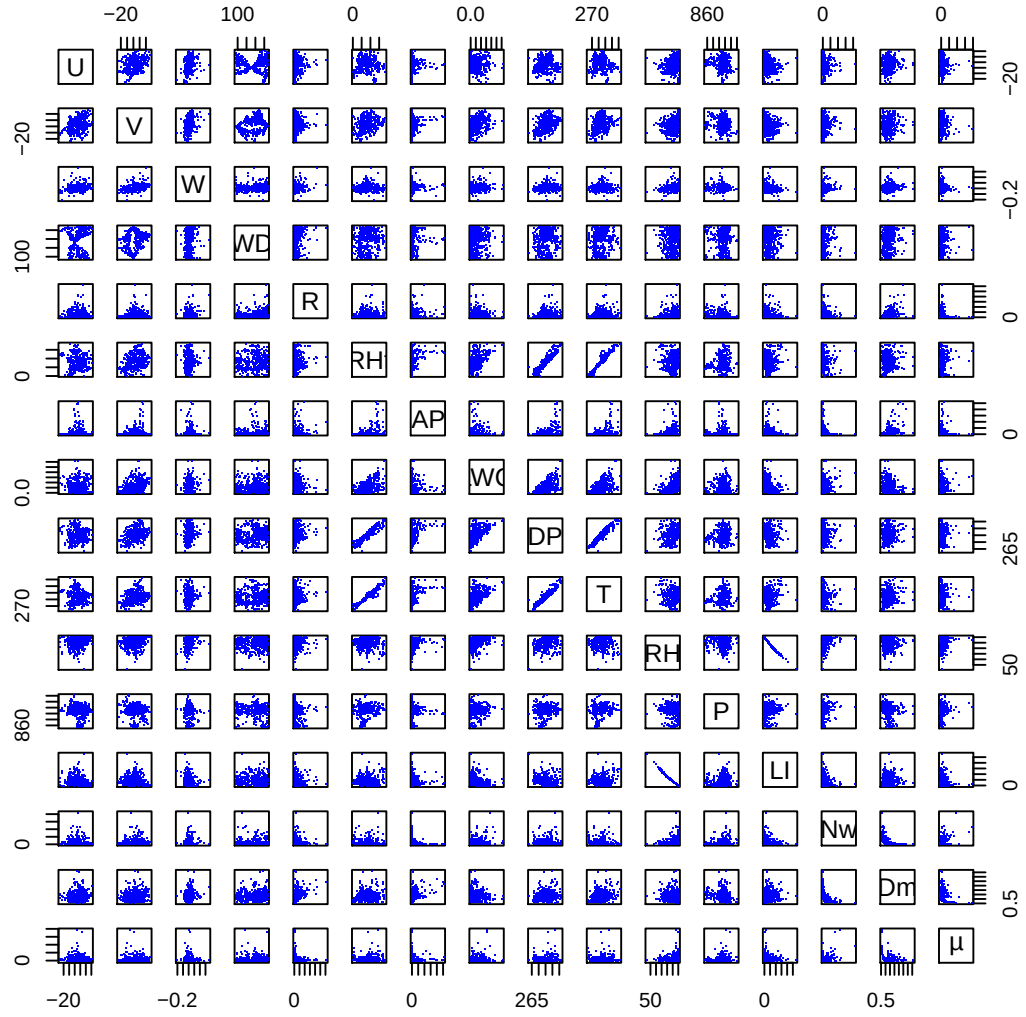


Figure 4.16: Collection of figures showing correlation between sets of meteorological variables at ≈1 km height and DSD parameters.

Table 4.4: Spearman's matrix of meteorological data at height of ≈1 km and DSD parameters.

| | U | V | W | WD | R | RHt | CAPE | LWC | DP | T | RH | P | LI | $N_w$ | $D_m$ | $\mu$ |
|---|---|---|---|---|---|---|---|---|---|---|---|---|---|---|---|---|
| U | 1.00 | 0.32 | 0.27 | 0.17 | 0.06 | 0.06 | 0.09 | 0.01 | 0.09 | 0.01 | 0.26 | -0.02 | -0.26 | -0.18 | 0.19 | -0.08 |
| V | 0.32 | 1.00 | 0.36 | 0.19 | 0.15 | 0.38 | 0.06 | 0.38 | 0.43 | 0.35 | 0.32 | -0.11 | -0.30 | 0.04 | 0.06 | 0.02 |
| W | 0.27 | 0.36 | 1.00 | 0.14 | 0.21 | 0.08 | 0.16 | 0.22 | 0.20 | 0.09 | 0.41 | -0.06 | -0.40 | 0.01 | 0.12 | -0.06 |
| WD | 0.17 | 0.19 | 0.14 | 1.00 | 0.17 | 0.12 | 0.05 | 0.03 | 0.14 | 0.13 | 0.11 | 0.04 | -0.10 | -0.05 | 0.17 | -0.06 |
| R | 0.06 | 0.15 | 0.21 | 0.17 | 1.00 | 0.09 | 0.20 | 0.10 | 0.14 | 0.14 | 0.05 | -0.23 | -0.05 | 0.18 | 0.51 | -0.16 |
| RHt | 0.06 | 0.38 | 0.08 | 0.12 | 0.09 | 1.00 | 0.21 | 0.51 | 0.96 | 0.97 | 0.07 | 0.14 | -0.04 | -0.04 | 0.11 | 0.11 |
| CAPE | 0.09 | 0.06 | 0.16 | 0.05 | 0.20 | 0.21 | 1.00 | -0.17 | 0.25 | 0.27 | -0.06 | -0.11 | 0.07 | -0.21 | 0.33 | 0.01 |
| LWC | 0.01 | 0.38 | 0.22 | 0.03 | 0.10 | 0.51 | -0.17 | 1.00 | 0.60 | 0.45 | 0.55 | 0.01 | -0.54 | 0.20 | -0.12 | 0.02 |
| DP | 0.09 | 0.43 | 0.20 | 0.14 | 0.14 | 0.96 | 0.25 | 0.60 | 1.00 | 0.94 | 0.24 | 0.13 | -0.21 | -0.01 | 0.12 | 0.06 |
| T | 0.01 | 0.35 | 0.09 | 0.13 | 0.14 | 0.97 | 0.27 | 0.45 | 0.94 | 1.00 | -0.04 | 0.15 | 0.07 | -0.05 | 0.15 | 0.08 |
| RHt | 0.26 | 0.32 | 0.41 | 0.11 | 0.05 | 0.07 | -0.06 | 0.55 | 0.24 | -0.04 | 1.00 | -0.11 | -1.00 | 0.16 | -0.10 | -0.03 |
| P | -0.02 | -0.11 | -0.06 | 0.04 | -0.23 | 0.14 | -0.11 | 0.01 | 0.13 | 0.15 | -0.11 | 1.00 | 0.12 | 0.07 | -0.25 | 0.00 |
| LI | -0.26 | -0.30 | -0.40 | -0.10 | -0.05 | -0.04 | 0.07 | -0.54 | -0.21 | 0.07 | -1.00 | 0.12 | 1.00 | -0.16 | 0.11 | 0.03 |
| $N_w$ | -0.18 | 0.04 | 0.01 | -0.05 | 0.18 | -0.04 | -0.21 | 0.20 | -0.01 | -0.05 | 0.16 | 0.07 | -0.16 | 1.00 | -0.70 | 0.05 |
| $D_m$ | 0.19 | 0.06 | 0.12 | 0.17 | 0.51 | 0.11 | 0.33 | -0.12 | 0.12 | 0.15 | -0.10 | -0.25 | 0.11 | -0.70 | 1.00 | -0.11 |
| $\mu$ | -0.08 | 0.02 | -0.06 | -0.06 | -0.16 | 0.11 | 0.01 | 0.02 | 0.06 | 0.08 | -0.03 | 0.00 | 0.03 | 0.05 | -0.11 | 1.00 |

### 4.6.4 Unified Model meteorological data at 3.3 km

Further analysis was conducted on Unified Model data at approximately 3.3 km compared to DSD parameters. This approximate height defines the meteorology where steering winds occur, which may provide some additional link to the DSD.

Figure 4.17 shows Unified Model meteorological parameters temperature and pressure compared with $D_m$, $\mu$ and $N_w$. The one-hour time period and height above the surface sensors yield no additional pattern between the meteorological and DSD parameters. Temperature and pressure show little correlation with $D_m$, $\mu$ and $N_w$. Both $\mu$ and $N_w$ have high standard deviation, especially in comparison to the mean, as shown by the solid and dashed white lines, representing the mean and standard deviation respectively.

Lifting index and relative humidity, compared in Figure 4.18, show very little correlation between the DSD parameters and a high variation. Figures 4.19 and 4.20 show wind speed separated into the three components, zonal, meridional and vertical, compared with the DSD parameters. There is little correlation between wind speed measured at ≈3.3 km and the DSD parameters.

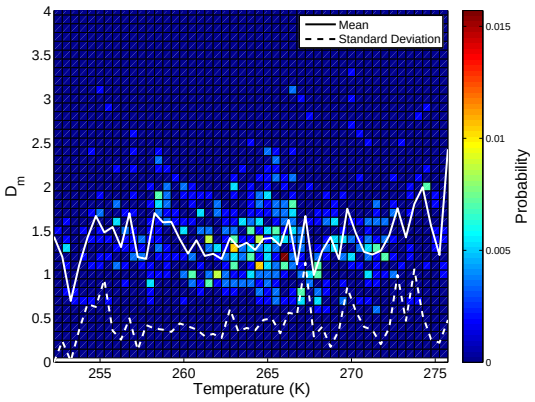


(a) Temperature compared against $D_m$.

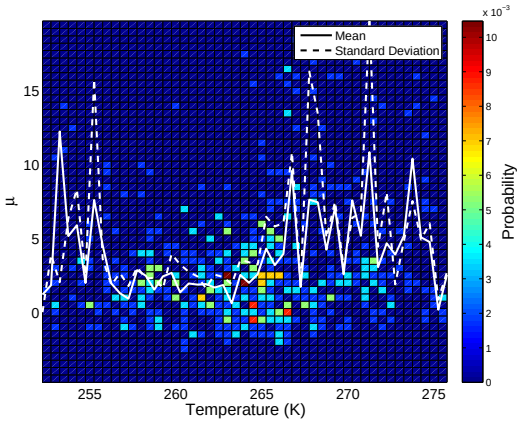


(b) Temperature compared against $\mu$.

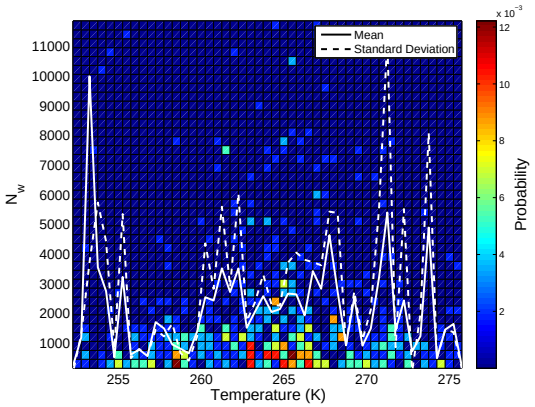


(c) Temperature compared against $N_w$.

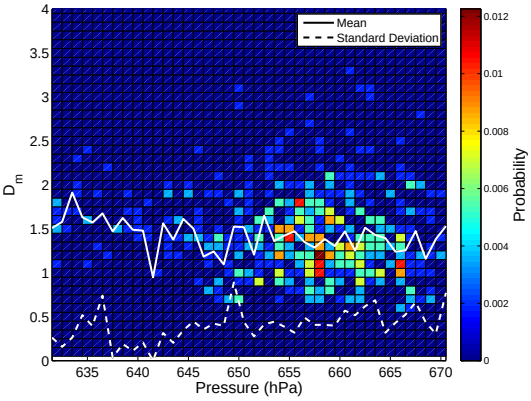


(d) Pressure compared against $D_m$.

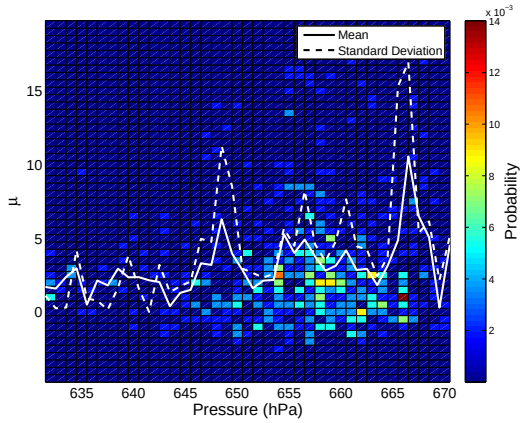


(e) Pressure compared against $\mu$.

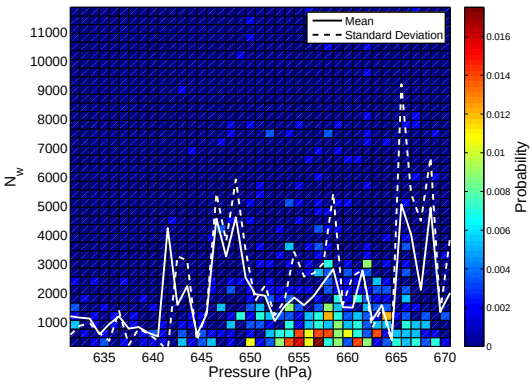


(f) Pressure compared against $N_w$.

Figure 4.17: Comparison of temperature and pressure at a height of ≈3.3 km with normalised gamma distribution parameters $D_m$, $\mu$ and $N_w$.

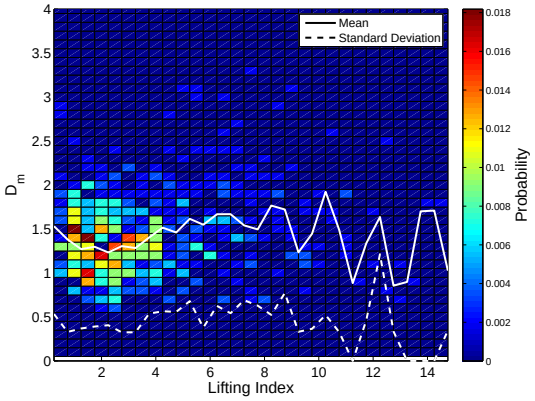


(a) Lifted index compared against $D_m$.

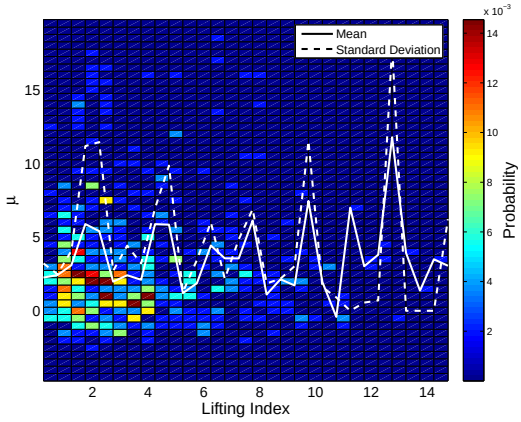


(b) Lifted index compared against $\mu$.

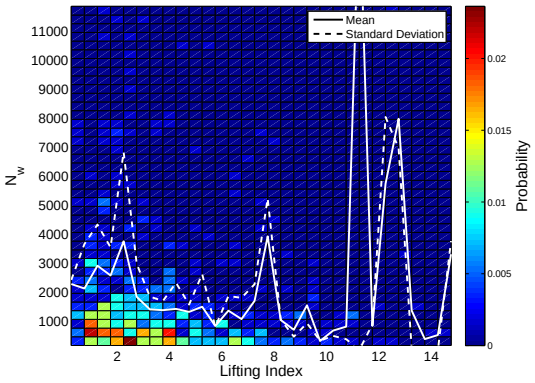


(c) Lifted index compared against $N_w$.

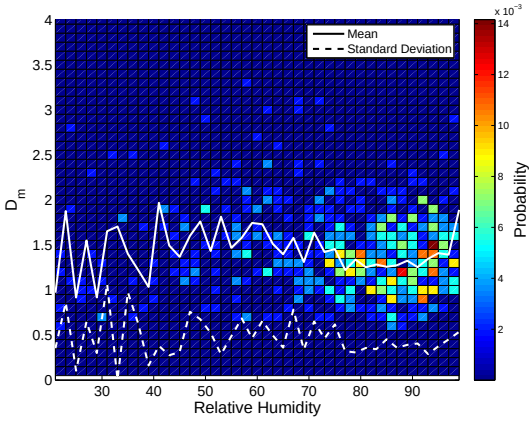


(d) Relative humidity compared against $D_m$.

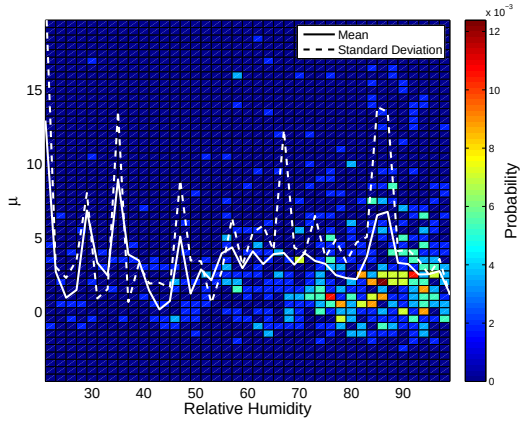


(e) Relative humidity compared against $\mu$.

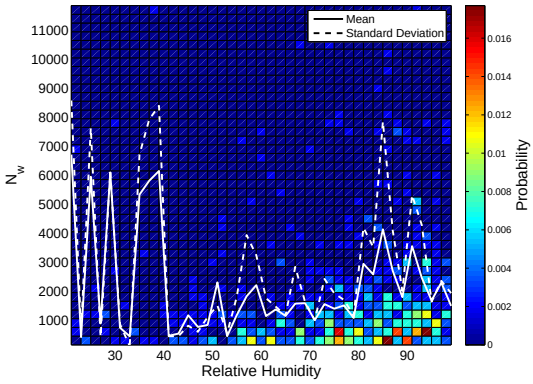


(f) Relative humidity compared against $N_w$.

Figure 4.18: Comparison of lifting index and relative humidity at a height of ≈3.3 km with normalised gamma distribution parameters $D_m$, $\mu$ and $N_w$.

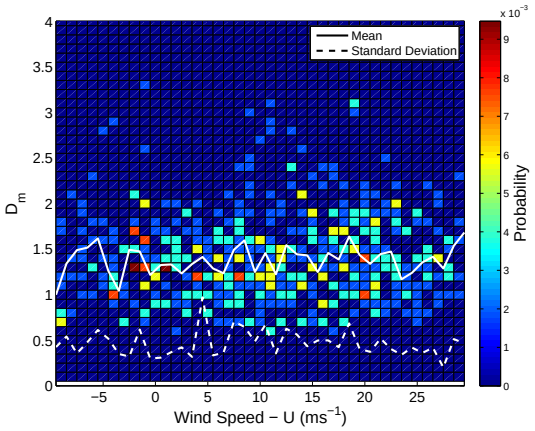


(a) Wind speed U compared against $D_m$.

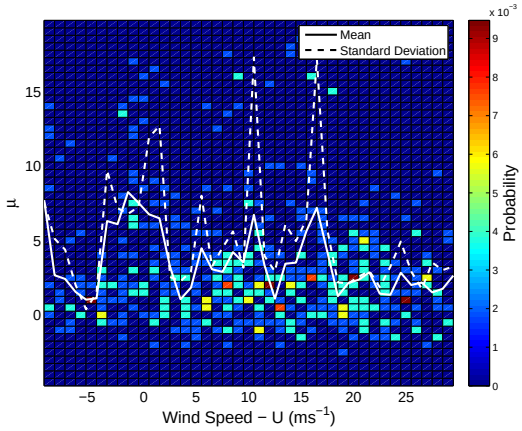


(b) Wind speed U compared against $\mu$.

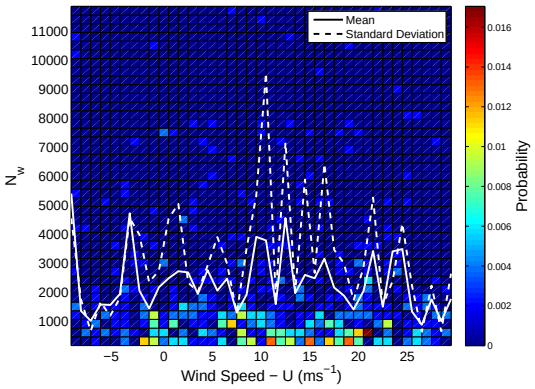


(c) Wind speed U compared against $N_w$.

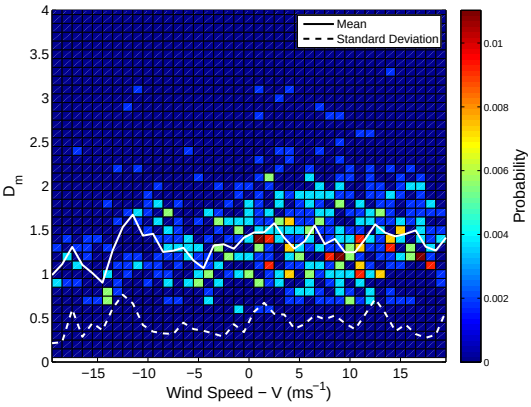


(d) Wind speed V compared against $D_m$.

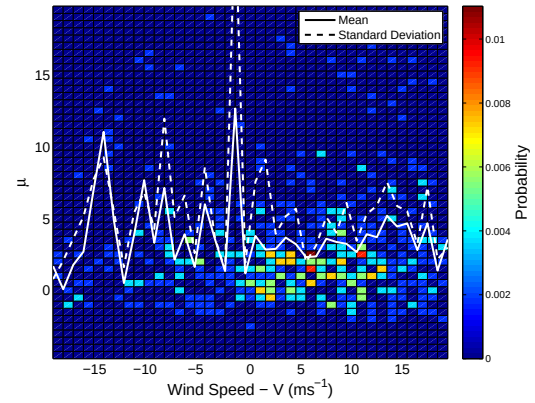


(e) Wind speed V compared against $\mu$.

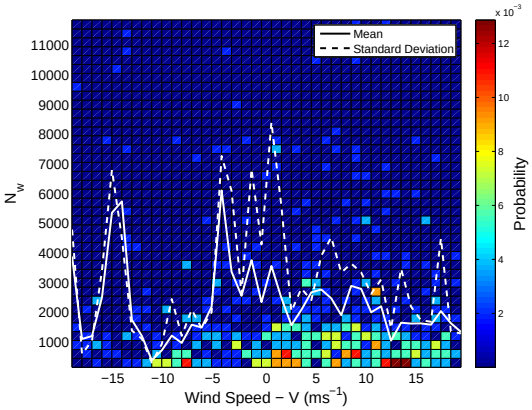


(f) V compared against $N_w$.

Figure 4.19: Comparison of wind speed $U$ and $V$ at a height of ≈3.3 km with normalised gamma distribution parameters $D_m$, $\mu$ and $N_w$.

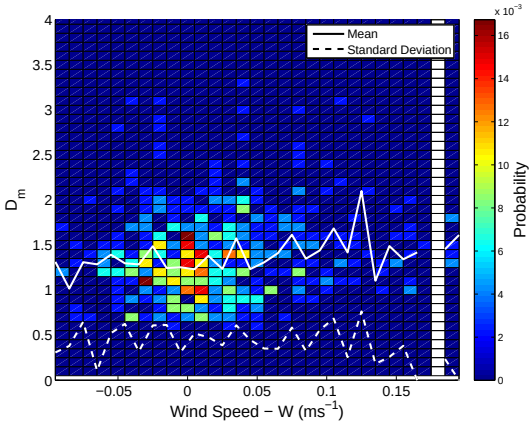


(a) Wind speed W compared against $D_m$.

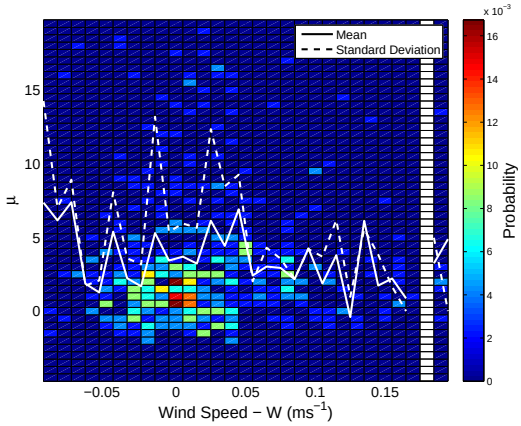


(b) Wind speed W compared against $\mu$.

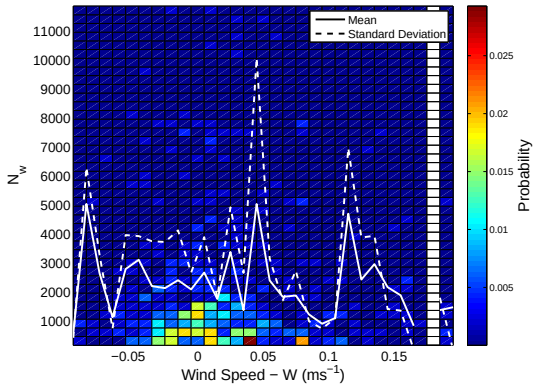


(c) Wind speed W compared against $N_w$.

Figure 4.20: Comparison of wind speed, $W$, at a height of ≈3.3 km with normalised gamma distribution parameters $D_m$, $\mu$ and $N_w$.

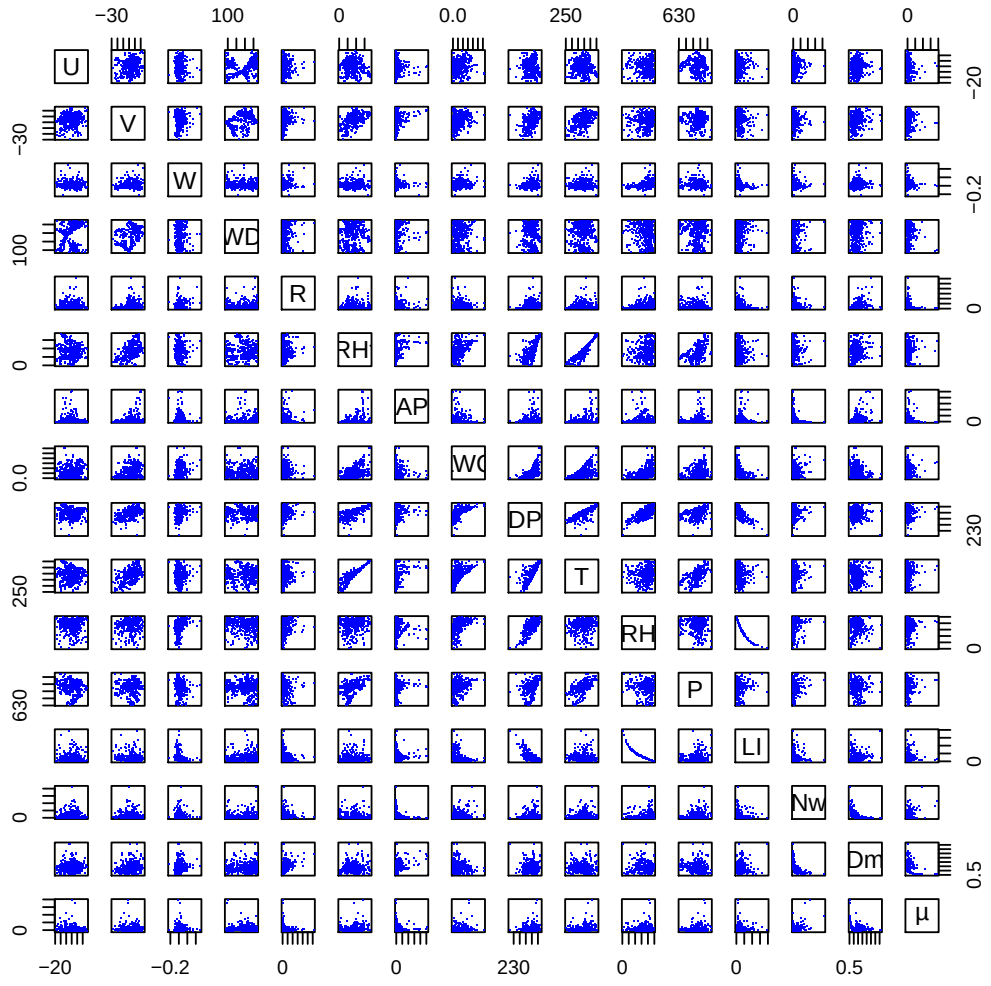


Figure 4.21: Collection of figures showing correlation between sets of meteorological variables at ≈3.3 km height and DSD parameters.

### 4.6.5 Correlation of meteorological data at a height of ≈3.3 km

Correlation was calculated for meteorological data determined at ≈3.3 km and the DSD parameters. Table 4.5 shows the results of the correlation matrix for all the variables. There is very little change in the correlation between the DSD parameters and the 3.3 km meteorological in comparison to correlation for 1 km data. Figure 4.21 summarises all the data relationships between individual variables. It is apparent there is little correlation between meteorological and DSD variables, with the exception of $D_m$ and rainfall rate.

Spearman's rank correlation was also calculated between all the variables. The results

Table 4.5: Correlation matrix of meteorological data at a height of ≈3.3 km and DSD parameters.

| | U | V | W | WD | R | RHt | CAPE | LWC | DP | T | RH | P | LI | $N_w$ | $D_m$ | $\mu$ |
|---|---|---|---|---|---|---|---|---|---|---|---|---|---|---|---|---|
| U | 1.00 | 0.17 | -0.03 | 0.25 | 0.03 | -0.07 | -0.04 | 0.10 | -0.05 | -0.05 | -0.02 | -0.09 | 0.02 | -0.01 | 0.08 | -0.11 |
| V | 0.17 | 1.00 | 0.07 | 0.32 | 0.17 | 0.52 | 0.21 | 0.33 | 0.43 | 0.50 | 0.14 | 0.02 | -0.09 | -0.04 | 0.17 | -0.02 |
| W | -0.03 | 0.07 | 1.00 | -0.10 | 0.25 | 0.00 | -0.02 | 0.24 | 0.22 | 0.06 | 0.32 | -0.10 | -0.26 | 0.00 | 0.13 | -0.03 |
| WD | 0.25 | 0.32 | -0.10 | 1.00 | 0.06 | 0.07 | 0.04 | -0.01 | -0.04 | 0.04 | -0.11 | -0.05 | 0.10 | -0.04 | 0.12 | -0.04 |
| R | 0.03 | 0.17 | 0.25 | 0.06 | 1.00 | 0.10 | 0.19 | 0.03 | 0.09 | 0.07 | 0.04 | -0.12 | -0.06 | 0.02 | 0.45 | -0.14 |
| RHt | -0.07 | 0.52 | 0.00 | 0.07 | 0.10 | 1.00 | 0.32 | 0.51 | 0.67 | 0.91 | 0.06 | 0.56 | -0.01 | 0.00 | 0.13 | 0.14 |
| CAPE | -0.04 | 0.21 | -0.02 | 0.04 | 0.19 | 0.32 | 1.00 | -0.07 | 0.08 | 0.26 | -0.21 | 0.10 | 0.16 | -0.14 | 0.38 | -0.01 |
| LWC | 0.10 | 0.33 | 0.24 | -0.01 | 0.03 | 0.51 | -0.07 | 1.00 | 0.65 | 0.58 | 0.43 | 0.30 | -0.34 | 0.22 | -0.16 | 0.11 |
| DP | -0.05 | 0.43 | 0.22 | -0.04 | 0.09 | 0.67 | 0.08 | 0.65 | 1.00 | 0.74 | 0.71 | 0.38 | -0.68 | 0.07 | -0.04 | 0.09 |
| T | -0.05 | 0.50 | 0.06 | 0.04 | 0.07 | 0.91 | 0.26 | 0.58 | 0.74 | 1.00 | 0.10 | 0.62 | 0.00 | 0.10 | 0.02 | 0.17 |
| RH | -0.02 | 0.14 | 0.32 | -0.11 | 0.04 | 0.06 | -0.21 | 0.43 | 0.71 | 0.10 | 1.00 | -0.07 | -0.95 | 0.03 | -0.09 | -0.03 |
| P | -0.09 | 0.02 | -0.10 | -0.05 | -0.12 | 0.56 | 0.10 | 0.30 | 0.38 | 0.62 | -0.07 | 1.00 | 0.10 | 0.12 | -0.11 | 0.11 |
| LI | 0.02 | -0.09 | -0.26 | 0.10 | -0.06 | -0.01 | 0.16 | -0.34 | -0.68 | 0.00 | -0.95 | 0.10 | 1.00 | 0.00 | 0.08 | 0.04 |
| $N_w$ | -0.01 | -0.04 | 0.00 | -0.04 | 0.02 | 0.00 | -0.14 | 0.22 | 0.07 | 0.10 | 0.03 | 0.12 | 0.00 | 1.00 | -0.46 | 0.43 |
| $D_m$ | 0.08 | 0.17 | 0.13 | 0.12 | 0.45 | 0.13 | 0.38 | -0.16 | -0.04 | 0.02 | -0.09 | -0.11 | 0.08 | -0.46 | 1.00 | -0.19 |
| $\mu$ | -0.11 | -0.02 | -0.03 | -0.04 | -0.14 | 0.14 | -0.01 | 0.11 | 0.09 | 0.17 | -0.03 | 0.11 | 0.04 | 0.43 | -0.19 | 1.00 |

are shown in Table 4.6. The association between the DSD parameters and meteorological data at ≈3.3 km is not significantly different to meteorological data determined at ≈1 km. With the exception of $D_m$ and rainfall rate there is little association between the DSD parameters and meteorological data.

Table 4.6: Spearman's rank correlation matrix of meteorological data at a height of ≈3.3 km and DSD parameters.

| | U | V | W | WD | R | RHt | CAPE | LWC | DP | T | RH | P | LI | $N_w$ | $D_m$ | $\mu$ |
|---|---|---|---|---|---|---|---|---|---|---|---|---|---|---|---|---|
| U | 1.00 | 0.13 | 0.00 | 0.34 | 0.08 | -0.05 | -0.01 | 0.12 | -0.06 | -0.05 | 0.04 | -0.06 | -0.04 | -0.07 | 0.09 | -0.11 |
| V | 0.13 | 1.00 | 0.01 | 0.28 | 0.20 | 0.50 | 0.16 | 0.36 | 0.40 | 0.45 | 0.16 | 0.05 | -0.14 | -0.02 | 0.17 | 0.05 |
| W | 0.00 | 0.01 | 1.00 | -0.07 | 0.14 | -0.03 | -0.03 | 0.23 | 0.24 | 0.03 | 0.44 | -0.12 | -0.44 | -0.04 | 0.15 | 0.07 |
| WD | 0.34 | 0.28 | -0.07 | 1.00 | 0.07 | 0.09 | 0.02 | 0.00 | -0.08 | 0.04 | -0.09 | 0.03 | 0.09 | -0.09 | 0.14 | -0.02 |
| R | 0.08 | 0.20 | 0.14 | 0.07 | 1.00 | 0.09 | 0.20 | 0.10 | 0.09 | 0.02 | 0.11 | -0.13 | -0.11 | 0.19 | 0.51 | -0.15 |
| RHt | -0.05 | 0.50 | -0.03 | 0.09 | 0.09 | 1.00 | 0.21 | 0.51 | 0.72 | 0.92 | 0.07 | 0.60 | -0.03 | -0.04 | 0.11 | 0.10 |
| CAPE | -0.01 | 0.16 | -0.03 | 0.02 | 0.20 | 0.21 | 1.00 | -0.17 | -0.07 | 0.10 | -0.28 | 0.02 | 0.29 | -0.22 | 0.33 | 0.01 |
| LWC | 0.12 | 0.36 | 0.23 | 0.00 | 0.10 | 0.51 | -0.17 | 1.00 | 0.73 | 0.59 | 0.53 | 0.29 | -0.50 | 0.21 | -0.12 | 0.02 |
| DP | -0.06 | 0.40 | 0.24 | -0.08 | 0.09 | 0.72 | -0.07 | 0.73 | 1.00 | 0.78 | 0.63 | 0.45 | -0.59 | 0.06 | 0.01 | 0.09 |
| T | -0.05 | 0.45 | 0.03 | 0.04 | 0.02 | 0.92 | 0.10 | 0.59 | 0.78 | 1.00 | 0.14 | 0.67 | -0.09 | 0.05 | -0.02 | 0.14 |
| RH | 0.04 | 0.16 | 0.44 | -0.09 | 0.11 | 0.07 | -0.28 | 0.53 | 0.63 | 0.14 | 1.00 | -0.06 | -1.00 | 0.14 | -0.06 | 0.00 |
| P | -0.06 | 0.05 | -0.12 | 0.03 | -0.13 | 0.60 | 0.02 | 0.29 | 0.45 | 0.67 | -0.06 | 1.00 | 0.09 | 0.05 | -0.15 | 0.03 |
| LI | -0.04 | -0.14 | -0.44 | 0.09 | -0.11 | -0.03 | 0.29 | -0.50 | -0.59 | -0.09 | -1.00 | 0.09 | 1.00 | -0.13 | 0.06 | 0.01 |
| $N_w$ | -0.07 | -0.02 | -0.04 | -0.09 | 0.19 | -0.04 | -0.22 | 0.21 | 0.06 | 0.05 | 0.14 | 0.05 | -0.13 | 1.00 | -0.70 | 0.04 |
| $D_m$ | 0.09 | 0.17 | 0.15 | 0.14 | 0.51 | 0.11 | 0.33 | -0.12 | 0.01 | -0.02 | -0.06 | -0.15 | 0.06 | -0.70 | 1.00 | -0.10 |
| $\mu$ | -0.11 | 0.05 | 0.07 | -0.02 | -0.15 | 0.10 | 0.01 | 0.02 | 0.09 | 0.14 | 0.00 | 0.03 | 0.01 | 0.04 | -0.10 | 1.00 |

## 4.7 Analysis of the effects of cloud type on the DSD

Data from Meteosat Second Generation (MSG) satellites, Meteosat 8 and 9, were used to determine cloud type. Cloud analysis image (CLAI) data provided by EUMETSAT determines cloud type based on measurements of brightness temperature (the temperature determined by observed intensity from a black body at a given frequency). CLAI data was used from 2003-2006 and is disseminated every third hour. The DSD parameters were compared with rainfall rate and cloud type in Figures 4.22(a)-4.22(c). Each DSD parameter is plotted against rainfall rate, where the colour of the data points show cloud type.

Figure 4.22(a) shows $D_m$ versus rainfall rate, with data segregated by cloud type. The spread of the data points for each cloud type demonstrates that the type of cloud presents little pattern with $D_m$ and rainfall rate. $N_w$ and $\mu$ show little correlation with cloud type, as shown by the spread of the data in Figures. 4.22(b) and 4.22(b).

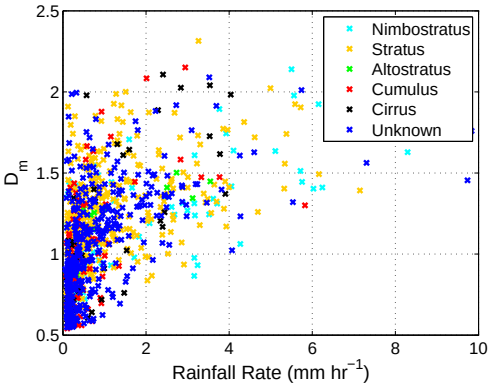


(a) $D_m$ compared against rainfall rate

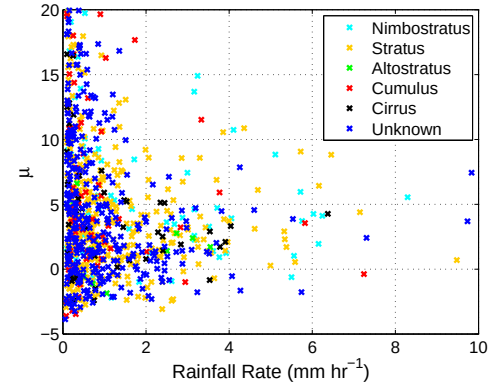


(b) $\mu$ compared against rainfall rate

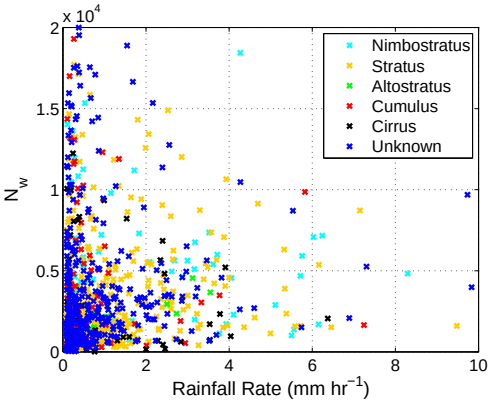


(c) $N_w$ compared against rainfall rate

Figure 4.22: Comparisons of normalised Gamma parameters against rainfall rate for various cloud types.

## 4.8 Conclusion

This chapter has compared 4 years of surface meteorological measurements, 3 years of Unified Model meteorological data and 4 years of satellite data with DSD parameters measured by a disdrometer at Chilbolton. It has been shown that there is a reasonable correlation between the parameter $D_m$ and rainfall rate, there is some correlation between $D_m$ and $N_w$, and little correlation between $N_w$ and $\mu$. However, there is large variability in the parameter relationships.

Surface meteorological measurements showed little correlation with the DSD parameters. Analysis of correlation between DSD parameters, rainfall rate and meteorological factors demonstrated some small relationships. Some correlation was evident between $D_m$, rainfall rate and wind speed, where the mean drop size increased more rapidly with rainfall rate for wind speeds above $10\,\mathrm{ms}^{-1}$ and below $5\,\mathrm{ms}^{-1}$. It has also been established that for high values of dew point temperature (above 283 K) and for low rainfall rates (less than $7\,\mathrm{mm\,hr}^{-1}$) there is an increase in the mean and standard deviation of $N_w$. The standard deviation for $N_w$ is also higher for low rainfall rates (less than $7\,\mathrm{mm\,hr}^{-1}$) and below wind speeds of $8\,\mathrm{ms}^{-1}$. Therefore, the variability in $D_m$ and $N_w$ could be decreased in determining the parameters according to rainfall rate. However, correlation analysis and principal component analysis showed correlation between meteorological variables and the DSD parameters is very small. The correlation is too small to generate reasonable estimates of the DSD in order out perform a standard power-law relationship between attenuation and rainfall rate. These measurements may only provide part of the process in shaping the DSD seen at the ground. Factors, such as change in meteorological variables with height and the conditions when rain drops are formed, will also affect the final shape of the DSD.

The analysis of the Unified Model results at 1 km and 3.3 km revealed no further significant correlation with the DSD parameters. Potential correlation between the DSD and meteorological parameters is hidden by turbulence in the boundary layer, the difference in height between the disdrometer and meteorological measurements, and change in meteorological parameters with height. Analysis of correlation and Spearman's rank correlation showed no significant relationships.

It has been concluded that there is little significant correlation between the DSD and meteorological data. Potential correlation between wind speed and DSD is convoluted not only by the turbulence within the boundary layer, but the change in wind speed as the raindrop falls from its point of origin. Other factors, such as temperature, may affect the shape of the DSD but the result is hidden by multiple factors, such as the change in height, time, and multiple parameters of the troposphere. Meteorological surface

measurements and numerical weather modelling results compared with disdrometer measurements may provide some link to convective and stratiform rain but do not provide enough information to determine the DSD.

# Chapter 5

# Relationships between attenuation and rainfall rate

This chapter investigates power-law and linear relationships between attenuation and rainfall rate ($A$-$R$), and discusses the use of $A$-$R$ relationships with terrestrial links. Attenuation measured on terrestrial links can be used to estimate surface rainfall rates along a link path. There is current interest in the use of inverse methods to estimate rainfall over areas inferred from terrestrial links. A power-law relationship can be used to estimate rainfall rate from attenuation measured by a terrestrial link. However, the inverse method is simplified with a linear relationship between attenuation and rainfall rate when determining path-averaged rainfall rates. The chapter examines the linear and power-law relationships goodness of fit for a range of frequencies and rainfall rates. Six years of disdrometer data (2003-2008) from Chilbolton in the UK has been used to study both linear and power-law fits to attenuation and quantify the associated errors.

The aim of this work is to quantify the conditions under which the $A$-$R$ relationship can be considered linear. Specific attenuation and rainfall were calculated from DSD derived from disdrometer data. The T-Matrix method, Barber and Hill [1990], was used to determine the raindrop scattering parameters over a range of frequencies between 10 and 95 GHz for both vertical and horizontal polarisations. The sensitivity of the $A$-$R$ relationship to frequency and rainfall rate interval is analysed. Finally, the suitability and performance of the power-law and linear relationships to express the conversion from rainfall rate to specific attenuation is evaluated. The dependence of the results on polarisation is also considered although the focus is on vertical polarisation since this is by far the most common for operational links (all 38 GHz links in the UK are vertically polarised).

## 5.1 Rainfall rate measurements from terrestrial microwave links

Measurements of attenuation on terrestrial microwave links have been widely used to estimate surface rainfall rate. Among the first measurements were those of Atlas and Ulbrich [1977]. Typically terrestrial links operate at frequencies between 10 GHz and 50 GHz and usually over a path of 1-50 km. At microwave frequencies, the terrestrial link signal is attenuated by raindrops falling along the link path due to electromagnetic scattering and absorption processes. Traditionally attenuation is expressed in terms of rainfall rate using a power-law relationship, Olsen et al. [1978]. Conversely, this relationship can also be used to determine rainfall rate from link attenuation.

The power-law is generally considered to be a good representation of the relationship between attenuation and rainfall ($A$-$R$). However, as will be shown, since the power-law relationship is potentially non-linear it is not always possible to estimate true average rainfall from path-average attenuation. The coefficients of the $A$-$R$ relationship are also highly dependent on the raindrop size distribution (DSD), which can vary significantly. The International Telecommunication Union Radiocommunications (ITU-R) sector provides a standard definition to calculate specific attenuation from rainfall rate based on the power-law relationship, ITU-R P.838-3, Rec. ITU-R P.838-3 [September, 2006]. In this recommendation, the listed fit coefficients are derived considering all available rainfall rates. This chapter investigates the sensitivity of the $A$-$R$ relationship to the upper limit of the rainfall rates over which the fit is derived.

The use of terrestrial links can be extremely valuable for measuring rainfall rate in areas lacking radar, rain gauges or other devices used for rain measurements, Upton et al. [2005]. Links may be most useful in urban areas or steep-sided valleys where it is difficult to place rain gauges or use radars to measure rainfall near the ground, Messer et al. [2006], Zinevich et al. [2008]. The use of path-averaged measurements has a number of further advantages over weather radar systems. Weather radars measure rainfall typically a few hundred metres above the Earth whereas surface rainfall is generally required for hydrology. Other factors such as fog, low-level cloud and evaporation can all affect the estimate of rainfall rate by radar, Austin [1987]. Other complicating factors for radar include the sample time for a complete volume scan and the choice of radar location. For link-derived rainfall rate, the sample time may only be a few seconds compared to a few minutes for a radar volume scan.

It is worth considering that there are certain caveats when inferring rainfall rate from terrestrial links. Antenna wetting will result in increased attenuation and therefore some inaccuracies in the inferred rainfall rate, Crane and Rogers [1998]. The surround-

ing environment, such as tall buildings, will also cause interference and reflections of propagating signals effecting both the measured attenuation and the accuracy of the inferred rainfall rate. However, methods can be used to minimise such problems. For example, antenna wetting may be reduced by the use of carefully designed antenna coverings.

Globally there are large numbers of microwave links. Reported link densities range from 0.3 links per $km^2$ to 3 links per $km^2$, Messer et al. [2006]. In the UK there are approaching 14,000 links in the 38 GHz frequency band alone. Furthermore, an increasing number of research experiments are also being conducted using purpose-built links to estimate rainfall rate, Leijnse et al. [2007]. It is reasonable to suggest that a network of links could be useful to provide new or complementary rainfall rate information over wide areas. All of these techniques require a relationship to convert the measured attenuation into a rainfall rate. This relationship should ideally be as independent of the DSD as possible and be applicable for a wide range of rainfall rates.

The DSD can cause significant variability in the $A$-$R$ relationship. The DSD is, in general, unknown and in turn can cause inaccuracy in estimating rainfall rate from path attenuation. Therefore, it is important to reduce the effects of the DSD as much as possible. Links operating at two different frequencies have been considered to reduce the impact of the DSD variability, Holt et al. [2000], Holt et al. [2003]. The method utilises the difference in attenuation between the two frequencies to give an estimate of rainfall rate. However, two suitable frequencies may not always be available. The effect of the variability of the DSD on single-frequency links has been considered by Berne and Uijlenhoet [2007]. The authors showed that the estimated rainfall rates are sensitive to the power-law fit coefficients.

## 5.2 Inverse methods

The current interest in the use of inverse methods to derive surface rainfall rates requires the use of either a linear $A$-$R$ relationship or complex linearisation techniques, Giuli et al. [1991]. The use of links at frequencies for which the $A$-$R$ relationship can be considered linear is restrictive, however it does imply independence of the DSD, Atlas and Ulbrich [1977]. Furthermore, for a non-linear $A$-$R$ relationship there can also be a significant difference between the true path-averaged rainfall rate and average rainfall rate inferred from path-averaged attenuation.

## 5.3 Attenuation data analysis

Six years of data, collected between 2003 and 2008, from a Joss impact disdrometer was used to determine DSDs over Chilbolton, UK (51.14° N,1.44° W). An analytical distribution was fitted to each measured DSD in order to remove any noise and anomalous results following the method outlined in Chapter 3.1.4. Specific attenuation (2.26) ($A$ in $\mathrm{dB\,km^{-1}}$) and rainfall rate (2.12) were calculated for each fitted raindrop size distribution. Attenuation was calculated for vertical and horizontal polarisations.

The $A$-$R$ relationship has been extensively studied by many, such as Olsen et al. [1978]. Analytically, the $A$-$R$ relationship can be shown to be linear when the moments of $N(D)$ in (2.26) and (2.12) are equal. Under these conditions the relationship becomes independent of the raindrop size distribution, Atlas and Ulbrich [1977], Watson et al. [1999]. Figure5.1 shows the resultant values of the of vertically polarised $Q_t$ plotted against $v(D)D^3$ for 10, 35, 50 and 90 GHz. The results show at 35 GHz the relationship between $Q_t$ and $v(D)D^3$ is more linear and has considerably less variation when compared to higher frequencies. Figure 5.1, illustrates that the A-R relationship is far more linear at ≈35 GHz, as the moments of $N(D)$ in (2.26) and (2.12) are almost equivalent. To investigate further where the best-fitting linear $A$-$R$ relationship region exists, the established power-law fit (5.1) was compared to a linear fit (5.2) and the $A$-$R$ relationship derived from disdrometer data. The comparison is repeated for $A$-$R$ relationships over a range of frequencies between 10 to 95 GHz. The power-law fit and linear fit were determined using a least-squares fitting procedure.

The power-law equation calculating specific attenuation ($A_p$ in $\mathrm{dB\,km^{-1}}$) is written as:

$$A_p = aR^b, \tag{5.1}$$

where $a$ and $b$ are coefficients determined by least-squares. The linear equation to calculate specific attenuation ($A_l$ in $\mathrm{dB\,km^{-1}}$) is given by:

$$A_l = \alpha R, \tag{5.2}$$

where $\alpha$ is a coefficient and $A_l$ is attenuation determined by a linear fit.

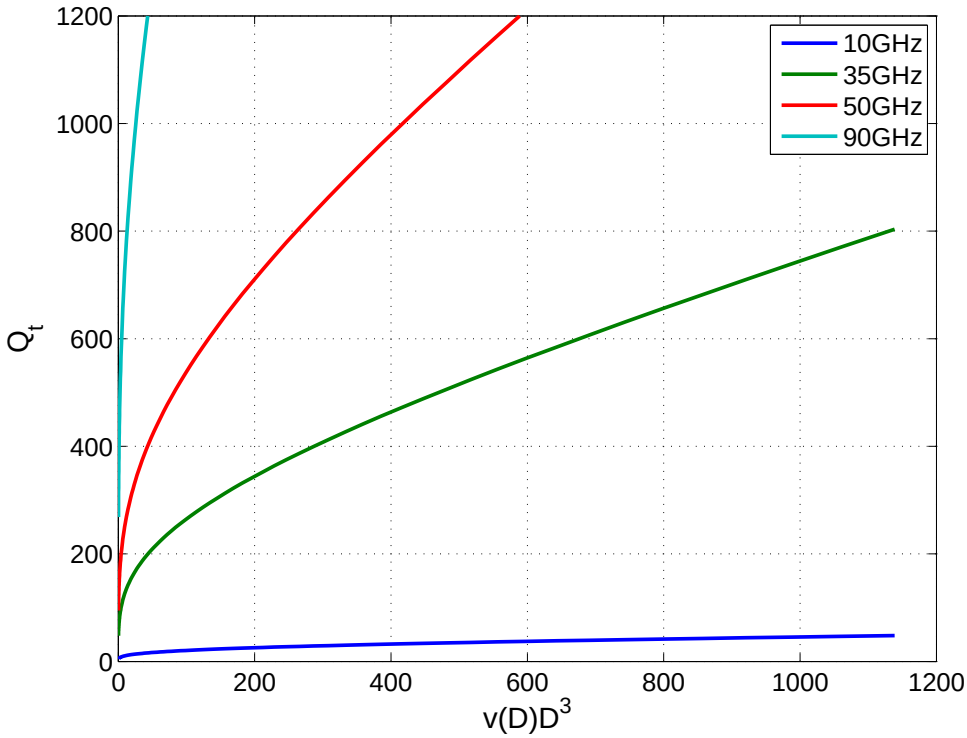


Figure 5.1: A plot of $Q_t$ against $v(D)D^3$ for frequencies 10, 35, 50 and 90 GHz.

## 5.4 Errors caused by path averaging

Errors may occur when averaging the non-linear power-law relationship between attenuation and rainfall rate along a path. For example, average specific attenuation, $\overline{K}_1$ (dB km$^{-1}$), determined from rainfall measured along a path $R(s)$ is not the same as specific attenuation, $\overline{K}_2$ (dB km$^{-1}$), determined by the average rainfall rate ($\overline{R}$) of the path.

$$\overline{K}_1 = \frac{1}{L_t}\int_0^{L_t} aR(s)^b ds, \tag{5.3}$$

$$\overline{K}_2 = a\left[\frac{1}{L_t}\int_0^{L_t} R(s)ds\right]^b = a\overline{R}^b, \tag{5.4}$$

where $L_t$ is link length (km), $a$ and $b$ as in (5.1), and $R(s)$ is rainfall rate (mm hr$^{-1}$). In the case of this paper the average rainfall rate is wanted from average attenuation measured. Only when the $A$-$R$ relationship is linear, therefore $b = 1$, are (5.3) and (5.4) the same, then $\overline{K}_1 = \overline{K}_2$.

Using the synthetic storm technique Matricciani [1996], disdrometer data from Chilbolton were used to generate a database of rain events. A total of approximately 2.4 million rain events were generated using the data available and a velocity of 10 ms$^{-1}$. The

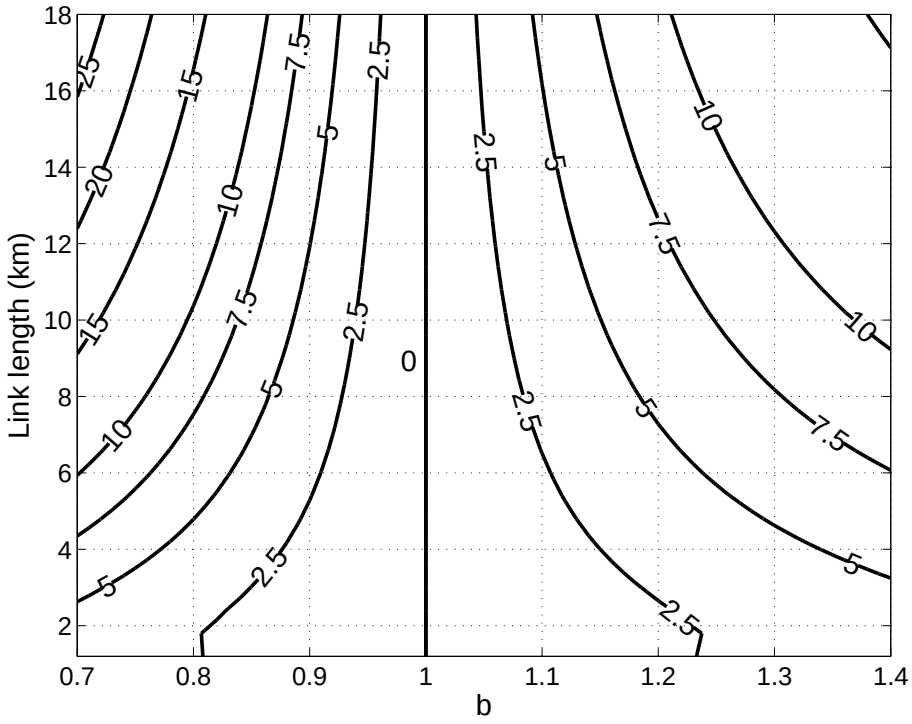


Figure 5.2: Percentage difference, $\Delta K$, of specific attenuation averages $\overline{K}_1$ and $\overline{K}_2$ as a function $b = 0.7$-$1.4$ and link length 1.2 - 18.0 km.

average attenuation was calculated for each synthetic rainstorm using (5.3) and (5.4), over link lengths ranging from 1.2 - 18 km (typical of links deployed in the UK). The percentage difference between the two estimates, $\Delta K$, was calculated using:

$$\Delta K = \left| \frac{\overline{K}_1 - \overline{K}_2}{\overline{K}_1} \right| \times 100. \tag{5.5}$$

The difference $\Delta K$ expresses the error caused by non-linearity of the power-law relationship, shown in Figure 5.2. It can be seen that, as $b$ diverges away from 1, the error $\Delta K$ increases. When $b \neq 1$ there is a big difference in error between a short link (2 km) and a long link (18 km). However, there is very little difference in error when comparing an 18 km link to a 12 km link. The error between the averages shows (5.4) is incorrect when used to average a non-linear relationship. In the case $b = 1$, the difference between the averages is zero.

## 5.5 Results

### 5.5.1 Power-law attenuation-rainfall relationships

The power-law fits were determined for all attenuation and rainfall rates calculated from the Chilbolton disdrometer data. To investigate the sensitivity of each of the fits to the rainfall rate interval, the data used in the fitting process was conditioned by maximum rainfall rate. Each fit was calculated up to maximum rainfall rates of 5-100 mm hr$^{-1}$ in steps of 5 mm hr$^{-1}$. To determine the effects of frequency on each fit, the process was repeated for frequencies in the range of 10-95 GHz in steps of 5 GHz.

At higher rainfall rates, above 30 mm hr$^{-1}$, the number of samples in each interval reduces, as evidenced by Figure 3.6 (Chapter 3). Even considering six years of data, the number of data points above 35 mm hr$^{-1}$ reduces from many thousands to tens approaching 100 mm hr$^{-1}$. The fits remain statistically significant as they include all values up to the maximum rainfall rate. The fitting procedure weights all data points uniformly. However, the sensitivity of the fit to data points above 60 mm hr$^{-1}$ is reduced.

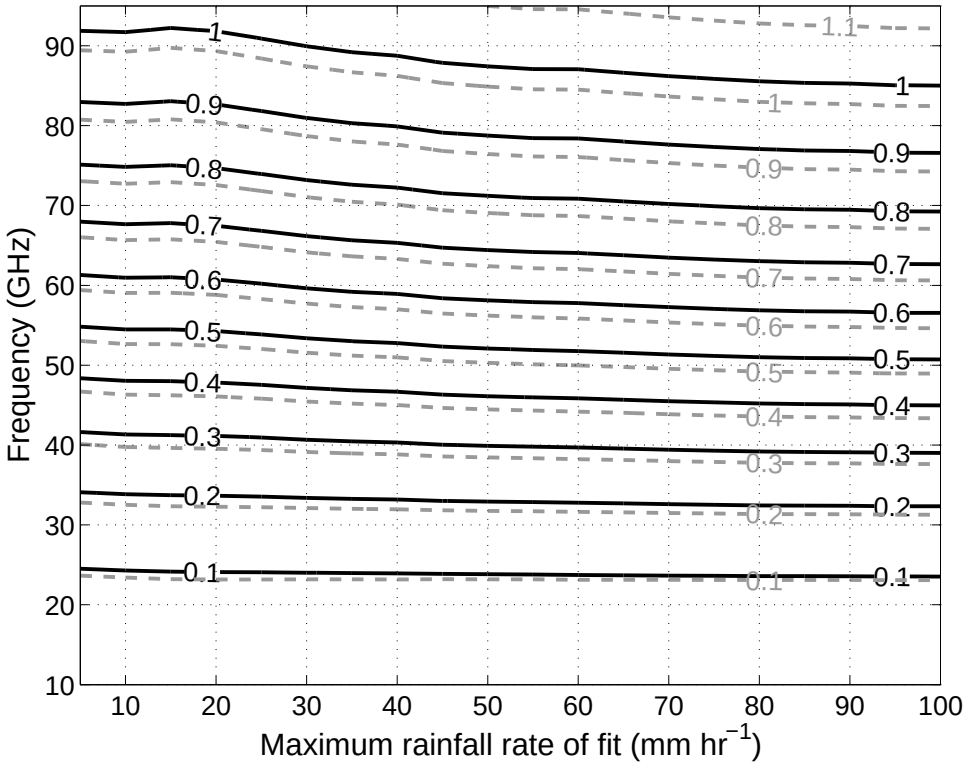


Figure 5.3: Contours of parameter $a$ of the power-law fit as a function of frequency and maximum fitted rainfall rate. Solid contours are for vertical polarisation, dashed contours are for horizontal polarisation.

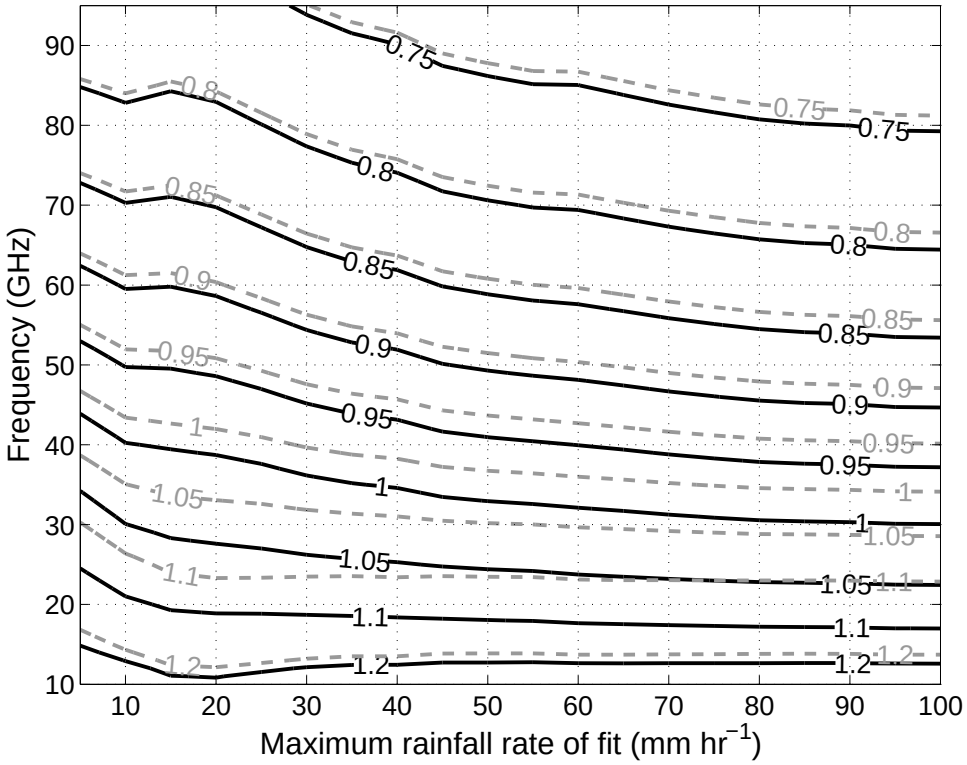


Figure 5.4: Contours of parameter $b$ of the power-law fit as a function of frequency and maximum fitted rainfall rate. Solid contours are for vertical polarisation, dashed contours are for horizontal polarisation.

Figure 5.3 shows the value of $a$ for the power-law fit. It can be seen that at $a$ is almost independent of the rainfall rate interval. At approximately 50 GHz the rate of increase in $a$ with frequency is at its highest, near 90 GHz the rate of increase declines. Figure 5.4 shows $b$, which demonstrates some dependence on rainfall rate interval. Parameter $b$ decreases with frequency, with the largest rate of decrease around 50 GHz. The decrease in $b$ is small such that the increase in $a$ is large enough to increase the resulting attenuation from the power-law equation. The region where $b = 1$, corresponding to a linear relationship, occurs for frequencies of approximately 30-40 GHz depending on the upper rainfall rate considered.

To determine the goodness of fit between the disdrometer derived data and power-law fit, the percentage variance accounted for (PVAF) or R-squared ($R^2$) has been calculated, Pitt and Myung [2002], Bevington and Roninson [1992]. PVAF was determined for all the fits, as a function of frequency (10-95 GHz) and rain rate interval (5-100 mm hr$^{-1}$). PVAF is given by:

$$\text{PVAF} = \left[1 - \frac{\sum(R_i - R_{pl})^2}{\sum(R_i - \overline{R})^2}\right] \times 100, \tag{5.6}$$

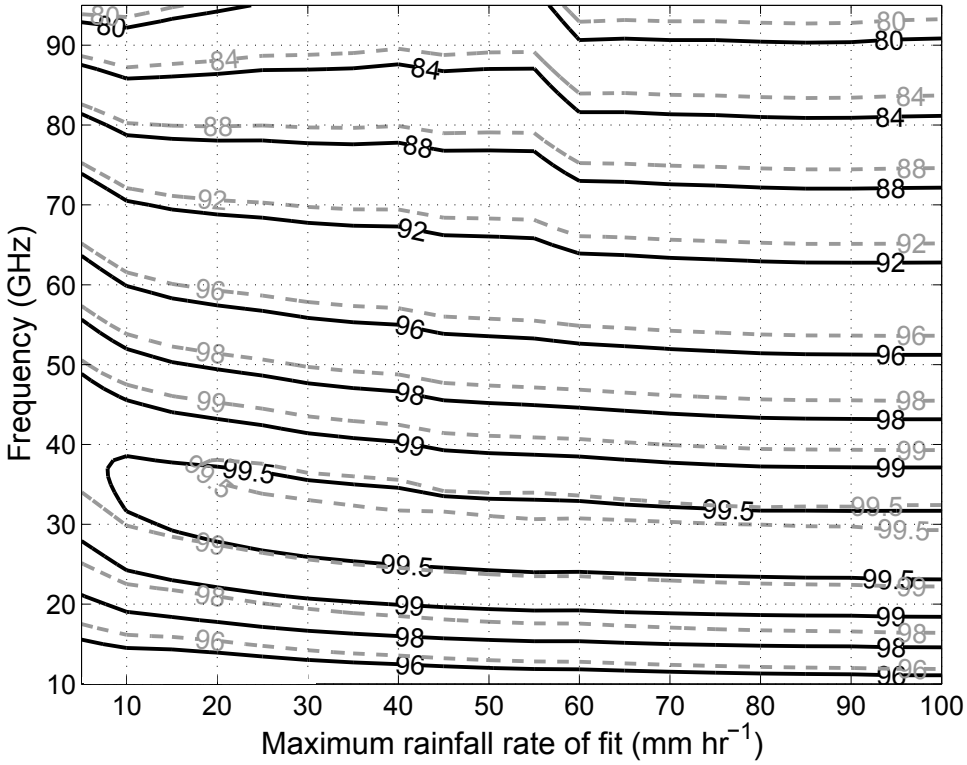


Figure 5.5: Contours of PVAF showing goodness of fit between disdrometer derived rainfall rate and rainfall rate calculated from power-law fits as a function of frequency and maximum fitted rainfall rate. Solid contours are for vertical polarisation, dashed contours are for horizontal.

where $R_i$ is rainfall rate determined from the disdrometer (mm hr$^{-1}$), $R_{pl}$ is rainfall rate determined by the power fit (dB km$^{-1}$) and $\overline{R}$ is mean rainfall rate measured from the disdrometer (mm hr$^{-1}$).

The PVAF for the power-law fit is at its highest around 35-38 GHz and above 15 mm hr$^{-1}$, as shown in Figure 5.5. This region is where the power-law fit accounts for the most variance in the data. As frequency increases above 38 GHz the goodness of fit reduces. Similarly, as the frequency decreases below 20 GHz the goodness of fit also degrades but more rapidly. The accuracy of the power-law fit tends to be fairly consistent over the rainfall rate interval. For frequencies above 40 GHz, fits up to a maximum rainfall rate of 10 mm hr$^{-1}$ have a marginally better PVAF than fits to higher rainfall rates. Natural variations in DSD make it difficult to estimate the $A$-$R$ relationship exactly using a fit to the data. However, the PVAF shows that the power-law relationship consistently captures a very high percentage of variance for data in the range of 15-60 GHz. The accuracy of the power-law fit is considerably lower above 60 GHz as the PVAF decreases below 90%.

### 5.5.2 Linear attenuation-rainfall relationship

Like the power-law fit, the linear fit was determined from attenuation and rainfall rate calculated from the disdrometer data. The linear relationship has only a single parameter $\alpha$ determined by least-squares fitting and shown by the contours in Figure 5.6. The single parameter limits the accuracy of the fit especially when applied to non-linear data. Obviously, while a linear fit may be applied to all frequencies it may only fit well over a limited range. Figure 5.6 shows that $\alpha$ increases with frequency, which is representative of the increase in attenuation with frequency. Above 45 GHz $\alpha$ becomes strongly dependent on the fitted maximum rainfall rate, which indicates increasing non-linearity of the $A$-$R$ relationship.

The PVAF has been calculated for all the linear fits between 10-95 GHz and for maximum rainfall rates 5 to 100 mm hr$^{-1}$. Figure 5.7 shows the PVAF for the linear fit. The highest PVAF occurs between 30 and 38 GHz. In this frequency range the $A$-$R$ relationship is very linear. At frequencies above 45 GHz the PVAF is larger for fits up to 10 mm hr$^{-1}$ rainfall rates. The larger PVAF implies the $A$-$R$ relationship is more linear at low rainfall rates above 45 GHz. At low frequencies (below 15 GHz) the goodness of

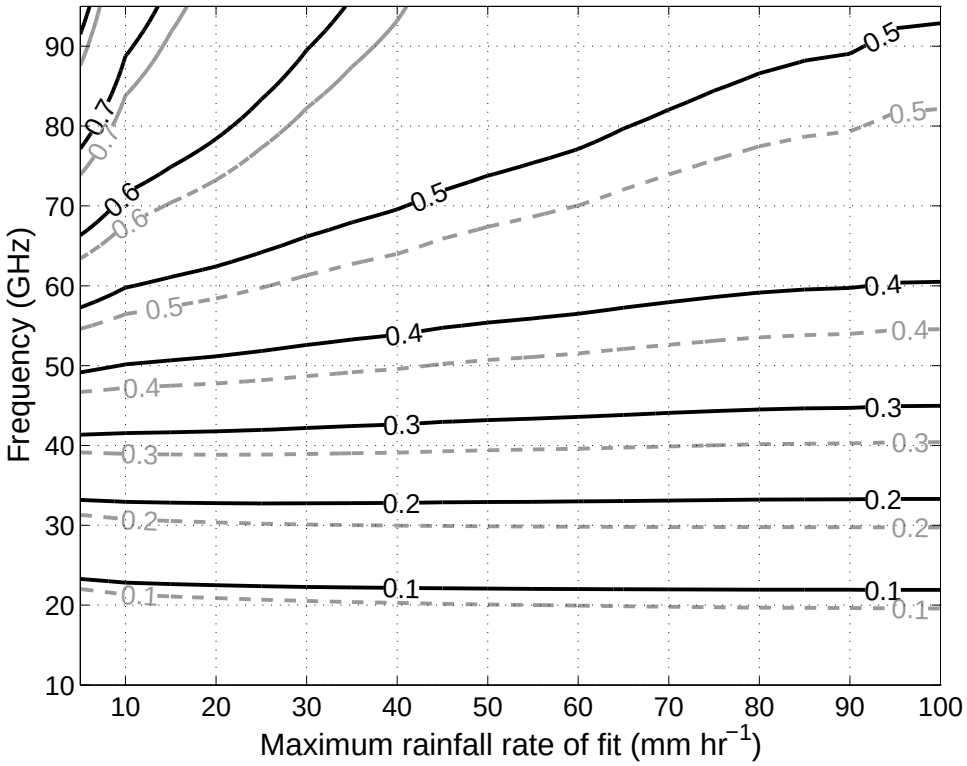


Figure 5.6: Contours of parameter $\alpha$ from linear fits as a function of frequency and maximum fitted rainfall rate. Solid contours are for vertical polarisation, dashed contours are for horizontal polarisation.

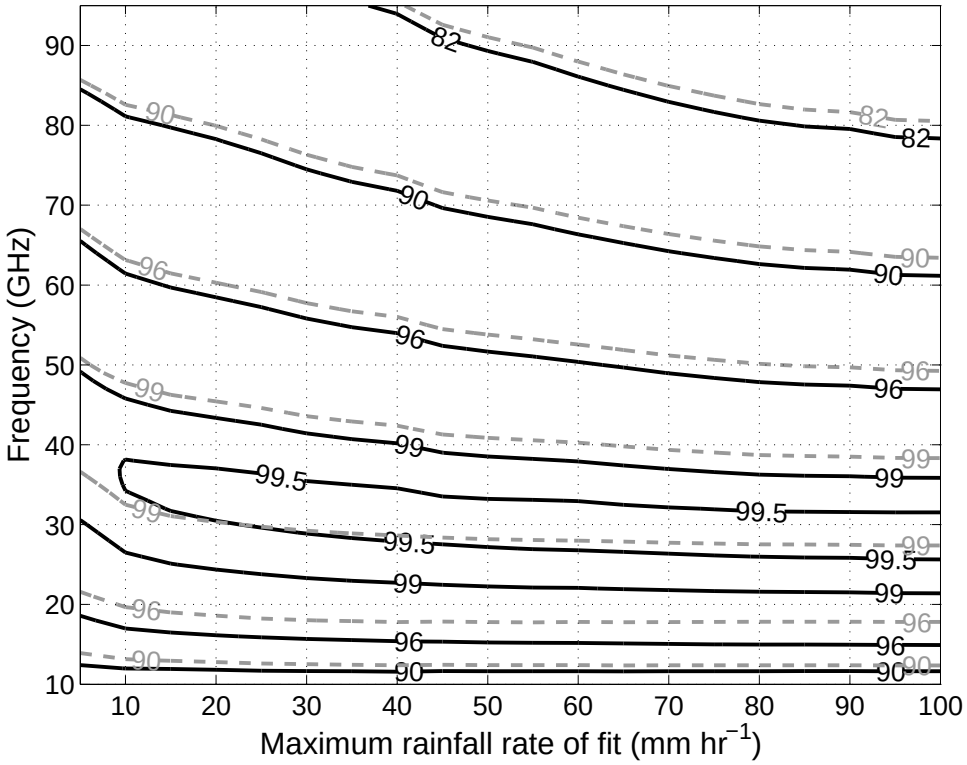


Figure 5.7: Contours of PVAF showing goodness of fit between disdrometer-derived rainfall rate and rainfall rate calculated from linear fits based on attenuation as a function of frequency and maximum fitted rainfall rate. Solid contours are for vertical polarisation, dashed contours are for horizontal polarisation.

fit degrades irrespective of the maximum rainfall rate and at a higher rate.

In summary the linear fit cannot be universally used to represent the $A$-$R$ relationship for all the frequencies in the range of 10-95 GHz. However, in the frequency range between 25-40 GHz the $A$-$R$ relationship becomes less sensitive to variability in the raindrop size distribution and the PVAF is at its highest value and is close to 100%.

### 5.5.3 Error in terms of percentage difference

The power-law relationship has been widely accepted and the results in Figure 5.5 show the power-law to be a good representation of the $A$-$R$ relationship up to 60 GHz. Due to the credibility of the power-law fit, the linear fit is further compared to the power-law as the standard to be achieved.

The PVAF is compared for 23, 33 and 38 GHz for maximum rainfall fits 5-100 mm hr$^{-1}$ in Figure 5.8; 33 GHz has been chosen to show the frequency with the highest PVAF

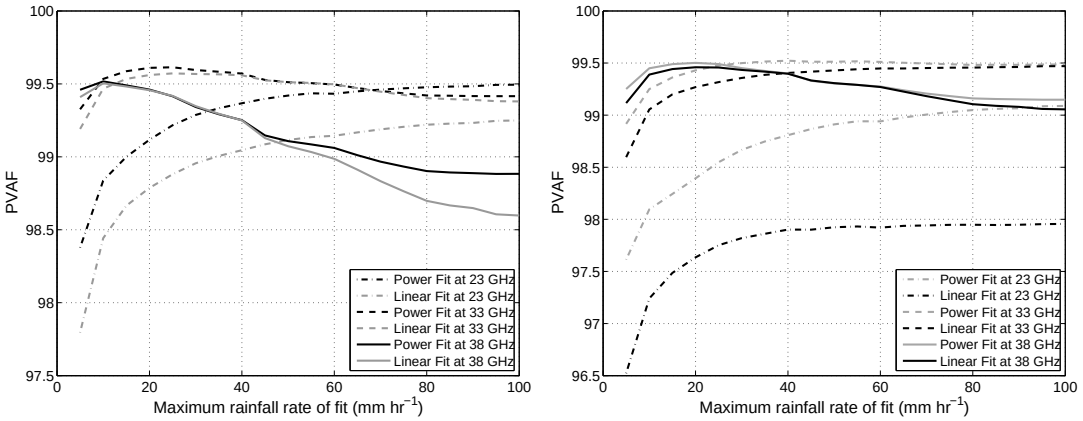


(a) PVAF vertical polarisation.

(b) PVAF horizontal polarisation.

Figure 5.8: PVAF for power-law and linear fit against maximum fitted rainfall rate for 23, 33 and 38 GHz.

(for vertical polarisation) while 23 GHz and 38 GHz have been chosen due to the high number of terrestrial links operating at these frequencies. For vertical polarisation at 33 GHz the power fit better estimates the $A$-$R$ relationship at rainfall rates below 35 mm hr$^{-1}$, above 35 mm hr$^{-1}$ the two fits are matched in performance. For both polarisations the linear fit PVAF at 23 GHz is not only less than 33 GHz but is smaller in comparison to the power-law relationship (at 23 GHz). This suggests a non-linear $A$-$R$ relationship. In the case of 38 GHz, the linear fit PVAF is very high, matching the power fit in performance up to 50 mm hr$^{-1}$. At 38 GHz horizontal polarisation outperforms vertical polarisation in terms of PVAF.

To illustrate the differences in the PVAF ($E_{\mathrm{PVAF}}$), the difference between the linear and power PVAF have been calculated as shown by:

$$E_{\mathrm{PVAF}} = P_{\mathrm{PVAF}} - L_{\mathrm{PVAF}}, \tag{5.7}$$

where $P_{\mathrm{PVAF}}$ is the PVAF of the power fit and $L_{\mathrm{PVAF}}$ is the PVAF of the linear fit.

Figure 5.9 shows a contour plot of $E_{\mathrm{PVAF}}$ for vertical and horizontal polarisations. The figures immediately illustrate that the smallest difference in variance is between 30 and 45 GHz. For horizontal polarisation the smallest frequency (between 10-95 GHz) where a zero difference occurs is 35 GHz, where vertical polarisation occurs at 33 GHz. For both polarisations the difference is also zero for 30-40 mm hr$^{-1}$ from 40-90 GHz. A more linear region exists below 30 mm hr$^{-1}$ and above 45 GHz as the linear fit outperforms the power fit. Above 40 mm hr$^{-1}$ and 40 GHz the power-law performs better than the linear fit as the $A$-$R$ relationship becomes increasingly varied and non-linear. The linear fit once again begins to match the performance of the power fit above 80 GHz and around 60 mm hr$^{-1}$. Above 70 GHz the variation in the $A$-$R$ relationship is very

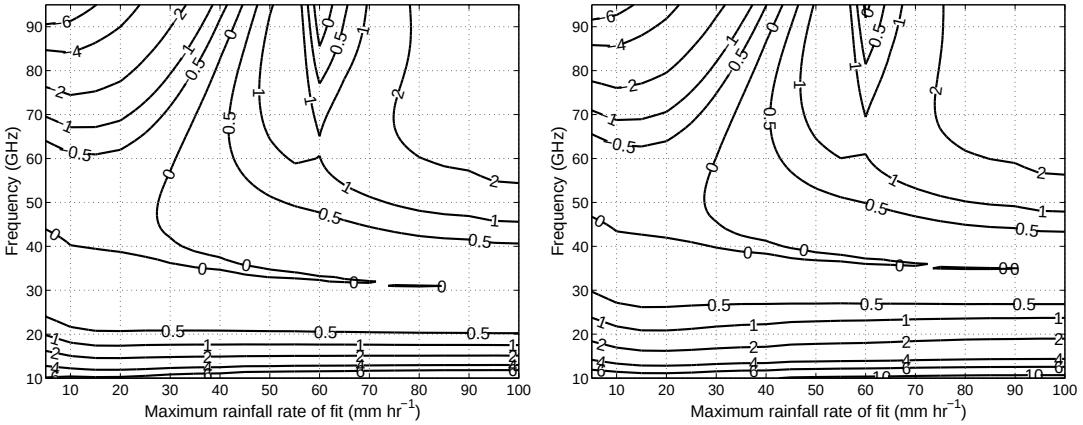


(a) Difference in PVAF vertical polarisation. (b) Difference in PVAF horizontal polarisation.

Figure 5.9: Difference between PVAF of power-law and PVAF of linear fit for frequencies 10-95 GHz and maximum rainfall rates of fits 5-100 mm hr$^{-1}$.

high such that neither the power-law or linear fit are representative.

### 5.5.4 Variation in PVAF as a function of rainfall rate

A fit to attenuation generated up to a maximum rainfall rate (e.g., 50 mm hr$^{-1}$) may be used to estimate higher or lower maximum rainfall rates (e.g., up to 100 mm hr$^{-1}$). In the case where the maximum rainfall rate is different to the maximum rainfall rate used to generate the fit, the PVAF will be different. Therefore, the PVAF has also been calculated over maximum rainfall rates from 5-100 mm hr$^{-1}$ in steps of 5 mm hr$^{-1}$ for each maximum rainfall rate used in the fitting process from 5-100 mm hr$^{-1}$. Figures 5.10(a) - 5.10(f) show the PVAF at 23, 33 and 38 GHz.

At 23 GHz, the $A$-$R$ relationship is not linear, as demonstrated by the results in Figure 5.10(a) and 5.10(b). The PVAF varies significantly over all fits. The variance accounted for is highest when both the maximum rainfall rate of each fit is the same as the maximum rainfall rate used in estimation. Variation unaccounted for decreases as rainfall rate increases. The linear fit PVAF is smaller than that of the power law fit, linear fit at 33 GHz and 38 GHz. At 23 GHz the $A$-$R$ relationship is more dependent on the raindrop size distribution and therefore not linear, hence the PVAF is smaller. PVAF is smaller for horizontal polarisation at 23 GHz than vertical polarisation. The $A$-$R$ relationship has been determined to be approximately linear over all rainfall rate intervals at 33 GHz for vertical polarisation from the disdrometer data available. This is emphasized by the results in Figure 5.10(c). Regardless of the rainfall rate the fit is applied to, the PVAF is very similar and very high for all rainfall rates. The dashed contours in Figure 5.10(c) show the power-law PVAF, which is very high and performs

very similar for all rainfall rate fits. The performance of the power-law fit is almost identical to the linear fit. The power-law fit is outperformed when the maximum fitted rainfall rate is below 10 mm hr$^{-1}$ and used to estimate high maximum rainfall rates

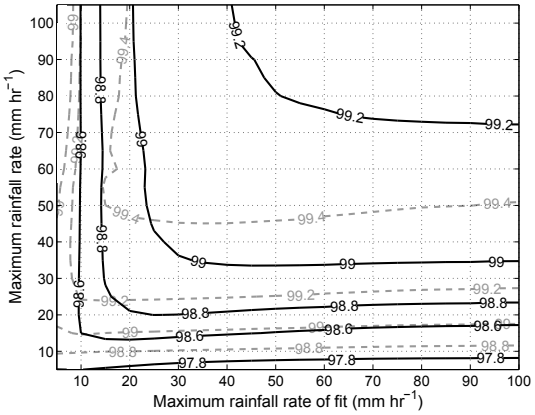


(a) PVAF at 23 GHz for vertical polarisation.

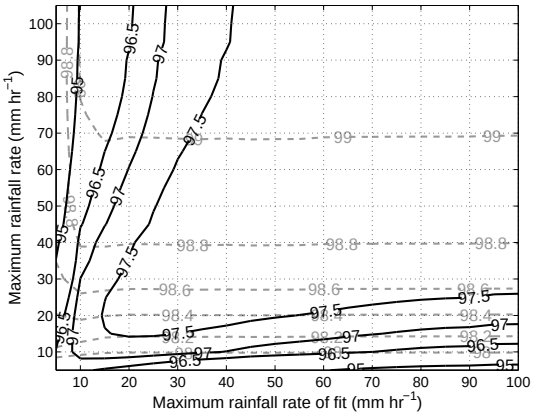


(b) PVAF at 23 GHz for horizontal polarisation.

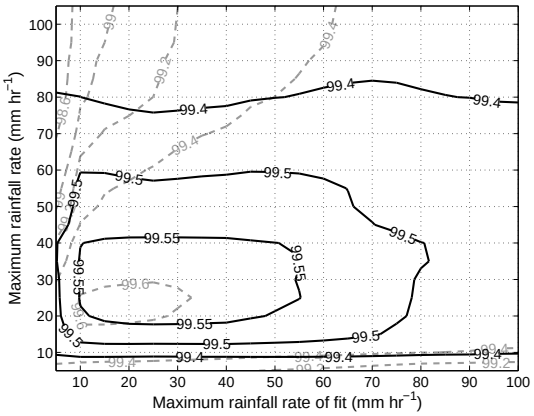


(c) PVAF at 33 GHz for vertical polarisation.

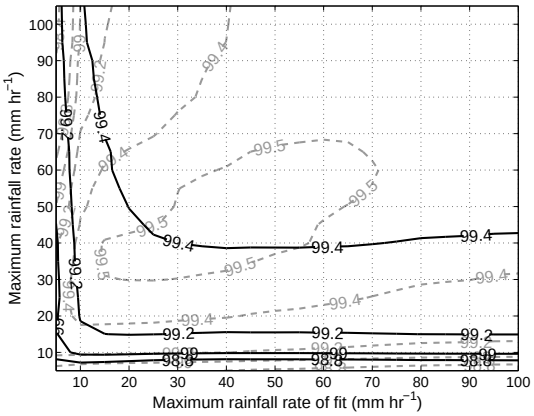


(d) PVAF at 33 GHz for horizontal polarisation.

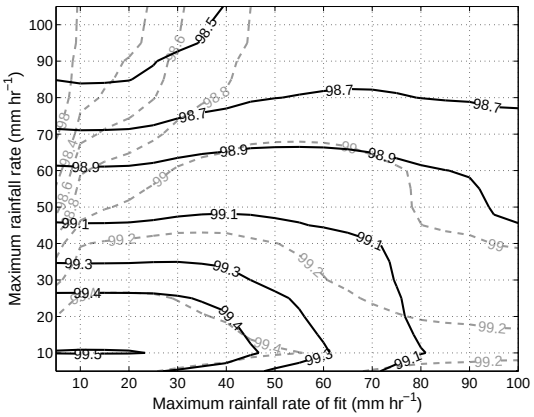


(e) PVAF at 38 GHz for vertical polarisation.

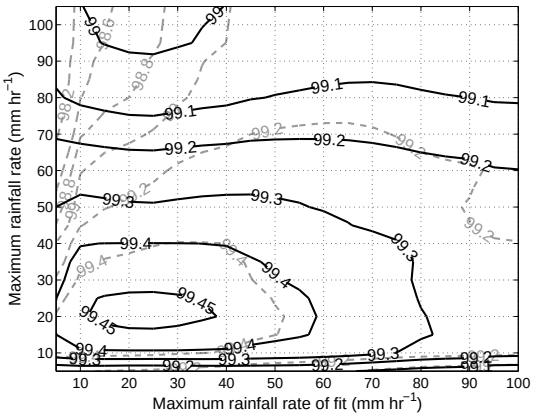


(f) PVAF at 38 GHz for horizontal polarisation.

Figure 5.10: The PVAF for maximum rainfall rates used to generate each fit for 5-100 mm hr$^{-1}$ when applied to different maximum rainfall rates of 5-100 mm hr$^{-1}$ at 23, 33 and 38 GHz. Linear fit is shown by the solid contour, power-law fit is shown by dashed contour.

(above 40 mm hr$^{-1}$). PVAF for horizontal polarisation is slightly less than vertical polarisation at 33 GHz. However, the PVAF is reasonably consistent for horizontal polarisation, as shown in Figure 5.10(d).

At 38 GHz the PVAF decreases as rainfall rate increases, therefore the $A$-$R$ relationship is more linear at low rainfall rates, shown in Figures 5.10(e) and 5.10(f). The maximum rainfall rate fit of 50 mm hr$^{-1}$ has the highest and most consistent variance accounted for over any rainfall rate in the range of 0-100 mm hr$^{-1}$. The power-law fit, shown by the dashed contours in Figures 5.10(e) and 5.10(f), have high and similar values of PVAF to the linear fit. At 38 GHz the linear fit is highly comparable to the power-law fit and is a good representation of the $A$-$R$ relationship. The horizontal polarisation outperforms vertical polarisations at 38 GHz.

### 5.5.5 Error in terms of attenuation difference

The power-law fit is once again assumed the best representation of the $A$-$R$ relationship. The fit was used as a bench mark to compare the linear fit. The $a$, $b$ and $\alpha$ parameters of each fit for maximum rainfall rate (5-100 mm hr$^{-1}$) were used to calculate attenuation from all the rainfall data derived from the disdrometer. The percentage difference of $A_p$ and $A_l$ were calculated as follows:

$$E_a = \left| \frac{A_p - A_l}{A_p} \right| \times 100. \tag{5.8}$$

Figure 5.11 shows the difference in attenuation ($E_a$) between the power-law fit and linear fit. The region bounded by the 5% contour in Figure 5.11 has been chosen to be representative of the area where the $A$-$R$ relationship can be considered linear. For vertical polarisation, this region lies between 28 GHz and 38 GHz for all rainfall rates. For horizontal polarisation error below 5% lies between 32 GHz and 42 GHz for all rainfall rates. For frequencies above and below 33 GHz, $E_a$ increases as the two estimates of attenuation become increasingly different. This is due to the $A$-$R$ relationship becoming increasingly non-linear.

Figure 5.12 shows an example of the $A$-$R$ relationship for specific attenuation at 38 GHz compared with rainfall rate calculated from all disdrometer data at Chilbolton. A linear and power-law fit have been applied to the data up to 100 mm hr$^{-1}$, shown by the solid and dashed lines on the figure respectively. Attenuation clearly increases with rainfall rate almost linearly at 38 GHz. The $R^2$ correlation coefficients are high for both linear (0.986) and power-law (0.990) fits. Visibly the power-law model is a better fit to data above 40 mm hr$^{-1}$. For rainfall rates below 30 mm hr$^{-1}$ both the linear and power-law

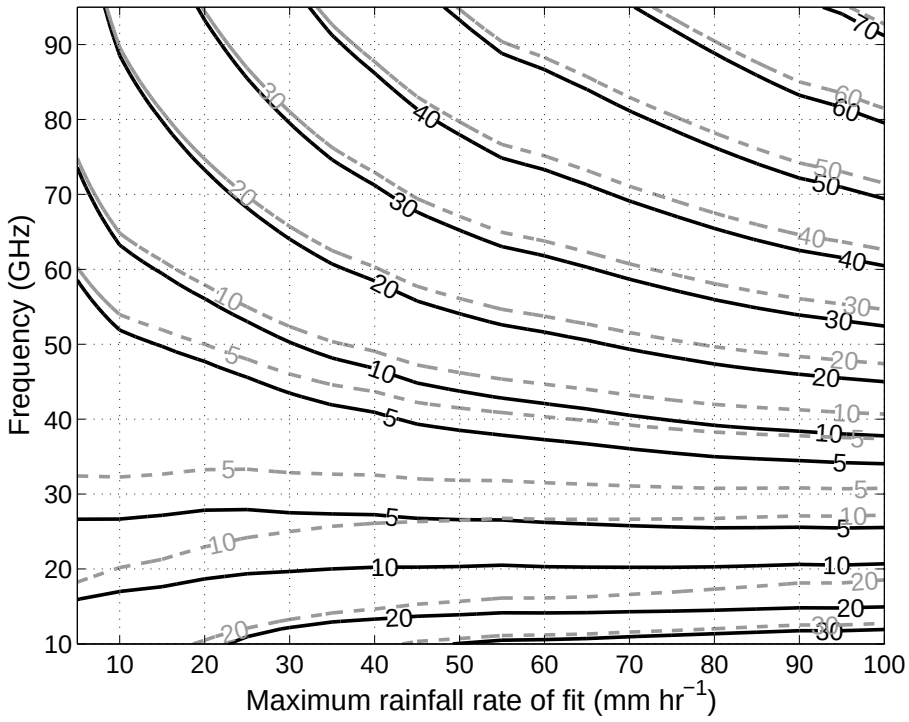


Figure 5.11: Percentage difference between attenuation calculated using power-law fit and linear fit plotted as a function of frequency and maximum fitted rainfall rate for vertical polarisation (solid contour) and horizontal polarisation (dashed contour).

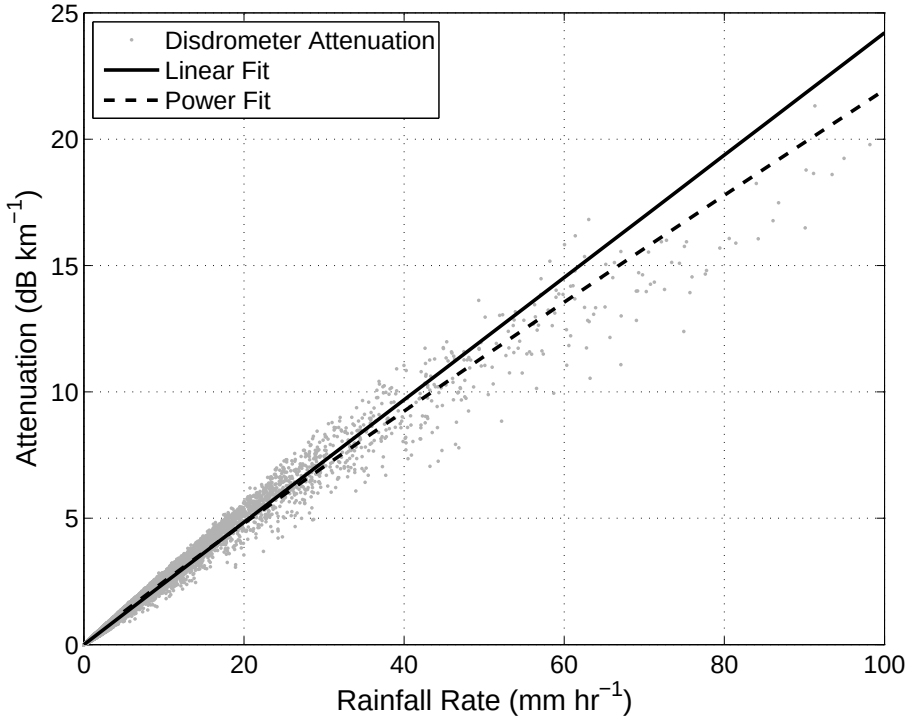


Figure 5.12: Vertically-polarised attenuation plotted against rainfall rate at 38 GHz showing a linear fit ($R^2 = 0.986$) and power-law fit ($R^2 = 0.990$) up to 100 mm hr$^{-1}$.

models are good fits to the $A$-$R$ relationship. This result is expected since the PVAF is almost identical for both fits at $30\,\mathrm{mm\,hr^{-1}}$, shown by Figure 5.10(e).

Table 5.1 summarises the values of $a$, $b$ and $\alpha$ for vertically polarised links for a range of frequencies and maximum rainfall rate fits. Table 5.2 summarises the same values over the same frequency and rainfall rate ranges for horizontally-polarised links. The percentage error in attenuation, $E_a$, has also been included to show the accuracy of the linear fit.

Table 5.1: Parameters $a$, $b$, $\alpha$ for calculating specific attenuation and percentage error of attenuation $E_a$ for vertical polarisation.

| | Maximum Rainfall Rate ($\mathrm{mm\,hr^{-1}}$) | | | | | | | | | | | | | | | |
|---|---|---|---|---|---|---|---|---|---|---|---|---|---|---|---|---|
| Frequency | 10 | | | | 30 | | | | 60 | | | | 100 | | | |
| (GHz) | $a$ | $b$ | $\alpha$ | $E_a$ | $a$ | $b$ | $\alpha$ | $E_a$ | $a$ | $b$ | $\alpha$ | $E_a$ | $a$ | $b$ | $\alpha$ | $E_a$ |
| 20 | 0.065 | 1.108 | 0.077 | 7.9 | 0.067 | 1.088 | 0.082 | 9.7 | 0.069 | 1.076 | 0.084 | 10.3 | 0.070 | 1.068 | 0.085 | 10.8 |
| 25 | 0.106 | 1.075 | 0.119 | 5.6 | 0.109 | 1.056 | 0.124 | 6.4 | 0.112 | 1.042 | 0.125 | 6.0 | 0.114 | 1.033 | 0.126 | 5.5 |
| 30 | 0.156 | 1.050 | 0.168 | 3.8 | 0.160 | 1.032 | 0.171 | 3.6 | 0.165 | 1.013 | 0.171 | 1.9 | 0.170 | 1.000 | 0.170 | 0.1 |
| 33 | 0.190 | 1.036 | 0.201 | 2.8 | 0.195 | 1.017 | 0.202 | 1.9 | 0.203 | 0.994 | 0.200 | 0.8 | 0.209 | 0.979 | 0.197 | 3.6 |
| 35 | 0.214 | 1.026 | 0.223 | 2.0 | 0.221 | 1.006 | 0.224 | 0.7 | 0.230 | 0.982 | 0.220 | 2.7 | 0.238 | 0.965 | 0.215 | 6.2 |
| 38 | 0.254 | 1.012 | 0.258 | 0.9 | 0.261 | 0.990 | 0.256 | 1.2 | 0.274 | 0.962 | 0.248 | 5.7 | 0.284 | 0.944 | 0.242 | 10.3 |
| 40 | 0.281 | 1.001 | 0.282 | 0.1 | 0.290 | 0.979 | 0.277 | 2.5 | 0.305 | 0.950 | 0.267 | 7.8 | 0.316 | 0.931 | 0.259 | 13.1 |
| 45 | 0.354 | 0.975 | 0.341 | 2.0 | 0.366 | 0.951 | 0.329 | 6.1 | 0.386 | 0.918 | 0.313 | 13.1 | 0.400 | 0.898 | 0.300 | 20.0 |
| 50 | 0.430 | 0.949 | 0.398 | 4.2 | 0.446 | 0.923 | 0.377 | 9.8 | 0.470 | 0.889 | 0.354 | 18.3 | 0.487 | 0.868 | 0.337 | 26.8 |
| 55 | 0.508 | 0.923 | 0.452 | 6.4 | 0.526 | 0.897 | 0.420 | 13.5 | 0.554 | 0.863 | 0.390 | 23.4 | 0.574 | 0.842 | 0.369 | 33.3 |
| 60 | 0.585 | 0.898 | 0.502 | 8.6 | 0.606 | 0.872 | 0.459 | 17.1 | 0.636 | 0.839 | 0.422 | 28.3 | 0.657 | 0.819 | 0.397 | 39.4 |

Table 5.2: Parameters $a$, $b$, $\alpha$ for calculating specific attenuation and percentage error of attenuation $E_a$ for horizontal polarisation.

| | Maximum Rainfall Rate ($\mathrm{mm\,hr^{-1}}$) | | | | | | | | | | | | | | | |
|---|---|---|---|---|---|---|---|---|---|---|---|---|---|---|---|---|
| Frequency | 10 | | | | 30 | | | | 60 | | | | 100 | | | |
| (GHz) | $a$ | $b$ | $\alpha$ | $E_a$ | $a$ | $b$ | $\alpha$ | $E_a$ | $a$ | $b$ | $\alpha$ | $E_a$ | $a$ | $b$ | $\alpha$ | $E_a$ |
| 20 | 0.071 | 1.140 | 0.088 | 10.1 | 0.072 | 1.122 | 0.095 | 13.1 | 0.072 | 1.123 | 0.100 | 15.9 | 0.072 | 1.123 | 0.104 | 18.4 |
| 25 | 0.115 | 1.108 | 0.136 | 7.9 | 0.118 | 1.091 | 0.144 | 10.0 | 0.119 | 1.086 | 0.149 | 11.6 | 0.120 | 1.082 | 0.152 | 12.8 |
| 30 | 0.169 | 1.080 | 0.191 | 5.9 | 0.173 | 1.061 | 0.199 | 6.9 | 0.178 | 1.047 | 0.202 | 6.6 | 0.182 | 1.037 | 0.203 | 6.1 |
| 33 | 0.206 | 1.062 | 0.227 | 4.7 | 0.212 | 1.043 | 0.233 | 4.9 | 0.219 | 1.024 | 0.233 | 3.4 | 0.226 | 1.010 | 0.232 | 1.7 |
| 35 | 0.233 | 1.050 | 0.251 | 3.8 | 0.239 | 1.030 | 0.256 | 3.5 | 0.249 | 1.008 | 0.254 | 1.1 | 0.257 | 0.992 | 0.251 | 1.3 |
| 38 | 0.274 | 1.033 | 0.288 | 2.5 | 0.283 | 1.011 | 0.290 | 1.3 | 0.296 | 0.985 | 0.284 | 2.3 | 0.306 | 0.967 | 0.279 | 5.9 |
| 40 | 0.303 | 1.020 | 0.313 | 1.6 | 0.313 | 0.998 | 0.312 | 0.3 | 0.329 | 0.970 | 0.304 | 4.6 | 0.341 | 0.951 | 0.296 | 9.0 |
| 45 | 0.379 | 0.990 | 0.374 | 0.8 | 0.393 | 0.966 | 0.364 | 4.2 | 0.414 | 0.934 | 0.349 | 10.4 | 0.429 | 0.914 | 0.337 | 16.5 |
| 50 | 0.458 | 0.961 | 0.432 | 3.1 | 0.474 | 0.935 | 0.412 | 8.1 | 0.500 | 0.902 | 0.389 | 16.0 | 0.519 | 0.882 | 0.372 | 23.7 |
| 55 | 0.537 | 0.933 | 0.485 | 5.5 | 0.556 | 0.907 | 0.454 | 12.0 | 0.586 | 0.874 | 0.424 | 21.3 | 0.606 | 0.853 | 0.402 | 30.5 |
| 60 | 0.615 | 0.906 | 0.534 | 7.8 | 0.636 | 0.881 | 0.491 | 15.8 | 0.668 | 0.848 | 0.453 | 26.4 | 0.690 | 0.828 | 0.428 | 36.8 |

## 5.6 Conclusion

Six years of disdrometer data calculating rainfall rate and attenuation were examined. Frequencies between 30 GHz and 45 GHz have been identified to have the most linear relationship between attenuation and rainfall rate. The attenuation-rainfall relationship determined by the fit at 38 GHz (a common link frequency in the UK) and 40 mm $hr^{-1}$ has one of lowest errors in attenuation up to a maximum rainfall rate of 50 mm $hr^{-1}$. In the UK over 99.99% of rainfall is included up to 40 mm $hr^{-1}$. The use of 38 GHz within the UK could be an ideal choice for using link measurements to infer rainfall rates.

The frequency band where the power-law fit parameter $b$ is equal to one indicates that the power-fit estimate predicts a linear $A$-$R$ relationship, for this range of frequencies. This is the area of best agreement between the fits, in terms of PVAF and attenuation. It has been shown that a linear fit at 33 GHz (vertically polarised) has the highest PVAF and is consistently so over 5-100 mm $hr^{-1}$. For horizontal polarisation 35 GHz has the highest PVAF. However, other nearby frequencies such as 38 GHz for vertical and horizontal polarisation have extremely similar PVAF and can also be used to estimate rainfall rate.

# Chapter 6

# Radar derived rain cell analysis

This chapter studies the horizontal structure of rain cells in the UK. Rainfall was measured using radars covering the UK. The rain cell structures were analysed with the use of two analytical models, the EXCELL and HYCELL models, which were fitted to each rain cell. A comparison was made between raindrop size distribution parameters and the characteristics of rain cells in order to determine if any relationship exists.

## 6.1 Introduction

The UK Met Office C-band rainfall radars were used to measure rainfall rate over the UK from 2004-2008. Rainfall rate data was determined by the Nimrod system, a fully automated system for weather analysis and nowcasting based around the Met Office network of C-band rainfall radars. The rainfall rate data was used to determine rain cells, which were defined by a rainfall rate threshold ($R_2$), as discussed in Chapter 2. The radar data has a spatial resolution of $1\,\mathrm{km} \times 1\,\mathrm{km}$. Figure 6.1 shows an example of surface rainfall rate derived from the UK Met Office radars. This work investigates the statistics of rain cells in the UK by studying the shape, area and sensitivity to rainfall rate. The EXCELL and HYCELL models have been fitted to every rain cell measured by the radar data over areas of $5\,\mathrm{km}^2$. A comparison has been made between the two models in order to determine the advantages and disadvantages of using each model.

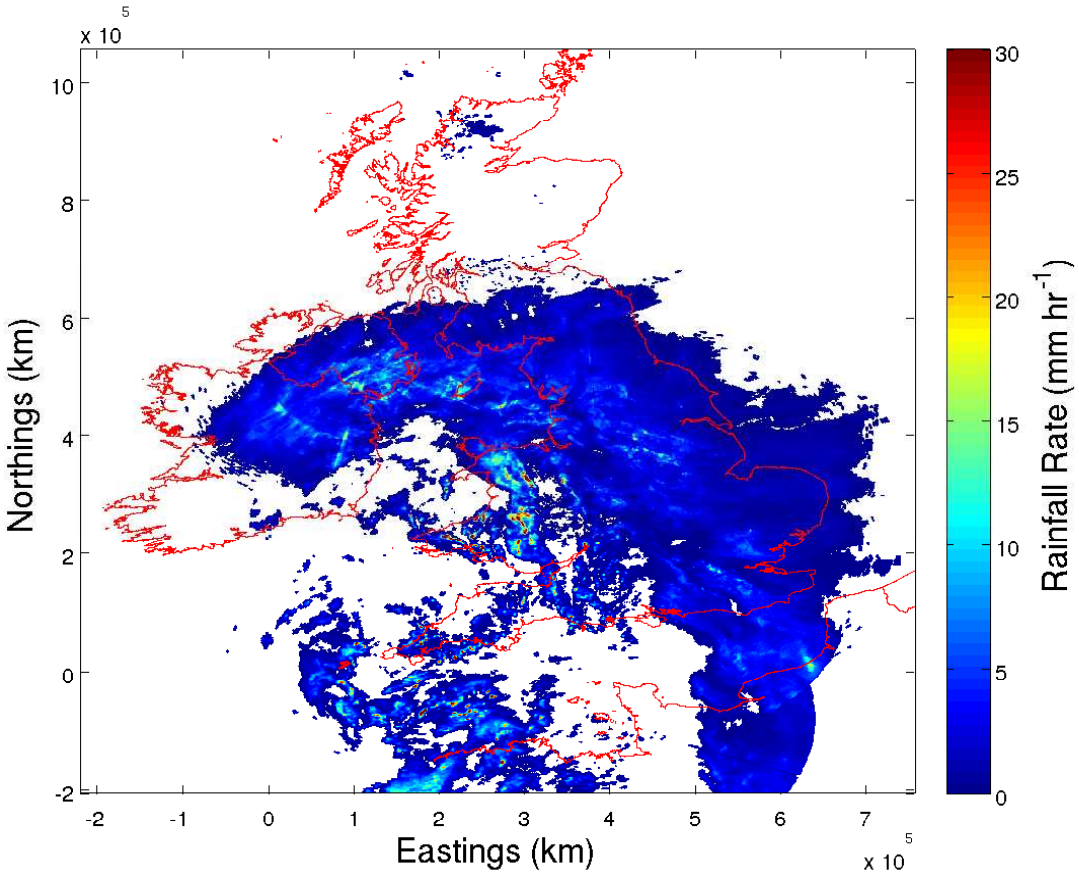


Figure 6.1: Example surface rainfall rate derived from the UK Met Office radar data showing an unusually high volume of rain on the 05/09/2008 12:35.

## 6.2 Rainfall rate data analysis

### 6.2.1 EXCELL model

The EXCELL model, Capsoni et al. [1987], analytically represents a rain cell as an exponential shape. The model assumes rainfall rate decays exponentially from a single peak rainfall rate. Figure 6.2 shows an example of the EXCELL model where the rainfall rate exponentially decays from the peak rainfall rate. There are two forms of the EXCELL model, a monoaxial model, where the cell is assumed round, and a biaxial model, where the model is assumed elliptical. The analytical expression for the biaxial EXCELL model of horizontal rainfall rate distribution within a cell is given by:

$$R(x,y) = R_M \exp\left[-\left(\frac{x^2}{\rho_x^2} + \frac{y^2}{\rho_y^2}\right)^{1/2}\right] R \geq R_2, \tag{6.1}$$

where $R_M$ is the peak rain rate, $R_2$ is the rainfall rate threshold defining the rain cell, $R(x,y)$ is the rainfall rate at coordinates $x$ and $y$, and $\rho_x$ and $\rho_y$ are the cell radii (distances along the respective axes for which the rain rate decreases by a factor of $1/e$). In this work the biaxial/elliptical shape rain cell is used. The peak rainfall rate is averaged over a 1 km grid space to match the peak rainfall rate measured by the radar on a 1 km resolution.

An automatic contouring procedure was used to determine each rain cell at 5 mm hr$^{-1}$ rainfall rates and above. In order to fit the model to the measured rain cells a series of fit-forcing equations were solved to determine parameters $R_M$, $\rho_x$ and $\rho_y$, Capsoni et al. [1987]. Measure cell area ($A_r$) and average rainfall rate ($\overline{R}$) were determined by:

$$A_r = \int_{\text{Cell}} dxdy, \tag{6.2}$$

$$\overline{R} = \frac{1}{A}\int_{\text{Cell}} R(x,y)dxdy. \tag{6.3}$$

The minimum cell area was restricted to 5 km$^2$ as areas smaller would introduce quantization error. EXCELL model area and average rainfall rate are defined as follows:

$$A_r = \pi\rho_x\rho_y \ln^2\left(\frac{R_M}{R_2}\right), \tag{6.4}$$

$$\overline{R} = 2R_M\left[1 - \left(\frac{R_2}{R_M}\right)\left(1 + \ln\frac{R_M}{R_2}\right)\right] / \ln^2\left(\frac{R_M}{R_2}\right). \tag{6.5}$$

Following the method outlined by Capsoni et al. [1987], $R_M$ was solved numerically from (6.5). The parameters $\rho_x$ and $\rho_y$ were determined from model cell area and the central moments of inertia. To calculate the moments of inertia the cell barycentre has

to be calculated. The cell barycentre point coordinates, $x_0$ and $y_0$ are given by:

$$x_0 = \frac{1}{Q_c}\int_{\text{Cell}} xR(x,y)dxdy, \tag{6.6}$$

$$y_0 = \frac{1}{Q_c}\int_{\text{Cell}} yR(x,y)dxdy, \tag{6.7}$$

where $Q_c$ is the cumulative rainfall rate given by $Q_c = A_r\overline{R}$. The central moments of inertia are given as follows:

$$I_x = \int_{\text{Cell}} (x-x_0)^2 R(x,y)dxdy, \tag{6.8}$$

$$I_y = \int_{\text{Cell}} (y-y_0)^2 R(x,y)dxdy. \tag{6.9}$$

The "gyration radii" of the cell, $\rho_{min}$ and $\rho_{max}$ are defined as

$$\rho_{max}^2 Q_c = I_{max}, \tag{6.10}$$

$$\rho_{min}^2 Q_c = I_{min}, \tag{6.11}$$

where $I_{max}$ and $I_{min}$ are defined by the maximum and minimum of (6.8) and (6.9) respectively. Given that $\rho_0^2 = \rho_x\rho_y$ and cell ellipticity is $\rho_x/\rho_y = \rho_{min}/\rho_{max}$, $\rho_x$ and $\rho_y$

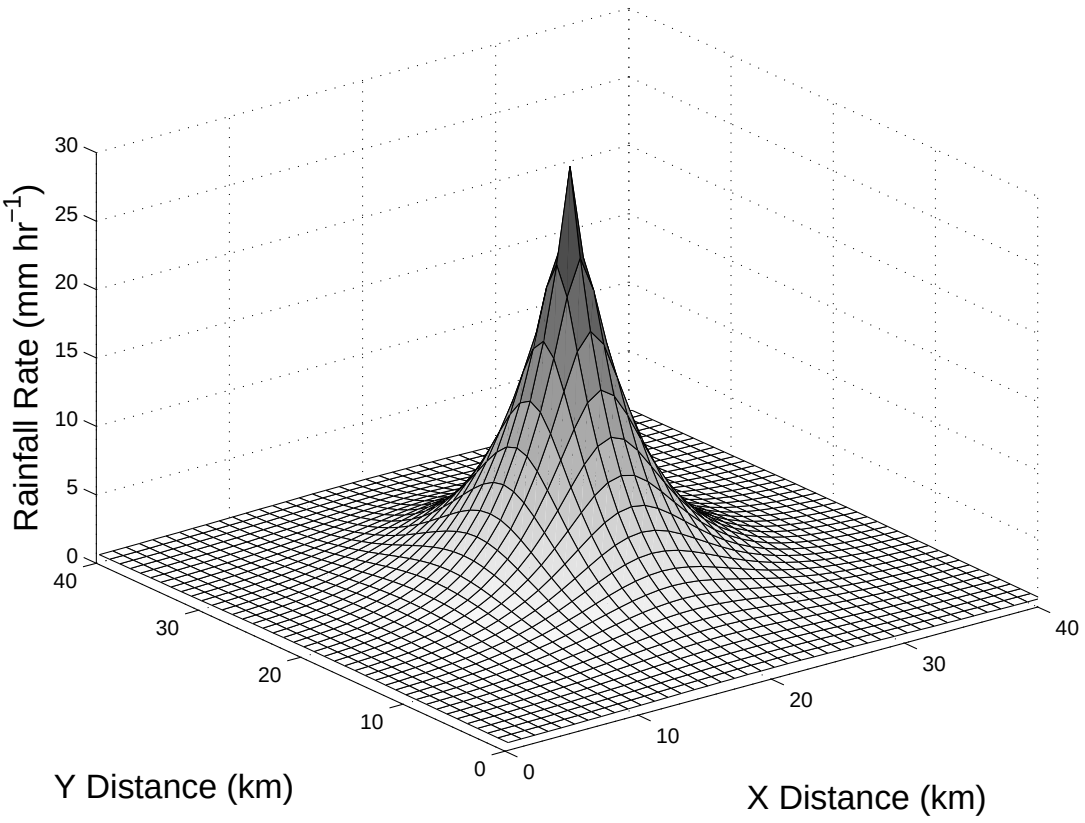


Figure 6.2: Example EXCELL rain cell model.

can be determined with some rearrangement.

### 6.2.2 HYCELL model

The HYCELL model describes the horizontal rainfall rate distribution as a combination of an exponential and Gaussian shape. Above a determined rainfall rate threshold ($R_1$) the model is Gaussian and below $R_1$ the model decays exponentially. Figure 6.3 shows an example of the HYCELL model. The HYCELL model was fitted to each rain cell identified using a series of fit forcing equations. The analytical expression for the HYCELL model is given by:

$$\begin{aligned} R(x,y) &= R_G \exp\left[-\left(\frac{x^2}{a_G^2}+\frac{y^2}{b_G^2}\right)\right] && \text{if } R \geq R_1, \\ &= R_E \exp\left[-\left(\frac{x^2}{a_E^2}+\frac{y^2}{b_E^2}\right)^{1/2}\right] && \text{if } R_2 \leq R < R_1, \end{aligned} \tag{6.12}$$

where $R_G$ is peak rainfall rate of the Gaussian component, and $a_G$ and $b_G$ are distances along the $x$ and $y$ axes where the rainfall rate decreases by a factor of $1/e$ of the Gaussian component. $R_E$, $a_E$ and $b_E$ are defined equivalently for the exponential component. $R_1$ is the rainfall rate that separates the Gaussian and exponential components.

The HYCELL model uses a set of force-fitting equations that are solved to determine the seven parameters of the model. The fit forcing equations were solved using the measured cell area, mean rainfall rate, RMS rainfall rate, mean horizontal gradient ($\overline{G}$) and RMS horizontal gradient ($G_{\text{rms}}$). Mean horizontal gradient is given by:

$$\overline{G} = \frac{1}{A_r}\int_{\text{Cell}} G(x,y)dxdy, \tag{6.13}$$

where $G(x,y)$ is the horizontal gradient at coordinates $x$ and $y$. The root mean squared gradient is given by:

$$\overline{G}^2_{\text{rms}} = \frac{1}{A_r}\int_{\text{Cell}} G^2(x,y)dxdy, \tag{6.14}$$

The radar measured rain cells were rotated to calculate horizontal gradient. The angle of rotation is given by the following, Féral et al. [2000]:

$$\theta = \frac{1}{2}\tan^{-1}\left(\frac{2I_{xy}}{I_y - I_x}\right), \tag{6.15}$$

where $I_{xy}$ is the moment of inertia in the barycentre reference, as defined below:

$$I_{xy} = \int_{\text{Cell}} (x - x_0)(y - y_0) R(x, y) dx dy. \tag{6.16}$$

The following equations give the HYCELL model average rainfall rate, root mean square rainfall rate, average horizontal gradient and root mean squared gradient, as determined in Féral et al. [2003a]. Parameters $R_G$, $R_1$ and $R_E$ may be calculated by

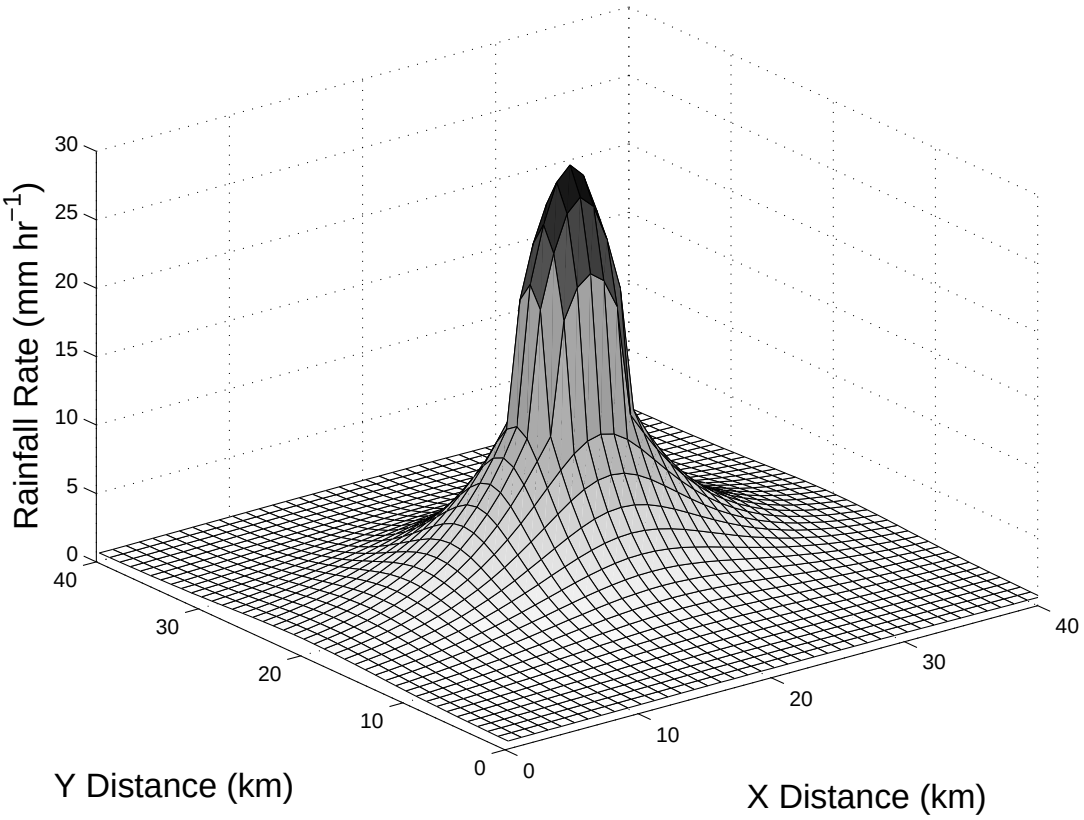


Figure 6.3: Example HYCELL rain cell model.

solving equations (6.17)-(6.20).

$$\overline{R} = \ln^{-2}\left(\frac{R_E}{R_2}\right)\left[\ln^2\left(\frac{R_E}{R_1}\right)\ln^{-1}\left(\frac{R_G}{R_1}\right)\cdot(R_G - R_1) + 2R_1\left(1+\ln\left(\frac{R_E}{R_1}\right)\right) - 2R_2\left(1+\ln\left(\frac{R_E}{R_2}\right)\right)\right], \tag{6.17}$$

$$2\left(R_{\mathrm{rms}}^2\right) = \ln^{-2}\left(\frac{R_E}{R_2}\right)\left[\ln^{-1}\left(\frac{R_G}{R_1}\right)\ln^2\left(\frac{R_E}{R_1}\right)\cdot\left(R_G^2 - R_1^2\right) + R_1^2\left(1+2\ln\left(\frac{R_E}{R_2}\right)\right) - R_2^2\left(1+2\ln\left(\frac{R_E}{R_2}\right)\right)\right], \tag{6.18}$$

$$\overline{G} = \frac{4E\left[(\pi/2),\left(1-e_r^2\right)^{1/2}\right]}{(A\pi e_r)^{1/2}\ln(R_E/R_2)}\left[R_G\frac{\pi^{1/2}}{2}\mathrm{erf}\left(\ln^{1/2}\frac{R_G}{R_1}\right)\cdot\ln\frac{R_E}{R_1}\ln^{-1/2}\frac{R_G}{R_1} + R_1 - R_2\left(1+\ln\frac{R_E}{R_2}\right)\right], \tag{6.19}$$

$$A_r\left(G_{\mathrm{rms}}^2\right) = \frac{\pi}{2}\left(e_r + \frac{1}{e_r}\right)\left[R_G^2 - R_1^2\left(1+2\ln\frac{R_G}{R_1}\right) + \frac{R_1^2}{2}\left(1+2\ln\frac{R_E}{R_1}\right) - \frac{R_2^2}{2}\left(1+2\ln\frac{R_E}{R_2}\right)\right], \tag{6.20}$$

where $E$ is the elliptic function of the second kind and erf is the error function. Let $\overline{R}_r$ be the radar-measured average rainfall rate and let $\overline{R}_H$ be the HYCELL average rainfall rate then, following the method of Féral et al. [2003a] to solve equations (6.17)-(6.20), the minimisation function (6.21) was used:

$$\epsilon = \left|\frac{\overline{R_H}}{\overline{R_r}} - 1\right| + \left|\frac{(R_{\mathrm{rms}})_H}{(R_{\mathrm{rms}})_r} - 1\right| + \left|\frac{\overline{G_H}}{\overline{G_r}} - 1\right| + \left|\frac{(G_{\mathrm{rms}})_H}{(G_{\mathrm{rms}})_r} - 1\right|. \tag{6.21}$$

Once $R_G$, $R_1$ and $R_E$ have been solved by minimising (6.21), the remaining four parameters, $a_G$, $b_G$, $a_E$ and $b_E$ are solved by substituting calculated values into the following:

$$b_E^2 = \frac{A_r}{\pi e_r \ln^2(R_E/R_2)}, a_E = e_r b_E, \tag{6.22}$$

$$b_G^2 = \frac{b_E^2\ln^2(R_E/R_1)}{\ln(R_G/R_1)}, a_G = e_r b_G. \tag{6.23}$$

## 6.3 Results

The rainfall rate threshold defining the boundary of a rain cell, $R_2$, was chosen to be $5\,\mathrm{mm\,hr^{-1}}$ in order to be comparable with the work of Capsoni et al. [1987] and reduce computational time. Choosing a boundary of $5\,\mathrm{mm\,hr^{-1}}$ will result in some bias as rain cells smaller than the threshold will be ignored. However, due to the sensitivity of the radar systems, rainfall rates such as $1\,\mathrm{mm\,hr^{-1}}$ may not be detected at ranges greater than 75 km from the radar, Kitchen and Jackson [1993]. Therefore, a larger rainfall rate threshold was chosen as higher rainfall rates are more easily detected. The rain cell data was filtered to remove rain cells with areas less than $5\,\mathrm{km^2}$ and peak rainfall rates less than $6\,\mathrm{mm\,hr^{-1}}$ to avoid quantisation errors. The peak rainfall rates of the EXCELL and HYCELL models were averaged over a 1 km area to match the resolution of peak radar rainfall rate. It is important to note that data from April 2004 until June 2005 only covers part of the UK, excluding Scotland. From June 2005 the number of UK rainfall radars increased covering the whole of the UK.

Figure 6.4 shows an example rain cell derived from radar data (top), fitted EXCELL model to radar data (middle) and fitted HYCELL model to radar data (bottom). The figure clearly illustrates that both the EXCELL and HYCELL models are good approximations of the original radar-derived rain cell. Table 6.1 includes numeric details of how well the rain cells compare with regards area, rainfall rate and gradient of the cell. In this example the EXCELL model better estimates peak rainfall rate, RMS rainfall rate, horizontal gradient and RMS horizontal gradient. The HYCELL model better approximates area and mean rainfall rate.

Cell area, rain rate and horizontal gradient have been compared to determine how well each model represents the radar-derived rain cells. The analysis begins with the comparison of peak rainfall rate of the EXCELL, HYCELL and radar-derived data.

### 6.3.1 Peak rainfall rate

Peak rainfall rates for the EXCELL and HYCELL models were averaged over $1\,\mathrm{mm\,hr^{-1}}$ intervals of measured peak rainfall rate from 0-100 $\mathrm{mm\,hr^{-1}}$. Figure 6.5(a) shows the

Table 6.1: Rain cell parameters $A$, $R_{\max}$, $\overline{R}$, $R_{\mathrm{rms}}$, $G_r$ and $G_{\mathrm{rms}}$.

| Cell | $A$ | $R_{\max}$ | $\overline{R}$ | $R_{\mathrm{rms}}$ | $\overline{G}$ | $G_{\mathrm{rms}}$ |
|---|---|---|---|---|---|---|
| Radar | 162 | 15.344 | 7.908 | 8.179 | 2.702 | 2.842 |
| Excell | 161 | 16.156 | 7.928 | 8.320 | 2.017 | 2.190 |
| Hycell | 162 | 24.855 | 7.908 | 8.655 | 1.136 | 1.794 |

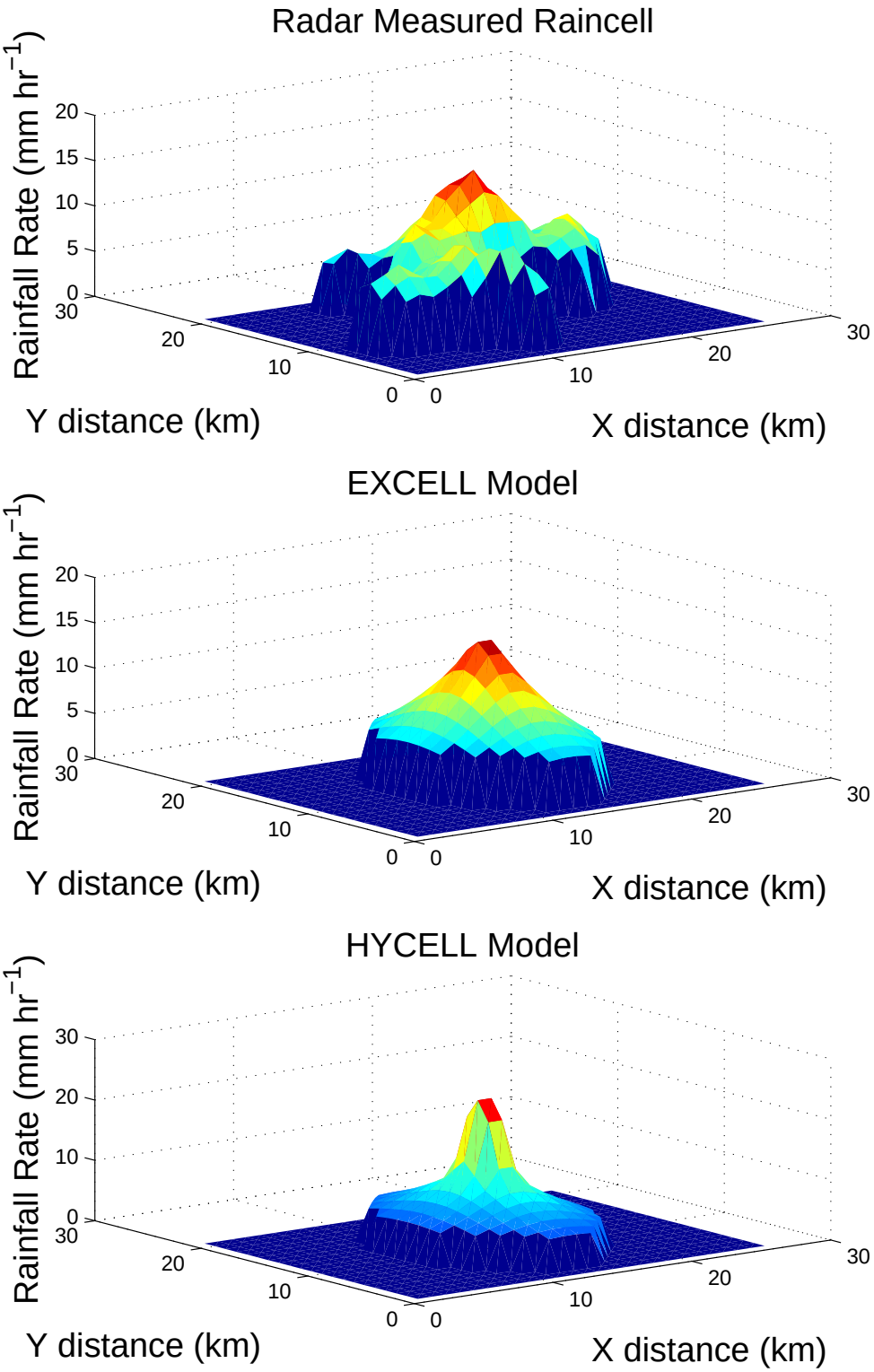


Figure 6.4: Example radar-derived rain cell (top), EXCELL model (middle) and HYCELL model (bottom) for rain cell measured on 07/07/2004.

mean and standard deviation of the peak rainfall rate, where the diagonal dotted line shows the ideal one to one ratio between peak rainfall rates. For rainfall rates up to $20\,\mathrm{mm\,hr^{-1}}$, $R_M$ is almost equal to the radar-estimated peak rainfall rate. Above $20\,\mathrm{mm\,hr^{-1}}$, $R_M$ increasingly overestimates the radar-derived peak rainfall rate. Over $40\,\mathrm{mm\,hr^{-1}}$ the HYCELL model increasingly underestimates mean peak rainfall rate and the standard deviation increases. Model peak rainfall rate becomes more variable and difficult to estimate as rain cell peak rainfall rate increases, which could be a result of multiple peaks.

Figure 6.5(b) shows peak rainfall rates separated into rain cells measured over land and sea. The results show that when estimating peak rainfall rate using the HYCELL or EXCELL, model discrimination between land and sea rain cells makes very little difference. In the case of the EXCELL model rain cells over sea approximate peak rainfall rates higher than rain cells over land. The HYCELL is opposite, where land cells are approximated higher. However, the difference in land and sea cells is minimal and holds little significance.

### 6.3.2 Mean rainfall rate

Mean rainfall rate for each model has been averaged over $1\,\mathrm{mm\,hr^{-1}}$ intervals of measured mean rainfall rate, Figure 6.5(c). Mean rainfall rate is approximated well by both models. Above $10\,\mathrm{mm\,hr^{-1}}$, which accounts for few rain cells, the models begin to overestimate (in the case of EXCELL) and underestimate (in the case of HYCELL). As mean rainfall rate increases, the standard deviation increases, which could be a result of magnification (due to larger mean rainfall rate) of variability in the cell shape (i.e. cells with small areas and large peaks could have the same mean rainfall rate as cells with large areas and smaller peaks). Figure 6.5(d) separates the results into rain cells over land and sea where the difference shows negligible effect.

### 6.3.3 RMS rainfall rate

Figure 6.5(e) shows the root mean square (RMS) rainfall rate, which has been averaged over $1\,\mathrm{mm\,hr^{-1}}$ intervals of measured RMS rainfall rate. The comparison shows good approximate agreement between the model rain cells and the measured rain cells. The EXCELL is shown to overestimate the RMS more than the HYCELL underestimates the RMS. The EXCELL has a higher standard deviation implying the EXCELL model does not estimate the RMS rainfall rate as accurately as the HYCELL model in the UK. Rain cells over land or sea have little effect on models cells estimating RMS rainfall

rate. Above 25 mm hr$^{-1}$ EXCELL model cells over sea increasingly overestimate RMS where the HYCELL model increasingly underestimates.

### 6.3.4 Mean gradient of rainfall rate

The average of the mean gradient has been determined for the EXCELL and HYCELL models over intervals of 1 mm hr$^{-1}$ km$^{-1}$ of cell mean gradient, and the results are shown in Figure 6.6(a). The EXCELL model almost matches the measured cell on a one to one basis. The HYCELL underestimates the mean gradient by a significant margin. The results show rain cells in the UK are approximated well by an exponential decay in rainfall rate from a cell peak. The gradient is not approximated well by a combination of Gaussian and exponential shapes. The rain cell location has very little effect on model estimation of mean gradient, as evident from Figure 6.6(b).

### 6.3.5 RMS gradient of rainfall rate

The RMS gradients for the EXCELL and HYCELL model have been averaged over 1 mm hr$^{-1}$ km$^{-1}$ intervals of radar estimated RMS gradient, Figure 6.6(c). The HYCELL and EXCELL models are in reasonable agreement with the measured rain cells. The EXCELL model overestimates and the HYCELL underestimates as the RMS gradient increases. The estimate of RMS gradient is not significantly affected by the difference of a land- and sea-based rain cell, as demonstrated by the results in Figure 6.6(d).

### 6.3.6 Cumulative distribution function

#### RMS rainfall rate

The cumulative distribution function of radar-derived RMS rainfall rate for land, sea and combined data, EXCELL and HYCELL models have been calculated. Figure 6.7(a) shows the EXCELL model estimates that a larger proportion of rain cells have higher RMS rainfall rates when compared to the radar-derived data. The HYCELL is in close approximation to the radar-derived data. The differentiation of the land- and sea-based rain cells show no significant difference in RMS rainfall rate.

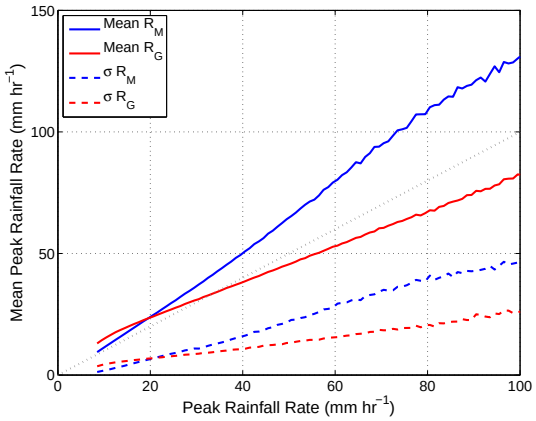


(a) Average peak rainfall rate averaged over 1 mm hr$^{-1}$ intervals of peak radar rainfall rate.

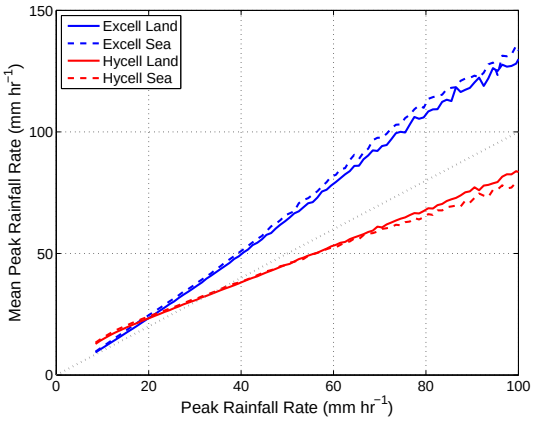


(b) Average mean rainfall rate averaged over 1 mm hr$^{-1}$ intervals of mean radar rainfall rate for cells over land and sea.

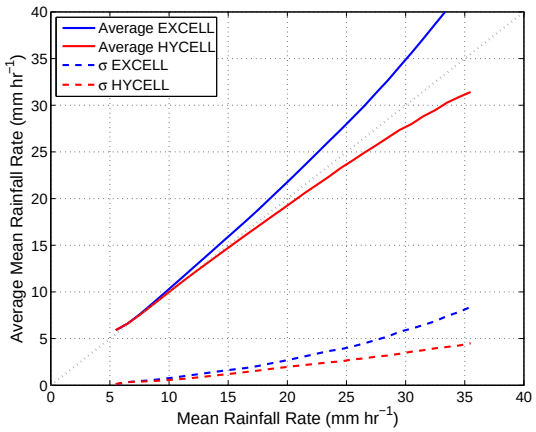


(c) Average mean rainfall rate averaged over 1 mm hr$^{-1}$ intervals of mean radar rainfall rate.

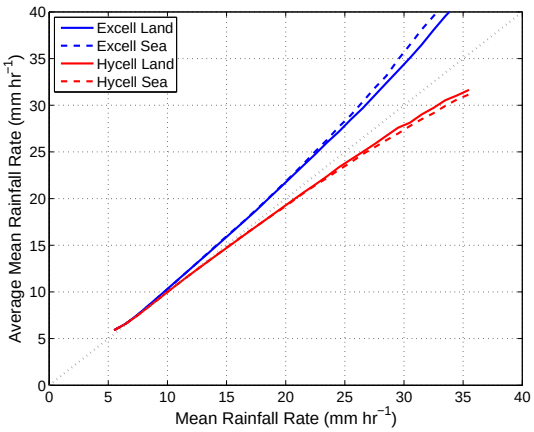


(d) Average mean rainfall rate averaged over 1 mm hr$^{-1}$ intervals of mean radar rainfall rate for cells over land and sea.

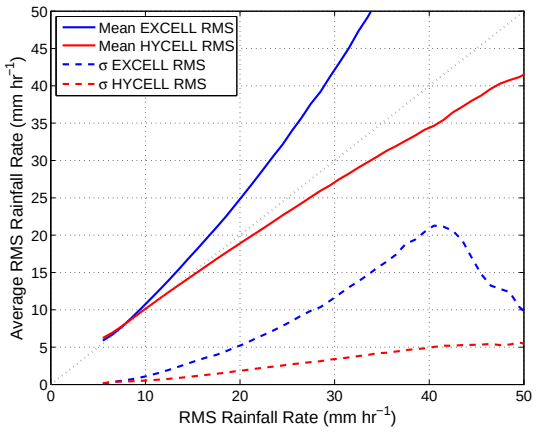


(e) Average RMS rainfall rate averaged over 1 mm hr$^{-1}$ intervals of RMS radar rainfall rate.

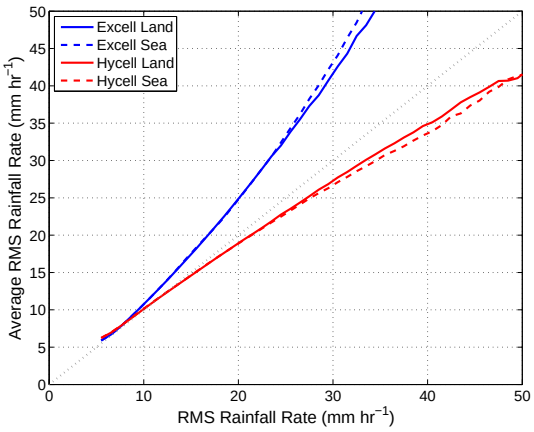


(f) Average RMS of rainfall rate averaged over 1 mm hr$^{-2}$ intervals of RMS gradient of radar rainfall rate for cells over land and sea.

Figure 6.5: Average peak, mean and RMS rainfall rates for EXCELL and HYCELL models compared to radar-derived data.

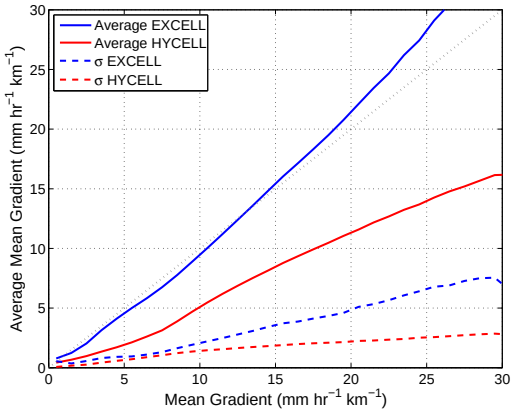


(a) Average mean gradient of rainfall rate averaged over 1 mm hr$^{-2}$ intervals of mean gradient of radar rainfall rate.

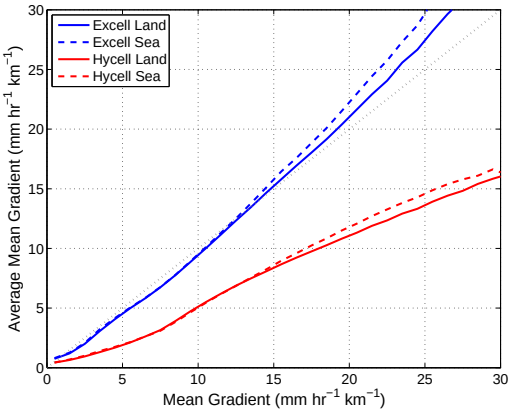


(b) Average mean gradient of rainfall rate averaged over 1 mm hr$^{-2}$ intervals of mean gradient of radar rainfall rate for cells over land and sea.

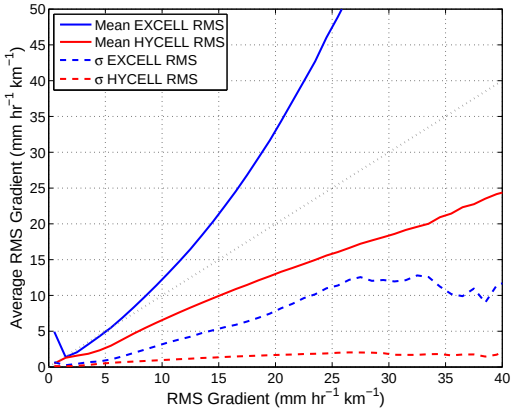


(c) Average RMS gradient of rainfall rate averaged over 1 mm hr$^{-2}$ intervals of RMS gradient of radar rainfall rate.

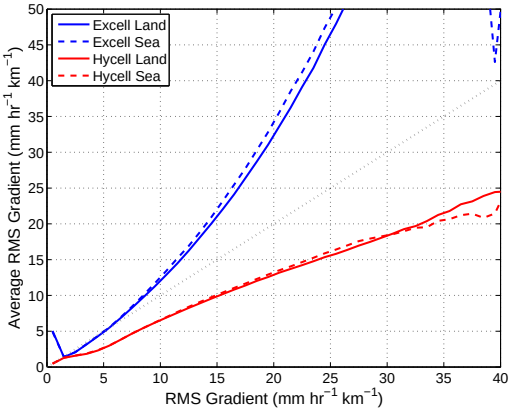


(d) Average RMS gradient of rainfall rate averaged over 1 mm hr$^{-2}$ intervals of RMS gradient of radar rainfall rate over land and sea.

Figure 6.6: Average peak, mean and RMS rainfall rates for EXCELL and HYCELL models compared to radar-derived data.

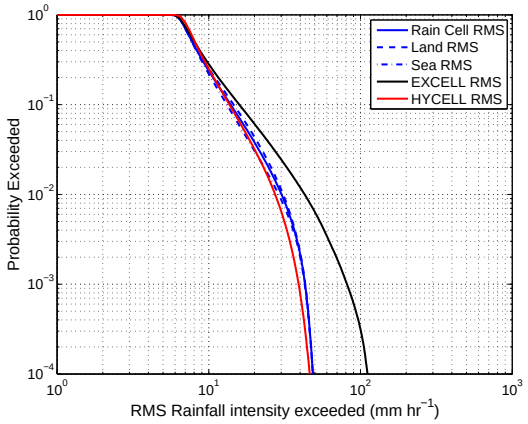


(a) CDF of RMS rainfall rate.

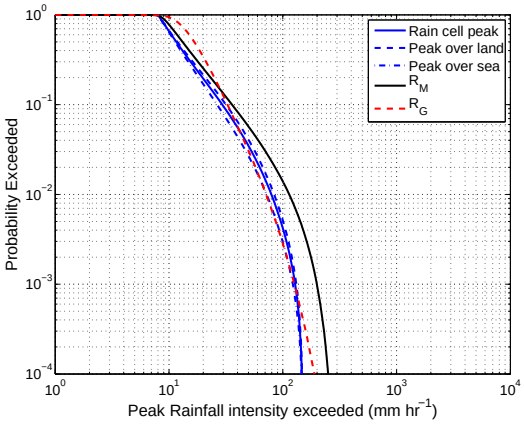


(b) CDF of Peak rainfall rate.

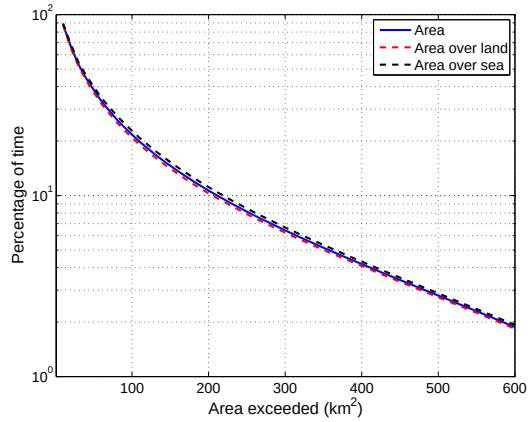


(c) CDF of area.

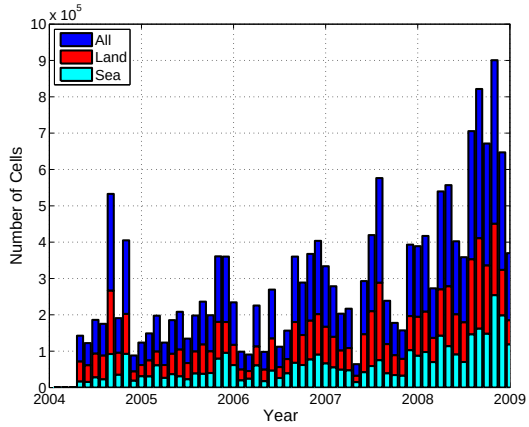


(d) Total number of rain cells recorded each month from April 2004 to December 2008.

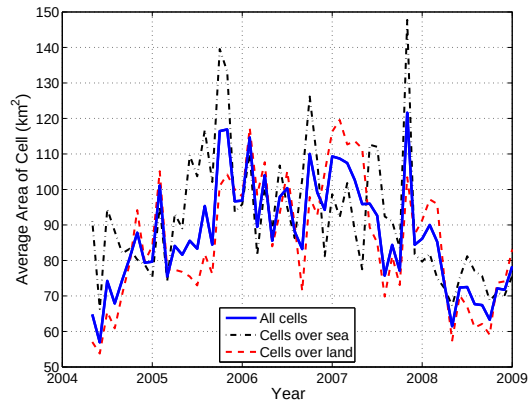


(e) Mean area of all, land and sea rain cells plotted over time of year.

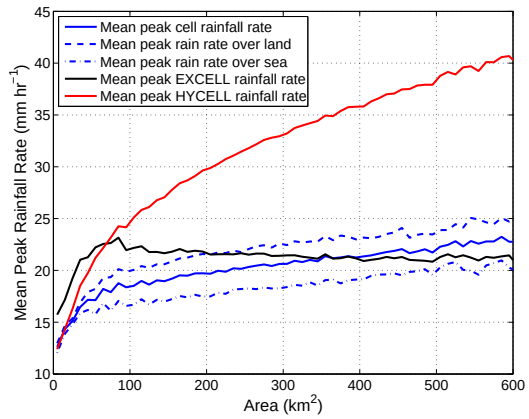


(f) Average peak rainfall rate determined over area intervals of 10 km$^2$ for model and all radar cells (including separation of land- and sea-based cells).

Figure 6.7: UK rain cell characteristics including CDFs of RMS rainfall rate, peak rainfall rate and area, number of cells, average area of rain cells and a comparison of peak rainfall rate with area.

#### Peak rainfall rate

Figure 6.7(b) shows the cumulative distribution for peak rainfall rates. The EXCELL model estimates a larger percentage of rain cells have higher peak rainfall rates in comparison to the HYCELL and radar-derived data. The HYCELL follows the trends of the radar-derived data over a larger range of rainfall rates when compared to the EXCELL model. However, below $30\,\mathrm{mm\,hr^{-1}}$, the EXCELL model is a closer approximation to the probability of exceedance of the radar-derived data in comparison to the HYCELL model. The close approximation below $30\,\mathrm{mm\,hr^{-1}}$ is particularly important as this accounts for the majority of rain cells. The results show no significant difference between peak rainfall rates of cells over land and sea.

#### CDF of area

The cumulative distribution function of area has been determined for land, sea and all radar-derived rain cells, Figure 6.7(c). The majority of rain cells have a total area between 5-150 $\mathrm{km^2}$, with very few rain cells above $200\,\mathrm{km^2}$. The area of the EXCELL and HYCELL models are an almost exact match and hence therefore been omitted for clarity. The CDFs of area between land and sea cells show very little difference.

### 6.3.7 Number and area of rain cells

The number of cells measured per month is shown in Figure 6.7(d). The number of rain cells increases at the end of summer and autumn. There is little increase in the number of rain cells from June 2005, when the radar coverage area was increased. For 2005 up to and including 2007, there are fewer rain cells in January and February. From 2004, 46% of the radar coverage was over land, and from June 2005 this decreased to 21%. Despite this decrease there are fewer rain cells measured over sea than land. The separated land and sea rain cell count follows the trends of the total number of cells.

The average cell area was determined each month from 2004 to the end of 2008, shown in Figure 6.7(e). The average is in the range 60 to $120\,\mathrm{km^2}$. The average area varies considerably over the 5 years of data. However, there is a general trend between the number of cells and the average size. The average size of a rain cell generally increases with the number of cells, with the exception of 2008. The overall average area for all the data available is 83.87 $\mathrm{km^2}$.

### 6.3.8 Peak rainfall rate and area

The average peak rainfall rate has been determined for area in intervals of 10 $km^2$. Figure 6.7(f) shows the EXCELL model tends to overestimate the peak rainfall rate for smaller rain cells (below 100 $km^2$) but is better at approximating larger rain cells. Conversely, the HYCELL model closely approximates the radar peak rainfall rate with area for areas less than 30 $km^2$, which applies to approximately 50% of rain cells. However, above 30 $km^2$ HYCELL significantly overestimates peak rainfall rate.

The peak rainfall rate and area has been divided up for cells over land and rain. The results show that cells larger than 30 $km^2$ become discriminated by land and sea. On average, land based rain cells have a higher peak rainfall rate with increasing area compared to rain cells over sea.

### 6.3.9 Mean rainfall rate and area

Figure 6.8(a) shows the mean rainfall rate determined over 10 $km^2$ intervals. The analytical models are in good agreement with the radar-derived mean rainfall rate. However, below 20 $km^2$ the EXCELL model overestimates the mean rainfall rate. On average, the HYCELL combination of gamma and exponential components is better at approximating small rain cells. The results suggest that larger rain cells are more exponential in shape as both the HYCELL and EXCELL models are similar to the radar-estimated rain cell results.

The rain cells have been divided into cells based over land and sea. The average rainfall rate of cells over land is consistently higher than rain cells over sea for areas of 5-600 $km^2$.

### 6.3.10 Mean and peak rainfall rate

Average peak rainfall rate was determined over 1 $mm\,hr^{-1}$ intervals of mean rainfall rate, with results shown in Figure 6.8(b). Mean rainfall rate increases with average peak rainfall rate. The HYCELL and radar-derived mean-peak rainfall rate relationships are in good agreement, except at mean rainfall rates above 30 $mm\,hr^{-1}$ where the number of sample cells is very few. The EXCELL model is the best approximation to the radar-derived data for mean rainfall rates less than 10 $mm\,hr^{-1}$. The mean and peak rainfall rates are very similar to those of Capsoni et al. [1987]. The exponential cell

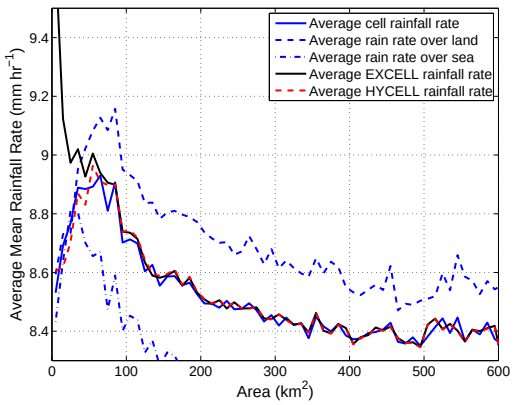


(a) Mean rainfall rate determined over area intervals of 10 km$^2$ for land, sea and all measured rain cells, the EXCELL and HYCELL models.

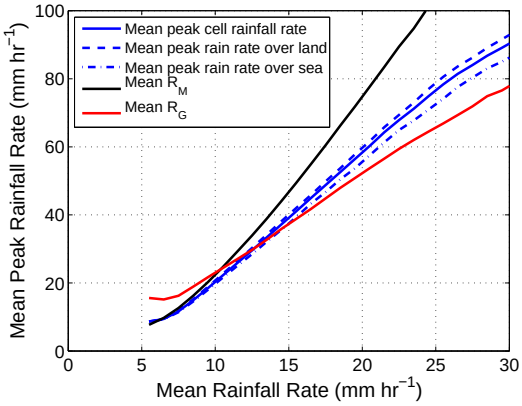


(b) Average peak rainfall rate determined over 1 mm hr$^{-1}$ intervals of mean rainfall rate.

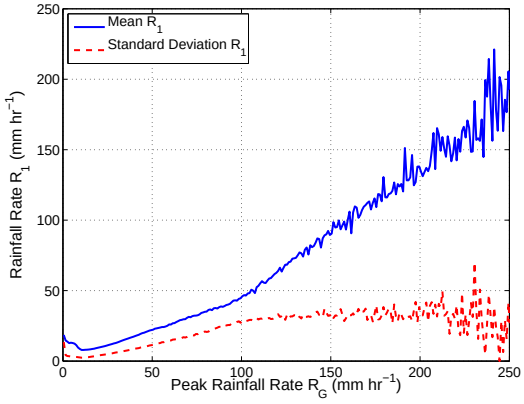


(c) Mean of $R_1$ determined over 1 mm hr$^{-1}$ intervals of peak rainfall rate, $R_G$.

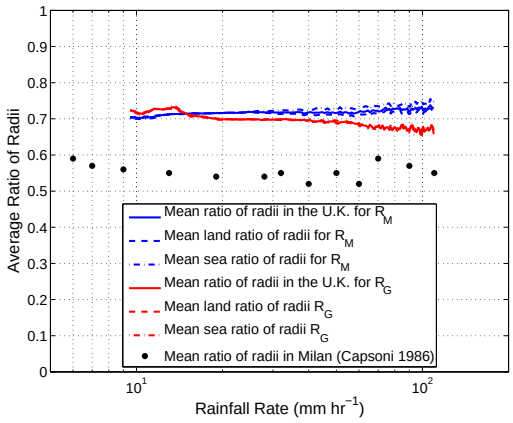


(d) Average axial ratio determined over peak rainfall rate intervals of 1 mm hr$^{-1}$ of $R_M$ and $R_G$.

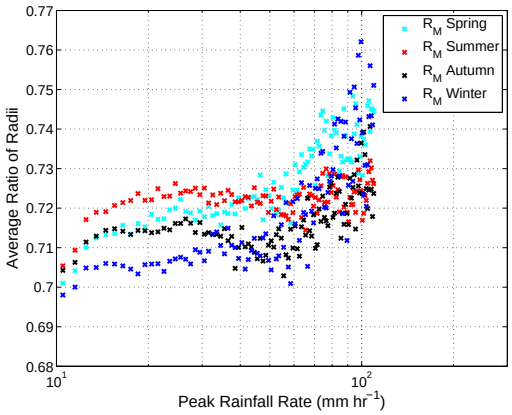


(e) Seasonal variation in average axial ratio determined over peak rainfall rate intervals of 1 mm hr$^{-1}$ of $R_M$.

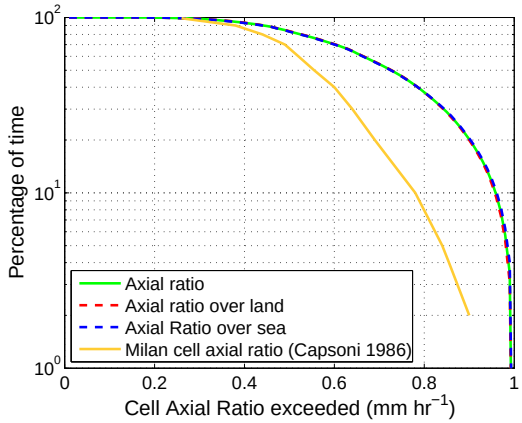


(f) Cumulative distribution function of elliptical ratio for all measured rain cells, land and sea based rain cells.

Figure 6.8: UK rain cell characteristics including mean rainfall rate and area comparison, peak rainfall rate and mean rainfall rate comparison, $R_1$ and $R_G$ comparison, peak rainfall rate and elliptical ratio comparison and CDF of elliptical ratio.

tends to over estimate peak rainfall rates, given mean rainfall rate, when compared to the radar-derived data. Capsoni et al. [1987] includes a comparison of Gaussian shaped cells, which demonstrated underestimation of peak rainfall rate to mean rainfall rate, which is similar to results here for the HYCELL model. Increase in peak rainfall rate with mean rainfall rate shows very little difference between land and sea rain cells.

### 6.3.11 $R_1$ and peak rainfall rate

The parameter $R_1$ determines the rainfall rate threshold where the HYCELL model changes between an exponential shape and Gaussian shape. The mean values of $R_1$ have been determined over $1\,\mathrm{mm\,hr^{-1}}$ intervals of peak rainfall rate $R_G$, as shown in Figure 6.8(c). The standard deviation has been included and shown by the second dashed line. High values of standard deviation show a strong variation in the horizontal structure of the rain cells. Above $100\,\mathrm{mm\,hr^{-1}}$ the gradient of the relationship between $R_1$ and $R_G$ increases, which differs slightly to Féral et al. [2003a]. Above $100\,\mathrm{mm\,hr^{-1}}$ the standard deviation remains at approximately $30\,\mathrm{mm\,hr^{-1}}$. However, the statistical significance of results above $50\,\mathrm{mm\,hr^{-1}}$ is small as the number of events occurring above $50\,\mathrm{mm\,hr^{-1}}$ is very low.

### 6.3.12 Cell radii and axial ratio

The EXCELL biaxial model requires two cell radii, $\rho_x$ and $\rho_y$. The average ratio of cell radius, $e_r$, was determined by $e_r = \rho_x/\rho_y$. The results in Figure 6.8(d) show the average axial ratio determined over peak rainfall rate intervals of $1\,\mathrm{mm\,hr^{-1}}$. The results of Capsoni et al. [1987] from Milan have been added for comparison. The mean has also been separated into rain cells for land and sea, which demonstrates that there is negligible difference between the land and sea cells when comparing mean peak rainfall rate with elliptical ratio.

The average ratio by Capsoni et al. [1987] has been determined to be 0.56. In the case of the results in the U.K. the average ratio of cell radius is 0.71. Therefore the cells in the U.K. are more round in shape in comparison to those measured in Milan. However, the mean elliptical ratio is dependent on the minimum area of the rain cells considered. Table 6.2 shows the average elliptical ratio for rain cells with minimum areas of $5\,\mathrm{km^2}$ to $75\,\mathrm{km^2}$. Once the minimum size has been increased the elliptical ratio averages around 0.68, where the rain cells are more elliptical. For rain cells around 5-15 $\mathrm{km^2}$ the resolution of the radar data may be too low to interpret the shape of the rain cells fully.

The results have also been divided up into seasons to determine if the shape of a cell has a link with the time of year, Figure 6.8(e). Therefore, the average axial ratio has been determined in the same manner, but for Spring (March, April, May), Summer (June, July, August), Autumn (September, October, November) and Winter (December, January, February). Winter has the lowest average axial ratio, therefore the cells are characteristically more elliptical during this period. The HYCELL model similarly has a lower elliptical ratio average for winter.

The cumulative distribution for the elliptical ratio is shown in Figure 6.8(f). The CDF shows that 60% of rain cells have an elliptical ratio less than 0.8. The CDF differs to that shown by Capsoni et al. [1987] in shape, however the minimum elliptical ratio is approximately the same at 0.3. The location of a rain cell (i.e. over land or sea) has no notable effect on the elliptical ratio.

The average ratio of $e_r$ has been investigated further by determining histograms of the ratio at selected $1\,\mathrm{mm\,hr^{-1}}$ intervals. Examples at 10-11 $\mathrm{mm\,hr^{-1}}$ and 20-21 $\mathrm{mm\,hr^{-1}}$ have been included in Figure 6.9. The two rainfall rates have been chosen as typical examples of the elliptical ratio histograms. The histograms show a large variance in the elliptical ratio, where a large number of almost circular rain cells exist. The EXCELL model mean elliptical ratio increases with maximum rainfall rate, where as the HYCELL model elliptical ratio decreases. The high variance in the elliptical ratio with peak rainfall rate demonstrates that rain cell structures cannot be determined by peak rainfall rate.

### 6.3.13 Model error

In order to determine the most suitable model to estimate rain cells in the UK, an error function has been devised. The error takes the mean difference between model parameters and the radar-derived cells for mean rainfall rate ($\epsilon_{\mathrm{mean}}$), RMS rainfall rate ($\epsilon_{\mathrm{RMS}}$), peak rainfall rate ($\epsilon_{\mathrm{peak}}$), mean horizontal gradient ($\epsilon_{G_r}$) and RMS gradient ($\epsilon_{G_{\mathrm{RMS}}}$). The error is normalised in terms of the radar-derived cell and given as a percentage.

$$E_R = [\epsilon_{\mathrm{mean}} + \epsilon_{\mathrm{RMS}} + \epsilon_{\mathrm{peak}} + \epsilon_{G_r} + \epsilon_{G_{\mathrm{RMS}}}] \cdot \frac{100}{5}, \tag{6.24}$$

Table 6.2: Mean Elliptical ratios of radar-derived rain cells.

| Minimum Area ($\mathrm{km^2}$) | 5 | 10 | 20 | 25 | 50 | 75 |
|---|---|---|---|---|---|---|
| Elliptical Ratio | 0.7093 | 0.7027 | 0.6923 | 0.6845 | 0.6765 | 0.6754 |

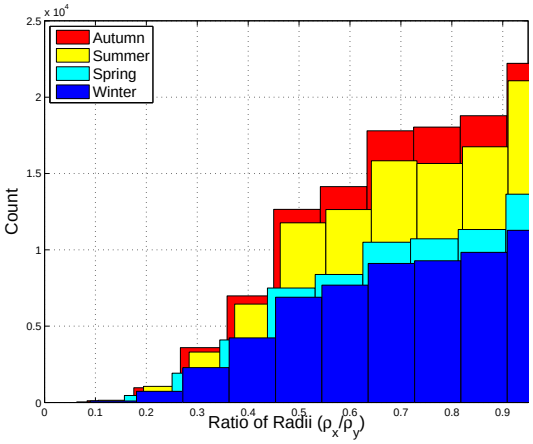


(a) Histogram of EXCELL Elliptical Ratio at $10\,\mathrm{mm\,hr^{-1}}$.

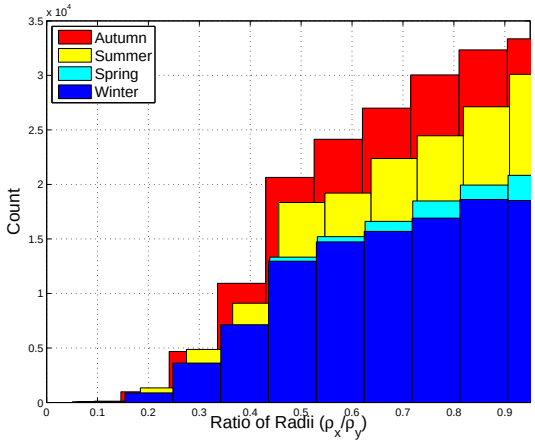


(b) Histogram of HYCELL Elliptical Ratio at $10\,\mathrm{mm\,hr^{-1}}$.

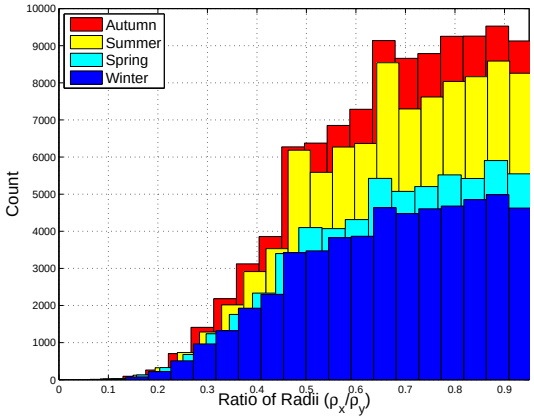


(c) Histogram of EXCELL Elliptical Ratio at $20\,\mathrm{mm\,hr^{-1}}$.

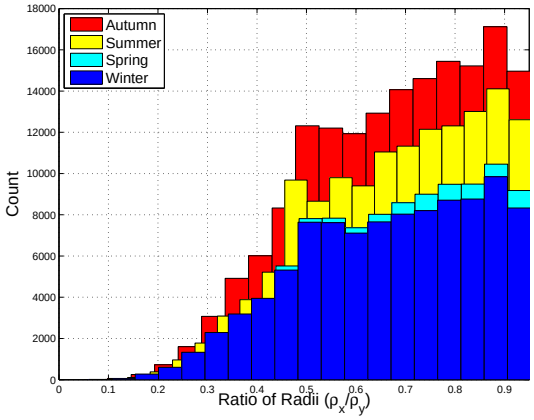


(d) Histogram of HYCELL Elliptical Ratio at $20\,\mathrm{mm\,hr^{-1}}$.

Figure 6.9: Histograms of elliptical ratio at $R_M = 10$ and $20\,\mathrm{mm\,hr^{-1}}$ and $R_G = 10$ and $20\,\mathrm{mm\,hr^{-1}}$.

where the errors are defined by.

$$\epsilon_{\text{mean}} = \left( \frac{\Sigma(\overline{R}_c - \overline{R}_r)/n}{\Sigma(\overline{R}_r)/n} \right), \tag{6.25}$$

$$\epsilon_{\text{RMS}} = \left( \frac{\Sigma(R_{\text{rmsc}} - R_{\text{rmsr}})/n}{\Sigma(R_{\text{rmsr}})/n} \right), \tag{6.26}$$

$$\epsilon_{\text{peak}} = \left( \frac{\Sigma(R_{\text{pc}} - R_{\text{pr}})/n}{\Sigma(R_{\text{pr}})/n} \right), \tag{6.27}$$

$$\epsilon_{G_r} = \left( \frac{\Sigma(\overline{G}_c - \overline{G}_r)/n}{\Sigma(\overline{G}_r)/n} \right), \tag{6.28}$$

$$\epsilon_{G_{\text{RMS}}} = \left( \frac{\Sigma(G_{\text{rmsc}} - G_{\text{rmsr}})/n}{\Sigma(G_{\text{rmsr}})/n} \right). \tag{6.29}$$

$$\tag{6.30}$$

The subscripts $c$ indicate analytical model parameters, and subscripts $r$ define radar-derived parameters.

Figure 6.10 shows the percentage difference between the model parameters and the radar-derived data. The EXCELL model has an overall lower percentage error in estimating the parameters of rain cells based in the UK.

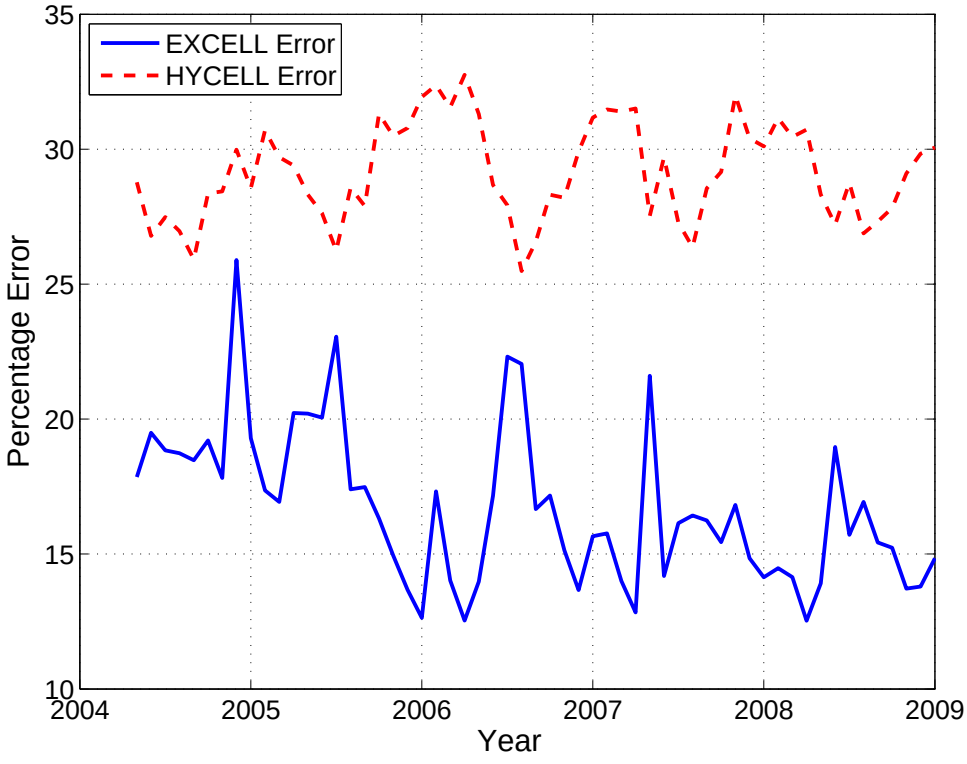


Figure 6.10: Percentage error between model and radar-derived parameters.

## 6.4 Raindrop size distribution comparison with rain cells

The raindrop size distribution parameters were compared with rain cell parameters to determine if a relationship existed to recreate the DSD. The rain cell parameters elliptical ratio, area, mean cell gradient, peak rainfall rate, mean cell rainfall rate and RMS rainfall rate were compared with DSD parameters $D_m$, $\mu$ and $N_w$. The rain cell was compared to DSDs determined by the Chilbolton disdrometer. Only rain cells of the same timestamp over Chilbolton were compared. A minimum distance of 10 km from the disdrometer and centre of the cell was chosen in order to ensure the DSD parameters had consistency with the rain cell location.

### 6.4.1 Elliptical ratio

Figures 6.11(a)-6.11(c) compare $D_m$, $\mu$ and $N_w$ with elliptical ratio, $e_r$. The mean and standard deviation were calculated for $D_m$, $\mu$ and $N_w$ over elliptical ratio intervals of 0.1. The elliptical ratio appears to have little correlation with the DSD parameters. The mean values of $\mu$ and $N_w$ are subject to a very high standard deviation. The mean of $D_m$ shows little relation to $e_r$ but has a low standard deviation.

### 6.4.2 Area

The area of a rain cell was analysed against DSD parameters $D_m$, $\mu$ and $N_w$, shown in Figures 6.11(d)-6.11(f). The mean and standard deviation were calculated over 10 $\mathrm{km}^2$ intervals. The size of a rain cell varies considerably for values of $\mu$ and $N_w$. The mean of $\mu$ and $N_w$ show little relation with area and the standard deviations are very high. Similarly, mean $D_m$ shows little correlation with area.

### 6.4.3 Mean cell gradient

The mean horizontal gradient determined for each rain cell was compared with $D_m$, $\mu$ and $N_w$, see Figures 6.12(a)-6.12(c). The mean and standard deviation were calculated over 1 $\mathrm{mm\,hr^{-1}\,km^{-1}}$ intervals. There is a high variation in $\mu$ and $N_w$ with horizontal gradient. All three DSD parameters show little correlation with the mean gradient.

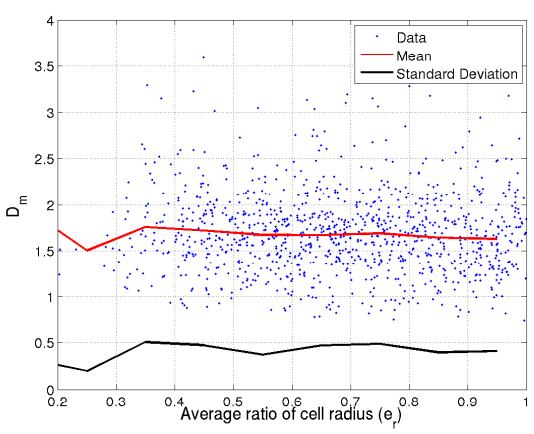


(a) Elliptical ratio of rain cell compared with $D_m$.

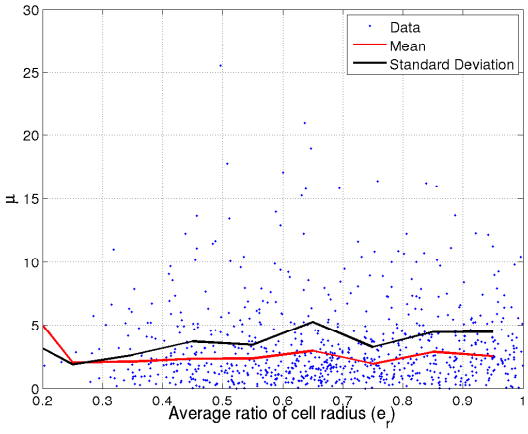


(b) Elliptical ratio of rain cell compared with $\mu$.

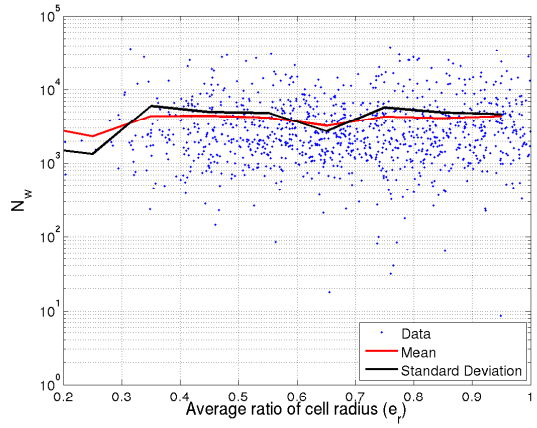


(c) Elliptical ratio of rain cell compared with $N_w$.

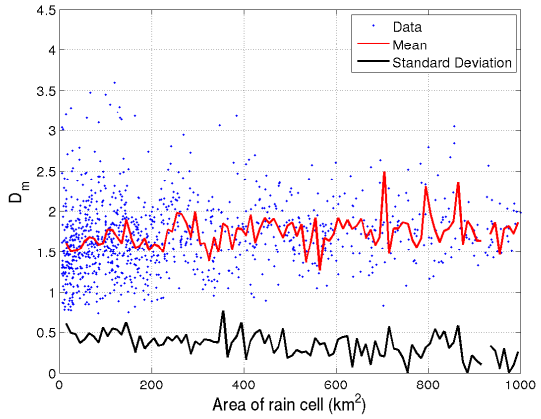


(d) Area compared with $D_m$.

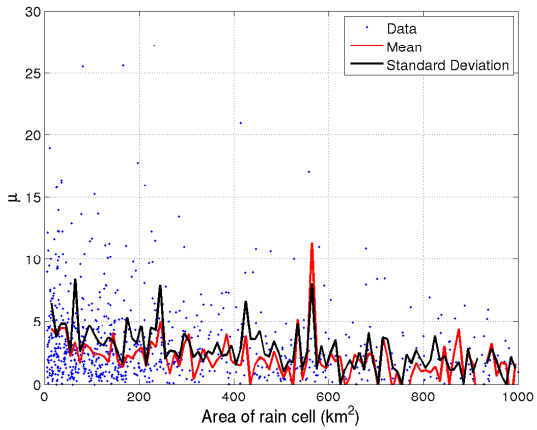


(e) Area compared with $\mu$.

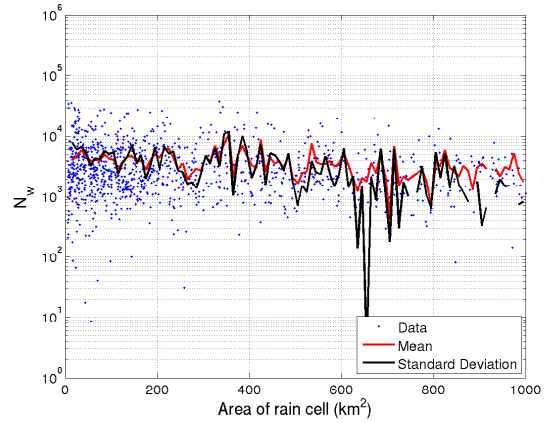


(f) Area compared with $N_w$.

Figure 6.11: Raindrop size distribution comparison of $D_m$, $\mu$ and $N_w$ with elliptical rate and area of a rain cell.

### 6.4.4 Peak, mean and RMS rainfall rate

Figures 6.12(d)-6.12(f) analyse the peak rainfall rate of a cell with corresponding values of $D_m$, $\mu$ and $N_w$. The results of the comparisons of $\mu$ and $N_w$ parameters are similar to the comparisons of the DSD with rainfall rate in Chapter 3. The mean and standard deviation for all were calculated over $1\,\mathrm{mm\,hr^{-1}}$ intervals. The standard deviation was high in respect to the calculated means. There is little correlation with peak, mean or RMS rainfall rate with $\mu$ or $N_w$, as shown in Figures 6.12 and 6.13. The mean $D_m$ has little correlation with peak, mean or RMS rainfall rate. The high variability in $D_m$ with rainfall rate is likely to be partly due to variation in the rain cell location compared to the disdrometer.

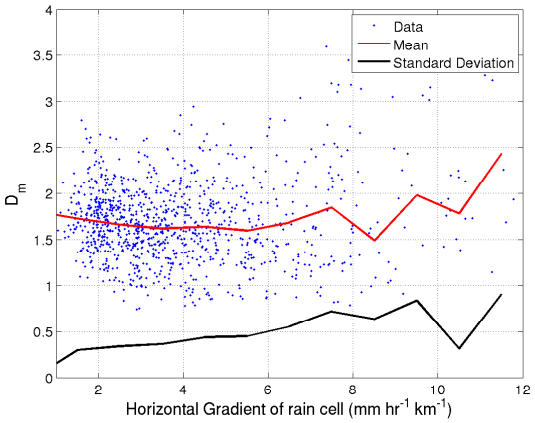


(a) Mean cell gradient compared with $D_m$.

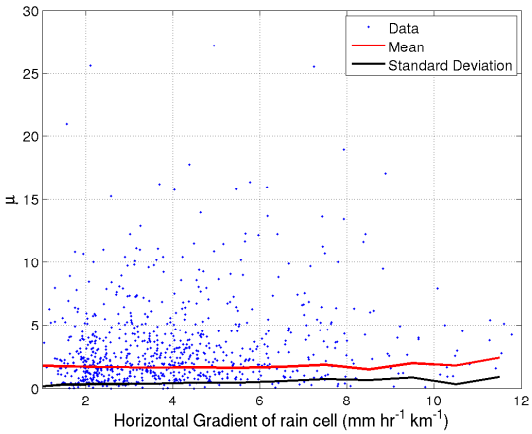


(b) Mean cell gradient compared with $\mu$.

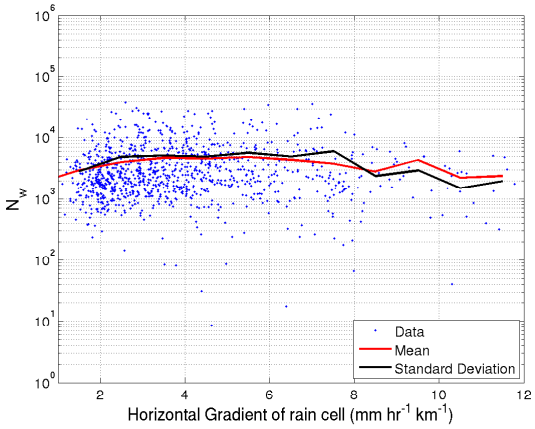


(c) Mean cell gradient compared with $N_w$.

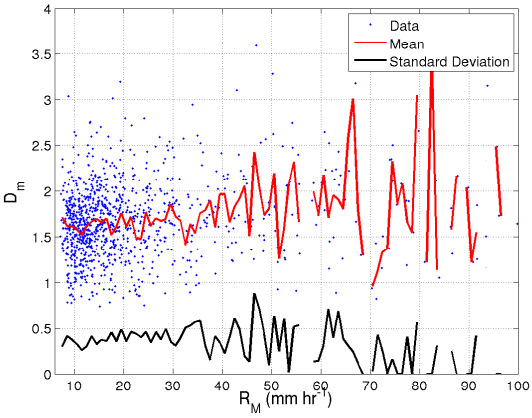


(d) Peak cell rainfall rate compared with $D_m$.

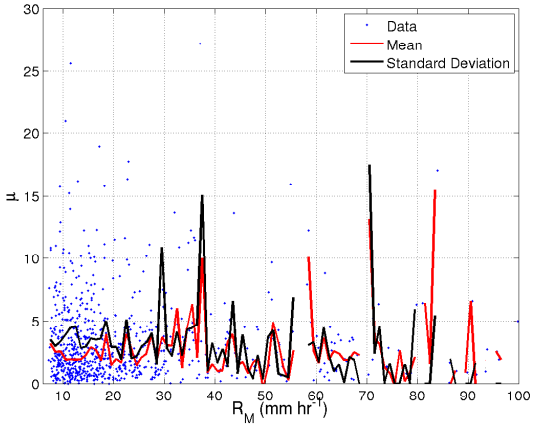


(e) Peak cell rainfall rate compared with $\mu$.

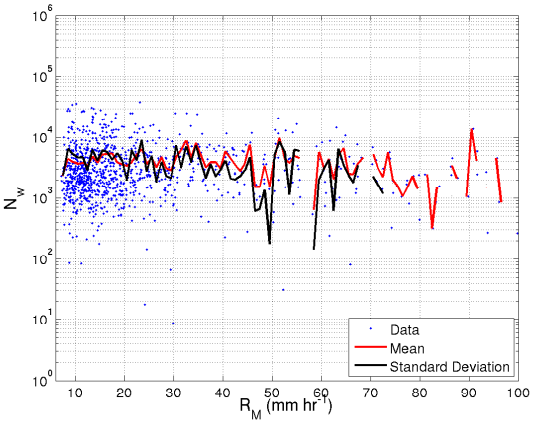


(f) Peak cell rainfall rate compared with $N_w$.

Figure 6.12: Raindrop size distribution comparison of $D_m$, $\mu$ and $N_w$ with mean gradient and peak rainfall rate of a rain cell.

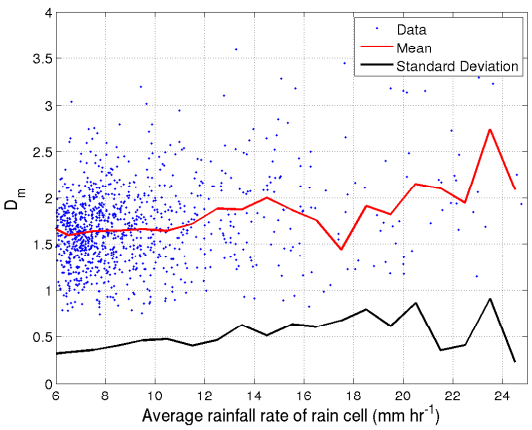


(a) Mean rainfall rate compared with $D_m$.

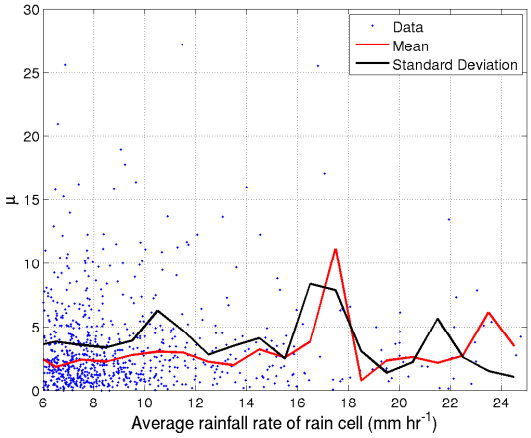


(b) Mean rainfall rate compared with $\mu$.

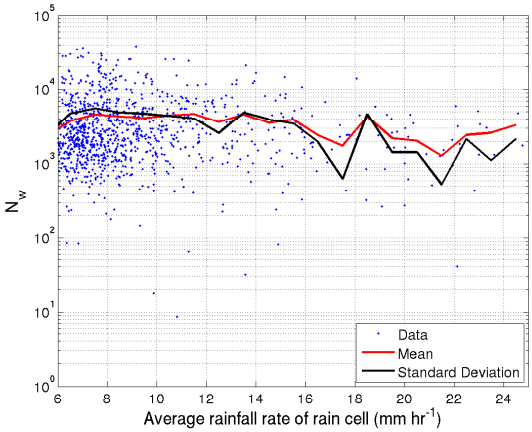


(c) Mean rainfall rate compared with $N_w$.

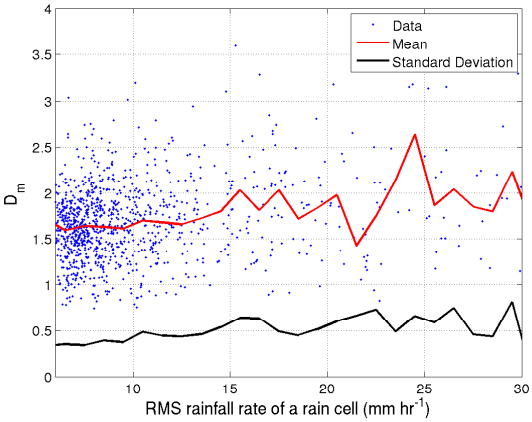


(d) RMS rainfall rate compared with $D_m$.

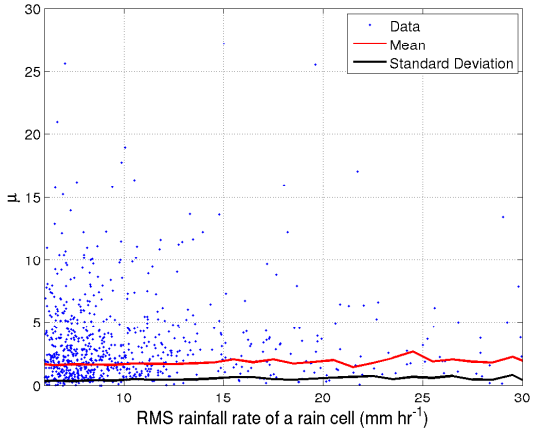


(e) RMS rainfall rate compared with $\mu$.

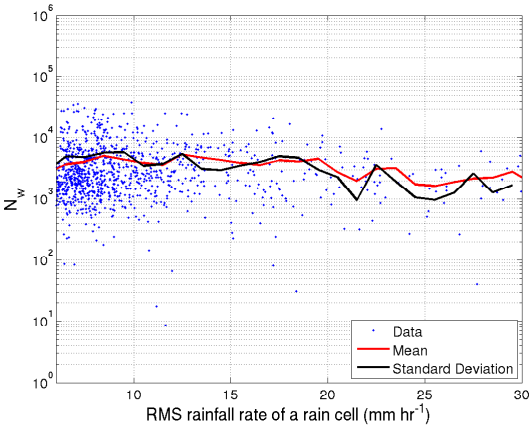


(f) RMS cell gradient compared with $N_w$.

Figure 6.13: Raindrop size distribution comparison of $D_m$, $\mu$ and $N_w$ with mean rainfall rate and RMS rainfall rate of a rain cell.

## 6.5 One-dimensional exponential model

In an attempt to correlate DSD parameters on a similar time and spatial scale with rain cell parameters, a one-dimensional exponential model has been devised. Using the synthetic storm technique, Yau and Rogers [1984], the disdrometer data was used to derive rain cells over time with a threshold at $1\,\mathrm{mm\,hr^{-1}}$. A comparison was made between the average DSD parameters measured by the disdrometer for the duration of the rain cell.

The one-dimensional exponential model assumes the rain cell is circular. The cell radius was determined by $\rho_x = L/[2\ln(R_p/R_2)]$, where $L$ is the length of the rain cell. Peak rainfall rate was determined by the measured peak rainfall rate for each rain cell.

### 6.5.1 Exponential model rain cells

Six examples of rain cells measured using the synthetic rainstorm technique with an exponential model derived are shown in Figure 6.14. The values of $D_m$, $\mu$ and $N_w$ are shown by the yellow, cyan and green lines, where $N_w$ has been normalised. The gradient of the rain cell has been included (shown by the black line). In all cases the exponential shape model fits well to the rainfall rate data. Therefore the model parameters will be subject to comparisons with the DSD parameters.

Figure 6.14(a) shows the first example of a synthetic rain cell. This example of a rain cell shows $\mu$ to be inversely related to change with rainfall rate, suggesting some pattern between the two exists. Figure 6.14(c) shows a similar pattern with rainfall rate and $\mu$. However, the pattern does not repeat for examples shown in Figures 6.14(b),6.14(d) and 6.14(e). It is possible that $\mu$ is inversely related to rainfall rate under certain circumstances that have not been discussed in this thesis and could be the subject of further work. Parameter $N_w$ shows some correlation with rainfall rate.

The value of $D_m$ has been included in order to investigate the stratiform and convective classification derived by Atlas et al. [1999]. Figure 6.14(f) shows an example rain cell of what could be a transition between convective to stratiform rain. The example rain cell shows a sharp increase in rainfall rate and little variation in $D_m$. This period could be described as convective rain, which matches the criteria determined by Atlas et al. [1999]. The transition period occurs when the rainfall rate and $D_m$ decrease simultaneously. A stratiform period is shown following the transition period where the rainfall rate begins to steady, below $10\,\mathrm{mm\,hr^{-1}}$, and $D_m$ increases. The variability in estimating $D_m$ with rainfall rate may be improved by determining stratiform and

convective rain. Further work could include determining stratiform and convective rain using a vertical radar and disdrometer data.

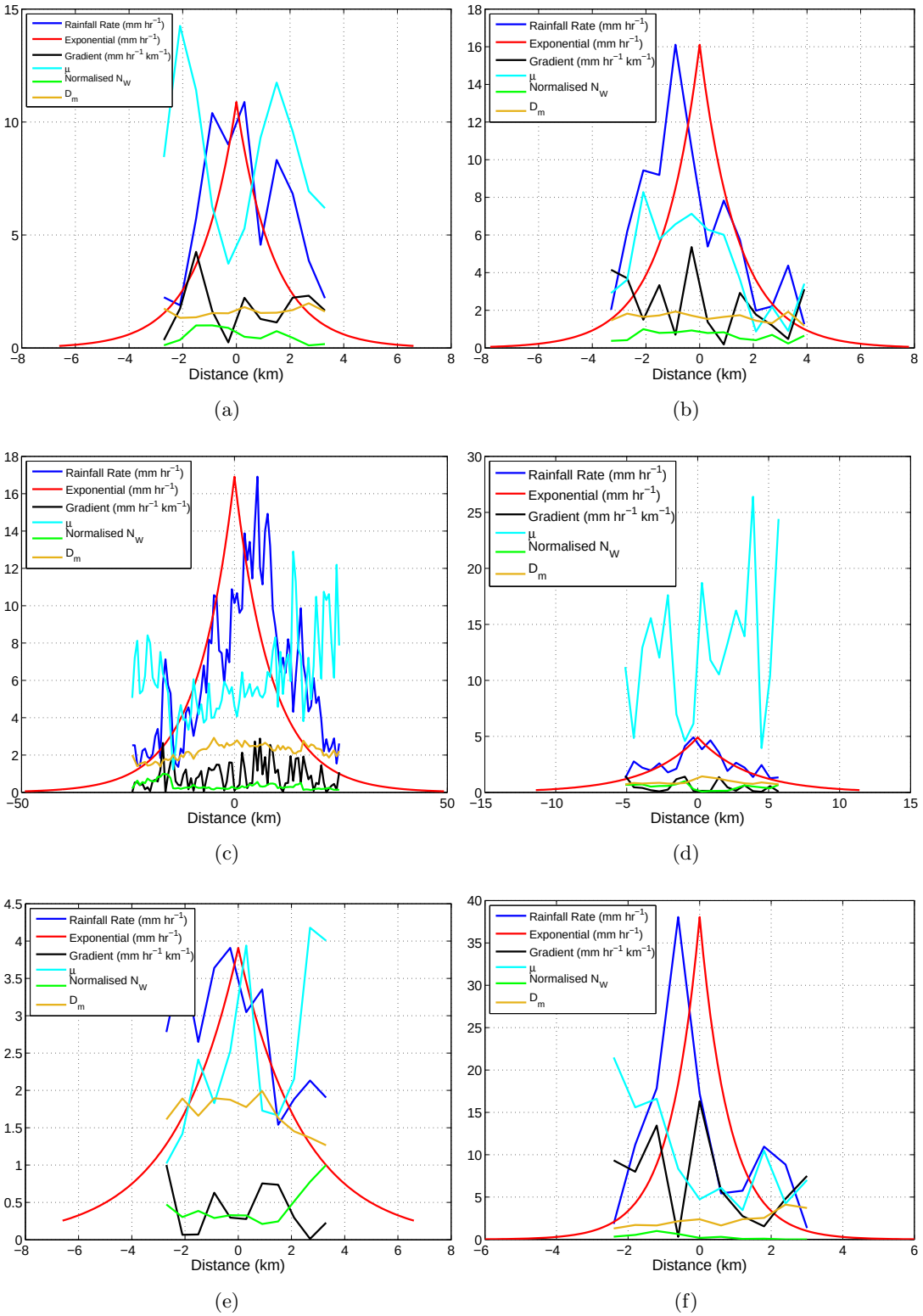


Figure 6.14: Example synthetic rain cells derived from disdrometer data including a one-dimensional exponential model, gradient of rainfall rate, $D_m$, $\mu$ and $N_w$.

### 6.5.2 Exponential model parameter comparison

Figure 6.15 compares maximum rainfall rate and mean rainfall rate of disdrometer measured rain cells with the mean of the DSD parameters of a rain cell event. Figures 6.15(a)-6.15(c) compare the maximum rainfall rate to $D_m$, $\mu$ and $N_w$ respectively. The mean and standard deviation were calculated over intervals of $1.5\,\mathrm{mm\,hr^{-1}}$ in order for each interval to be comparable with the uncertainty in rainfall rate and to incorporate a sufficient number of events. The DSD parameters $\mu$ and $N_w$ show little correlation with maximum rainfall rate and exhibit high variation. The mean of $D_m$ increases with rainfall rate but shows some variation. The correlation with rainfall rate is similar to that described in Chapter 3. However $D_m$ has been subject to averaging over the duration of the rain cell therefore there is less correlation with rainfall rate.

Mean rainfall rate of a rain cell has been compared with the mean parameters of the rain cells. Figures 6.15(d)-6.15(c) show $D_m$, $\mu$ and $N_w$ compared with mean rainfall rate. The mean and standard deviation have been calculated over intervals of $0.25\,\mathrm{mm\,hr^{-1}}$ in order for each interval to be comparable with the uncertainty in rainfall rate. Similar to maximum rainfall rate, $D_m$ shows correlation with mean rainfall rate, while $\mu$ and $N_w$ show little correlation and exhibit high variance.

Figures 6.15(a)-6.15(c) compare the mean cell gradient with $D_m$, $\mu$ and $N_w$. The mean and standard deviation were determined over $0.02\,\mathrm{mm\,hr^{-1}\,km^{-1}}$ intervals. The mean of $D_m$ demonstrates some correlation, since this parameter increases with cell gradient. The standard deviation is high with respect to the mean for both $\mu$ and $N_w$. The results show little correlation between mean cell gradient and $\mu$ and $N_w$.

The axial ratio was compared with $D_m$, $\mu$ and $N_w$, shown in Figures 6.16(d) and 6.16(f). The DSD parameters mean and standard deviation were calculated over axial ratio intervals of 0.75 km. Both $\mu$ and $N_w$ show little correlation with $\rho_x$ and exhibit high variance. Similarly, $D_m$ shows little relation with axial ratio and considerable variation. However, for an axial ratio below 3 km, the mean of $D_m$ decreases with increasing axial ratio.

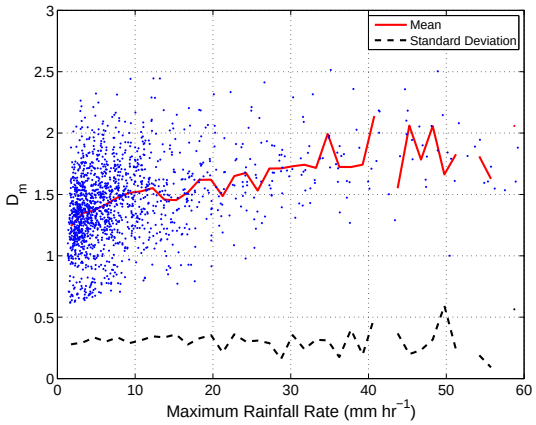


(a) Comparison of $D_m$ with maximum rainfall rate.

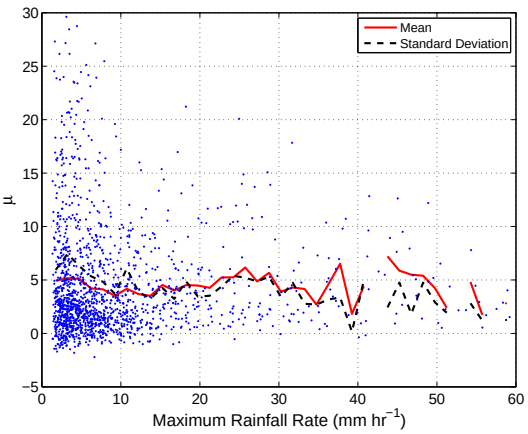


(b) Comparison of $\mu$ with maximum rainfall rate.

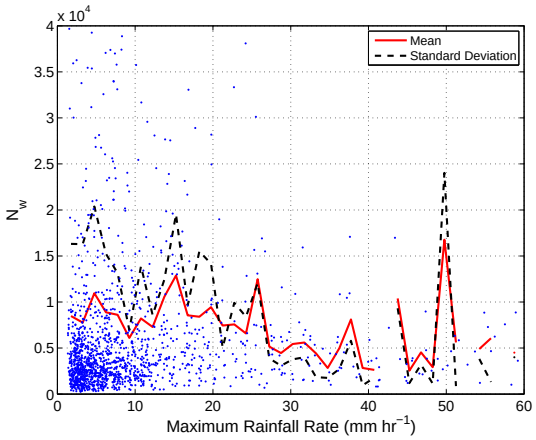


(c) Comparison of $N_w$ with maximum rainfall rate.

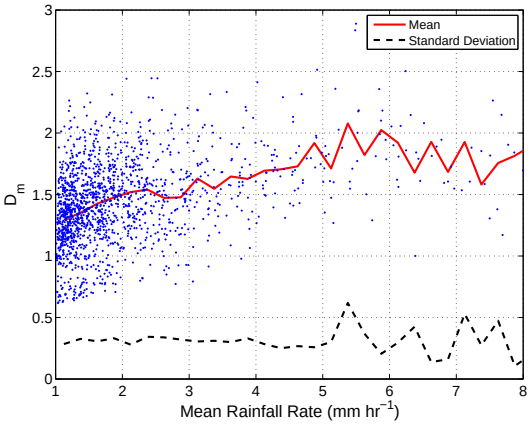


(d) Comparison of $D_m$ with mean rainfall rate.

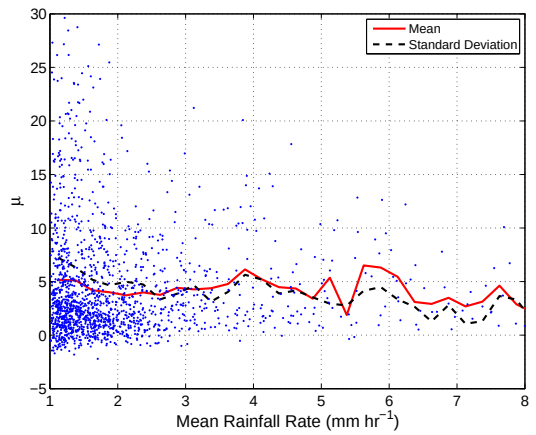


(e) Comparison of $\mu$ with mean rainfall rate.

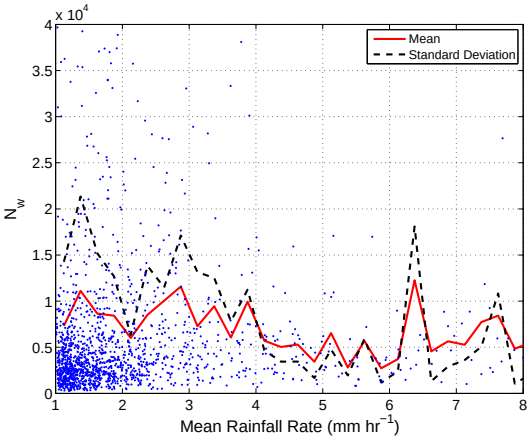


(f) Comparison of $N_w$ with mean rainfall rate.

Figure 6.15: Comparison of $D_m$, $\mu$ and $N_w$ with the one-dimensional exponential rain cell parameters maximum rainfall rate and mean rainfall rate.

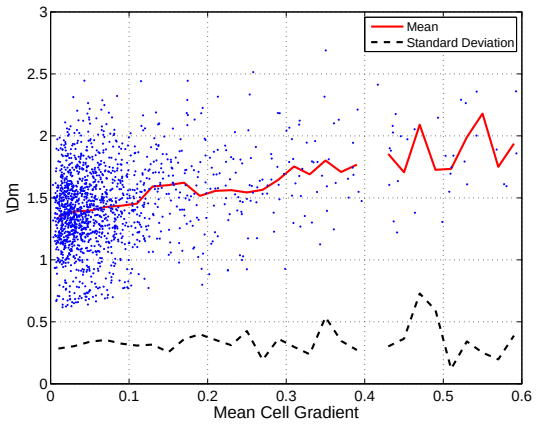


(a) Comparison of mean gradient with $D_m$.

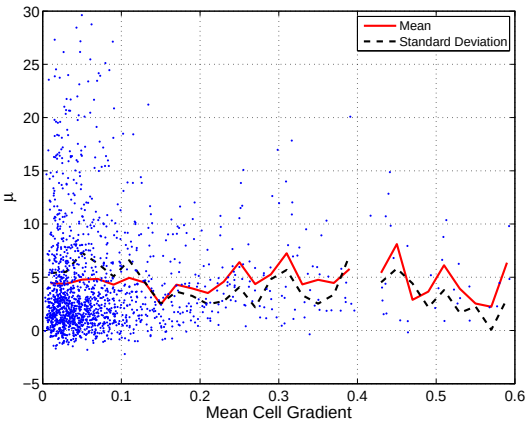


(b) Comparison of mean gradient with $\mu$.

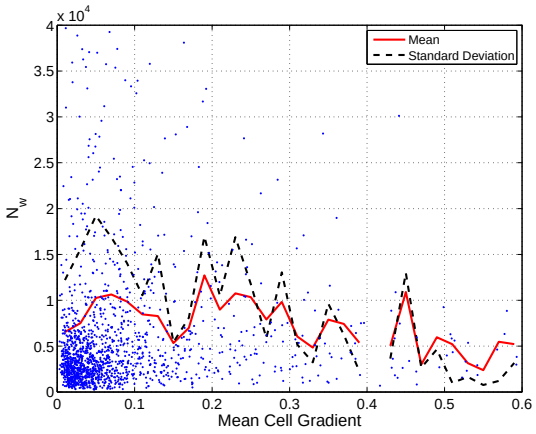


(c) Comparison of mean gradient with $N_w$.

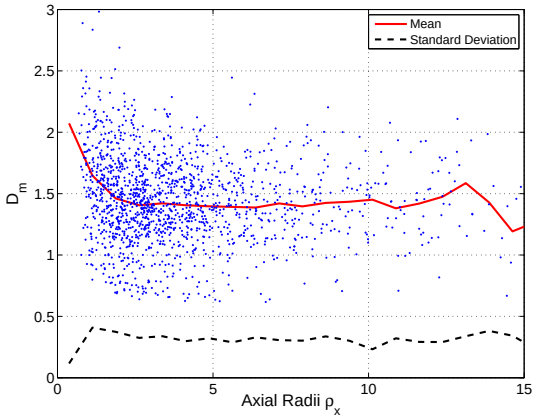


(d) Comparison of $\rho_x$ with $D_m$.

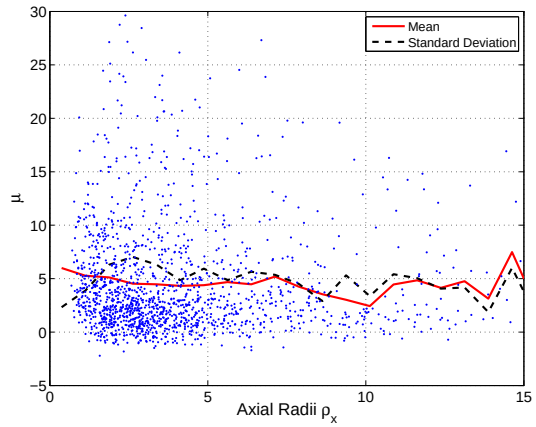


(e) Comparison of $\rho_x$ with $\mu$.

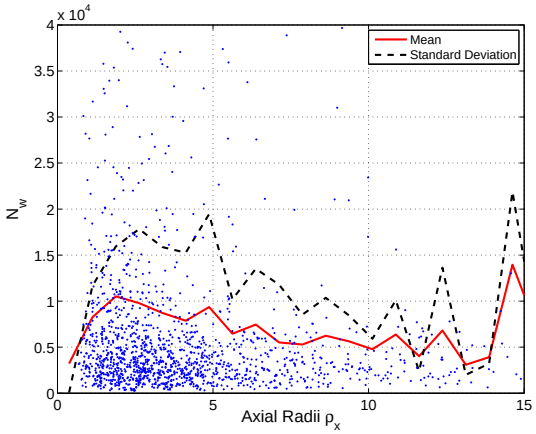


(f) Comparison of $\rho_x$ with $N_w$.

Figure 6.16: Comparison of $D_m$ $\mu$ and $N_w$ with the one-dimensional exponential rain cell parameters $G_r$ and $\rho_x$.

## 6.6 Conclusions

Five years of rainfall data measured from the UK Met Office rainfall radars has been analysed. The EXCELL and HYCELL model have been fitted to each rain cell measured. Both models are excellent representations of rain cells in the UK. Both HYCELL and EXCELL have unique advantages. The HYCELL is better at estimating the peak rainfall rate of a cell and the EXCELL model is better at estimating the gradient of rain cells. Rain cells with large areas are better estimated by the EXCELL model where small rain cells were better approximated by the HYCELL model. Whilst both cells are good, the EXCELL model demonstrates less error in estimating all rain cell parameters.

Rain cells in the UK are elliptical in shape with an average ratio of radii at approximately 0.68, which is more circular than those of Milan's. The average area of a rain cell has been shown to be approximately 100 $\mathrm{km}^2$. The peak rainfall rate has been shown to increase with rain cell area, which is agreement with results of those by Féral et al. [2003b]. It has been shown that mean rainfall rate increases with rain cell area to $\approx$75 $\mathrm{km}^2$ before it begins to decrease. Stratiform rain will generally cover an area several times greater than that of convective cells. Therefore, it is suggested rain cells of an area approximately 75 $\mathrm{km}^2$ are likely to be more convective in nature due to the high mean rainfall rate and smaller area. Further, the results are in agreement with Féral et al. [2000] where the ellipticity factor has little correlation with rain cell location, over land or sea. However, the results have shown for a given area, a rain cell tends to have a higher peak rainfall rate and mean rainfall rate over land than sea. This result could be due to orographic lift of air as it reaches land or even a cold front reaching land resulting in more intense and convective rain over land.

The DSD parameters $D_m$, $\mu$ and $N_w$ show little, if any, relation to rain cell parameters such as area, elliptical ratio and mean rainfall rate. A one-dimensional exponential model showed little correlation with mean DSD parameters and parameters of a rain cell. However, the synthetic rain cells showed some correlation exists for $D_m$, $\mu$ and $N_w$ with rainfall rate. It has been shown that stratiform and convective rain could potentially be determined from disdrometer data taking into account the transition of rainfall rate and $D_m$.

# Chapter 7

# Summary and conclusions

## 7.1 Summary

A total of 12 years of disdrometer data, five years of radar rainfall rate data, four years of surface meteorological data, three years of unified model data and four years of cloud data have been examined. Disdrometer data analysis in Chapter 3 showed the raindrop size distribution was best represented by the normalised gamma distribution in comparison to an exponential distribution for 60 second time intervals. Chapter 3 also compared the normalised gamma distribution parameters of each DSD to rainfall rate and demonstrated some patterns between $D_m$ and $N_w$ with rainfall rate and season. The non-linear relationship between $D_m$ and rainfall rate could be represented by a power-law fit. The relationship is subject to considerable variability but it is not subject to changes in frequency. DSD parameter $N_w$ showed some correlation with rainfall rate but exhibited high variance at rainfall rates below $10\,\mathrm{mm\,hr^{-1}}$. The rainfall rate threshold ($10\,\mathrm{mm\,hr^{-1}}$) could be used as part of a classifier to determine stratiform and convective rain.

A comparison of the DSD parameters with meteorological data in Chapter 4 showed little correlation in order to recreate the raindrop size distribution and improve on the accuracy of existing $A$-$R$ relationship. Meteorological comparison showed that variance in the rainfall rate and $D_m$ relationship is partially correlated to wind speed (Figure 4.8(a)). Further analysis showed variability in $N_w$ below $10\,\mathrm{mm\,hr^{-1}}$ is correlated to dew point and wind speed (Figures 4.4(e) and 4.8(e)). During low dew point temperatures (below 283 K) variability in $N_w$ for rainfall rates below $7\,\mathrm{mm\,hr^{-1}}$ is smaller compared to dew points above 283 K. Variability in $N_w$ for rainfall rates below $7\,\mathrm{mm\,hr^{-1}}$ is also smaller when wind speed is greater than $8\,\mathrm{ms^{-1}}$. Strong winds

and low dew point temperatures could be an indicator of more convective or stratiform rain where the DSD is potentially more predictable.

Chapter 5 investigated the effect of frequency on the attenuation and rainfall rate relationship using six years of disdrometer data measured at Chilbolton. Frequencies between 30 GHz and 45 GHz have been identified to be least affected by the raindrop size distribution and have the most linear $A$-$R$ relationship. A common link frequency at 38 GHz has been shown to have one of the lowest errors in estimating the $A$-$R$ relationship for a linear fit at 40 mm hr$^{-1}$ using rainfall rates up to a maximum of 50 mm hr$^{-1}$. Over 99.99% of rainfall rate is accounted for up to 40 mm hr$^{-1}$, which makes 38 GHz links within the UK an ideal choice to infer rainfall rate using a linear relationship on link measurements.

Further investigation of the linear $A$-$R$ relationship in Chapter 5 showed that for vertical polarisation 33 GHz has the highest PVAF and is consistent over the range of 5-100 mm hr$^{-1}$. Similarly for horizontal polarisation 35 GHz has the highest PVAF. Nearby frequencies such as 38 GHz for vertical and horizontal polarisation have extremely similar and good PVAF for both linear and power-law fits.

Chapter 6 examined five years of rain cell data derived from the UK Met Office rainfall radars, which showed the EXCELL and HYCELL models are good representations of rain cells in the UK. Whilst both model cells have their merits, the EXCELL model has the lowest error between all rain cell parameters and provides a better estimate of rain cells in the UK. The HYCELL model better estimates peak rainfall rate where the EXCELL model is better at approximating the mean horizontal gradient. The results have shown rain cells in the UK to be, on average, elliptical in shape with an average ratio of radii of approximately 0.68. However, this result is more circular than rain cells measured in Milan. The average area of a rain cell is approximately 100 km$^2$.

Further study in Chapter 6 showed rain cell parameters to have little if any relation to raindrop size distribution parameters. The disdrometer-derived synthetic rain cells also showed no correlation to the DSD parameters. The synthetic rain cells could be used to derive stratiform and convective rain taking into account the transition of rainfall rate and $D_m$. The knowledge of convective and stratiform rain could potentially improve the estimation of DSD parameters given rainfall rate.

Raindrop size distribution parameters have little correlation with rain cell parameters and meteorological variables. Both $N_w$ and $D_m$ show some relation to rainfall rate, which could be improved by combining rainfall rate data with dew point temperature and wind speed. Parameter $\mu$ also shows some correlation with $N_w$. Using this information the raindrop size distribution could be recreated. However, there is significant

variability in estimating the parameters. Variability in the $A$-$R$ relationship over the frequency range of 10-95 GHz is less than that caused when using attenuation calculated from DSD estimations.

## 7.2 Conclusions

The raindrop size distribution has been shown to have a considerable impact on variability of attenuation, which increases with frequency. The impact of the variability can lead to significant problems in maintaining consistent availability of telecommunication systems. The results have shown that the traditional power-law relationship between attenuation and rainfall rate may result in significant errors in estimating attenuation at EHF due to increased variability caused by the DSD.

Analysis has shown the mean raindrop diameter increases with rainfall rate, whilst the drop concentration reduces, and the shape parameter of the DSD shows considerable variability. The investigation also demonstrated that the DSD varied with season. Further analysis of the DSD in Chapter 4 showed some correlation with meteorological parameters, such as wind and dew point. Whilst these correlations are informative, they have little impact in attempts to account for the variability seen within the DSD. It has been concluded there are too many unaccounted variables to recreate the DSD. Factors such as the local environment (i.e. buildings and trees) will cause large variance due to generated turbulence. Turbulence will severely impact the distribution of raindrops measured. Temperature and dew point may have some impact on the formation of raindrops but the resultant DSD seen at the ground is exposed to many other factors, such as drop collisions, break up, wind and pressure as the drop falls.

This work has shown variability in the $A$-$R$ relationship caused by the DSD is magnified as frequency increases above 40 GHz. However, disdrometer analysis illustrated the DSD has little impact on the $A$-$R$ relationship at frequencies between 30 GHz and 40 GHz. This frequency range is significant as the $A$-$R$ relationship can be considered linear and the impact of the DSD is minimal. Complex linearisation techniques could be avoided when using inverse methods to determine surface rainfall rates when using a linear $A$-$R$ relationship. Frequency scaling techniques are easier to implement as there is less variance caused by the DSD. For example, satellite uplinks generally operate at a different frequency to downlinks; frequency scaling could be used to infer the attenuation from one link to the other.

The analyses of rain cells in the UK has illustrated that they are on average elliptical in shape but are more circular than those measured in Milan. The rain cells have been

shown to have an average area of 100 $km^2$, where there is likely to be a division of stratiform and convective rain cells. Above 100 $km^2$ the mean rainfall rate of a cell begins to decrease with area, suggesting a more widespread or stratiform type of rain cell. Peak rainfall rate has been shown to rapidly increase with area up to 100 $km^2$. Above 100 $km^2$ the rate of increase in peak rainfall rate is much more gradual with respect to area, which is more consistent with widespread stratiform rain cells. In agreement with Féral et al. [2000], the results show the elliptical shape of a rain cell has little correlation with location over land or sea. However, the area and rainfall rate relationship has shown some correlation with the location of a rain cell. The results showed higher average rainfall rates and larger peak rainfall rates with respect to area for rain cells over land than sea. More intense rain over land could be a result of orographic lift as air reaches land, or cold sea air undercutting warmer air over land causing more sudden uplift and convective rain.

Finally, exponential (EXCELL) rain cells have been shown to be a good fit to rain cells measured in the UK. The study and parameterization of rain cells will aid future development in understanding and derivation of rain cell structure. Derivation of rain cell structure will help improve the prediction of attenuation due to rain along multiple path radio links.

## 7.3 Further work

This section briefly describes potential areas of research and methods that could be investigated leading on from this research. Potential work ranges from further investigation into the polarisation effects on attenuation using disdrometer measurements, the effect of the different time samples of disdrometer measurements, classification of stratiform and convective rain from a disdrometer and enhancing fade mitigation techniques such as spot beam satellites.

### 7.3.1 Polarisation

The effect of the raindrop size distribution on polarisation could be investigated further. The disdrometer could be used to calculate specific attenuation for different polarisations including circular and elliptical, as well as vertical and horizontal. Polarisation has been investigated within this thesis, however, the effects of different polarisations on attenuation and DSD could be further studied.

### 7.3.2 Disdrometer time samples

Disdrometers measure rainfall every ten seconds, which can be aggregated for longer periods. As previously discussed, an appropriate time interval was chosen to capture individual rain events whilst maintaining sufficient drop samples for comparison, see Chapter 3. The time period could be investigated further by aggregating over larger or smaller time periods and comparing the resultant rainfall rates and DSDs. Different time samples may be useful for other applications such as hydrology or comparison with other meteorological effects that could be recorded over longer or shorter time periods. Further work could investigate which analytical distribution, such as exponential or Gamma, is the best representation of the DSD for different time samples.

### 7.3.3 Classification of stratiform and convective rain from a disdrometer

The classification of stratiform and convective rain could potentially be achieved using a disdrometer. Atlas et al. [1999] use a combination of disdrometer and vertical radar data to determine the two types of rain from drop size. Work by Capsoni et al. [2006] investigates the use of rain cells to determine stratiform and convective rain. Meteorological, radar and satellite data could be used to determine convective and stratiform rain. Combining this data with disdrometer data could potentially reveal a method to determine the type of rain from a single disdrometer. The synthetic rain cell technique could potentially lead to a method to determine the type of rain.

### 7.3.4 Fade mitigation techniques

Fade mitigation techniques are used to avoid or compensate for radio wave attenuation in order to maintain the availability of a communication system.

#### Implementation of fade mitigation

Services are expected to have a very high availability, which is defined as the percentage of the year where the signal bit-error-ratio is lower than a set boundary. This means the user will be able to maintain a usable service for a set percentage of time.

Traditionally, link budgets are used to compensate for fading on a communications

link. The traditional link budget consisted of a calculation of the power required to maintain a clear and quasi error free (QEF) link in clear sky conditions, only accounting for effective isotropic radiated power (EIRP), antenna gain and free space path loss (FSPL). A fade margin is then added to cover the excess variable attenuation from other sources. This excess attenuation is calculated from statistical models such as those provided by ITU-R recommendations.

At Ka-band frequencies and above, attenuation can no longer be mitigated using a static fade margin. The fade margin would need to be large, which would be inefficient during periods of clear sky or low attenuation. In order to efficiently counteract system fade to ensure that the quality of service is maintained, fade mitigation techniques (FMTs) can be implemented. FMTs can largely be grouped into three categories: power control, adaptive waveform and diversity.

Diversity approaches use a re-routeing strategy, either with multiple sites, satellites, frequencies or time to avoid a fade. Adaptive waveform techniques include changing signal code, modulation or data rate. Power control involves up-link and down-link power control or beam shaping. When choosing the most suitable technique the operating frequency, performance objectives (typically the quality-of-service) and system architecture must be taken into consideration.

**Spot Beam Satellites**

With the use of Ka-band frequencies and above, the antenna size can be reduced and directivity of a beam increased. These factors have allowed for the design of spot beam satellites. The technique uses multiple antennas to distribute signals over many areas. The separated beams allow for frequency reuse and higher system capacity. The techniques can be used to counteract attenuation by redistributing power between beams. It is easier to redistribute the power from travelling wave tube amplifiers (TWTAs) than reduce its power. Excess power from several beams could be redistributed to another beam to overcome fade based on propagation predictions or real time information. The service area is covered by many overlapping spot beams to support two-way communications.

The evolution of this work would be to combine propagation modelling (such as the Bath propagation model) with an implementation of fade mitigation techniques, in particular with spot beam satellites. Figure 7.1 shows an example of spot beam coverage over Europe illustrating possible coverage and an example of attenuation may be modelled in place of range.

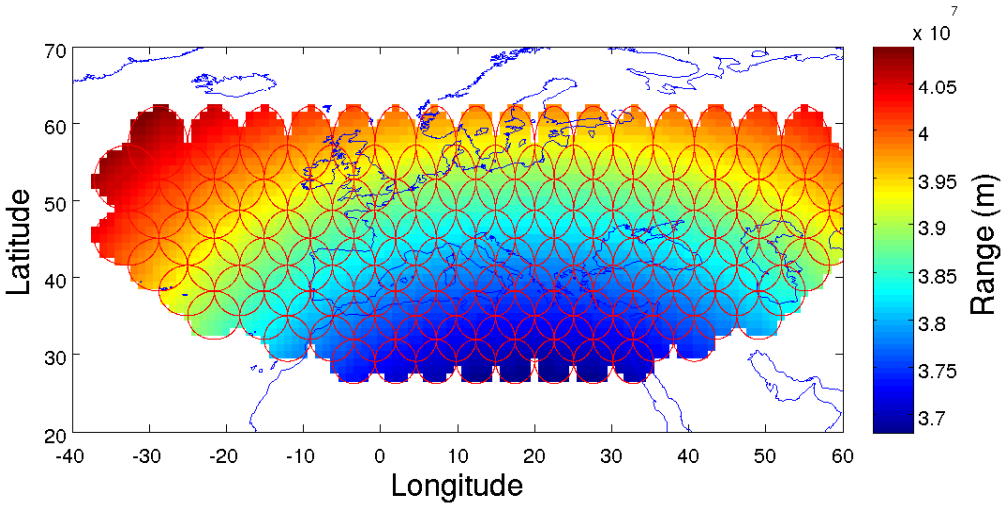


Figure 7.1: Projection of a spot beam satellite from a geostationary orbit showing range.

# Appendix A

# Published journal papers

# References


M Abramowitz and I A Stegun. *Handbook of Mathematical Functions*. Dover Publications, New York, 1965.

M O Ajewole and T Oguchi. Effects of multiple scattering on communication at millimetre and centimetre wavelengths in tropical rainfall conditions. *Electronics Letters*, 37 (2):121–123, 2001.

B R Arbesser-Rastburg and A Paraboni. European research on Ka-band slant path propagation. *Proc. IEEE*, 85:843–852, 1997.

D Atlas and C W Ulbrich. Path- and area-integrated rainfall measurements by microwave attenuation in the 1-3 cm band. *Journal of Applied Meteorology*, 16(4): 327–332, 1977.

D Atlas, C W Ulbrich, F D Marks Jr., E Amitai, and C R Williams. Systematic variation of drop size and radar-rainfall relations. *Journal of Geophysical Research*, 104(D6):6155–6169, 1999.

P M Austin. Relation between measured radar reflectivity and surface rainfall. *Monthly Weather Review*, 115:1053–1070, 1987.

K Aydin and Y-M Lure. Millimeter wave scattering and propagation in rain: A computational study at 94 and 140 GHz for oblate spheroidal and spherical raindrops. *IEEE Transactions Geoscience And Remote Sensing*, 29(4):593–601, 1991.

E A Baltas and M A Mimikou. The use of the Joss-type disdrometer for the derivation of Z-R relationships. *Proceedings of ERAD*, pages 291–294, 2002.

P W Barber and S C Hill. *Light Scattering by Particles: Computational Methods*. World Scientific Publishing, Singapore, 1990.

K V Beard. Raindrop oscillations: Evaluation of a potential flow model with gravity. *Journal of the Atmospheric Sciences*, 41(10):1765–1774, 1984.

K V Beard and C Chuang. A new model for the equilibrium shape of raindrops. *Journal of the Atmospheric Sciences*, 44(11):1509–1524, 1986.

A Berne and R Uijlenhoet. Path-averaged rainfall estimation using microwave links: Uncertainty due to spatial rainfall variability. *Geophysical Research Letters*, 34 (L07403):1–5, 2007.

A C Best. The size distribution of raindrops. *Quaterly Jour. Royal Met. Soc*, 76:16–36, 1950.

P R Bevington and D K Roninson. *Data reduction and error analysis for the physical sciences*. McGraw-Hill, New York, 1992.

B. Bossa and E. Villermaux. Single-drop fragmentation determines size distribution of raindrops. *Nature Physics*, 5:697 – 702, 2009.

K O Bowman and L R Shenton. *Properties of estimators for the Gamma distribution*. Marcel Dekker, New York, 1988.

D Brawn and G Upton. Estimation of an atmospheric gamma drop size distribution using disdrometer data. *Atmospheric Research*, 87:66–79, 2008.

G Brussaard. Rain-induced crosspolarisation and raindrop canting. *Electronics Letters*, 10(20):411–412, 1974.

G H Bryant, I Adimula, C Riva, and G Brussaard. Rain attenuation statistics from rain cell diameters and heights. *International Journal of Satellite Communications*, 19:263–283, 2001.

C Capsoni, F Fedi, C Magistroni, A Paraboni, and A Pawlina. Data and theory for a new model of the horizontal structure of rain cells for propagation applications. *Radio Sci.*, 22(3):395–404, 1987.

C Capsoni, L Luni, A Paraboni, and C Riva. Stratiform and convective rain discrimination deduced from local P(R). *IEEE Transactions on Antennas and Propagation*, 54(11):3566–3569, 2006.

L Castanet. *Fade mitigation techniques for new SatCom systems At Ka and V Bands*. PhD thesis, Department of Electromagnetism and Radar, university of Toulouse, 2001.

L Castanet, T Deloues, and J Lemorton. Channel modelling based on N-state Markov chains for satcom systems simulation. *Proc. International Conference on Antennas and Propagation*, pages 119–122, 2003.

C C Chuang and K V Beard. A numerical model for the equilibrium shape of electrified raindrops. *Journal of the Atmospheric Sciences*, 47(11):1374–1389, 1990.

R K Crane. Space-time structure of rain rate fields. *Journal of Geophysical Research*, 95:2011–2020, 1990.

R K Crane and D V Rogers. Advanced communications technology satellite (acts) propagation campaign in north america. *Antennas and Propagation Magazine, IEEE*, 40(6):2328, 1998.

N A Crook. Sensitivity of moist convection forced by boundary layer processes to low-level thermodynamic fields. *Monthly Weather Review*, 124:1767–1785, 1996.

R C Srivastava D Atlas and R S Sekhon. Doppler radar characteristics of precipitation at vertical incidence. *Review of Geophysics and Space Physics*, 11(1):1–35, 1973.

M M J L Van de Kamp. *Climatic radiowave propagation models for the design of satellite communication systems*. PhD thesis, University of Eindhoven, 1999.

L Dossi. Real-time prediction of attenuation for applications to fade countermeasures in satellite communications. *Electronics Letters*, 26(4):250–251, 1990.

C A Doswell-III and E N Rasmussen. The effect of neglecting the virtual temperature correction on CAPE calculations. *American Meteorological Society*, 9:625–629, 1994.

G Drufuca. Rain attenuation statistics for frequencies above 10 GHz from rain gauge observations. *J. Rech. Atmos*, 1(2):399–411, 1974.

G Feingold and Z Levin. The lognormal fit to raindrop spectra from frontal convective clouds in israel. *Journal of Climate and Applied Meteorology*, 25:1346–1363, 1986.

L Féral, F Mesnard, H Sauvageot, L Castanet, and J Lemorton. Rain cells shape and orientation distribution in South-West of France. *Phys. Chem. Earth B*, 25(10-12): 1073–1078, 2000.

L Féral, H Sauvageot, L Castanet, and J Lemorton. Hycell - a new hybrid model of the rain horizontal distribution for propagation studies: 1. Modeling of the rain cell. *Radio Science*, 38(3):1056, 2003a.

L Féral, H Sauvageot, L Castanet, and J Lemorton. Hycell - a new hybrid model of the rain horizontal distribution for propagation studies: 2. Statistical modeling of the rain rate field. *Radio Science*, 38(3):1057, 2003b.

D Giuli, A Toccafondi, G Biffi Gentili, and A Freni. Tomographic reconstruction of rainfall field through microwave attenuation measurements. *Journal of Applied Meteorology*, 30:1323–1340, 1991.

J Goldhirsh. Two-dimension visualization of rain cell structures. *Radio Science*, 35(3): 713–729, 2000.

B Gremont, M Filip, P Gallois, and S Bate. Comparative analysis and performance of two predictive fade detection schemes for ka-band fade countermeasures. *IEEE Journal On Selected Areas in Communications*, 17(2):180–192, 1999.

R Gunn and G D Kinzer. The terminal velocity of fall for water. *Journal of Meteorology*, 6:243–248, 1949.

D Hodges, R J Watson, and G Wyman. Attenuation time series model for propagation forecasting. *IEEE Transactions on Antennas and Propagation*, 54(6):1726–1733, 2006.

D D Hodges. *Propagation forecasting for EHF and SHF systems*. PhD thesis, Department of Electronic and Electrical Engineering, University of Bath, 2006.

D D Hodges and R J Watson. An analysis of conditional site diversity: A study at Ka-band. *IEEE Transactions on Antennas and Propagation*, 57(3):721–727, 2009.

A R Holt, J W F Goddard, G J G Upton, M J Willis, A R Rahimi, P D Baxter, and C G Collier. Measurement of rainfall by dual-wavelength microwave attenuation. *Electronics Letters*, 36(25):2099–2101, 2000.

A R Holt, G G Kuznetsov, and A R Rahimi. Comparison of the use of dual-frequency and single-frequency attenuation for the measurement of path-averaged rainfall along a microwave link. *IEE Proceedings - Microwaves, Antennas and Propagation*, 150 (5):315–320, 2003.

J R Holton, J A Curry, and J A Pyle. *Encyclopedia of Atmospheric Sciences*, volume 3. Elsevier, 2003.

R A Houze. *Cloud Dynamics*. Academic, San Diego, California, 1993.

A J Illingworth. Improved precipitation rates and data quality by using polarimetric measurements. In *Weather Radar: Principles and Advanced Applications*, page 130166. Springer-Verlag, Berlin, 2004.

A J Illingworth and T M Blackman. The need to represent raindrop size spectra as normalized gamma distributions for the interpretation of polarization radar observations. *Journal of Applied Meteorology*, 41(3):286–297, 2002.

A J Illingworth and I J Caylor. Polarization radar estimates of raindrop size spectra and rainfall rates. *J. Atmos. Oceanic Technol*, 6:939949, 1989.

A Ishimaru. *Electromagnetic Wave Propagation, Radiation, and Scattering*. Prentice-Hall, Washington, 1991.

G James. *Advanced modern engineering mathematics*. Addison-Wesley, Wokingham, England, 1993.

I T Jolliffe. *Principal Component Analysis*. Springer, New York, 2002.

J Joss and E G Gori. Shapes of raindrop size distributions. *Journal of Applied Meteorology*, 17:1054–1061, 1978.

V K Katsambas and J D Kanellopoulos. Rain attenuation and cross-polarization effects in interference between adjacent satellite and terrestrial dual polarized systems. *Antennas and Propagation Society International Symposium, 2003. IEEE*, 4:920–923, 2003.

M Kitchen and P M Jackson. Weather radar performance at long range-simulated and observed. *Journal of Applied Meteorology*, 32(5):975–985, 1993.

D Kliche, P Smith, and R W Johnson. Estimators for parameters of drop-size distribution functions sampling from gamma distributions. *12$^{th}$ Conference on Cloud Physics, Madison, WI, Amer. Meteor. Soc*, 2006.

D Kliche, P Smith, and R W Johnson. L-moment estimators as applied to gamma drop size distributions. *33$^{rd}$ Conf. on Radar Meteorology*, P8A.15, 2007.

T G Konrad. Statistical models of summer rainshowers derived from fine-scale radar observations. *Journal of Applied Meteorology*, 17:171–188, 1978.

R J Kubesh and K V Beard. Laboratory measurements of spontaneous oscillations for moderate-size raindrops. *Journal of the Atmospheric Sciences*, 50(8):1089–1098, 1993.

M G Lawrence. The relationship between relative humidity and the dewpoint temperature in moist air. *American Meteorological Society*, 86:225–233, 2005.

J O Laws and D A Parsons. The relation of raindrop size to intensity. *Trans. Amer. Geophys. Union*, 24:452–460, 1943.

H Leijnse, R Uijlenhoet, and J N M Stricker. Hydrometeorological application of a microwave link: 2. Precipitation. *Water Resources Research*, 43, 2007.

M J Leitao and P A Watson. Method for prediction of attenuation on earth-space links based on radar measurements of the physical structure of rainfall. *Proceedings of the IEEE*, 133(4):429–441, 1986.

J S Marshall and W McK Palmer. The distribution of raindrops with size. *Journal of Meteorology*, 5:165–166, 1948.

J Mass. A simulation study of rain attenuation and diversity effects on satellite links. *COMSAT Technival Review*, 17(1):159–187, 1987.

E Matricciani. Physical-mathematical model of the dynamics of rain attenuation based on rain rate time series and a two layer vertical structure of precipitation. *Radio Science*, 31(2):281–295, 1996.

H Messer, A Zinevich, and P Alpert. Environmental monitoring by wireless communication networks. *Science*, 312:713, 2006.

M Montopoli, F S Marzano, and G Vulpiani. Analysis and synthesis of raindrop size distribution time series from disdrometer data. *IEEE Transactions on Geoscience and Remote Sensing*, 46(2):466–478, 2008.

I J Myung. Tutorial on maximum likelihood estimation. *Journal of Mathematical Psychology*, 47:90–100, 2003.

Met Office. Met office unified model. Technical report, Jan 2009. URL `http://www.metoffice.gov.uk/science/creating/daysahead/nwp/um.html`.

T Oguchi. Electromagnetic wave propagation and scattering in rain and other hydrometeors. *Proceedings of The IEEE*, 71(9):1029–1078, 1983.

T Oguchi. Effects of incoherent scattering on microwave and millimetre wave communications through rain. *Electronics Letters*, 27(9):759–761, 1991.

R L Olsen, D V Rogers, and D B Hodge. The $aR^b$ relation in the calculation of rain attenuation. *IEEE Transactions on Antennas and Propagation*, AP-26(2):318–329, 1978.

A D Panagopoulos, P-D M Arapoglou, and P G Cottis. Satellite communications at Ku, Ka, and V bands: Propagation impairments and mitigation techniques. *IEEE Communications Surveys and Tutorials*, 6(3):2–14, 2004.

A Paraboni and C Riva. A new method for the prediction of fade duration statistics in satellite links above 10 GHz. *International Journal of Satellite Communications*, 12:387–394, 1994.

S R Pennock and P R Shepherd. *Microwave Engineering With Wireless Applications*. Macmillan Press LTD, London, 1998.

M A Pitt and J Myung. When a good fit can be bad. *TRENDS in Cognitive Sciences*, 6(10):421–425, 2002.

W H Press, S A Teukolsky, W T Vetterling, and B P Flannery. *Numerical Recipes*. Cambridge University Press, New York, 2007.

H R Pruppacher and K V Beard. A wind tunnel investigation of the internal circulation and shape of water drops falling at terminal velocity in air. *Quart. J. R. Met. Soc.*, 96:247–256, 1970.

H R Pruppacher and R L Pitter. A semi-empirical determination of the shape of cloud and rain drops. *Journal of Atmospheric Sciences*, 28:86–94, 1971.

Rec. ITU-R P.837-5. *Characteristics of precipitation for propagation modelling*. ITU-R Recommendations and Reports, ITU, Geneva, Switzerland, August, 2007.

Rec. ITU-R P.838-3. *Specific attenuation model for rain for use in prediction methods.* ITU-R Recommendations and Reports, ITU, Geneva, Switzerland, September, 2006.

C A Robertson and J G Fryer. The bias and accuracy of moment estimators. *Biometrika*, 57:57–65, 1970.

E Salonen and S Uppala. New prediction method of cloud attenuation. *Electronics Letters*, 1991.

L R Shenton. Moment estimators and maximum likelihood. *Biometrika*, 45:411–420, 1958.

B E Sheppard and P I Joe. Comparison of raindrop size distribution measurements by a Joss-Waldvogel disdrometer, a PMS 2DG spectrometer, and a POSS dopler radar. *Journal of Atmospheric and Oceanic Technology*, 11:874–887, 1994.

J Shlens. A tutorial on principal component analysis. Technical report, Systems Neurobiology Laboratory, Salk Institute for Biological Studies, April 2009. URL `http://www.snl.salk.edu/~shlens/pca.pdf`.

A F Spilhaus. Raindrop size, shape, and falling speed. *Journal of Meteorology*, 5: 108–110, 1947.

J Testud, S Oury, R A Black, P Amayenc, and X Dou. The concept of "normalized" distribution to describe raindrop spectra: A tool for cloud physics and cloud remote sensing. *Journal of Applied Meteorology*, 40:1118–1140, 2001.

H C S Thom. A note on the Gamma distribution. *Monthly Weather Review*, 86(4): 117–122, 1958.

A Tokay and K V Beard. A field study of raindrop oscillations. Part I: Observation of size spectra and evaluation of oscillation causes. *Journal of Applied Meteorology*, 35 (11):1671–1687, 1996.

A Tokay, A Kruger, and W F Krajewski. Comparison of drop size distribution measurements by impact and optical disdrometers. *Journal of Applied Meteorology*, 40: 2083–2097, 2001.

A J Townsend and R J Watson. The linear relationship between attenuation and average rainfall rate for terrestrial links. *IEEE Transaction on Antennas and Propagation*, 59(3):994–1213, 2011.

A J Townsend, R J Watson, and D D Hodges. Analysis of the variability in the raindrop size distribution and its effect on attenuation at 20-40 GHz. *IEEE Antennas and Wireless Propagation Letters*, 8:1210–1213, 2009.

C W Ulbrich. Natural variations in the anlytical form of the raindrop size distribution. *Journal of Climate and Applied Meteorology*, 22:1764–1775, 1983.

G J G Upton, A R Holt, R J Cummings, A R Rahimi, and J W F Goddard. Microwave links: The future for urban rainfall measurement? *Atmospheric Research*, 77(1-4): 300–312, 2005.

M M J L van de Kamp. Short-term prediction of rain attenuation using two samples. *Electronics Letters*, 38(23):1476–1477, 2002b.

J M Wallace and P V Hobbs. *Atmospheric Science: An Introductory Survey*. Academic Press, Burlington, 2006.

P C Waterman. Scattering by dielectric obstacles. *Alta Freq*, 38:34–35, 1969.

R J Watson, A R Holt, V Marécal, and J Testud. A rainrate-attenuation-reflectivity relation for use in the spaceborne and airborne sensing of rain. *IEEE Transactions Geoscience And Remote Sensing*, 37(3):1447–1450, 1999.

P T Willis. Functional fits to some observed drop size distributions and parametrization of rain. *Journal of the Atmospheric Sciences*, 41(9):1648–1661, 1984.

M K Yau and R R Rogers. An inversion problem on inferring the size distribution of precipitation areas from raingage measurements. *Journal of Atmospheric Sciences*, 41(3):439–447, 1984.

A Zinevich, P Alpert, and H Messer. Estimation of rainfall field using commercial microwave communication networks of variable density. *Advances in Water Resources*, 31:1470–1480, 2008.